The Dissertation Committee for Shreyas Rajasekhara certifies that this is the approved version of the following dissertation:

Development of Nano/Sub-micron Grain Structures in Metastable Austenitic Stainless Steels

Committee:

Paulo J. Ferreira, Supervisor

Llewellyn K. Rabenberg

Desiderio Kovar

Miguel J. Yacaman

Peter F. Green

Leo P. Karjalainen

Antero Kyröläinen

Development of Nano/Sub-micron Grain Structures in Metastable Austenitic Stainless Steels

by

Shreyas Rajasekhara, M.S., B. Tech.

Dissertation

Presented to the Faculty of the Graduate School of

The University of Texas at Austin

in Partial Fulfillment

of the Requirements

for the Degree of

Doctor of Philosophy

The University of Texas at Austin

August, 2007

Acknowledgements

I take this opportunity to thank Dr. Paulo J. Ferreira for his advice, patience and belief in me, Dr. L. P. Karjalainen, professor at the University of Oulu, Finland for insightful comments regarding the dissertation work, and Antero Kyröläinen, senior research engineer at Outokumpu Stainless Oy, Finland for sharing his broad experience in stainless steels and give a direction to this dissertation work. I also thank the other dissertation committee members (Dr. L. K. Rabenberg, Dr. D. Kovar, Dr. P. F. Green and Dr. M. J. Yacaman) for reading the dissertation manuscript and offering constructive criticism.

I once again thank Antero Kyröläinen and Dr. L. P. Karjalainen for inviting me for summer internships at Outokumpu Stainless Oy and the University of Oulu, Finland respectively. I acknowledge the National Science Foundation – USA (Award #DMR-0344234), TEKES – Finland, and the Finnish companies (Outokumpu Stainless Oy, Sanmina Oy, LaserPlus Oy) for providing the financial support for this work. I thank Dr. J. P. Zhou, Transmission Electron Microscopy (TEM) Manager at the Center for Nano & Molecular Science, and Technology, for his training, suggestions and encouragement in the context of TEM work. Also, I would like to acknowledge Ms. Larayne J. Dallas, Assistant Librarian at the Engineering Library, who helped me to trace out hard-to-find literature for this work. I acknowledge Jin H. An and Christopher E. Carlton - graduate students, Jeff C. Pickering and Greg Power – undergraduate students, whose helpful comments were valuable in developing the vision for this work. Additionally, I thank the

faculty and staff in the Materials Science and Engineering program of The University of Texas at Austin for creating a great environment to work.

Lastly, I would like to thank Dr. Rohini Srivathsa – a University of Texas at Austin alumna – who through the Open Mentorship Program at the College of Engineering of the University of Texas - Austin, has mentored me since October 2005 and helped me plan a life after graduate school.

Development of Nano/Sub-micron Grain Structures in Metastable Austenitic Stainless Steels

Publication No.______________

Shreyas Rajasekhara, Ph.D.
The University of Texas at Austin, 2007

Supervisor: Paulo J. Ferreira

This dissertation is a part of a collaborative work between the University of Texas, Austin-Texas, the University of Oulu, Oulu-Finland, and Outokumpu Stainless Oy, Tornio-Finland, , to develop commercial austenitic stainless steels with high strength and ductility. The idea behind this work involves cold-rolling a commercial metastable austenitic stainless steel – AISI 301LN stainless steel to produce strain-induced martensite, followed by an annealing treatment to generate nano/sub-micron grained austenite. AISI 301LN stainless steel sheets are cold-rolled to 63% reduction and subsequently annealed at 600°C, 700°C, 800°C, 900°C and 1000°C for 1, 10 and 100 seconds. The samples are analyzed by X-Ray diffraction, SQUID, transmission electron microscopy, and tensile testing to fundamentally understand the microstructural evolution, the mechanism for the martensite → austenite reversion, the formation of nano/sub-micron austenite grains, and the relationship between the microstructure and the strength obtained in this stainless steel.

The results show that cold-rolled AISI 301LN stainless steel consist of dislocation-cell martensite, heavily deformed lath-martensite and austenite shear bands. Subsequent annealing at 600°C for short durations of 1 and 10 seconds leads to negligible martensite to austenite reversion. These 600°C samples exhibit a similar microstructure to the cold-rolled sample. However, for samples annealed at 600°C for 100 seconds and those annealed at higher temperatures (700°C, 800°C, 900°C and 1000°C) exhibit equiaxed austenitic grains of sizes 0.2μm-10μm and secondary phase precipitates. The microstructural analysis also reveals that the martensite → austenite reversion occurs *via* a diffusion-type reversion mechanism. In this regard, a generalized form of Avrami's equation is used to model the kinetics of martensite → austenite phase reversion. The results from the model agree reasonably well with the experiments.

Furthermore, the activation energy for grain growth in nano/sub-micron grained AISI 301LN stainless steel is found to be ~ 205kJ/mol, which is comparable to values observed in coarse grained commercial stainless steels (AISI 304, 316). However, the driving force for grain growth in nano/sub-micron grained AISI 301LN stainless steel is considerably higher when compared to other stainless steels. Finally, the average grain sizes in AISI 301LN stainless steels are related to the mechanical properties obtained, through the Hall-Petch relationship.

Table of Contents

List of Tables

List of Figures

Chapter 1: Introduction

1.1 MOTIVATION: THE BIG PICTURE

Almost 1.1B tons of steel was consumed worldwide in 2006 [1] representing a global economy of ~ \$0.8 trillion [1]. Following the current trend in globalization, the demand for steel continues to be strong owing to increased consumption from emerging economies (Brazil, Russia, India and China) and a continued demand from developed countries to maintain/upgrade their infrastructural needs [1]. Considering the importance of this industry, one of the goals of scientists and engineers working in this field has been to develop alloys that exhibit both high strength and high ductility. This combination of properties would allow scientists and engineers working in industries, such as Oil & Gas, Construction, Food, Machinery and Automotive to design safer, durable, more fuel-efficient (in case of the automotive industry) structures. Unfortunately, until the 1910-30s all of the abovementioned industries were using only a few steel grades, namely high carbon steel and medium carbon steel, with a tensile strength of approximately ~ 450MPa and a total elongation of ~ 30% [2]. These steels were adequate for simple engineering structures but became inadequate as design complexities grew and safety requirements became more stringent. Moreover, the development of new steel grades was hampered by 1) lack of theoretical understanding, 2) lack of available technology, and 3) the onset of two world wars, which kept new developments in secret.

The 1940-70s saw rapid progress in steel manufacturing, as well as research, resulting in the development of advanced ferrous alloys with enhanced properties. Of particular importance was the development of various families of stainless steels (SS) (austenitic, ferritic, martensitic, duplex stainless steels), dual-phase steels (steels with a combination of ferrite and martensite phases), and TRIP steels (steels with a good combination of strength and ductility, achieved through phase transformations). More recently, further developments have produced steels that have either high strength and poor ductility (Complex phase and Martensite steels) or low strength and high ductility (IF Steels) (Fig. 1.1).

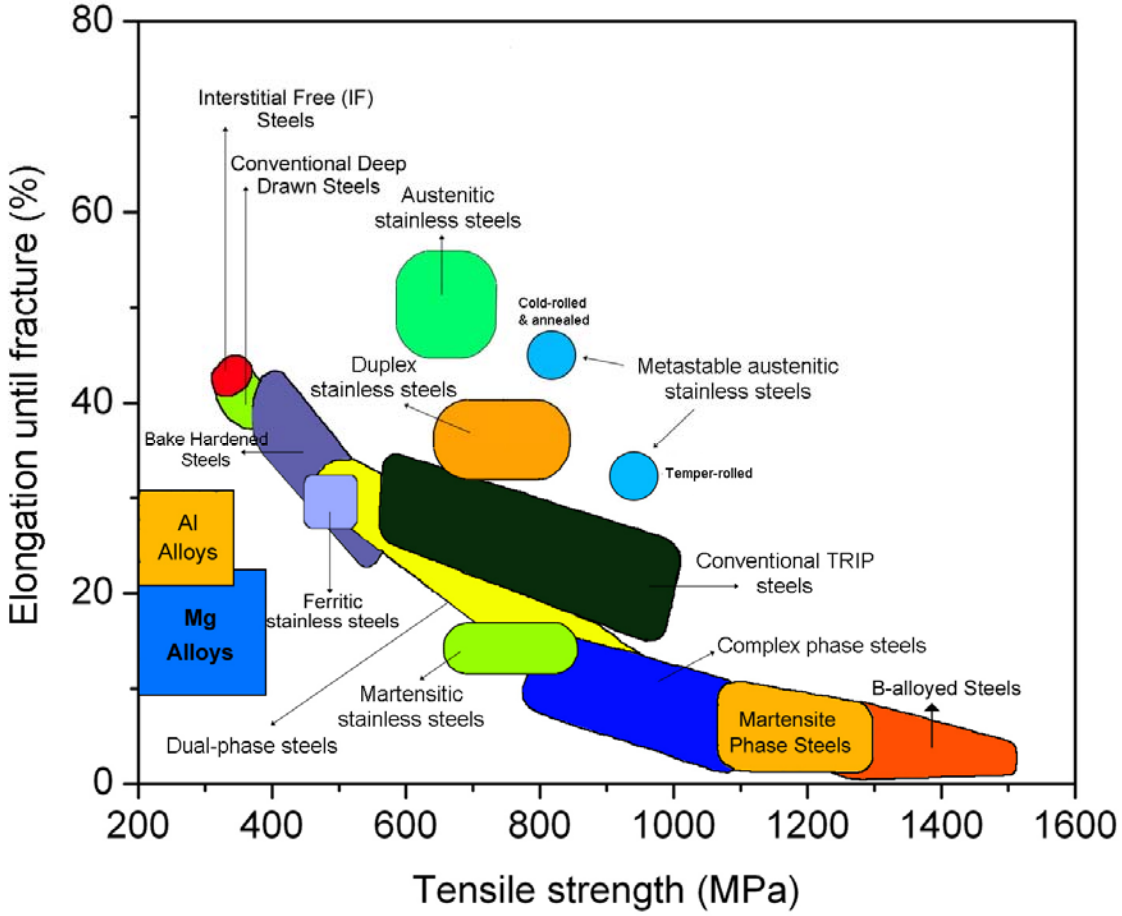

Figure 1.1: Elongation until fracture (%) versus tensile strength for a variety of alloys [Adapted from 3-8].

In this context, the roadmap for the next twenty-five years of the ferrous industry, as laid out by the European Steel Technology Platform [4] is to develop Fe-based alloys that have exceptional strength, ductility (Fig. 1.2) [3-7]. With these novel materials, engineers will be able to design complex structures that can sustain natural environments (such as humid air and corrosive media), be durable and light-weight. In this regard, SS are good candidates due to their excellent corrosion resistance properties, but they lack the combination of high strength and ductility. As we uncover exciting potential applications for SS, an important question arises: *Is it possible to develop commercial SS with high strength and high ductility?* This is the focus of this dissertation.

More specifically, this work is the result of a project that was jointly proposed in 2003 to the National Science Foundation – USA and TEKES – Finland, by the University of Texas at Austin, the University of Oulu, the second largest university in Finland, and one of the largest stainless steel producers in the world – Outokumpu Stainless Oy with headquarters in Finland (www.outokumpu.com). The materials used in this work were developed at Outokumpu Stainless Oy while the research and analysis was carried out at the University of Texas, Austin and the University of Oulu.

Furthermore, publications resulting from the independent research by our collaborators in Finland during this collaborative work and in the context of this project are included where deemed necessary [5-8].

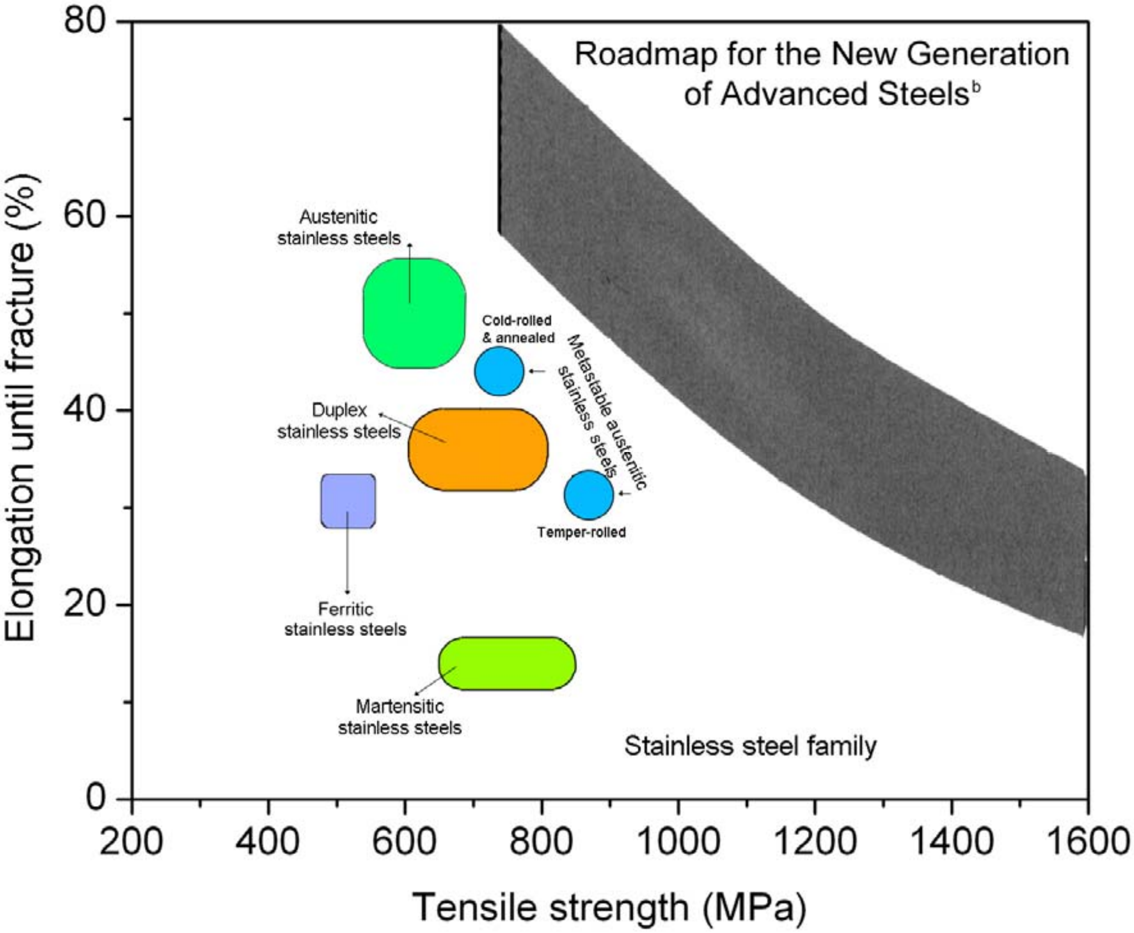

Figure 1.2: Roadmap for the new generation of SS with high strength and ductility [Adapted from 3-8].

1.2 THE APPROACH

In order to obtain a SS with desired high strength and ductility capable of following the roadmap show in Figure 1.2, a commercial metastable austenitic SS was developed and cold-rolled at Outokumpu Stainless Oy, Tornio-Finland to obtain deformation-induced martensite, followed by a short annealing treatment, carried out at the University of Oulu, to revert the martensite phase to nano/submicron grained austenite (Fig. 1.3). This idea can be better understood by following the sequence of microstructures shown in Fig. 1.4. Initially, a coarse-grained metastable austenitic SS (Fig 1.4a), is transformed into lath-type martensite by cold-rolling (Fig. 1.4b). Further cold-rolling results in the formation of dislocation-cell type martensite with a large number of defects and high dislocation density (Fig. 1.4c). Annealing of the deformation induced martensite reverts the microstructure to nano/sub-micron grained austenite with enhanced strength, high ductility and good formability.

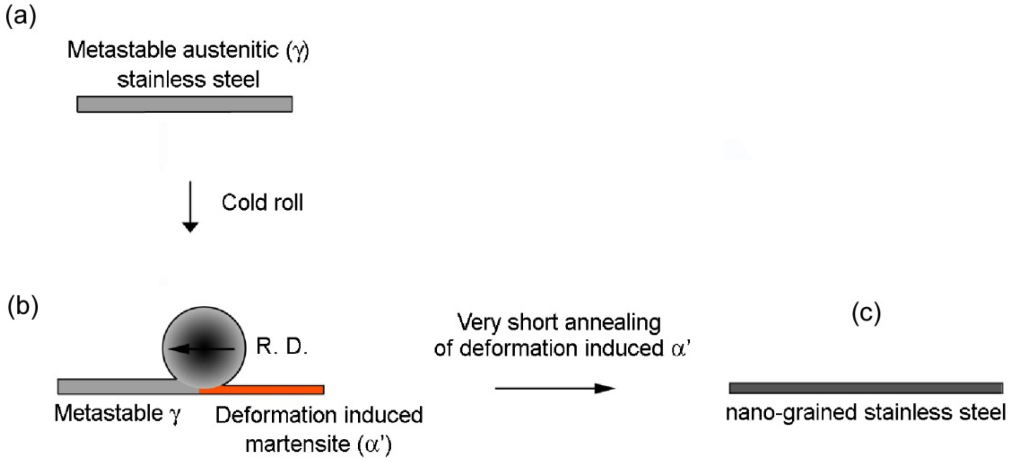

Figure 1.3: Processing route for producing nano/sub-micron grained austenite in metastable austenitic SS.

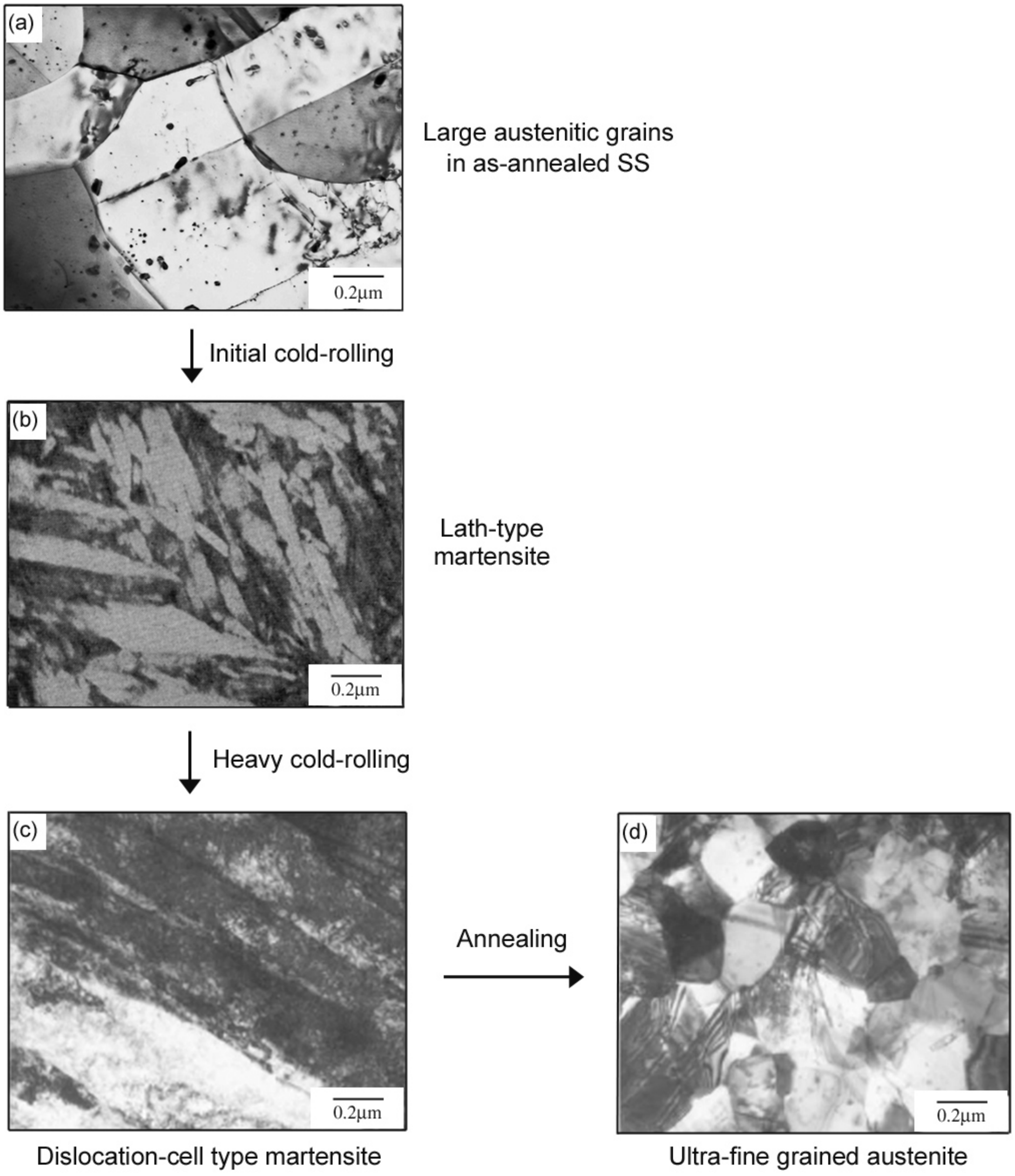

Figure 1.4: Desired microstructure at the end of each processing step [9, 10, 11]. The images shown were obtained by a transmission electron microscopy.

1.3 DISSERTATION OBJECTIVES & MAIN CONTRIBUTIONS

1.3.1 Objectives

In order to develop nano/submicron SS with high strength and high ductility, the specific objectives of this dissertation are as follows:

1. To understand the kinetics of the martensite (α') → austenite (γ) phase reversion in AISI 301LN SS, in particular whether the phase transformation occurs through a diffusion-controlled versus a shear-controlled mechanism.
2. To identify and understand the formation of nano/submicron austenite grains and microstructural evolution in AISI 301LN SS.
3. To understand the kinetics of grain growth in nano/submicron grained AISI 301LN SS.
4. To establish a relationship between the microstructure of nano/submicron grained AISI 301LN SS and the mechanical properties.

1.3.2 Main Contributions

The main contributions of this dissertation are:

1. Identifying and understanding the effect of annealing time and temperature on the microstructure evolution and formation of nano/submicron austenite grain in AISI 301LN SS by transmission electron microscopy analysis of microstructure images. These studies allow us to understand the morphology of the cold-rolled AISI 301LN SS, as well as nano/sub-micron grained SS obtained after short annealing. In addition, the microstructural work enables us to estimate whether

the annealing treatment is efficient in reverting the martensite to austenite, and determine the α' → γ reversion mechanism occurring in this SS.

2. Modeling the martensite → austenite reversion mechanism occurring in SS. The current understanding of austenite phase reversion is restricted to microstructural observations made in several non-commercial SS [12-15]. No theoretical basis exists to support these microstructural observations. In the present collaborative work between the University of Texas, the University of Oulu, and Outokumpu Stainless Oy, extensive microstructural observations has been carried out on both commercial and non-commercial SS, and phenomenological models have been put forth to explain α' → γ reversion in different SS (commercial and non-commercial) [7, 8]. However, the fundamental understanding of the α' → γ reversion is not yet available. In this dissertation, the governing α' → γ reversion mechanism in AISI 301LN SS is identified through annealing experiments to induce the α' → γ phase transformation. Subsequently, a theoretical model is developed from first principles to explain the α' → γ reversion observed in AISI 301LN SS.

3. Understanding the kinetics of grain growth in nano/submicron grained AISI 301LN SS, particularly, the parameters that govern grain growth, such as the activation energy and driving force. From this analysis, grain growth models are developed allowing us to predict optimal annealing conditions for nano/sub-micron austenite grain formation.

4. Establishing and understanding the relationship between the microstructure of nano/submicron AISI 301LN SS and the mechanical properties, as a function of

annealing time and temperature. In particular, this work shows the effect of annealing time and temperature on the role played by various strengthening mechanisms and their direct influence on the Hall-Petch relationship.

1.4 OUTLINE OF SUBSEQUENT CHAPTERS

This dissertation is organized, to facilitate the reader in following the approach described in section 1.2.

Chapter 2 starts by describing the fundamental premises behind reducing the grain size to the nano/submicron range to promote grain size strengthening. Next, a description of the basic ideas behind the formation of nano/submicron grained SS by heavy cold rolling SS, followed by a short annealing is presented. The discussion then turns into the selection of the commercial SS that can be used for the demonstration of the aforementioned concept. Subsequent attention is focused on understanding the role of alloying elements present in AISI 301LN SS, which was selected for this work. Next, attention is focused on the mechanisms associated with the formation of deformation - induced martensite from metastable austenite, upon cold-rolling. The discussion then turns into the $\alpha' \rightarrow \gamma$ reversion phase transformation taking place during the annealing treatment.

In Chapter 3, the experimental procedures required to accomplish the objectives of this thesis are discussed. In particular, the processing methods to produce AISI 301LN SS, as well as X-Ray diffraction, SQUID magnetic measurements, transmission electron microscopy and tensile testing techniques are discussed.

Chapter 4 presents the results obtained from the experimental procedures described in Chapter 3, in particular the phase fraction of austenite and martensite, grain size and microstructure evolution of AISI 301LN SS obtained, as a function of annealing time and temperature.

In Chapter 5, the dissertation addresses the key issues pertaining to the development of nano/submicron grained SS, namely 1) the influence of annealing conditions on the kinetics of α' → γ phase reversion, 2) the influence of annealing conditions on microstructure evolution, 3) the influence of annealing conditions on the kinetics of nano/sub-micron grain formation, 4) the influence of annealing conditions on the mechanical properties. The discussion of these topics relates the experimental results obtained in this thesis and their relation with previous results obtained from several authors. The discussion presented herein will hopefully improve the current state of understanding and help develop this relatively new field of nano/submicron grained SS.

Finally, the general findings of this work are summarized in Chapter 6. The dissertation concludes with a discussion of possible future work.

Chapter 2: State of Understanding

2.1 BASIS FOR DEVELOPING NANO/SUB-MICRON GRAINED STAINLESS STEELS

In recent years, the topic of grain size strengthening has been receiving wide attention due to the production of ultra-fine grains materials with enhanced mechanical properties. This concept has been demonstrated in various types of steels, where tensile strengths of ~ 800MPa have been reported [20, 21].

Classically, grain size strengthening can be described by the Hall-Petch equation [22, 23, 24] given by:

$$\sigma_Y=\sigma_0+kd^{-1/2} \tag{2.1}$$

where σ_0 is the friction stress in the absence of grain boundaries, *k* is a constant and *d* is the grain size. In other words, the yield stress increases as grain size decreases because pile-ups in fine grained materials contain fewer dislocations, the stress at the tip of the pile-up decreases and thus, a larger applied stress is required to generate dislocations in the adjacent grain.

Past experiments have demonstrated tensile strengths of ~ 800MPa with grain sizes in the range 0.5μm-1μm in low-carbon steels [20, 21]. In the case of SS, a similar effect has been demonstrated by di Schino in a low nickel (LNi) non-commercial SS, where a ~ 25% increase in tensile strength was observed when the austenite grain size was decreased from 50μm to ~ 3μm. A comparable effect was observed for AISI 304 SS (Fig. 2.1) [16-18]. In this regard, producing nano/sub-micron grains SS would lead to a significant improvement in strength (Fig. 2.1). Previous research has demonstrated the production of submicron grains sizes of ~ 0.8µm in non-commercial SS [12-14], and nanoscale grain sizes of ~ 100nm in non-commercial SS [11]. However prior to this collaborative work between Outokumpu Stainless Oy, the University of Oulu, and the University of Texas at Austin, the production of commercial SS with nano/submicron grain sizes and their impact on mechanical properties, in particular – strength, has not been demonstrated and discussed.

As discussed in section 1.2, by heavily cold rolling of a metastable austenitic SS steel to produce deformation induced martensite can be produced. The martensite phase consists of regions of martensite laths and martensitic dislocation cells [20, 21, 25-29]. These regions, especially the dislocation-cell martensite are ideal for the nucleation of nano/sub-micron grains upon annealing. This thermo-mechanical treatment has seen tremendous interest from researchers, who have demonstrated ultra-fine grains produced by this technique in non-commercial SS [12-14, 19].

.

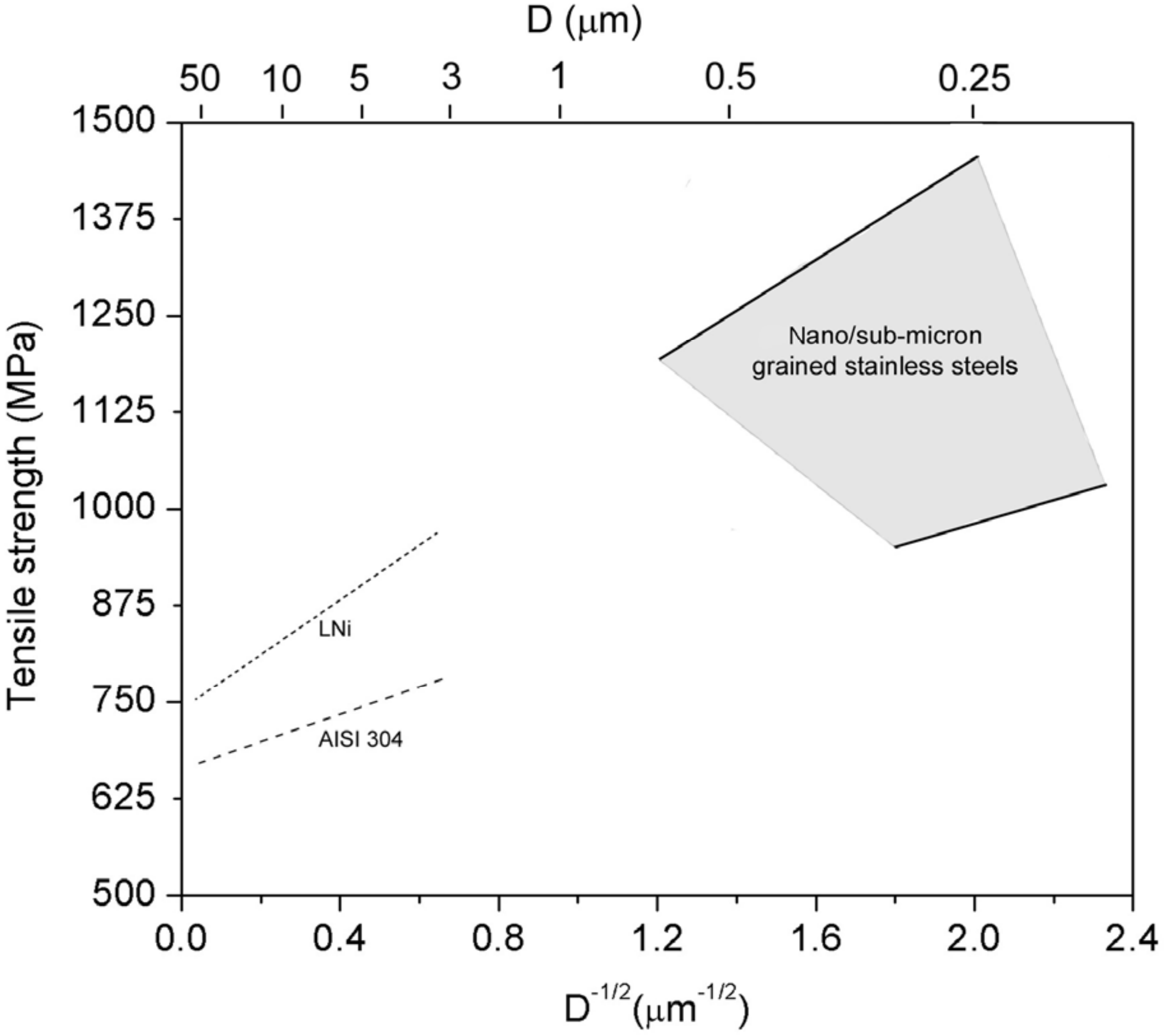

Figure 2.1: The relationship between grain size and tensile strength in an low nickel (LNi) alloy and AISI 304 SS [18]. The gray band shows the envisaged strength enhancement due to grain boundary refining for nano/sub-micron grained SS.

2.2 STAINLESS STEEL SELECTION

In order to obtain nano/sub-micron SS it is crucial to be able to attain deformation-induced martensite upon cold rolling. While the cold rolling reduction per rolling pass is an important consideration to obtain deformation-induced martensite in SS, the stability of austenite determines to a large extent the amount of deformation-induced martensite that can be obtained after cold rolling reduction. In particular, metastable austenitic SS are ideal materials for this process. Thus, several commercial metastable austenitic SS grades – AISI 301LN, 301, 304 and 316 – whose composition is shown in Table 2.1, were initially considered as candidates for the present work. In this regard, the amount of deformation induced martensite as a function of cold reduction was obtained for these alloys (Fig. 2.2). Previous research conducted by Shrinivas & Murr [27] demonstrated that for 60% cold reduction, negligible fraction of martensite was produced in AISI 316 SS, whereas ~ 40% martensite was observed in AISI 304 SS (Fig. 2.2).

Table 2.1: Composition of various metastable austenitic SS (wt %).

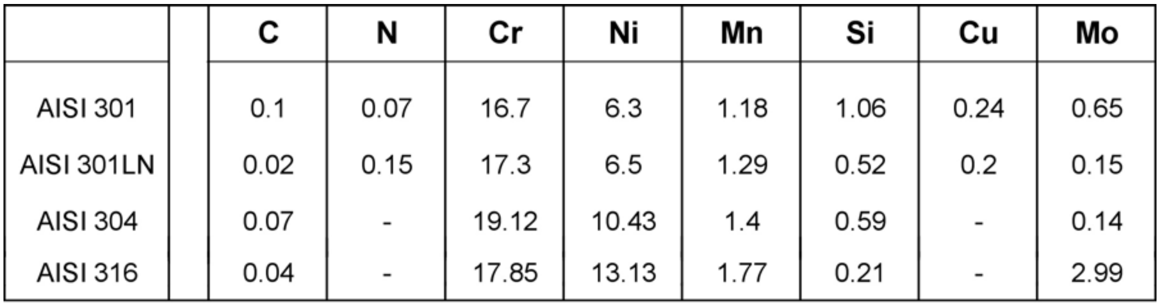

		C	N	Cr	Ni	Mn	Si	Cu	Mo
AISI 301		0.1	0.07	16.7	6.3	1.18	1.06	0.24	0.65
AISI 301LN		0.02	0.15	17.3	6.5	1.29	0.52	0.2	0.15
AISI 304		0.07	-	19.12	10.43	1.4	0.59	-	0.14
AISI 316		0.04	-	17.85	13.13	1.77	0.21	-	2.99

Additional ferritoscope measurements carried out at the Outokumpu Stainless Oy, Tornio Research Center, Finland, determined that AISI 301 SS exhibited close to 75% deformation-induced martensite when cold rolled to ~ 60% reduction, whereas ~ 100% deformation-induced martensite was observed for AISI 301 LN SS. Based on this data

(Fig 2.2), the AISI 301LN SS was considered the best choice for the thermo-mechanical processing described above.

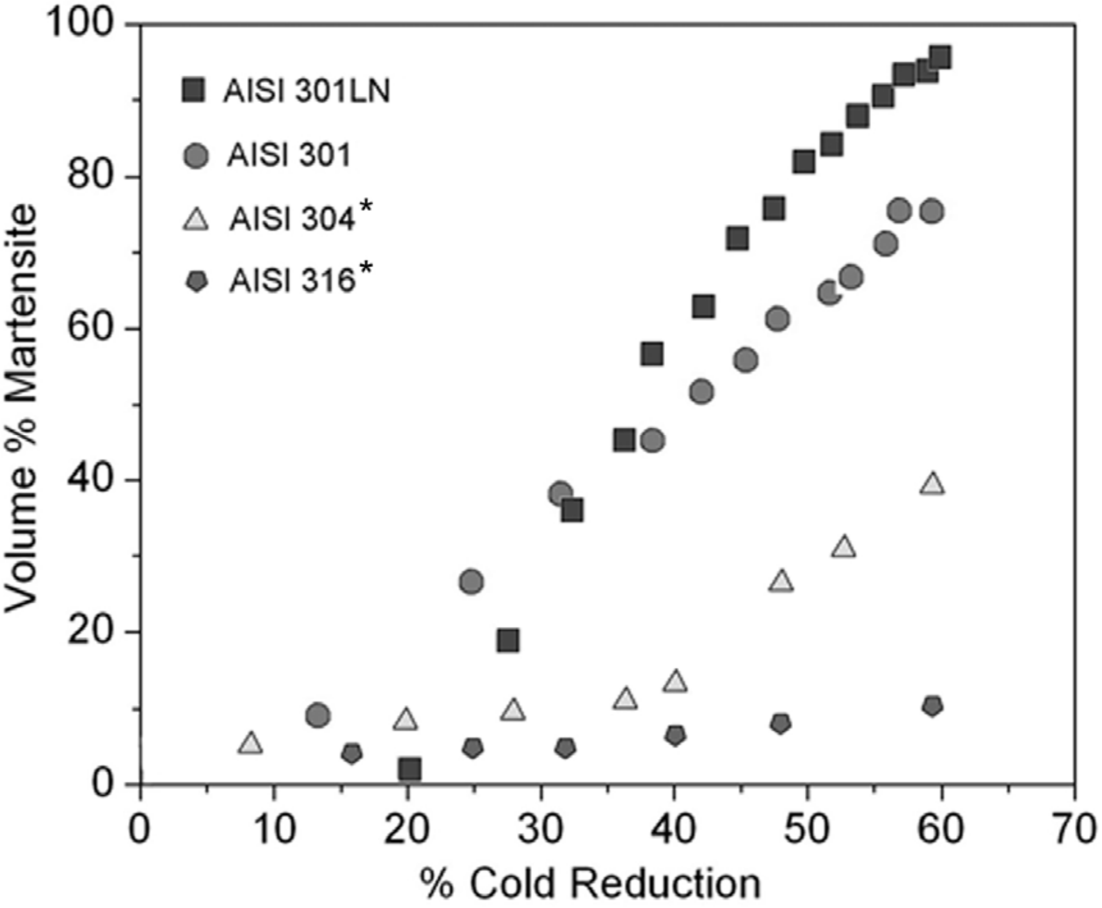

Figure 2.2: Volume percentage of martensite as a function of cold reduction for various commercial SS grades. Data for AISI 304 and 316 SS was adapted from Shrinivas & Murr [27].

2.3 COMPOSITION OF AISI 301LN AUSTENITIC STAINLESS STEEL

AISI 301LN SS metastable austenitic SS contain various alloying elements, namely chromium, nickel, manganese, molybdenum, nitrogen, trace concentrations of carbon, silicon and copper. In this regard, the influence of each of these elements on the properties is discussed briefly in the subsequent sections.

2.3.1 Substitutional Alloying Elements

2.3.1.1 Chromium

Chromium is responsible for the 'stainless' characteristic of AISI 301LN SS steels. Within SS, Cr forms a thin oxide Cr_2O_{3-x} on the surface of Fe-Cr alloys, preventing further oxidation and corrosion. AISI 301LN SS has ~ 16-18% Cr content, resulting in excellent corrosion resistance properties [30]. As Cr is a ferrite stabilizer, additional alloying elements, such as Ni are normally added to a SS to stabilize the austenite phase [31].

2.3.1.2 Nickel

Nickel is added to AISI 301LN SS to stabilize the austenite phase and make the SS heat treatable. As Ni expands the austenite phase loop (Fig. 2.3), SS with ~ 5-10% Ni can be solution annealed and cooled to obtain a metastable austenite phase [32]. In addition, Ni decreases the susceptibility to form Cr-rich sigma phase due to its ability to stabilize the austenite phase [33], thereby improving the toughness and bending properties of SS. Furthermore, the low Ni content in AISI 301LN SS (~6.5%) makes it attractive from an economic perspective, because worldwide nickel resources are scarce [33].

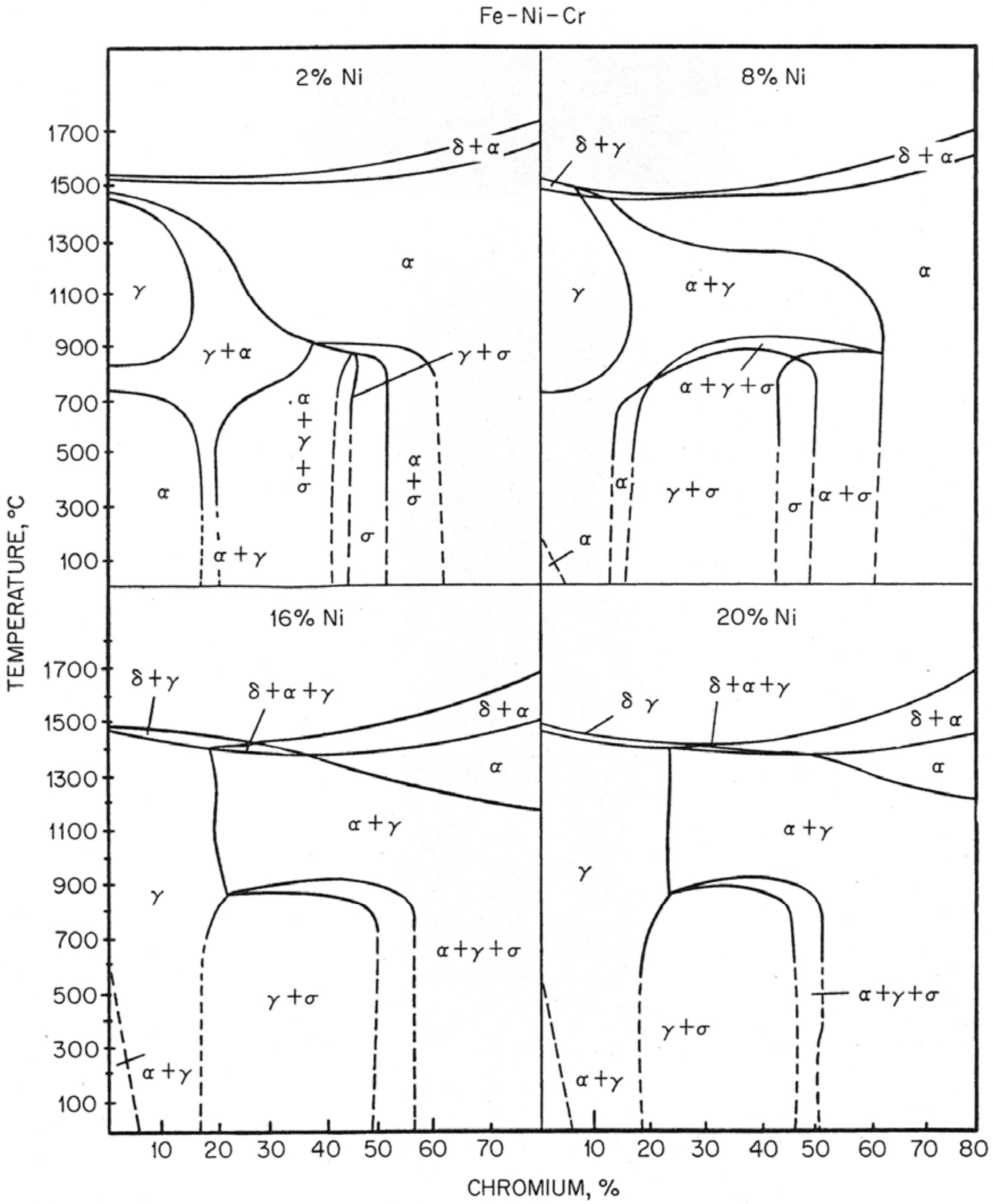

Figure 2.3: Influence of nickel on austenite phase stability in various Fe-Cr alloys [32].

2.3.1.4 Molybdenum

In addition to Cr, Mo also plays an important in enhancing the corrosion resistance of AISI 301LN SS. The addition of Mo raises the threshold potential needed for galvanic current to flow when SS are exposed to corrosive media (HCl, H_3PO_4, NaCl solutions) [34]. The corrosion resistance due to the presence of Mo becomes even more pronounced at high temperatures – for instance, AISI 304 SS (0% Mo) registered almost ten times more weight loss when compared with AISI 316 SS (3% Mo), when they were both exposed to phosphoric acid maintained at 113°C [35]. On the other hand, high Mo content (>1 %) in Fe-Cr-Ni alloys promotes the formation of chi phase, which may lead to brittle failure [35]. For low temperature applications, the Mo concentration is typically less than 0.5%, (AISI 301LN SS used for this work contains ~ 0.15% Mo).

2.3.1.3 Manganese

The presence of Mn in SS increases the solubility of nitrogen (a strong solid solution strengthener, as well as a strong austenite stabilizer), in the austenite matrix making it possible to produce high nitrogen SS, such as AISI 301LN SS. Mn also plays an indirect role in aiding corrosion resistance by combining with sulfur to form manganese sulphides [36, 37]. This is important because the presence of free sulfur leads to the formation of chromium sulphide precipitates, thereby decreasing the local Cr concentration. The result is an increased possibility for localized corrosion, also termed as pitting corrosion. On the other hand, an excess concentration of Mn in the SS composition should be avoided due its deleterious effect on the refractory lining leading to the formation of inclusions (CaO, MgO) in SS [38]. Manganese additions to SS are administered with caution and are typically limited to ~ 1-2%.

2.3.2 Interstitial alloying elements

2.3.2.1 Nitrogen

Despite the important role played by substitutional elements, they do not provide a significant strengthening effect [39]. For this reason, the interstitial element nitrogen is added to AISI 301LN SS (Fig. 2.4). The strengthening effect is due to the elastic interaction between nitrogen atoms, which causes lattice distortions, and dislocations, leading to dislocation pinning and higher strength. In addition, nitrogen helps stabilizing the austenite phase [40, 41].

2.3.2.2 Carbon

Besides nitrogen, carbon is also used to provide solid solution strengthening in SS (Fig. 2.4b) and to stabilize the austenite phase. The strengthening effect of carbon is similar to that of nitrogen where it elastically interacts with dislocations, thereby reducing the mobility of dislocations [41-43]. However in SS, carbon readily combines with chromium to form Cr-carbides that deplete the austenite matrix from Cr, resulting in a significant loss of corrosion resistance. This phenomenon is termed “sensitization”. In AISI 301LN SS used in this work, sensitization is avoided due to the negligible carbon concentration (~ 0.017%).

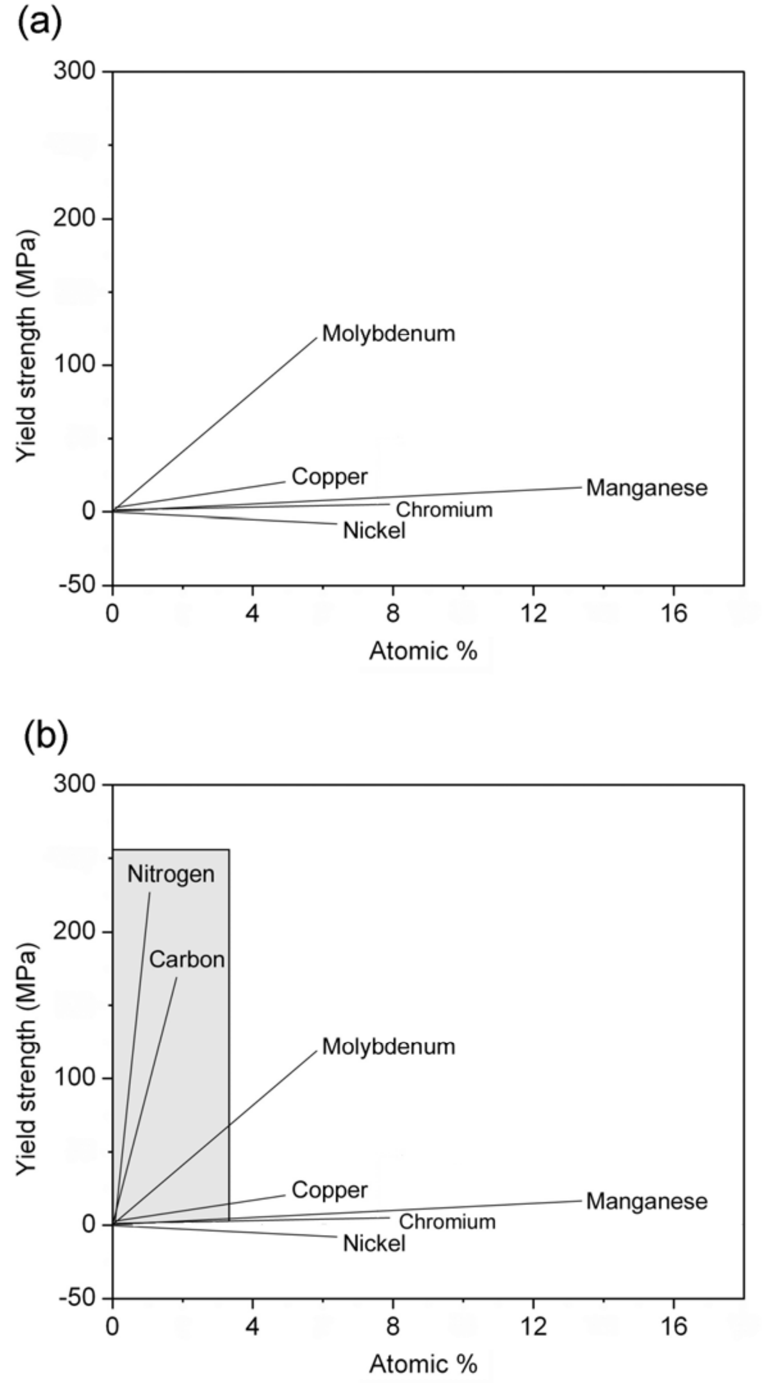

Figure 2.4: (a) Effect of substitutional elements on the yield strength of AISI 301LN SS, (b) Effect of interstitial elements on the yield strength of AISI 301LN SS [39].

2.4 THERMO-MECHANICAL TREATMENT

In order to produce nano/sub-micron grained AISI 301LN SS, the alloy is subjected to a thermo-mechanical treatment, which consists of two parts: 1) cold rolling reduction of metastable austenitic SS leading to the formation of deformation-induced martensite, and 2) annealing of deformation-induced martensite to obtain nano/sub-micron grained austenite phase. The following sections discuss these two steps in the process.

2.4.1 Cold reduction: Austenite → Martensite Transformation

2.4.1.1 Martensite nucleation

In terms of crystal structure, two kinds of martensites are observed in stainless steels – 1) hcp ε-martensite, and 2) bcc α' martensite [44-47] . Typically, α' martensite embryos nucleate at shear band intersections [27, 44], which form upon minimal deformation. These shear bands consist of stacking faults, deformation twins and ε-martensite.

Several models have been proposed to describe the mechanisms of α' nucleation [48-52]. In particular, the model proposed by Cohen is the most intuitive, where perfect dislocations initially dissociate into partial dislocations due to the low stacking fault energy of SS. The transformation of the parent austenite starts when a $\frac{a_{fcc}}{2}\langle 110\rangle$ screw dislocation (Fig. 2.5a) dissociates into partial dislocations of type $\frac{a_{fcc}}{6}\langle 112\rangle$. One of the partial dislocations advances on every third $(111)_{fcc}$ plane of the austenite and spreads its core over three $(111)_{fcc}$ planes to become a $\frac{a_{fcc}}{18}\langle 112\rangle$ partial (Fig. 2.5b). This process increases the distance between successive $(111)_{fcc}$ planes (by ~ 5.4%), causes the angle between the modified $(111)_{fcc}$ plane and the unchanged $(100)_{fcc}$ planes to change from 60° to 70°32' [48], and increases the spacing in one of the six $(110)_{fcc}$ planes. Such displacements of the $\frac{a_{fcc}}{18}\langle 112\rangle$ partials result in the appropriate $\{110\}_{bcc}$ planes but not the proper stacking [48]. In order to complete the transition to the BCC structure, the stacking in Fig. 2.5b is sheared in such a way to produce a new stacking sequence comprising of seven $\frac{a_{bcc}}{8}\langle 011\rangle$ partial dislocation planes followed by a combination of $\frac{a_{bcc}}{6}\langle 112\rangle+\frac{a_{bcc}}{8}\langle 011\rangle$ partial dislocations on every eighth plane (Fig. 2.5c). This structure is a semi-coherent martensitic structure that contains residual strain due to the motion of partial dislocations [49, 50]. The addition of $\frac{a_{fcc}}{2}\langle 110\rangle$ screw dislocations to the structure in Fig. 2.5c mitigates the residual strain field produced by the partial dislocations to create the martensitic structure shown in Fig. 2.5d. The martensite obtained through this sequence of operations is related to the austenite phase through the Kurdjumov-Sachs relationship [44, 53], given by $(111)_{fcc} \,||\, (101)_{bcc}$ and $[1\bar{1}0]_{fcc} \,||\, [11\bar{1}]_{bcc}$.

In order for the transformation from martensite to austenite to take place, a sufficient amount of energy is required to overcome the activation barrier for nucleation. As shown in Fig.2.6, the temperature T_o defines the point where the chemical free energies of martensite and austenite are equal. Therefore, to initiate the transformation, it is necessary to undercool the austenite phase to a temperature M_s, well below T_o in order to provide the required Gibbs free energy $\Delta G_{M_s}^{\gamma\to\alpha'}$. One other method of inducing martensite formation is to deform the austenite phase by an applied stress. This external stress provides an additional energy U (Fig. 2.6). Consequently, the necessary $\Delta G_{M_s}^{\gamma\to\alpha'}$ can be attained at higher temperatures (Fig. 2.6). This analysis is mathematically expressed as [54, 55]:

$$\Delta G_{M_s}^{\gamma\to\alpha'} = \Delta G_{T_1}^{\gamma\to\alpha'} + U\,, \tag{2.2}$$

where $\Delta G_{T_1}^{\gamma \to \alpha'}$ is the difference in chemical free energy between martensite and austenite phases and U the strain energy associated with an externally applied stress.

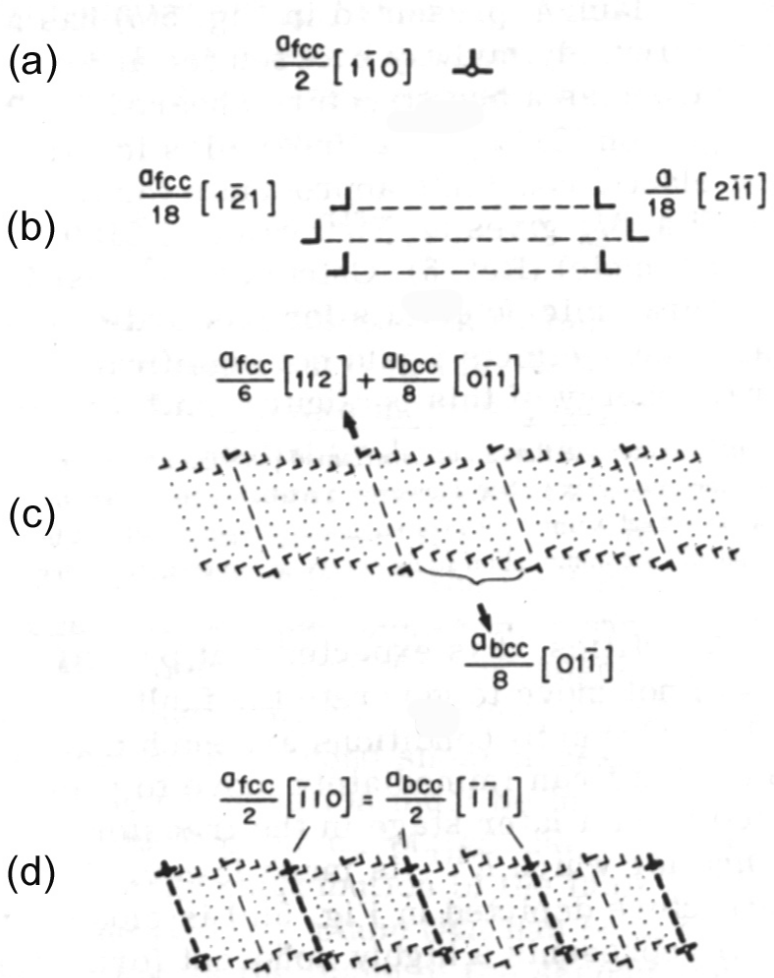

Figure 2.5: (a) Existing $\frac{a_{fcc}}{2}\langle 110\rangle$ perfect dislocation, (b) Dissociation of partial dislocations by spreading of the dislocation core over consecutive planes to produce a fault structure, (c) Relaxation of the fault to a bcc structure, and (d) fault structure after new screw dislocations are added, which mitigate the remaining strain field associated with the presence of partial dislocations [49, 50].

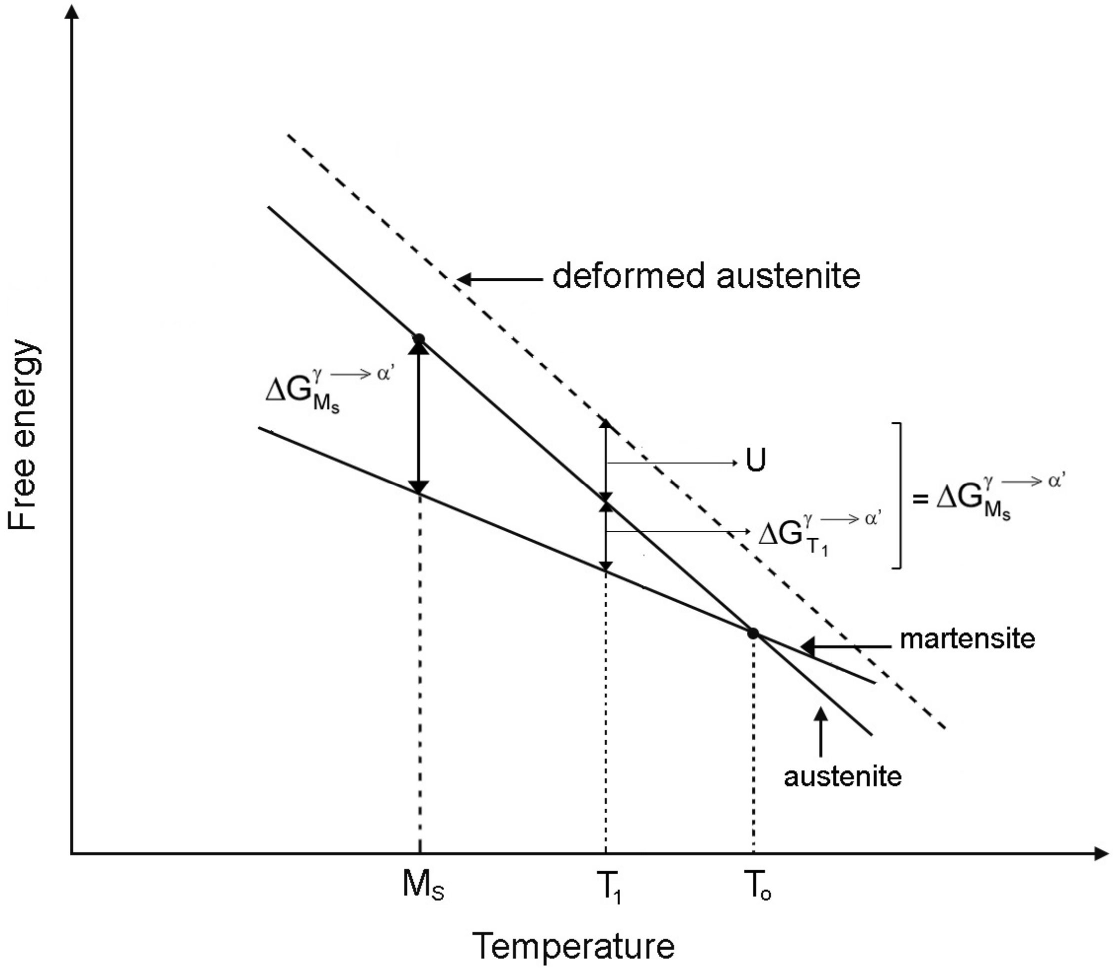

Figure 2.6: Gibbs free energy for the austenite and martensite. The presence of a mechanical driving force *U* when an external stress is applied leading to a less stable austenite phase [54].

2.4.1.2 Deformation-induced martensite

According to the work of Tamura [54], Fisher [56], and Patel [57], *U* is comprised of two terms: 1) the shear stress that is resolved along the γ/α'habit planes, and (2) the normal stress that is resolved perpendicular to these habit planes. Thus, *U* can be written as:

$$U = \tau\gamma_o + \sigma\varepsilon_o, \tag{2.3}$$

where τ is the shear stress, γ_o the shear strain, σ the normal stress and ε_o the normal strain. τ is always positive since all habit plane permutations allow the activation of martensitic transformation due to shear stress. However, normal stresses can either help (positive) or oppose (negative) the martensitic transformation depending on the type applied stress.

Assuming a uniaxial stress condition, the magnitude of normal and shear stress components are obtained from a Mohr's analysis shown in Fig. 2.7. Thus, the influence of an applied uniaxial stress can be estimated through the expressions [56, 57]:

$$\tau = \frac{1}{2}\sigma_1 \sin 2\theta, \tag{2.4}$$

$$\sigma = \pm\frac{1}{2}\sigma_1(1 + \cos 2\theta), \tag{2.5}$$

where σ_1 is the absolute value of applied stress (compressive or tensile) and θ is the angle between the specimen axis and the normal to the habit plane.

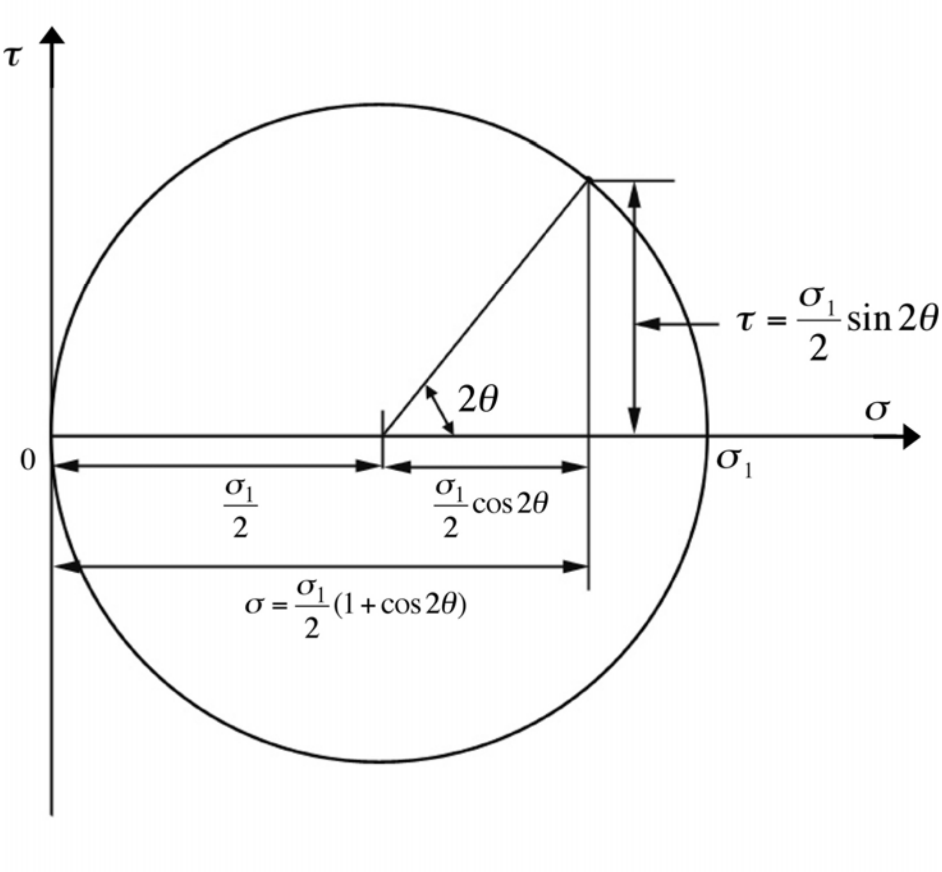

Figure 2.7: Mohrs' circle analysis to resolve the applied external stress σ_1 into normal and shear components [57].

On this basis, the work done for the martensitic tranformation can be rewritten as:

$$U = \frac{1}{2}\gamma_o \sigma_1 \sin 2\theta \pm \frac{1}{2}\varepsilon_o \sigma_1 (1 + \cos 2\theta), \tag{2.6}$$

where all the symbols have the same meaning as before. The maximum value of U achieved for the martensitic transformation can obtained by differentiating U with respect to θ, as follows:

$$\frac{dU}{d\theta} = \frac{1}{2}\gamma_o \sigma_1 \cos 2\theta \mp \frac{1}{2}\varepsilon_o \sigma_1 (\sin 2\theta) = 0, \tag{2.7}$$

This gives $\tan 2\theta = \pm\frac{\gamma_o}{\varepsilon_o}$, from which the values of $\sin 2\theta$ and $\cos 2\theta$ can be obtained as:

$$\sin 2\theta = \frac{\gamma_o}{\sqrt{\gamma_o^2 + \varepsilon_o^2}}, \tag{2.8}$$

$$\cos 2\theta = \frac{\varepsilon_o}{\sqrt{\gamma_o^2 + \varepsilon_o^2}} \tag{2.9}$$

Thus, U_{max} is given by:

$$U_{\max} = \pm\frac{\gamma_o^2 \sigma_1}{\sqrt{\gamma_o^2 + \varepsilon_o^2}} \pm \varepsilon_o \sigma_1 \left(1 \pm \frac{\varepsilon_o^2}{\sqrt{\gamma_o^2 + \varepsilon_o^2}} \right), \tag{2.10}$$

where all the terms have their previous definitions. Equation (2.10) can then be used to estimate the change in M_s as a function of temperature, according to the relationship [56]:

$$\frac{dM_s}{dT} = \frac{U_{\max}}{d(\Delta G_{M_s}^{\gamma\to\alpha'})/dT}, \tag{2.11}$$

where the term $\frac{d(\Delta G_{M_s}^{\gamma\to\alpha'})}{dT}$ has been experimentally determined by Fisher & Turnbull [56], and Patel & Cohen [57] for various Fe-Ni-C alloys. According to equation (2.11), the change in M_s as a function of applied stress is shown in Fig. 2.8. While uniaxial tensile and compressive stresses raise the martensitic start temperature M_S, a hydrostatic stress (where $\tau = 0$ and $U_{\max} = -\varepsilon_o \sigma$) can depress the martensite start temperature (Fig. 2.8).

So far, equations (2.3)-(2.11) assume a range of applied stresses within the elastic regime of the parent austenite phase, such that upon the application of stress σ_B (lower than the yield stress of austenite phase), the martensite start temperature is raised to the point B in Fig. 2.9. Thus, for the case where the magnitude of the applied stress equals the yield strength of the austenite phase σ_C, the martensite start temperature is raised to the point C given by M_s^σ (Fig. 2.9). When the applied stress exceeds the yield strength of the austenite phase σ_D, the austenite phase deforms plastically, resulting in the creation of more nucleation sites [58]. Such a process is termed plastic strain-induced martensite nucleation and the formation of strain-induced martensite occurs at a temperature T^D greater than M_s^σ (Fig. 2.9). In general, the strain-induced martensite nucleation can be achieved up to a temperature M_d.

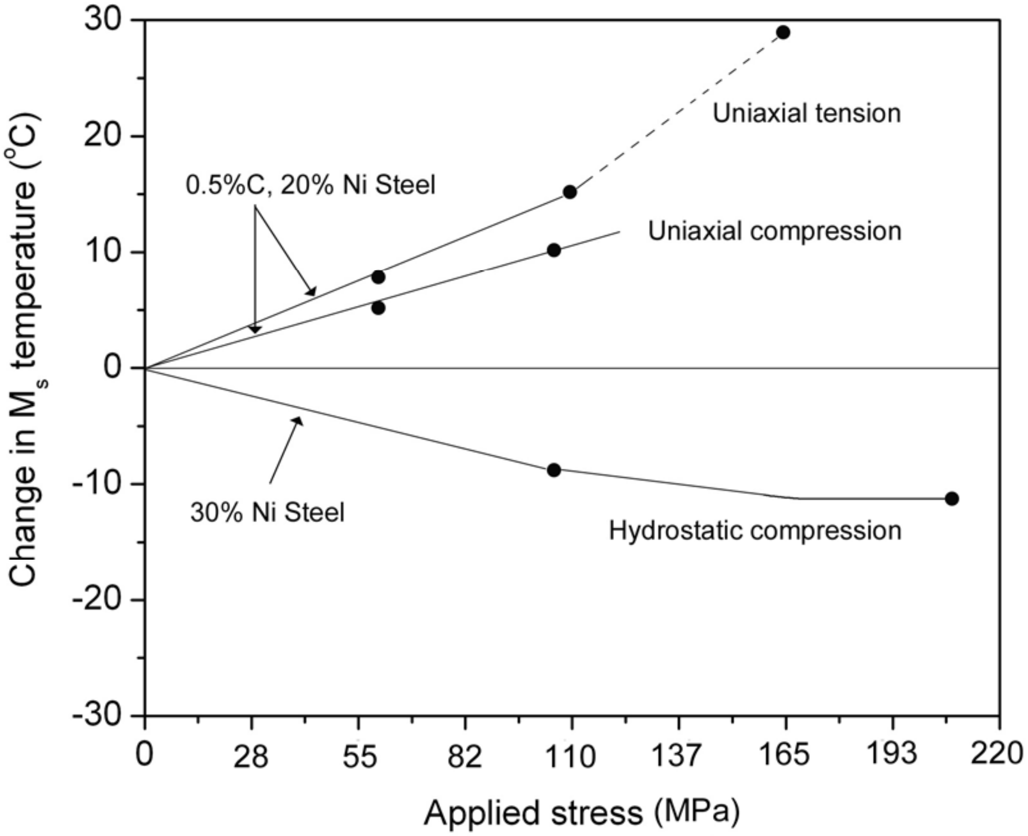

Figure 2.8: Change in martensite start temperature as a function of applied stress [56].

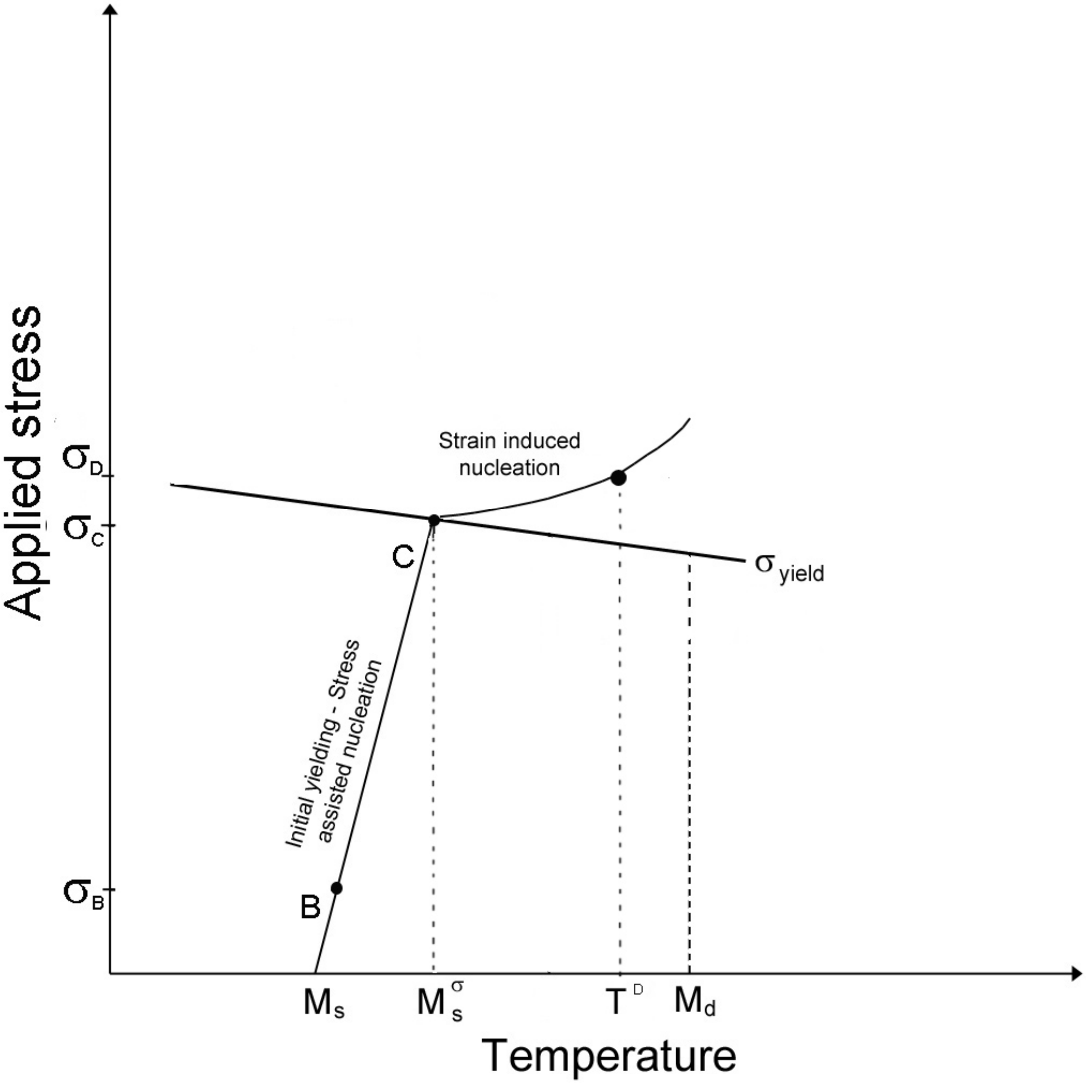

Figure 2.9: Stress assisted and strain-induced nucleation of martensite [58].

To estimate the M_d temperature, several empirical relationships have been developed. The most typical estimates the M_{d30} temperature, which indicates the temperature at which for a 30% true strain, 50% austenite to martensite transformation can be achieved, as a function of alloying elements [59]. This can be given by:

$$M_{d30}(^{\circ}C) = 497 - 467[C+N] - 9.2[Si] - 8.1[Mn] - 20[Ni] - 13.7[Cr] - 18.5[Mo], \qquad (2.12)$$

where element concentrations are in wt%. From equation (2.12), the M_{d30} for AISI 301LN SS was estimated to be ~ 35°C, indicating that room temperature cold-rolling can produce strain-induced martensite in this SS.

2.4.1.3 Morphology of martensite during $\gamma \rightarrow \alpha'$ transformation

One of the earliest works that attempted to experimentally obtain martensite through deformation was the work of Kelly & Nuttig [10]. They demonstrated that Fe-Cr-Ni-C alloys with a stable austenitic phase at room temperature, when deformed to ~ 5% cold reduction at -196°C displayed a lath type martensite, with laths of dimension ~ 0.5μm × 2μm (Fig. 2.10). More recently, Shrinivas & Murr [27] have discussed the microstructure of martensite in AISI 304 SS when subjected to various cold-reductions. As AISI 304 is a stable austenitic SS with relatively high stacking fault energy, the propensity for martensite formation upon deformation is quite low. Indeed, upon ~ 16% cold deformation, the AISI 304 SS yielded a micro-shear band type martensitic structure (Fig. 2.11a). Further deformation to ~ 60% resulted in plates of martensite with many dislocations (Fig. 2.11b). In the end, the total martensite transformed after 60% cold deformation was ~ 40%, while ~ 60% of the microstructure was deformed austenite

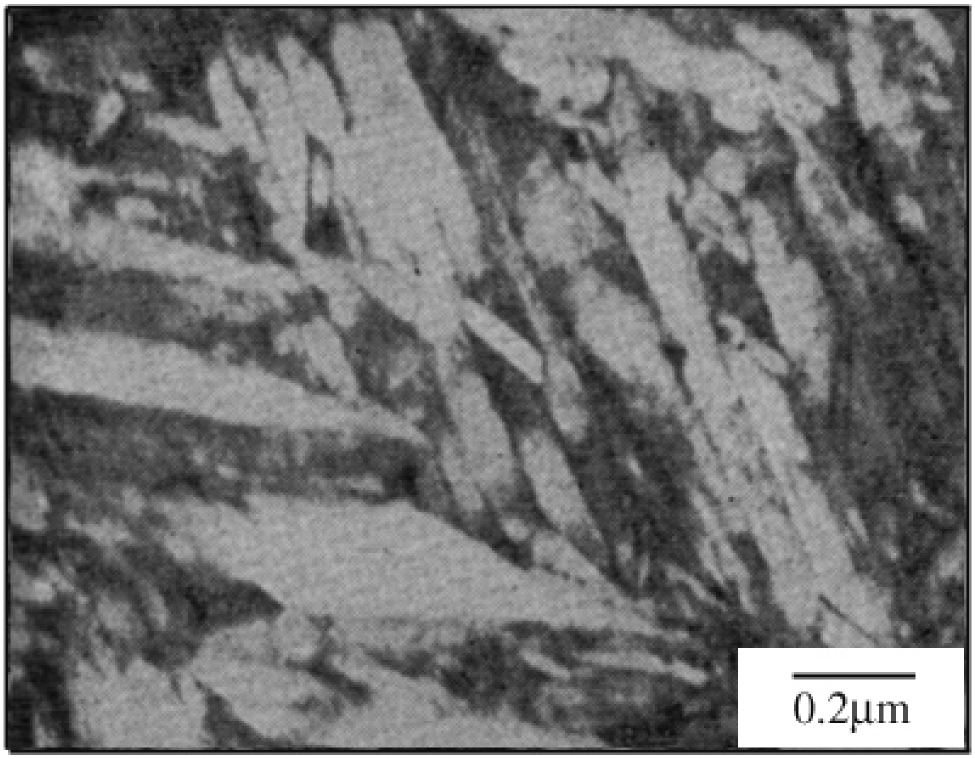

Figure 2.10: TEM image showing deformation induced martensite in a Fe-Cr-Ni-C alloy at -196°C [10].

.

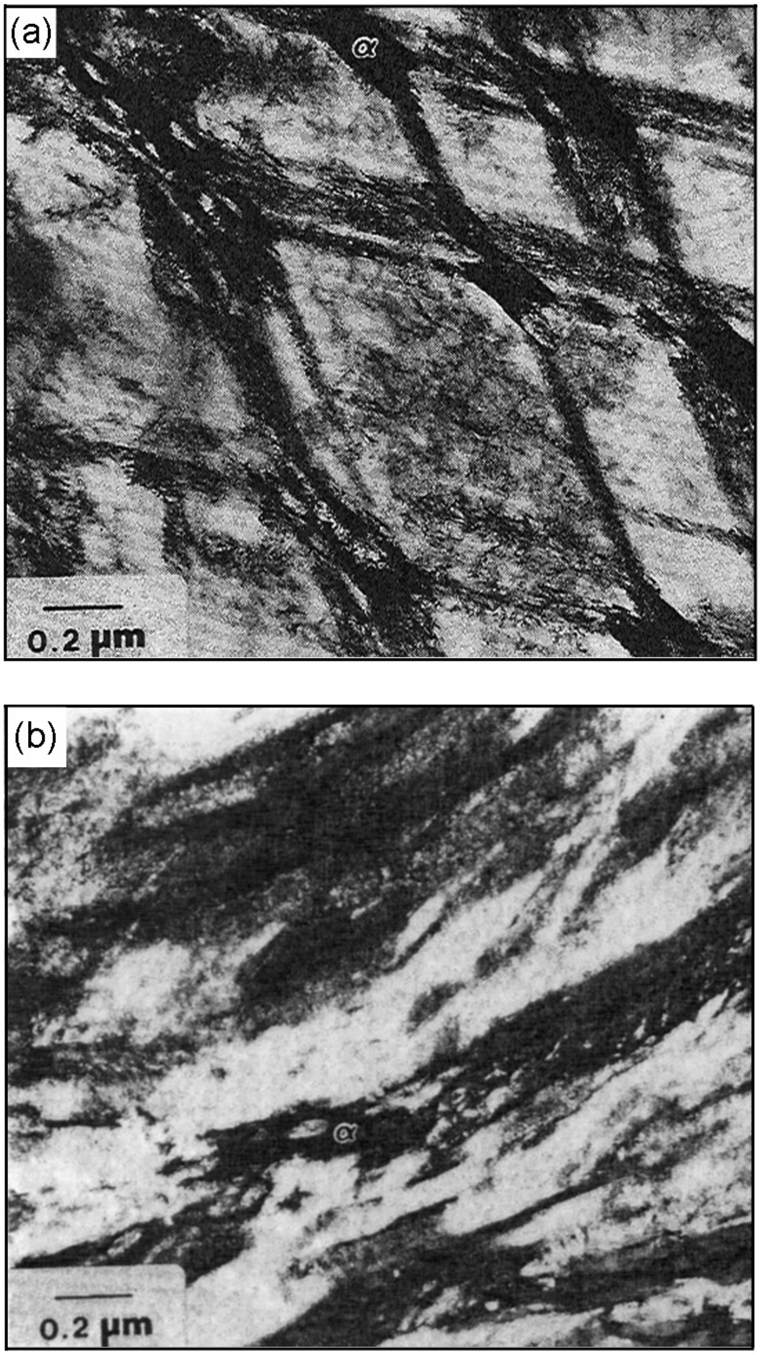

Figure 2.11: TEM images showing (a) Shear bands in cold rolled AISI 304 SS, (b) Martensitic plates with a high density of dislocations [27].

More success in obtaining fine-grained microstructures upon deformation has been achieved in dual-phase steels and low carbon steels [20, 21, 60]. In particular, Korzekwa *et al.* [60] have shown that in C-Mn-Si steels the formation of thin planar dislocation walls occured at ~ 1% deformation. These dislocation walls become dislocation tangles with high dislocation density when the deformation is increased to ~ 2%. Upon application of 7-14% deformation, these dislocations arrange themselves into regular dislocation-cells bounded by thick dislocation walls (Fig. 2.12a and 2.12b). Such dense dislocation regions are desirable due to the presence of many heterogeneous nucleation sites.

In a separate work, Ueji *et al.* discussed at length the morphology of martensite obtained after 50% cold reduction of a low-carbon steel [21]. These authors suggested the appearance of three kinds of martensite namely: 1) very fine lamellar martensite, 2) irregularly bent lamellar martensite, and 3) dislocation-cell martensite bounded by dislocation walls and forests. The very fine lamellar martensitic structure exhibits a wavy structure possibly due to the irregular orientation of the micro-shear bands (Fig. 2.13a). These lamellae have dimensions of ~ 0.06µm, which makes them ideal for nucleation of ultra-fine grain upon annealing. Irregularly bent martensitic lamellae seen in a separate region are martensitic laths that are bent to different orientations due to cold deformation (Fig. 2.13b). Such regions are also desirable for the formation of ultra-fine grains because they offer many heterogeneous sites for nucleation. Finally, dislocation-cell martensitic structures observed in Fig. 2.13c are bound by dislocation walls and are ultra-fine in nature. Ueji *et al.* demonstrated the development of ultra-fine ferritic grains (~0.5µm) upon annealing the abovementioned structures.

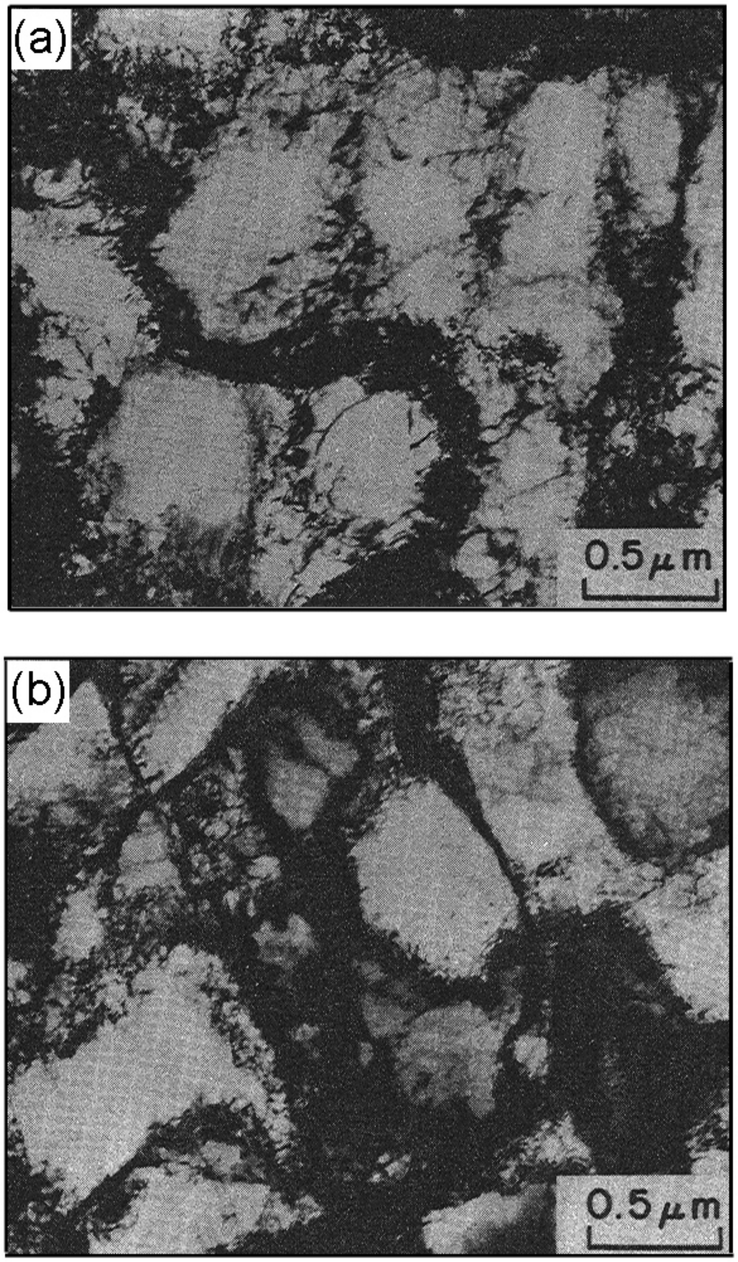

Figure 2.12: (a) and (b); TEM images showing dislocation cell structures ~ 0.5μm in size that are bounded by dislocation forests, in different regions of dual phase C-Mn-Si steels deformed to 14% strain [60].

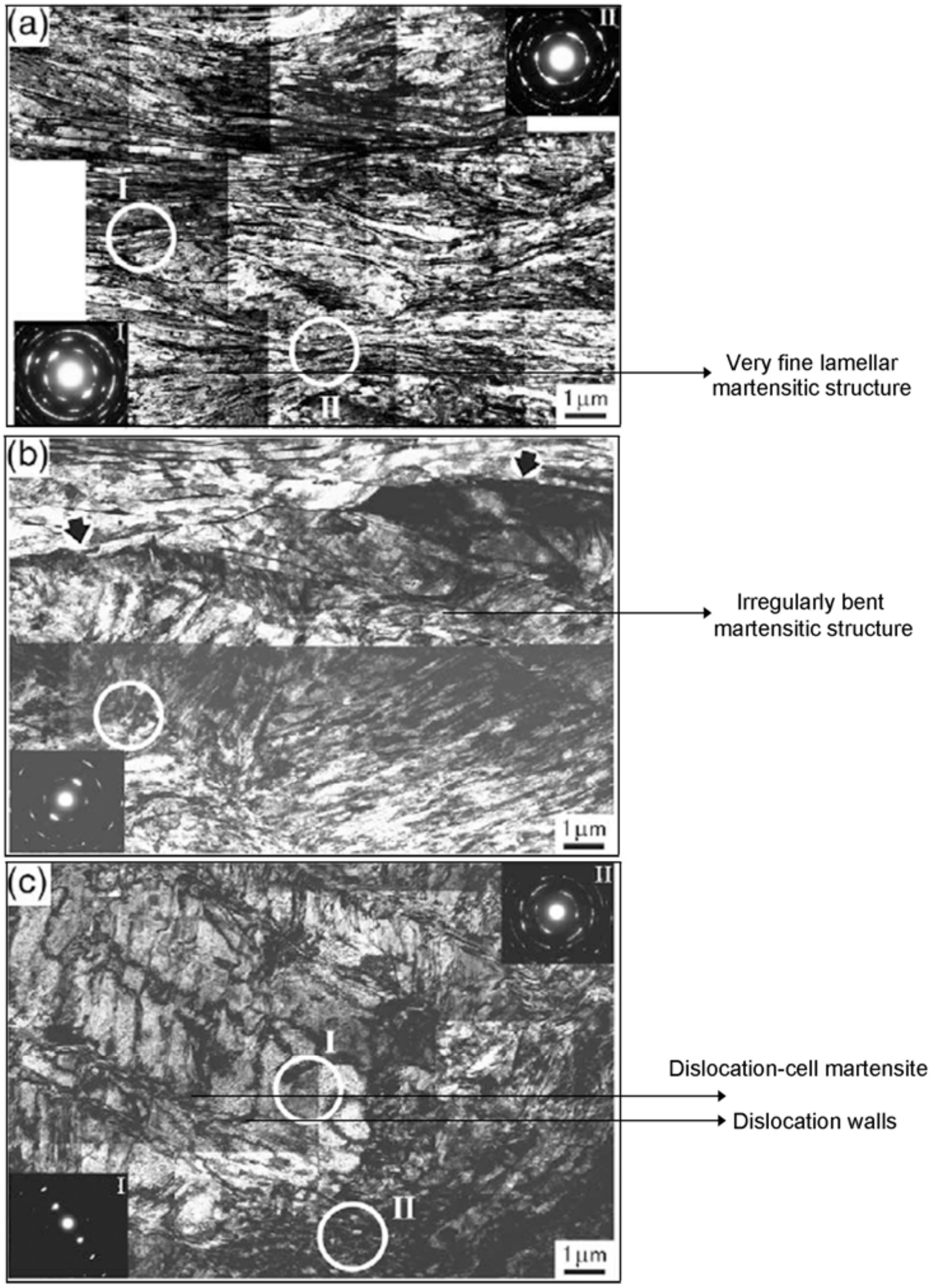

Figure 2.13: TEM images of 0.13% carbon steel cold rolled to 50% reduction. (a) Very fine lamellar martensite – lamellar dislocation cells, (b) Irregularly bent martensitic laths, and (c) Kinked laths, dislocation cells and dislocation walls, [21].

These authors have shown that it is absolutely crucial to achieve an ultra-fine martensitic structure through deformation, in order to form ultra-fine austenitic grains upon annealing. In the case of SS, such efforts have been carried out in specialty non-commercial SS alloys [12-14] with ~ 16%-18% Cr, 8-10% Ni and negligible concentrations of Cu, Si, Mn, and C, N. Cold rolling to about 10% reduction resulted in a lath type martensite (Fig. 16a) similar to that obtained by Shrinivas *et al.* [27]. However, by increasing the cold reduction to about 90%, a dislocation-cell type martensite similar to that obtained by Tsuji *et al.* [20], Ueji *et al.* [21], Korzekwa *et al.* [60] in steels was obtained (Fig. 2.14b). These results were very encouraging because it was demonstrated for the first time by Tomimura *et al*. that ultra-fine grained martensitic structures could be obtained in SS. More recently, Johannsen *et al.* demonstrated dislocation-cell martensite in 90% cold-deformed AISI 301 SS (Fig. 2.14c) [61].

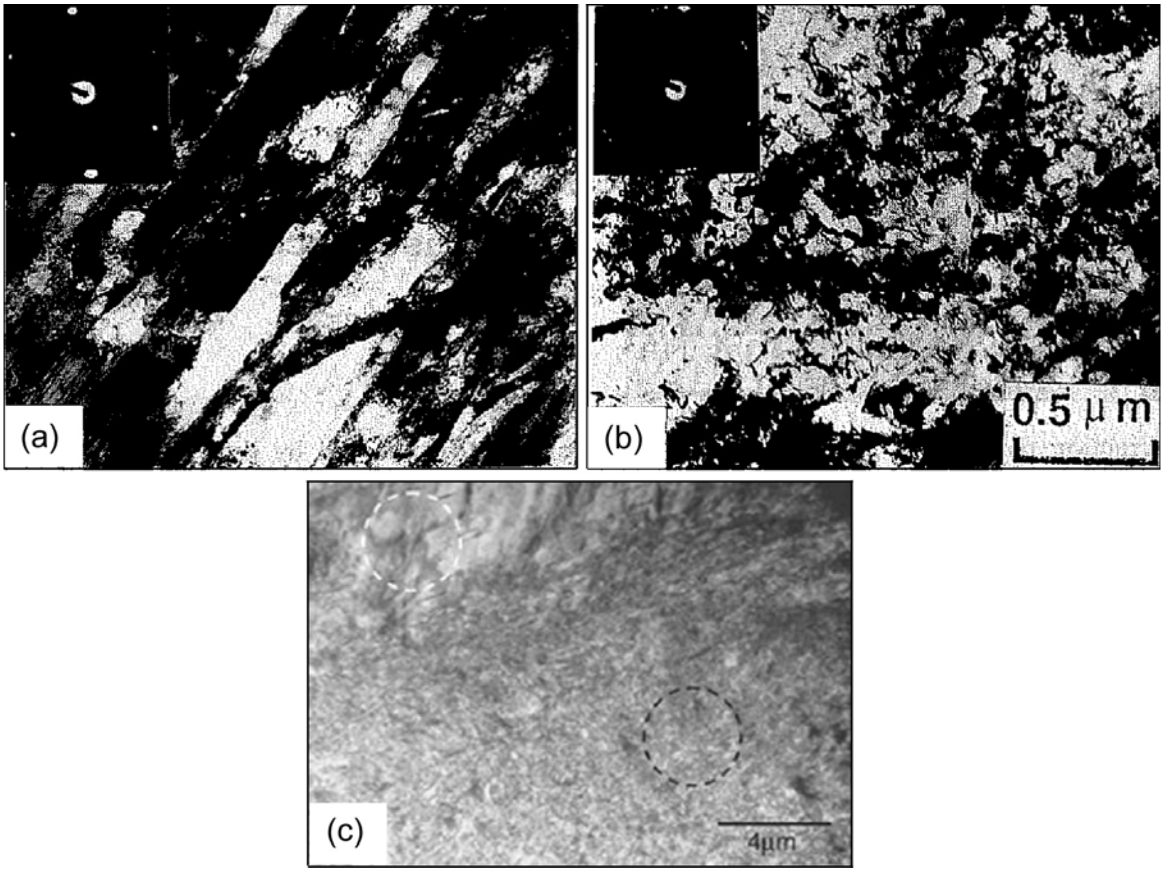

Figure 2.14: TEM images of 18% Cr – 8.5% Ni SS (a) lath type martensite in 50% cold rolled SS, and (b) dislocation cell type martensite in 90% cold rolled SS [11]. In (c) regions of lath-type (white dashed ring) and dislocation-cell type martensite (black dashed ring) in 90% cold-rolled AISI 301 SS can be observed [61].

2.4.2. Annealing Treatment: Martensite → Austenite Reversion

2.4.2.1 Reversion from thermal martensite

One of the first known reverse martensite transformations (α' → γ) in ferrous alloys was demonstrated by Krauss & Cohen [62], in a 33.5% nickel Fe-Ni alloy, (which initially contained ~ 60% thermal martensite), by heating this alloy above the austenite start temperature followed by quenching. Optical microscopy observations seemed to show that the reverted austenite inherited lattice imperfections from the parent martensite phase [62]. This was attributed to difficulties in transforming a complex martensite structure comprising of laths and shear bands into austenite. Subsequent works by Breedis, Kessler & Pitsch, Smith & West, and Jana & Weyman [63-66], revealed additional information on the morphology of reverted austenite in other Fe-Ni alloys, Fe-Ni-C and Fe-Cr-Ni alloys. In all of these works, the initial martensite phase was obtained by quenching the alloy from room temperature to a temperature below the M_s temperature (~ -195°C).

Breedis demonstrated in Fe-Cr-Ni alloys that the reversion products consisted of thin austenitic twins formed in a martensitic matrix (Fig. 2.15), whereas Kessler & Pitsch showed time-dependent austenite nucleation in martensitic plates (Fig. 2.16a and 2.16b). Jana & Weyman employed electron microscopy techniques to delineate austenite nucleation on lath-martensite boundaries (Fig. 2.16c).

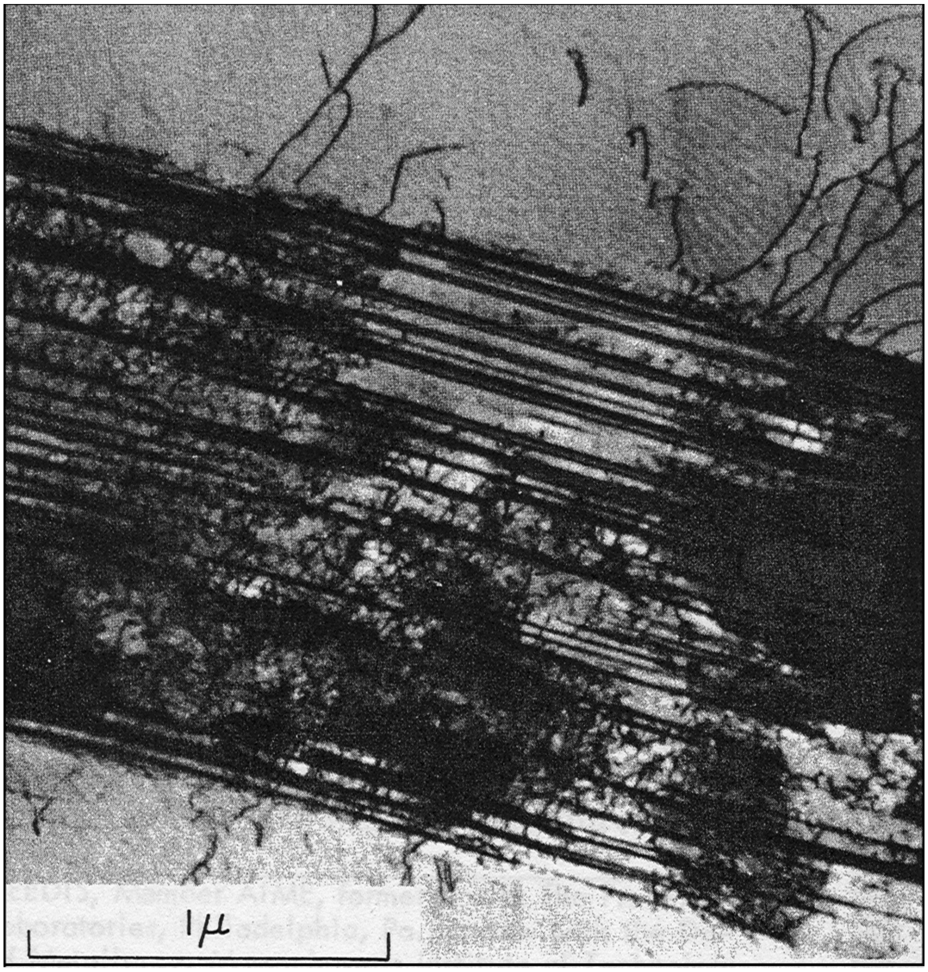

Figure 2.15: TEM image of thin twins produced after annealing a Fe-Cr-Ni alloy for 2 minutes at 600°C [63].

.

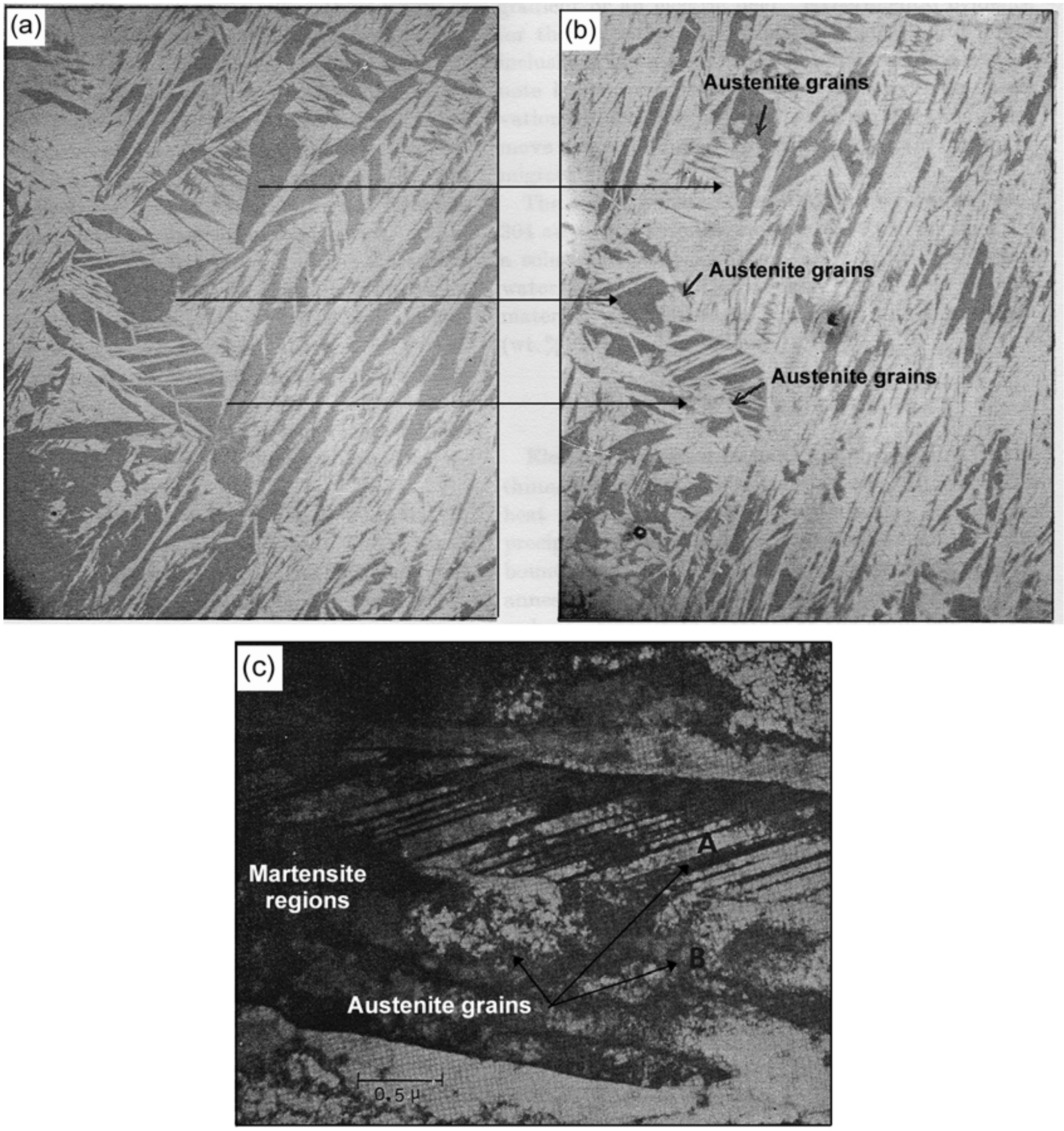

Figure 2.16: (a) Fe-Ni alloy heated to 473°C showing negligible $\alpha' \rightarrow \gamma$ reversion, (b) the same region from image (a) heated to 498°C shows nucleation of austenite in martensite plates [64], and (c) TEM image of partially reverted austenite within the martensitic matrix [65].

The aforementioned research led to considerable debate regarding the mechanism of austenite nucleation. Several researchers were able to demonstrate a shear-type mechanism where the austenite nucleation was time independent and retained the parent martensite morphology [64-67]. In parallel, diffusion controlled mechanisms were also proposed where time-dependent growth of equiaxed austenitic grains occurred [63, 66, 67]. In addition, a mixed mode reversion mechanism involving an initial shear-type reversion, with an intermediate incubation period followed by a diffusion-controlled $\alpha' \rightarrow \gamma$ reversion was also proposed [68]. The consensus among various researchers was that the heating rate played an important role in determining the type of $\alpha' \rightarrow \gamma$ reversion mechanism operating, with high heating rates (> 3°C/sec) promoting a shear-type reversion [63-68].

2.4.2.2 Reversion from deformation induced martensite

Tomimura *et al.* [13] demonstrated that the mechanisms controlling the austenite reversion from deformation induced martensite were in fact similar to the mechanisms proposed by early researchers to describe the austenite reversion from thermal martensite [13]. Accordingly, they claimed two possible reversion mechanisms - 1) diffusion-type mechanism and 2) shear-type mechanism (Fig. 2.17).

The diffusion-type reversion consists of austenite nucleation at martensite grain boundaries (Fig. 2.18b). The morphology of austenite grains formed through a diffusion-type reversion depends on the morphology of the parent martensite phase. When the initial martensite structure is lath-type, the austenite phase nucleates at the lath boundaries and intersections (Fig. 2.18b). Subsequently, the austenite grains grow from these nucleation sites and extend into the martensite lath. As martensite laths typically exist in bundles or blocks, annealing of such structures results in austenite that has similar geometric characteristics as that of the martensite blocks (Fig. 2.18). At longer annealing durations, austenite grain growth takes place.

When dislocation-cell type martensite or ultra-fine lath type martensite is present, the characteristics of the nucleated austenite are different due to the fine nature of martensite and concomitant high dislocation density that results in a large number of sites present for heterogeneous nucleation (Fig. 2.19a). Upon annealing such structures, austenite nucleates and grows into an equiaxed shape [11]. Depending on the annealing duration, ultra-fine grained austenite has been demonstrated in various steels [20, 21, 69] and specialty non-commercial SS [12-14]. Since the curvature of ultra-fine grains is high, rapid grain growth occurs leading to a non-uniform grain size distribution, which is clearly seen in the work of Ma *et al.* [11] (Fig. 2.19c).

In a diffusion-type reversion, the number of austenite nuclei formed is directly correlated to the available number of martensite boundaries. Since the number of martensite boundaries can be increased by cold-rolling the martensite phase, the diffusion-type reversion is directly correlated to the amount of prior cold-work of an alloy.

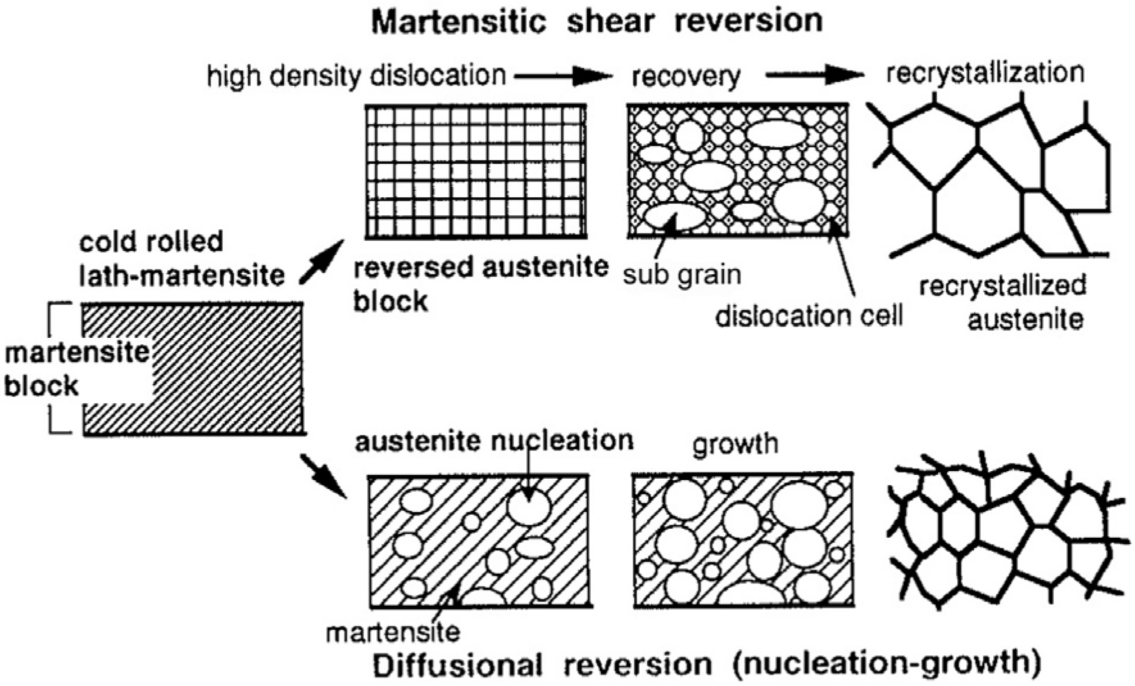

Figure 2.17: The shear-controlled and the diffusion-controlled α’ → γ reversion mechanisms [13].

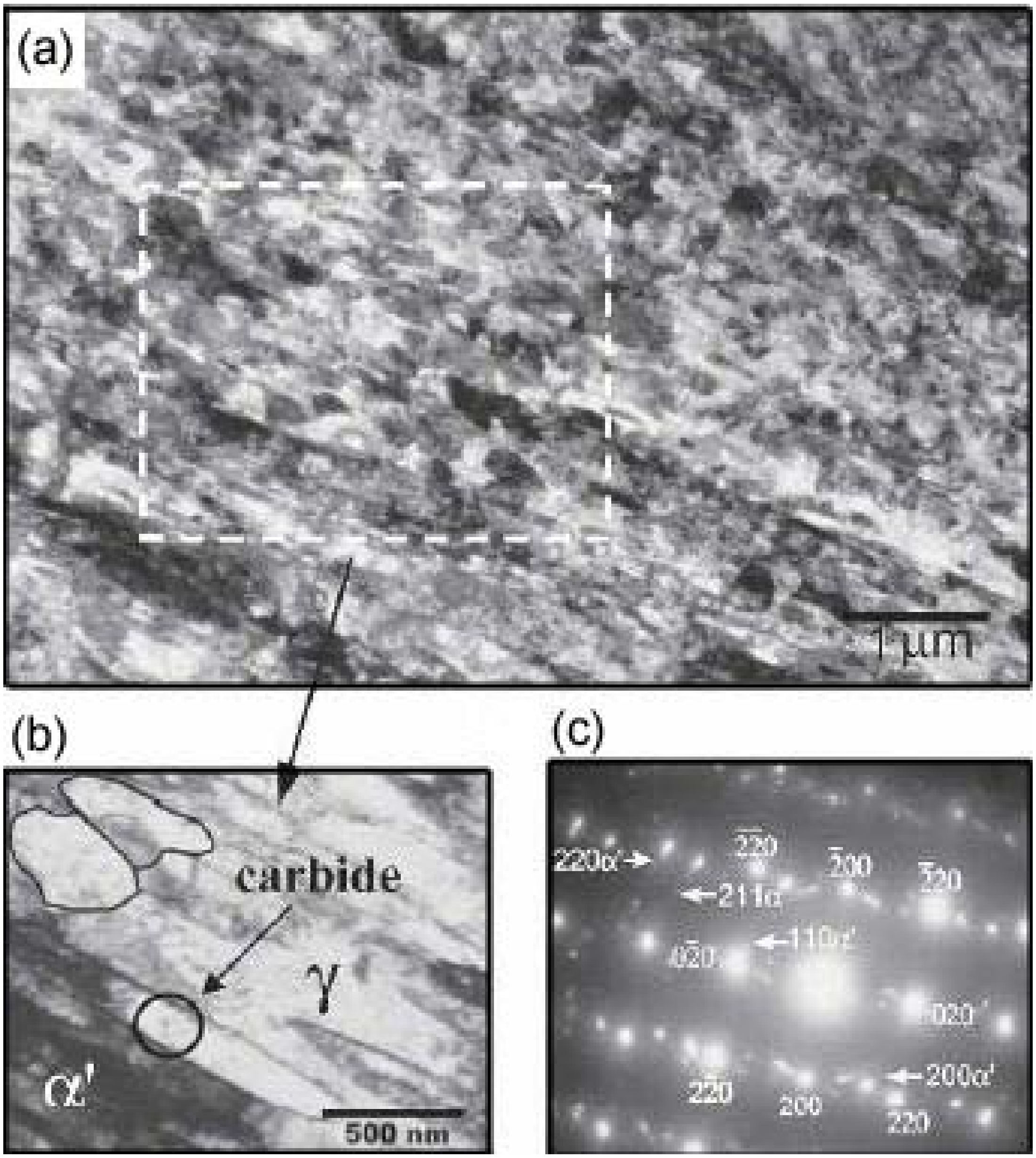

Figure 2.18: (a) Microstructure of 90% cold rolled AISI 301 SS annealed at 600°C, showing newly formed fine-grained austenite, (b) Higher magnification of the white box region in a) shows the presence of lath martensite adjacent to austenite grains, and (c) electron diffraction pattern indicating the presence of austenite [61].

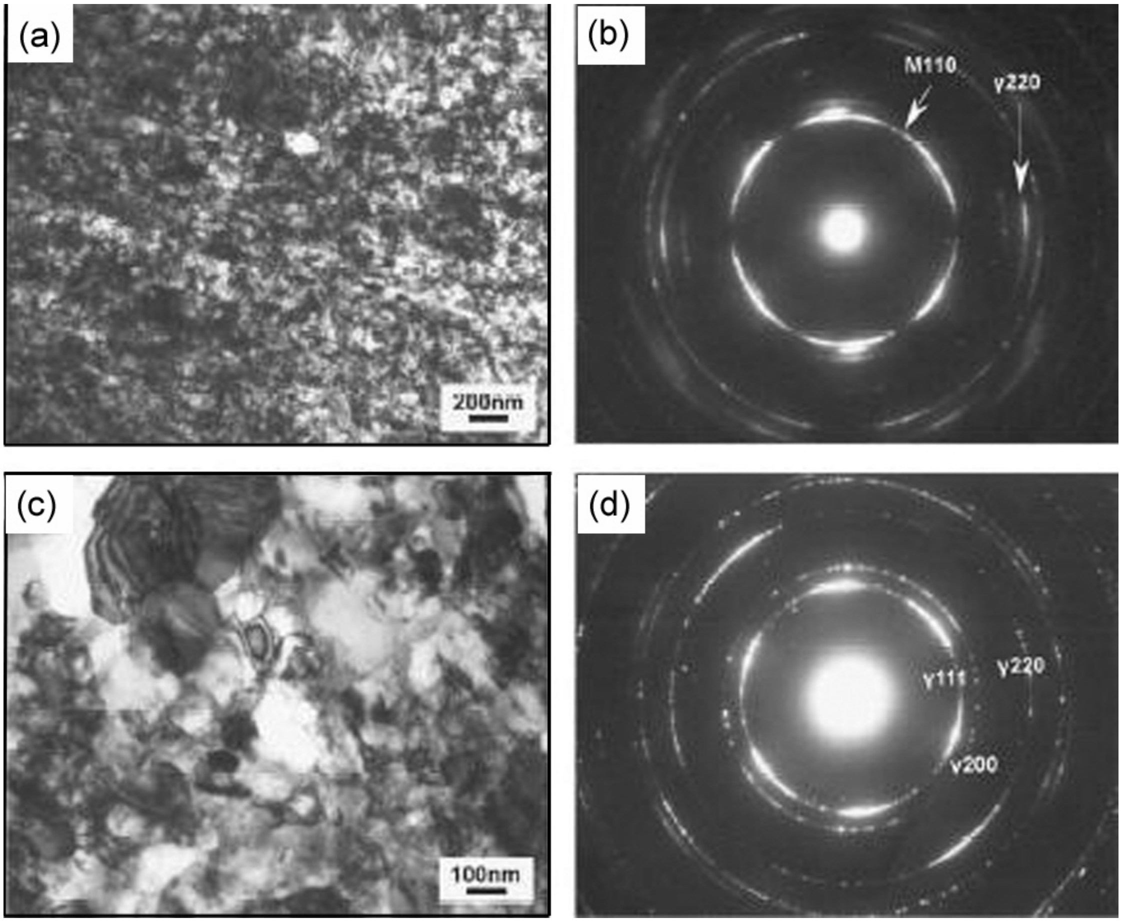

Figure 2.19: TEM images of 10Cr-5 Ni-8Mn SS (a) dislocation-cell martensite, (b) diffraction pattern of (a), (c) nano-austenitic grains formed after annealing (a), and (d) diffraction pattern from (c) [11].

In the case of the shear-type reversion mechanism, the martensite parent phase reverts to austenite phase via a diffusionless transformation. The austenite phase formed initially consists of high dislocation density and retains the morphology associated with the parent martensitic phase. Annealing after a long time results in the recovery of defects to form sub-grains that coalesce into larger austenitic grains (Fig. 2.17).

Experiments have demonstrated that the shear-type reversion occurs within a small temperature range (Fig. 2.20a) of ~ 50K whereas the diffusion-type reversion occurs over a large temperature range of ~ 200K. Due to the diffusionless nature of the shear-type reversion, the reverted austenite retains the morphology of the parent martensite. Indeed, as shown in Fig. 2.20b, 16Cr-10Ni samples exhibit a primarily martensitic structure after 10 seconds annealing, while reverting to an austenitic structure comprising of austenite sub-grains and defect laden austenitic grains at an annealing duration of 600 seconds. Furthermore, the morphology of this alloy after 1,000 minutes (60,000 seconds) of annealing remains similar to that observed at 10 minutes (600 seconds) of annealing. In contrast, in 18Cr-9Ni samples, which follow a diffusion-type austenitic reversion, the morphology after 1,000 minutes is substantially different, with the evolution of large defect-free austenitic grains.

These experiments are significant because they show for the first time that in addition to the heating rate used for annealing, the SS composition may also play an important role in determining the type of $\alpha' \rightarrow \gamma$ reversion mechanism taking place upon annealing. An in-depth discussion of the influence of heating rate and composition on the type of reversion is discussed in the following sections.

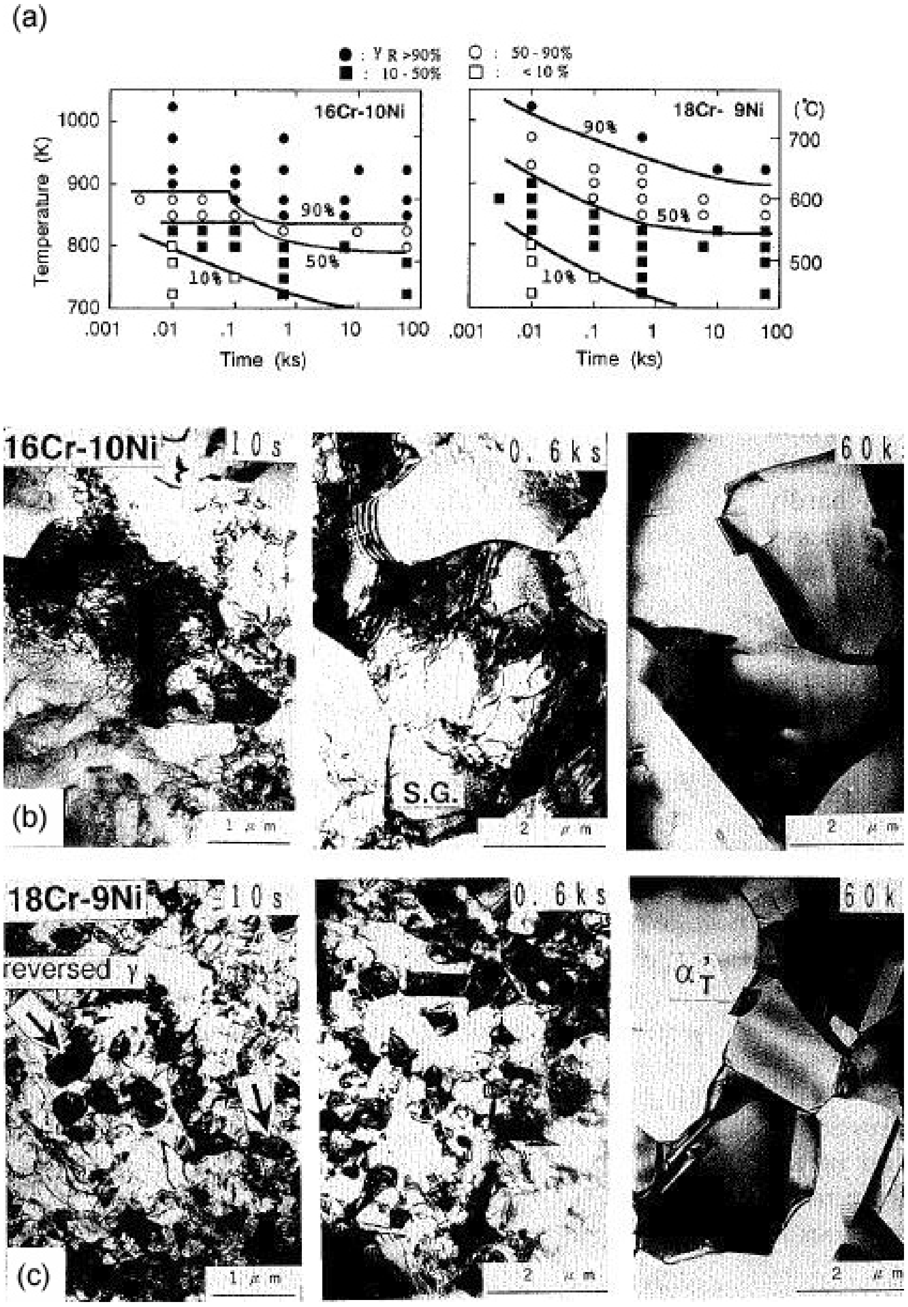

Figure 2.20: (a) Reversion-Temperature-Time maps for 16Cr-10Ni and 18Cr-9Ni with 90% cold-rolling. Percentages correspond to amounts of reverted austenite, (b) Bright field images of 16Cr-10Ni annealed for different durations, and (c) Bright field images of 18Cr-9Ni annealed for different durations [13].

2.4.3 Influence of heating rate on martensite → austenite reversion

Equiaxed austenitic grains were observed upon heating thermal martensite at a rate of ~ 0.3°C/sec by Kessler & Pitsch [64]. Apple & Krauss heated Fe-Ni-C alloys with varying carbon contents (0.05%, 0.3%) at heating rates of 3°C/sec and 1500°C/sec, respectively and noted considerable differences in the morphology of reverted austenite (Fig. 2.21) [68]. In the case of a slow heating rate of 3°C/sec, equiaxed austenitic grains were observed (Fig.2.21a). In contrast, at a heating rate of 1500°C/sec the morphology resembled that of the parent martensitic phase (Fig. 2.21b). From these observations, Apple & Krauss concluded that at lower heating rates, sufficient time was available for short range diffusion of Ni (austenite stabilizer) into the newly formed austenite nucleus, resulting in a diffusion-controlled reversion [68]. Such diffusion was not possible at higher heating rates leading to a shear type reversion.

In a different work on a 16Cr-12Ni alloy with negligible amounts of interstitial elements, Coleman & West [68] proposed that the reversion from $\alpha' \rightarrow \gamma$ occurred in three stages, namely a shear-type reversion stage, followed by a second stage consisting of an incubation time and a third stage involving diffusion-controlled kinetics where an increase in austenite phase over a range of temperature was observed. Although this work did not report the heating rate used, it can be conjectured that the mechanism proposed by Coleman & West is similar to the shear-type mechanism explained by Tomimura *et al.* [12] where the initial diffusionless transformation results in defect laden austenite. The second stage of the incubation period corresponds to the recovery of defect laden austenite leading to sub-grain formation (Fig. 2.17), and the time-dependent period corresponding to the recrystallization of these sub-grains, as proposed by Tomimura *et al.* [13].

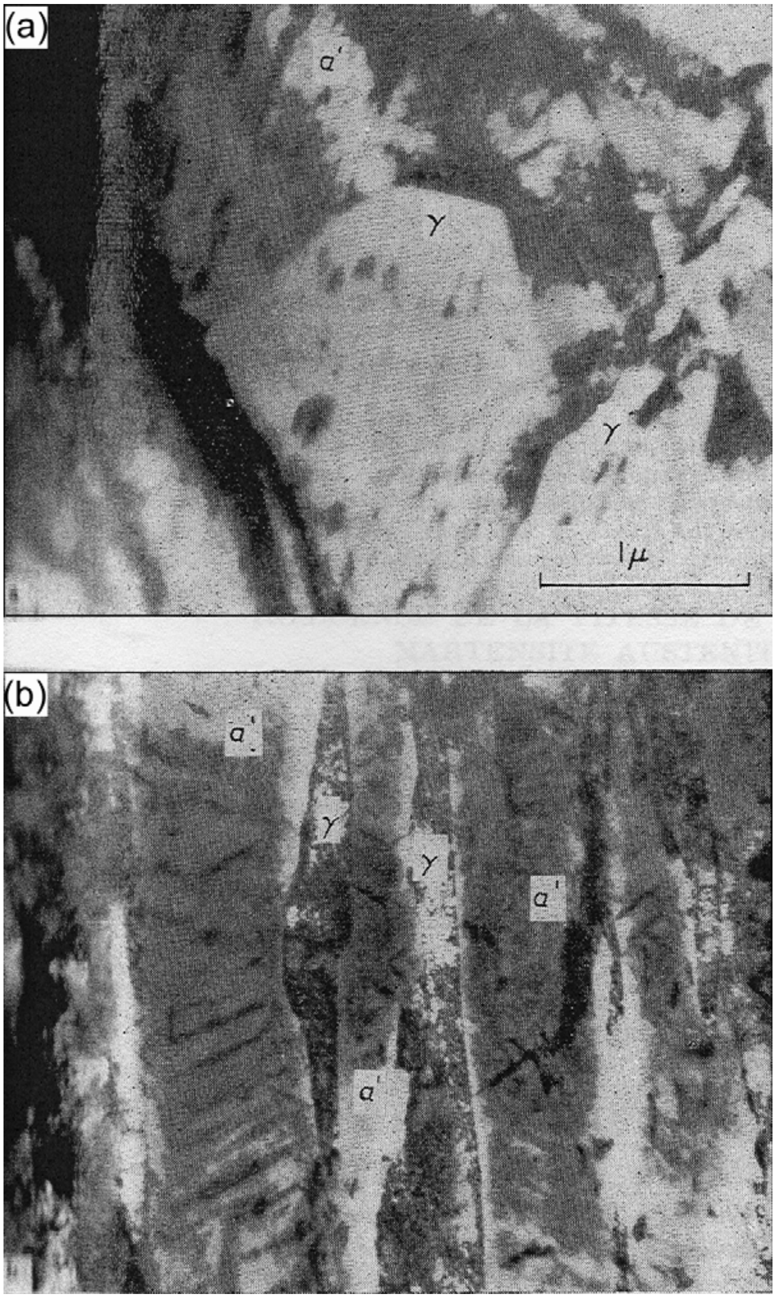

Figure 2.21: TEM images of partially austenitized areas of a 0.3% C, Fe-Ni-C alloy heated at (a) 3°C/sec, and (b) 1500°C/sec [68].

In an independent work, Montanari discussed the reversion mechanism in AISI 304 SS, for which a diffusion-controlled reversion was reported for heating rates of 1-100K/min [71]. As these heating rates are comparable to those used by Kessler & Pitsch [64], and considerably less than those used by Apple & Krauss [67], Montaneri's work seems to confirm that slow heating rates result in a diffusion-type reversion [71]. Finally, the recent work of Choi *et al.* [72, 73], on the reversion mechanism of Fe-3Si-13Cr-7Ni martensitic SS also demonstrates a diffusion-type reversion for slow heating rates of less than 10K/sec and a shear-type reversion for higher heating rates (Fig. 2.22).

It should be taken into consideration that most of the alloys used in the abovementioned research were non-commercial Fe-Cr-Ni alloys with negligible carbon and/or nitrogen [12, 66, 68], while Apple & Krauss used Fe-Ni-C alloys with no Cr [67]. However, the alloy composition does play a role in determining the type of $\alpha' \rightarrow \gamma$ reversion mechanism, as was demonstrated by Tomimura *et al*. The next section discusses in more detail the role of alloy composition on the type of reversion mechanism observed.

2.4.4 Influence of alloy composition on the martensite→ austenite reversion

Breedis showed austenite twins in Fe-Ni-C alloys upon annealing from the martensitic phase [63]. This was attributed to the low stacking fault energy of these alloys where twin formation was energetically favorable. Since the stacking fault energy depends on alloy composition [70], the formation of twins and/or stacking faults observed upon annealing, should be composition dependent. However, no work has been carried out regarding the influence of SFE on the type of reversion (shear or diffusion controlled).

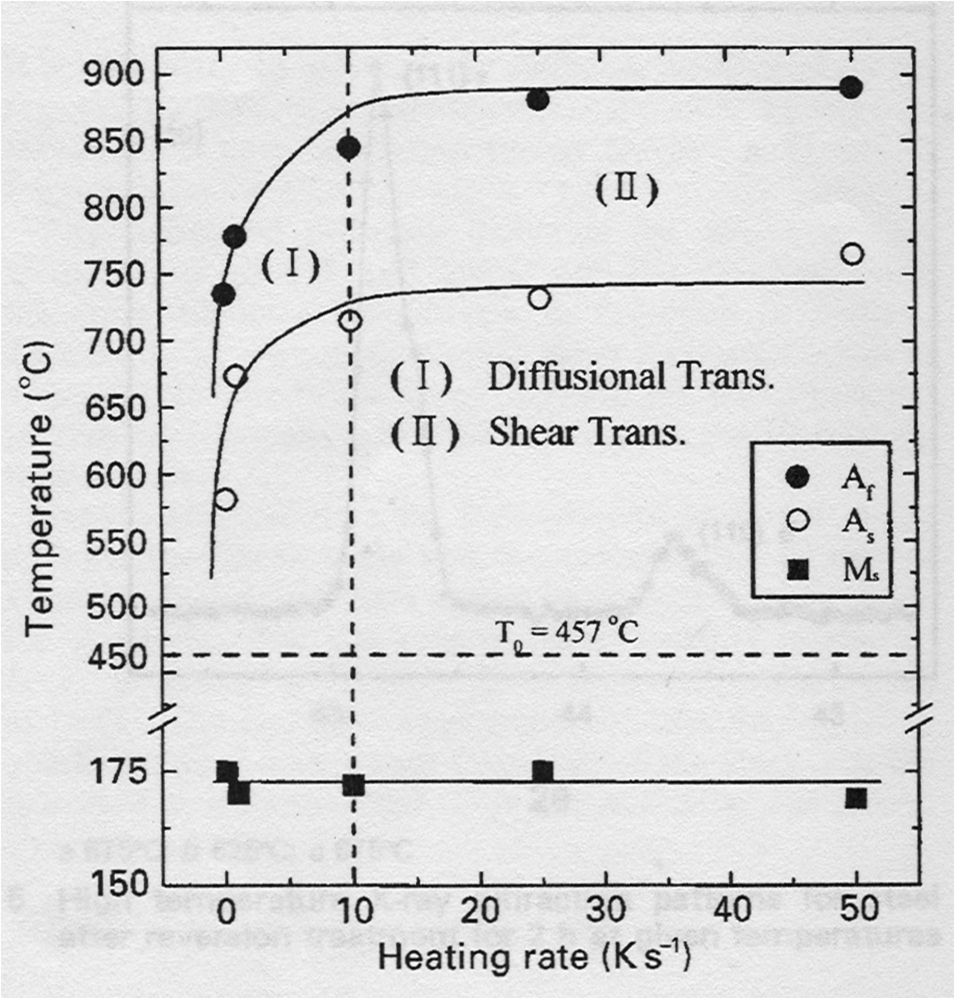

Figure 2.22: Austenite reversion as a function of heating rate [73].

In a later work, Tomimura *et al.* [13] demonstrated experimentally the various reversion mechanisms in 16Cr-10Ni and 18Cr-9Ni non-commercial SS. They explained the observed dependence on alloy composition from a thermodynamic viewpoint whereby the free energy change $\Delta G^{\alpha'\to\gamma}$ involved in the α’ → γ transformation, was given by [13]:

$$\Delta G^{\alpha'\to\gamma} = \sum \Delta G_i^{\alpha'\to\gamma} + \sum \Omega_{ij}^{\alpha'\to\gamma} x_i x_j \ , \tag{2.13}$$

where $\Delta G_i^{\alpha'\to\gamma}$ is the Gibbs free energy change between α’ and γ phases in the i^{th} element, $\Omega_{ij}^{\alpha'\to\gamma}$ the difference in the interaction parameter between α’ and γ phases for the i^{th} and the j^{th} element present in the alloy, x_i, x_j the fraction of i^{th} and the j^{th} elements in the alloy. From equation (2.13) and experimental observations, Tomimura *et al.* inferred that the shear-type reversion involves a free energy change of ~ 500J/mol, which is attained for the 16Cr-10Ni alloy at 923K (Fig. 2.23). In contrast, the 18Cr-9Ni alloy has a Gibbs free energy change that is less than 500J/mol at 923K (~ 375J/mol from Fig. 2.23) resulting in a diffusion-type reversion. According to this model, the 18Cr-9Ni can undergo a shear-type reversion only if a temperature of ~ 1023K is achieved and the Gibbs free energy change for reversion exceeds 500J/mol. In addition, the authors claimed that if the heating rates were fast enough to attain 1023K, even the 18Cr-9Ni alloy would undergo a shear-type transformation.

The abovementioned model is restricted to alloys that contain negligible interstitial elements (C or N). Therefore, assuming the presence of C and N in the alloy adds a significant level of complexity due to the following factors: (1) the interaction parameters $\Omega_{ij}^{\alpha'\to\gamma}$ become more complex [80-83] and (2) secondary phase precipitates may form, which may resist the shear-type reversion and aid the diffusion-type reversion by providing additional nucleation sites [61, 67].

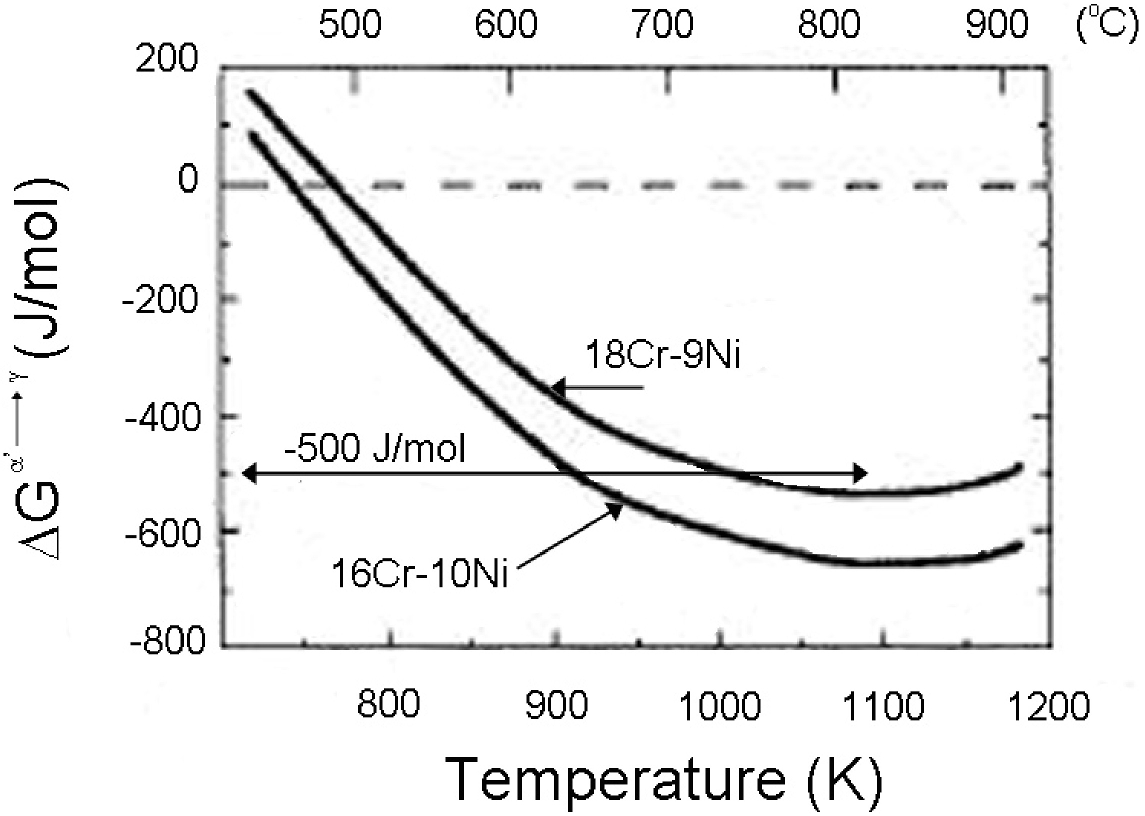

Figure 2.23: Relationship between Gibbs free energy change between ferrite and austenite and temperature in 16Cr-10Ni and 18Cr-9Ni SS [13].

2.4.5 Formation of secondary phases

In case of SS containing interstitial elements (C and/or N), the possibility of secondary phase precipitation exists. For carbon-rich SS alloys (C~0.30wt%), research has demonstrated the formation of $M(=Cr, Fe)_{23}C_6$ carbides in AISI 304 and 316 SS upon prolonged annealing at high temperatures [61, 74-76]. On the other hand, SS alloys with high N content are susceptible to secondary phase nitride (CrN, Cr_2N) precipitation (Fig.2.24c and 2.24d). The formation of secondary Cr-rich precipitates is of concern because they deplete the matrix of Cr and adversely influence the corrosion resistance of SS. Simultaneously, the formation of precipitates depletes the austenite matrix of interstitial elements (C or N), leading to a less stable austenite and thereby raising the M_S temperature. Typically, the formation of carbides in austenitic SS can occur in time periods less than 10 minutes for annealing temperatures between 575-850ºC [76], whereas stable Cr_2N nitrides form in high nitrogen SS after annealing at ~ 900°C for time periods in excess of 24 hrs [77, 78]. Finally, prior research indicates that secondary phase precipitates may inhibit the shear type reversion mechanism [67].

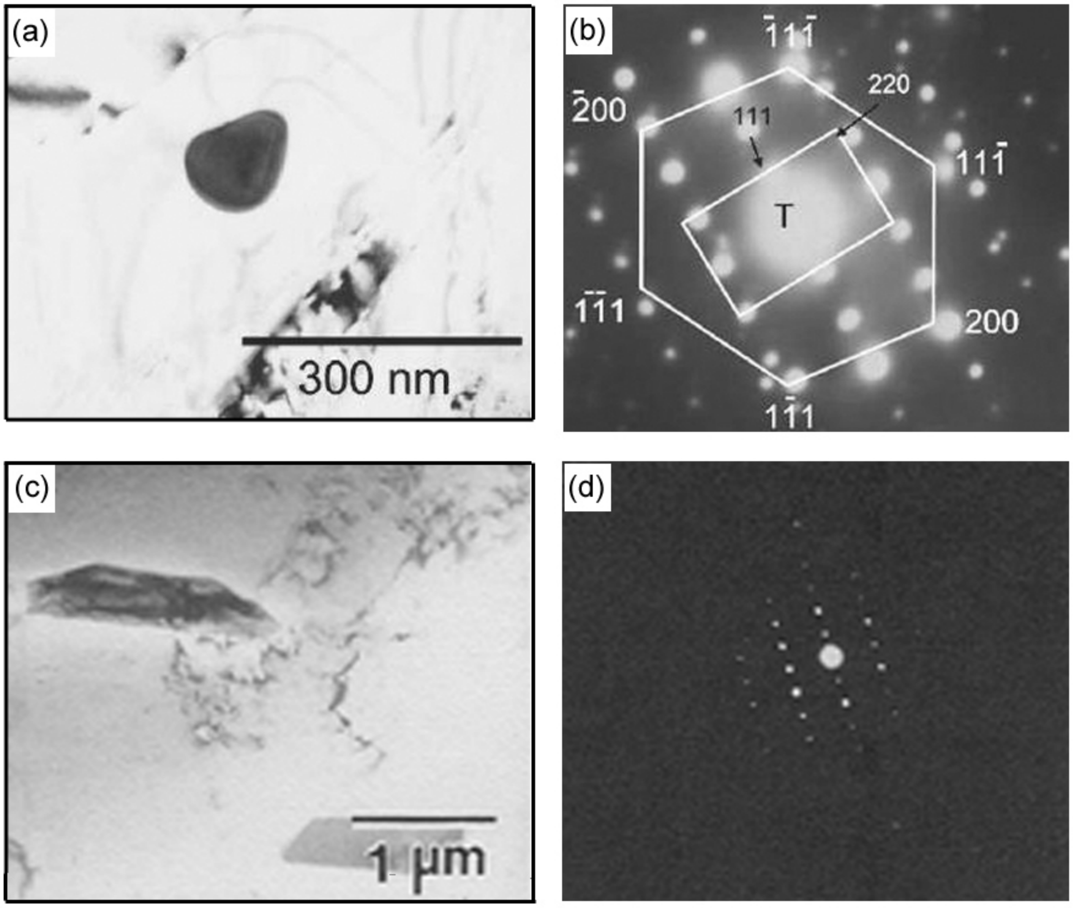

Figure 2.24: (a) TEM image of a $M_{23}C_6$ carbide, (b) Diffraction pattern corresponding to the carbide, [61], (c) Bright field image of Cr_2N nitride precipitates, (d) Diffraction pattern corresponding to the precipitate [78].

2.5 CHARACTERISTICS OF THERMOMECHANICALLY PROCESSED STAINLESS STEELS

The properties obtained in non-commercial metastable SS, which have been subjected to heavy cold rolling and subsequent annealing, demonstrate that this thermo-mechanical process has great potential. In particular, a 18% Cr- 8.5% Ni subjected to a cold reduction of 90% exhibited sub-micron grains of the order of ~ 1μm and almost ~ 80% reversion to the austenite phase (Fig. 2.25). Due to grain refinement, considerable strengthening was possible – an yield strength of ~ 580MPa was acheived for this alloy. This is a considerable achievement since the yield strength of a conventional commercial SS is in the ~ 250-300MPa range.

Similar results have also been demonstrated by di Schino *et al.* in low nickel specialty SS and AISI 304 SS, where tensile strengths of ~ 950MPa and 800MPa were respectively obtained [16-19]. In a different work on a non-commercial SS (10Cr-5Ni-8Mn-0.1C) subjected to multiple thermo-mechanical processes, Ma *et al.* demonstrated an excellent tensile strength of ~ 1100MPa and an elongation of ~ 33% due to the presence of nano-crystalline austenitic grains [11]. Furthermore, Johannsen *et al.* [61] have demonstrated for AISI 301 SS subjected to a 90% cold reduction, followed by 30 minutes of annealing, ultra-fine grains of ~ 5μm with a yield strength of ~ 500MPa, which is considerably higher than conventional processed AISI 301 SS. However, substantial carbide precipitation was observed in AISI 301 SS, which could have deleterious effect on the corrosion properties [61].

Finally, our collaborators in Finland have demonstrated within the realization of this project, exceptional mechanical properties in AISI 301 SS, AISI 301LN SS that were cold-rolled to different reductions and annealed for various annealing times [5-8].

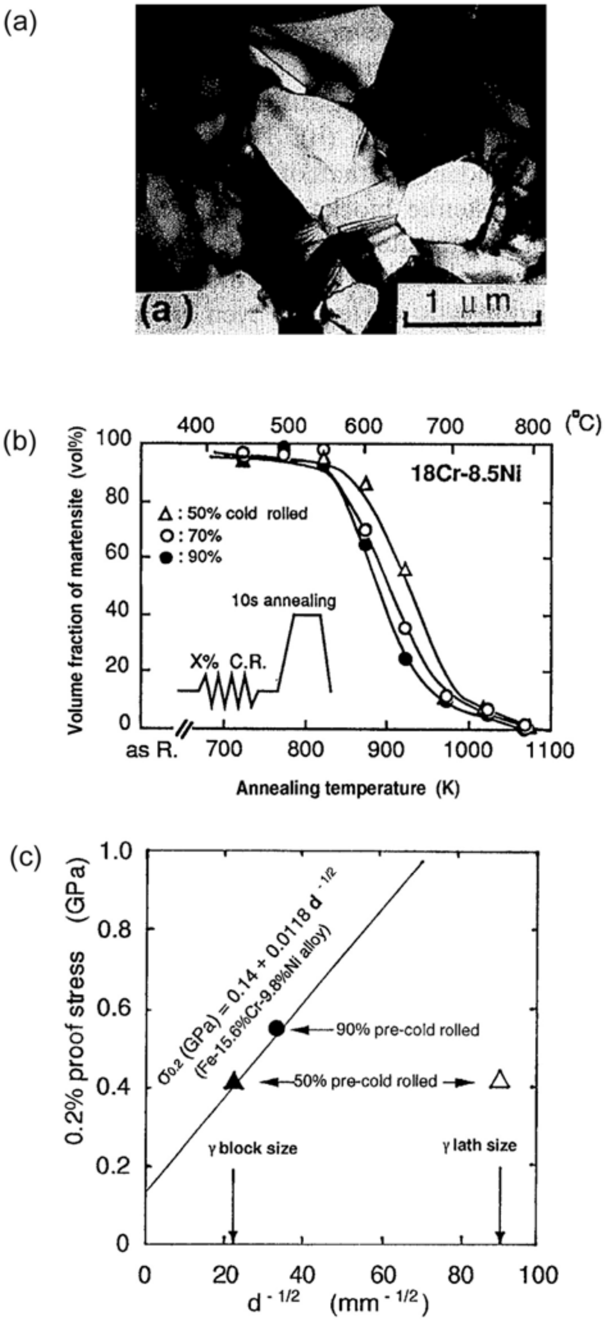

Figure 2.25: Characteristics of a 18% Cr – 8.5% Ni SS subjected to annealing after 90% cold reduction; (a) Microstructure, (b) martensitic phase fraction, and (c) mechanical properties. [14].

2.6 APPLICABILITY OF THE THERMO-MECHANICAL PROCESS TO AISI 301LN SS

The discussion in the preceding sections on 1) the mechanism of martensite formation, 2) the mechanisms of deformation induced martensite formation, 3) the desired morphology of the deformation induced martensite, and 4) the possible α' → γ reversion mechanisms upon rapid annealing indicates that AISI 301LN SS is a good choice for obtaining nano/submicron grain size with enhanced strength and ductility.

Chapter 3: Experimental Procedure

Due to the collaborative nature of this work, the experimental work for this dissertation was carried out at Outokumpu Stainless Oy, the University of Oulu, and the University of Texas at Austin. Specifically, 1) the AISI 301LN SS alloy casting, cold-rolling and tensile testing were carried out at Outokumpu Stainless Oy, 2) the heat treatments of cold-rolled AISI 301LN SS were done at the University of Oulu, and 3) the phase fraction (X-Ray diffraction and SQUID), and microstructural characterization (Transmission Electron Microscopy) were conducted at the University of Texas at Austin. These techniques are discussed in detail in the subsequent sections.

3.1 MATERIALS

A 165 mm thick AISI 301LN stainless steel slab, with composition shown in Table 3.1, was produced by continuous casting at Outokumpu Stainless Oy, Finland. The slab was solution annealed at 1100°C for 1 hour to dissolve any secondary phase precipitates and subsequently hot rolled to ~ 1.5mm thickness. Samples from this 1.5 mm thick sheet were then cold-rolled through 19 consecutive passes in a four-calendar rolling mill at the Research & Development Center of Outokumpu Stainless Oy, Tornio, to achieve a cold-reduction of 63%.

Table 3.1: Chemical composition (in wt %) of AISI 301LN SS used in this work.

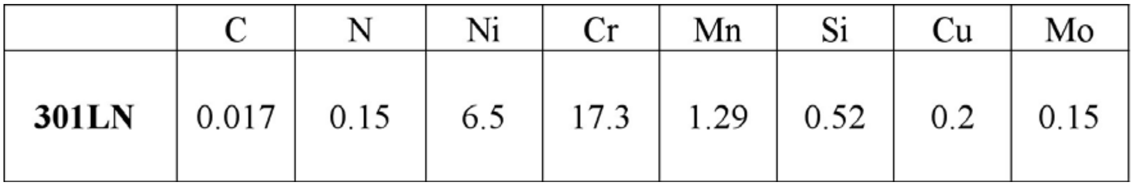

	C	N	Ni	Cr	Mn	Si	Cu	Mo
301LN	0.017	0.15	6.5	17.3	1.29	0.52	0.2	0.15

The M_{d30} and M_s values, defined in section 2.4.1.2, were calculated for the AISI 301LN SS, according to the following expressions [59]:

$$M_s(^\circ C) = 502 - 810[C] - 1230[N] - 13[Mn] - 30[Ni] - 12[Cr] - 54[Cu] - 6[Mo] \quad (3.1a)$$

$$M_{d30}(^\circ C) = 497 - 467[C + N] - 9.2[Si] - 8.1[Mn] - 20[Ni] - 13.7[Cr] - 18.5[Mo] \quad (3.1b)$$

From equations (3.1a) and (3.1b), the M_{d30} and M_s were found to be 35°C and -127°C, respectively. The M_{d30} temperature above room temperature indicates that more that 50% strain-induced martensite will form when samples are deformed by 30% true strain at ambient temperature.

3.2 METHODS

3.2.1 Annealing Treatment

Cold-rolled samples were heat-treated in the Gleeble-1500 thermomechanical simulator facility available at the University of Oulu. The samples were annealed at 600°C, 700°C, 800°C, 900°C and 1000°C for 1, 10 and 100 seconds at a heating rate of approximately 200°C/sec and forced-air-cooled at a cooling-rate of around 200°C/sec that is possible in a Gleeble-1500 thermomechanical simulator. The sample is heated in an inert chamber and connected to an electric circuit (Fig. 3.1). Current is passed through the circuit and the sample is resistively heated. The instrument is designed in a way to relate the current supply with the temperature of the sample inside the chamber. As a consequence, by controlling the current, the temperature of the sample can be accurately defined. In fact, the instrument design permits heating and cooling rates in excess of 500°C/sec.

For our experiments, according to the heating and cooling rates employed, the times needed to reach the abovementioned temperatures were 2.9 sec for 600°C, 3.4 sec for 700°C, 3.9 sec for 800°C, 4.4 sec for 900°C and 4.9 sec for 1000 C. Subsequently, the samples were subjected to dwell annealing times of 1, 10 and 100 seconds (Fig. 3.2)

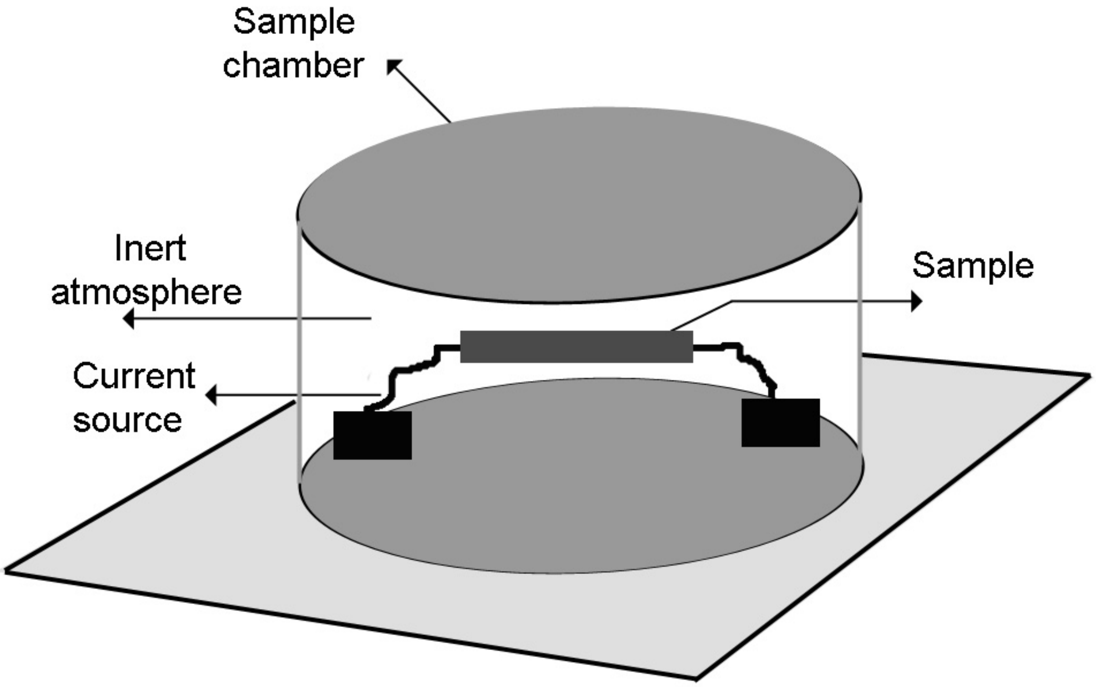

Figure 3.1: Illustration of the principle of the Gleeble thermo-mechanical simulator system.

(a)

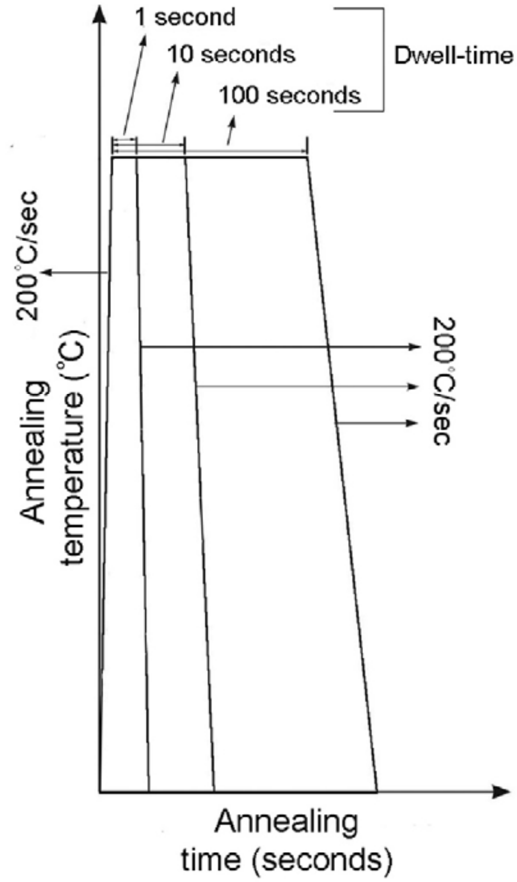

(b)

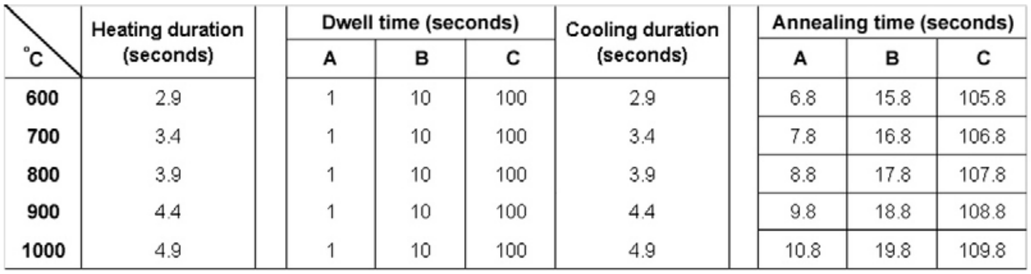

°C	Heating duration (seconds)	Dwell time (seconds) A	B	C	Cooling duration (seconds)	Annealing time (seconds) A	B	C
600	2.9	1	10	100	2.9	6.8	15.8	105.8
700	3.4	1	10	100	3.4	7.8	16.8	106.8
800	3.9	1	10	100	3.9	8.8	17.8	107.8
900	4.4	1	10	100	4.4	9.8	18.8	108.8
1000	4.9	1	10	100	4.9	10.8	19.8	109.8

Figure 3.2: (a) Typical annealing profile for the samples annealed in the Gleeble thermo-mechanical simulator, (b) Duration of the heating cycle, dwell time, cooling cycle and full annealing treatment time at each annealing temperature.

3.2.2 X-Ray Diffraction

X-ray diffraction studies were carried out on rectangular sections of cold rolled AISI 301LN SS with dimension ~ $5 \times 5 \times 0.8$ mm^3. Cut sections were polished using 600-grit silicon carbide grinding paper to remove surface oxidation and cleaned in acetone to remove contaminants. Subsequently, the sample was glued on to a glass slide as shown in Fig. 3.3. Using a glass slide with a step ensured proper focusing of x-ray beam on the sample. X-Rays were generated by a Phillips PW1720 X-Ray Diffractometer, which operated at a voltage of 40 keV, a current of 40 mA and used CuKα radiation. The x-ray source was kept fixed and peaks corresponding to various Bragg reflections were recorded by rotating the sample from 40˚ to 90˚ (2-theta) in steps of 0.1˚ with a dwell time of 4 seconds at each angle. The obtained peaks were plotted as function of 2-theta and MDI Jade 6.5 software was used to index the peaks, as well as obtain intensity magnitudes for those peaks. Intensities corresponding to different phases (austenite, martensite) were then used to estimate their phase fractions through a procedure described by Dickson [87].

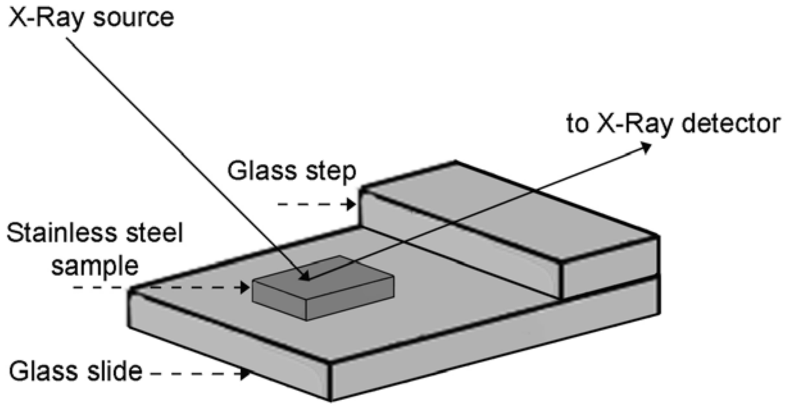

Figure 3.3: Experimental setup for X-ray diffraction studies.

According to this method, the diffraction intensity obtained from a single-phase material is given by [87]:

$$I = \frac{K}{2\mu\Omega^2} \times \left[|F|^2 p \left(\frac{1+\cos^2 2\theta}{\sin^2\theta \cos\theta} \right) \right], \tag{3.2}$$

where K is a constant that depends on the reference intensity I_o and the wavelength of the x-rays used, Ω the atomic volume, μ the absorption coefficient of the sample, $|F|$ the structure factor magnitude of the phase being analyzed, p the coordination number of the reflecting plane, and θ the Bragg angle corresponding to the reflecting plane. Equation (3.2) can be rewritten as:

$$I = \frac{KR}{2\mu}, \tag{3.3}$$

where

$$R = \frac{1}{\Omega^2} \left[|F|^2 p \left(\frac{1+\cos^2 2\theta}{\sin^2\theta \cos\theta} \right) \right] \tag{3.4}$$

When there are multiple phases, the intensity, I_n of an x-ray peak satisfying the Bragg condition for the (*hkl*) plane is related to the phase concentration, C_n through the expression:

$$I_{n,hkl} = \frac{KR_{hkl}}{2\mu} C_n, \tag{3.5}$$

In the case of a SS with two phases – martensite and austenite, the concentration ratio of these two phases is related to their x-ray intensities through the expression:

$$\frac{I_{\gamma,hkl}}{I_{\alpha',hkl}} = \frac{R_{\gamma,hkl} C_{\gamma}}{R_{\alpha',hkl} C_{\alpha'}} \tag{3.6}$$

where

$$\frac{C_{\gamma}}{C_{\alpha'}} = \frac{\left[\dfrac{I_{\gamma,hkl}}{R_{\gamma,hkl}}\right]}{\left[\dfrac{I_{\alpha',hkl}}{R_{\alpha',hkl}}\right]} \tag{3.7}$$

Finally, to mitigate the influence of any texture present in the sample on the $\frac{C_{\gamma}}{C_{\alpha'}}$ ratio, an average of at least three intensities corresponding to three different *hkl* reflections for each phase was considered. Thus:

$$\frac{C_{\gamma}}{C_{\alpha'}} = \frac{\left[\dfrac{1}{\mathrm{n}_{\gamma}}\right] \times \sum_{0}^{\mathrm{n}_{\gamma}} \left(\dfrac{I_{n_{\gamma}}}{R_{n_{\gamma}}}\right)}{\left[\dfrac{1}{\mathrm{n}_{\alpha'}}\right] \times \sum_{0}^{\mathrm{n}_{\alpha'}} \left(\dfrac{I_{n_{\alpha'}}}{R_{n_{\alpha'}}}\right)}, \tag{3.8}$$

where n_{γ} and $n_{\alpha'}$ are the number of intensities for the phases γ and α. The relative intensities $R_{n,\gamma}$ and $R_{n,\alpha'}$ for three *hkl* selected reflections of the γ and α’ phases are shown in Fig. 3.4. Thus, by estimating the $\frac{C_{\gamma}}{C_{\alpha'}}$ ratio and assuming that $C_{\gamma} + C_{\alpha'} = 1$, C_{γ} and $C_{\alpha'}$ are calculated as:

$$C_{\gamma} = \frac{1}{1 + \left(\dfrac{C_{\gamma}}{C_{\alpha'}}\right)} \tag{3.9a}$$

$$C_{\alpha'} = \frac{\left(\frac{C_\gamma}{C_{\alpha'}}\right)}{1+\left(\frac{C_\gamma}{C_{\alpha'}}\right)}. \tag{3.9b}$$

Table 3.2: Relative intensities for the measured reflections in martensite and austenite.

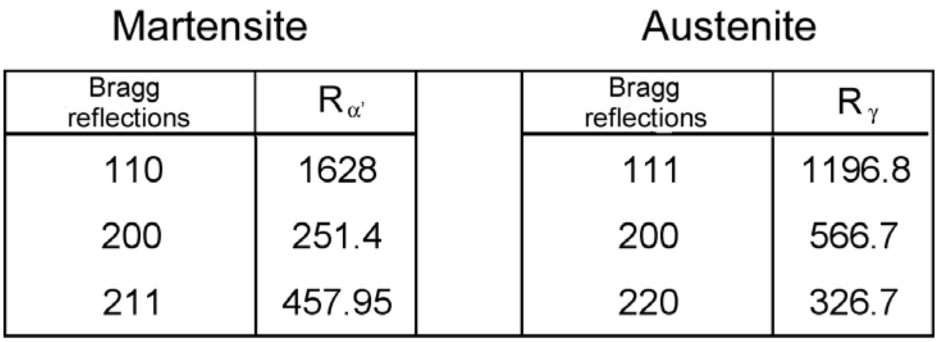

Martensite			Austenite	
Bragg reflections	$R_{\alpha'}$		Bragg reflections	R_γ
110	1628		111	1196.8
200	251.4		200	566.7
211	457.95		220	326.7

3.2.3 SQUID Magnetic Measurements

A set of samples was prepared for magnetic tests in the superconducting quantum interference device (SQUID), to obtain the volume fraction of each phase for all the annealed samples. Using the SQUID, a sample's response to an applied magnetic field is determined, which is used to calculate the saturation magnetization per unit volume. The data obtained is helpful in measuring the fractional amount of austenite (paramagnetic) versus martensite (ferromagnetic) that are present in a sample. The results are very accurate (error of ± 0.01%) since the SQUID can detect minute variations (of the order of 1×10^{-14}T) of a sample's response to an applied magnetic field.

For the current work, samples were placed in the SQUID with their rolling direction parallel to the applied magnetic field. This method of testing was chosen because it was found from a separate set of experiments that the magnetic response of samples positioned in this way was strongest. Subsequently, samples were subjected to a magnetic field that increased from 0T to 0.2T in increments of 0.025T. Thereafter, the field increased in increments of 0.1T until the maximum applied field was 1.0T. This field was chosen because at 1.0T, the saturation magnetization was reached for all samples at this stage. Data was collected at each step of the applied field path. Each data point was measured 5 times and averaged. A typical SQUID response from a SS sample is shown in Fig. 3.4.

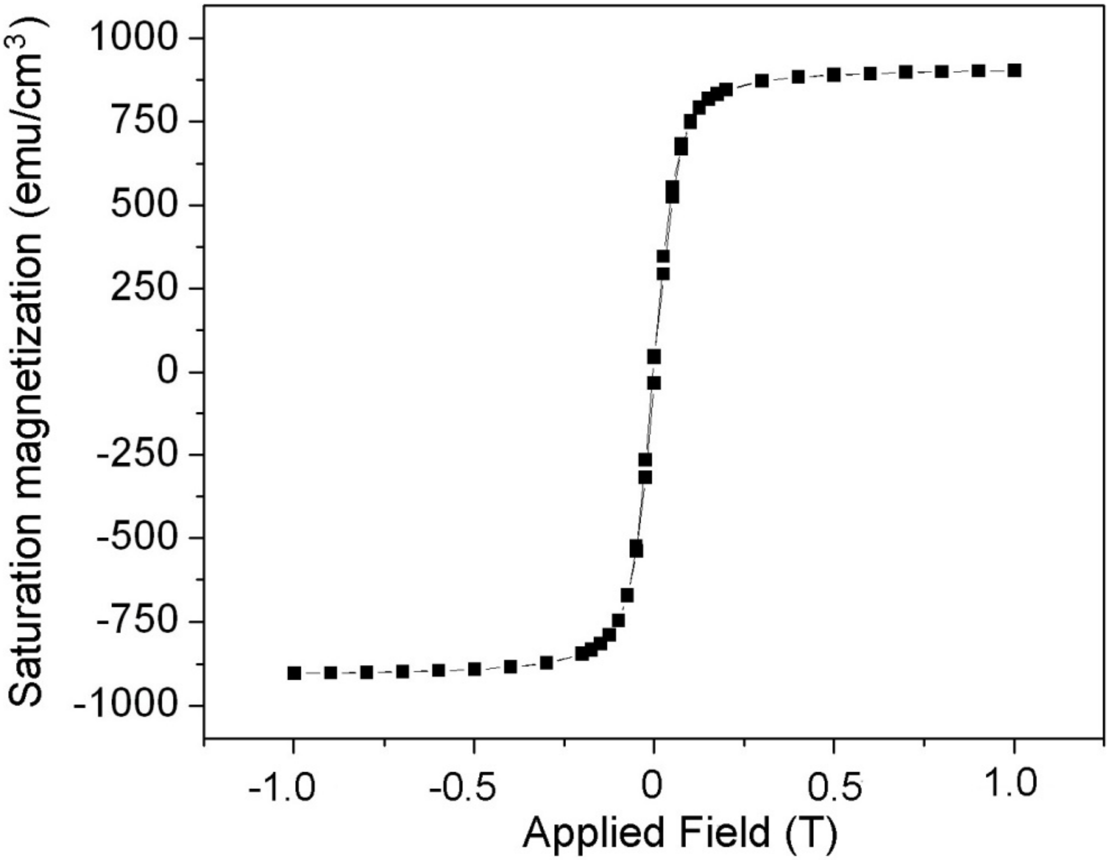

Figure 3.4: Typical SQUID response from a SS sample.

3.2.4 Transmission Electron Microscopy

For the transmission electron microscopy (TEM) observations, the annealed samples were first thinned to ~ 100 μm by mechanical polishing. Subsequently, these samples were thinned to electron transparency in a jet-polishing apparatus (Struers Tenupol-5). The 100μm thin sample was maintained at a potential of ~ 32V and a current of ~50-60mA. Under these conditions, the sample was polished at -10°C, with a continuous jet composed by a mixture of 59 vol.% methanol, 35vol.% m-butanol and 6 vol.% perchloric acid. At this temperature, the viscosity of the electrolyte was adequate to create an optimal boundary layer on the sample and thin the sample to electron transparency.

Two different TEMs – JEOL 200CX and JEOL 2010F - were used in this work to identify i) the martensite morphology in the cold rolled sample, ii) the morphology of the austenite formed after reversion, iii) the austenite grain size and iv) secondary phase precipitates. The JEOL 200CX is ideal for viewing large areas at low magnification, whereas the JEOL 2010F, which is equipped with a field emission gun and an EDS detector, is ideal for studying the microstructure at high magnifications, as well as carrying out secondary phase analysis. In both microscopes, the magnification was calibrated using a Mag*I*cal® sample – an ion-milled single crystal silicon containing epitaxially grown SiGe interlayers of known widths [88].

The JEOL 2010F TEM was also utilized to identify secondary phase precipitates present in the annealed samples by operating the microscope in the nano-beam mode. The difference between this mode and the conventional TEM mode is illustrated in Figures 3.5 and 3.6 respectively. In the conventional TEM mode the second condenser lens is strongly excited resulting in a small focal length and an electron beam that diverges significantly as it enters the condenser mini-lens. Simultaneously, the condenser mini-lens is strongly excited while the objective lens is weakly excited so that a nearly parallel beam of electrons enters the specimen. In contrast, when the TEM is in the nano-beam mode (Fig. 3.6), both the second condenser lens and the condenser mini-lens are weakly excited such that a divergent beam of electrons enters the objective lens. On the other hand, the objective lens is strongly excited, producing a small focal length. This causes the electron beam to converge sharply before entering the specimen. The final result is a focused electron beam with a width of 1- 2.5nm, which is ideal to characterize nanoscale precipitates.

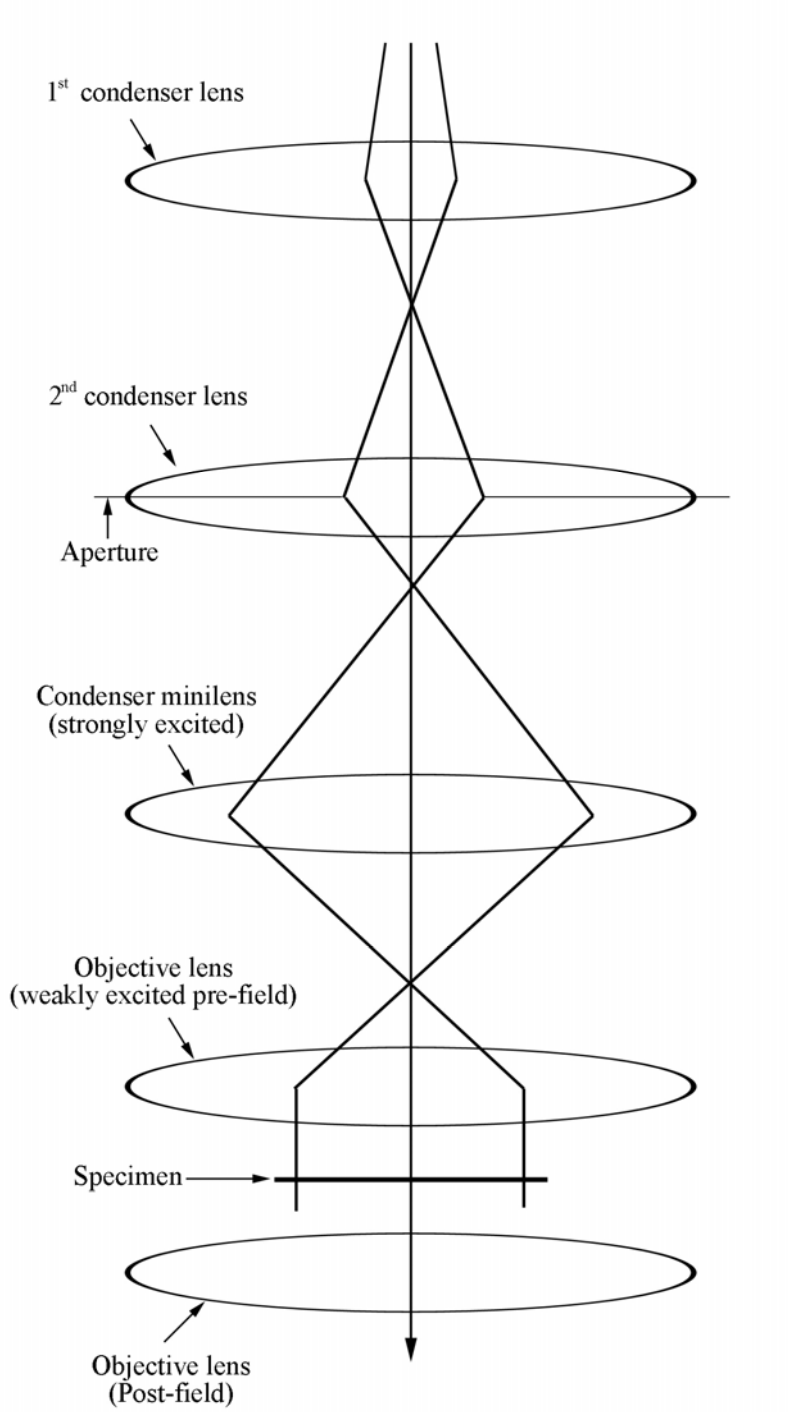

Figure 3.5: Conventional TEM mode [89].

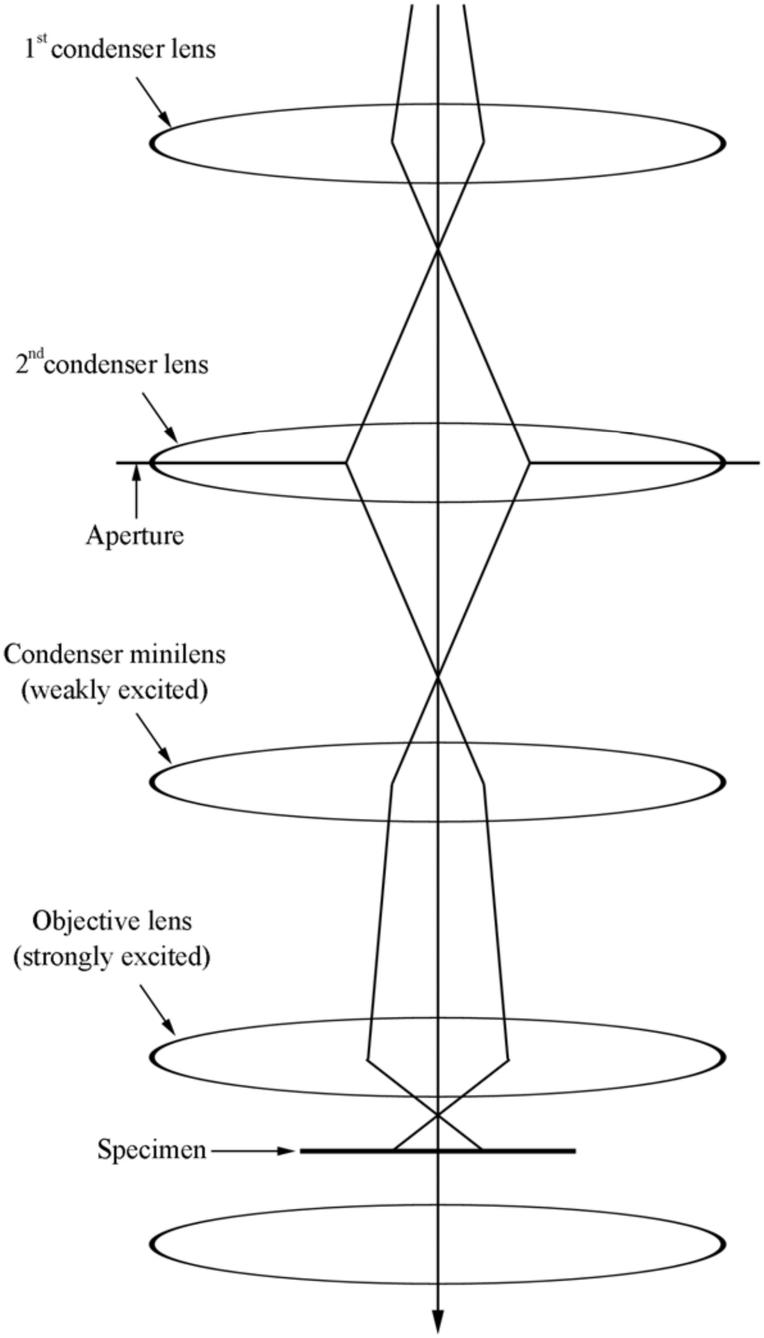

Figure 3.6: Nano-beam mode [89].

3.2.5 Grain Size Measurements

After the TEM microstructural analysis, scanned negatives were analyzed for their grain sizes. Although, grain size measurements are typically done using the ASTM E-112 standard, this method does not capture clusters of nano/sub-micron grains. This is because the grain size estimated by this method depends on the number of grain boundary intersections with three concentric rings of pre-determined standard diameters [90]. Additionally, by using the ASTM E-112 standard, no information regarding the grain size distribution within the annealed samples can be obtained.

Therefore, the following alternative method was used. First, scanned TEM negatives were analyzed using the Image J software (National Institute of Health, Bethesda – Maryland) from which individual grains were measured. For each grain, measurements were taken along the longest direction within the grain and its perpendicular, from which the mean was calculated and used as the average grain size $\bar{\mathbf{d}}$ for a particular sample (Fig. 3.7). A statistically significant sample-size of 100 grains from each of the annealed samples was measured. Nano/sub-micron (0.03μm-0.2μm) measured through this technique exhibit an errror of ~ 10%, while the larger austenitic grains (>1μm) have a reduced of error ~ 4%.

3.2.6 Tensile Testing – Mechanical properties

Samples annealed in the Gleeble 1500 thermo-mechanical simulator at the University of Oulu, were used for testing the mechanical properties. Coupons of dimensions, $150 \times 15 \times 0.9$ mm^3 were tensile tested under a strain rate of 3×10^{-3} s^{-1} on a Zwick Z250 testing machine at Outokumpu Stainless Oy, Tornio. This non-standard geometry was used since the uniform annealed zone in the coupon was small (~15mm).

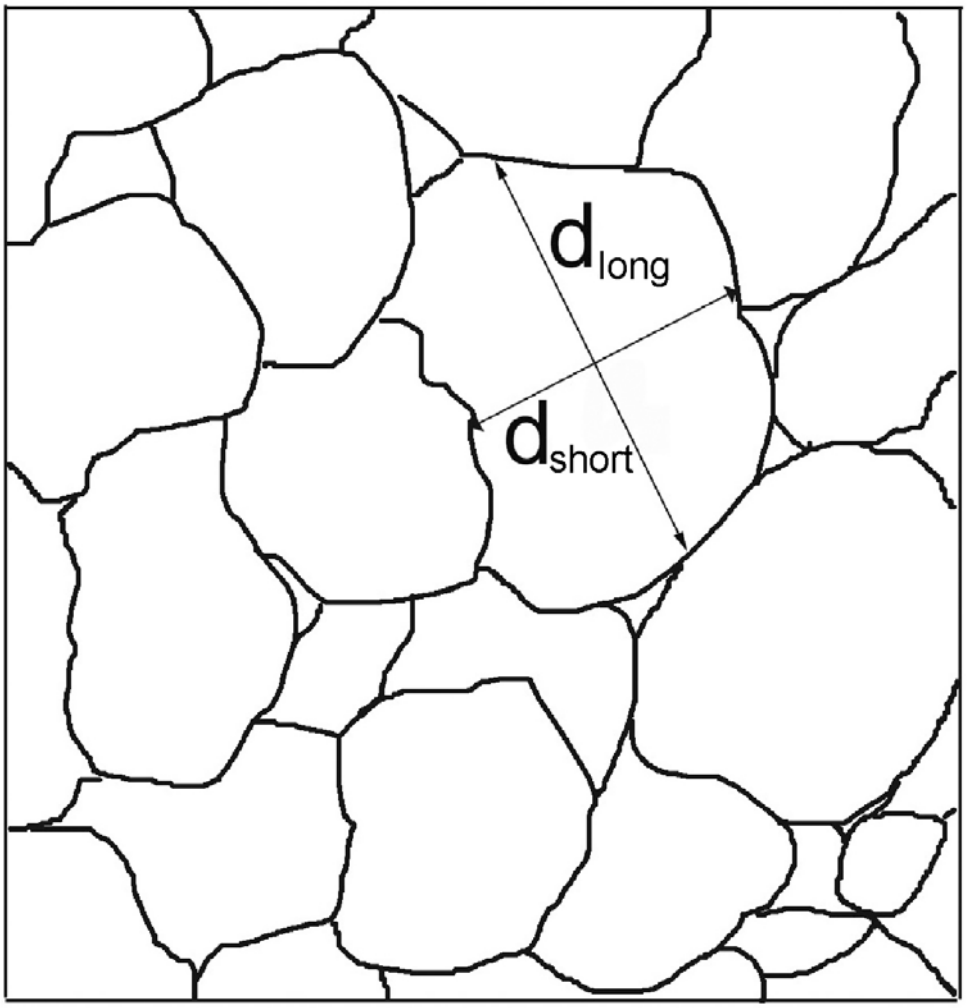

Figure 3.7: Grain size measurement along the longest direction within the grain and the short direction perpendicular to it.

Chapter 4: Experimental Results

4.1 X-RAY DIFFRACTION

The X-Ray diffraction spectrum of the 63% cold-rolled (CR) AISI 301LN sample is shown in Fig. 4.1a. The sample consists of primarily martensitic (α’) with a strong (211) α’ peak and a weak (220) austenite (γ) peak related to retained austenite that failed to convert to martensite upon deformation. When compared to the relative intensities of a randomly oriented austenite and martensite polycrystalline material, the cold-rolled AISI 301LN sample exhibits a preferred orientation (Fig. 4.1). Since there is the presence of texture associated with the cold-rolled sample, in order to estimate the austenite and martensite phase fractions, the procedure described in Chapter 3 (section 3.3.1.1) was employed. On this basis, the volume percentage of martensite in the CR sample was calculated to be 95.7%. This value was used as a reference, from which the saturation magnetization data obtained by the SQUID experiments (section 3.3.2) was correlated. In this fashion, the superior sensitivity of the SQUID instrument can be used to our advantage, which limits the error to about ~ 2% from the X-ray measurements of the CR sample.

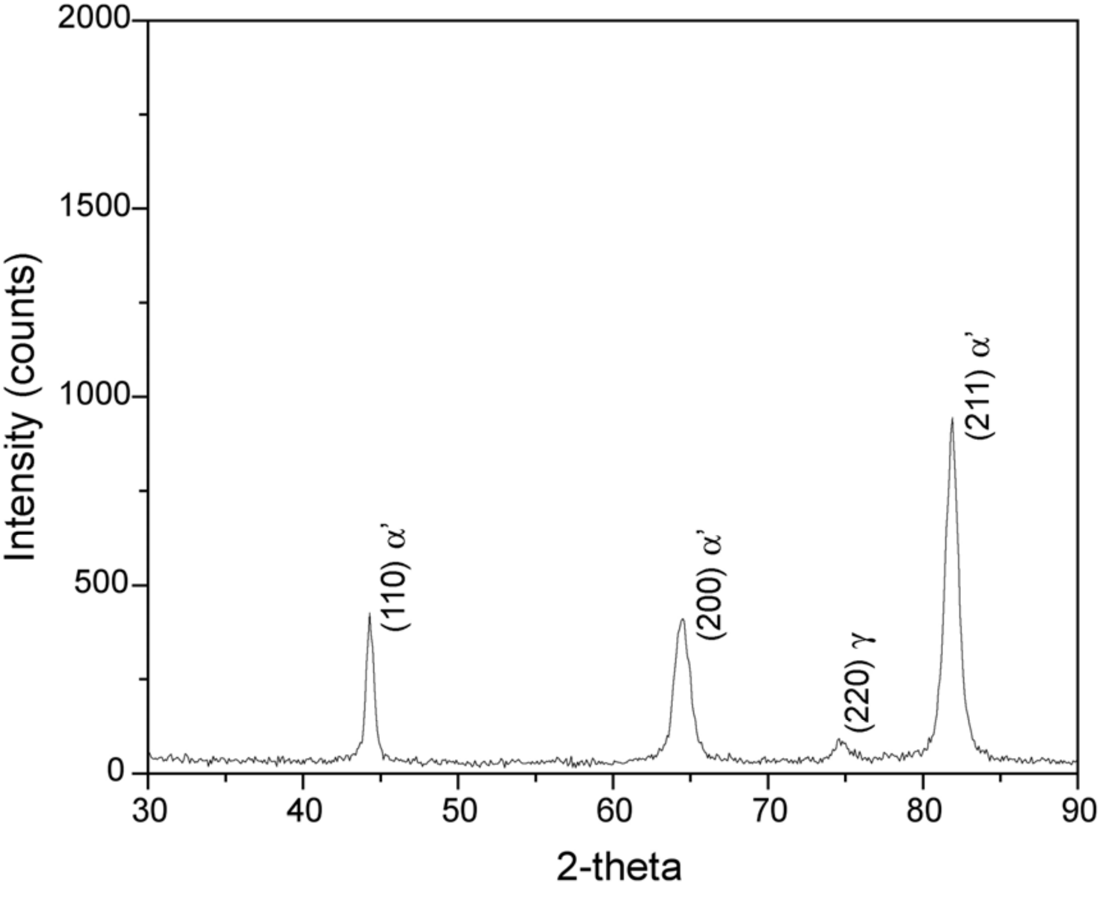

Figure 4.1: X-ray diffraction analysis of 63% cold rolled AISI 301LN SS.

4.2 MAGNETIC MEASUREMENTS

Using the method described in Chapter 3 (section 3.3.2) the saturation magnetization of the CR sample with dimensions of ~ $5 \times 1 \times 0.8$ mm^3 was obtained to be ~ 903 emu/cm^3 (Fig. 4.2). However, this value corresponds to 95.7% of martensite, as discussed in the preceding section. Thus, assuming a linear behavior, the saturation magnetization for a sample containing 100% martensite is calculated as ~ 944 emu/cm^3. This value is set as the standard and designated, **$m_{S\alpha'}$** - reference against which the saturation magnetization of all subsequent annealed samples, (**$m_{\alpha'}$**) is normalized.

Based on the $m_{\alpha'}$ and $m_{S\alpha'}$ values, the volume fraction of martensite in the annealed samples can be obtained through the expression:

$$V_{\alpha'} = \left[\frac{m_{\alpha'}}{m_{S\alpha'}} \right] \times 100 \tag{4.1}$$

where $V_{\alpha'}$ is the volume percentage of martensite in the sample. Assuming that the only paramagnetic phase present in the sample is austenite, the volume percentage of austenite can be calculated by subtracting $V_{\alpha'}$ from 100%. The results for all the annealed samples are shown as a function of temperature in Fig. 4.3. At 600°C, hardly any reversion to austenite occurs for samples annealed for 1 and 10 seconds. However, partial reversion to austenite is shown in samples annealed at 600°C for 100 seconds and 700°C for 1 second. For all other annealing parameters, almost complete reversion to austenite is observed (Fig. 4.3).

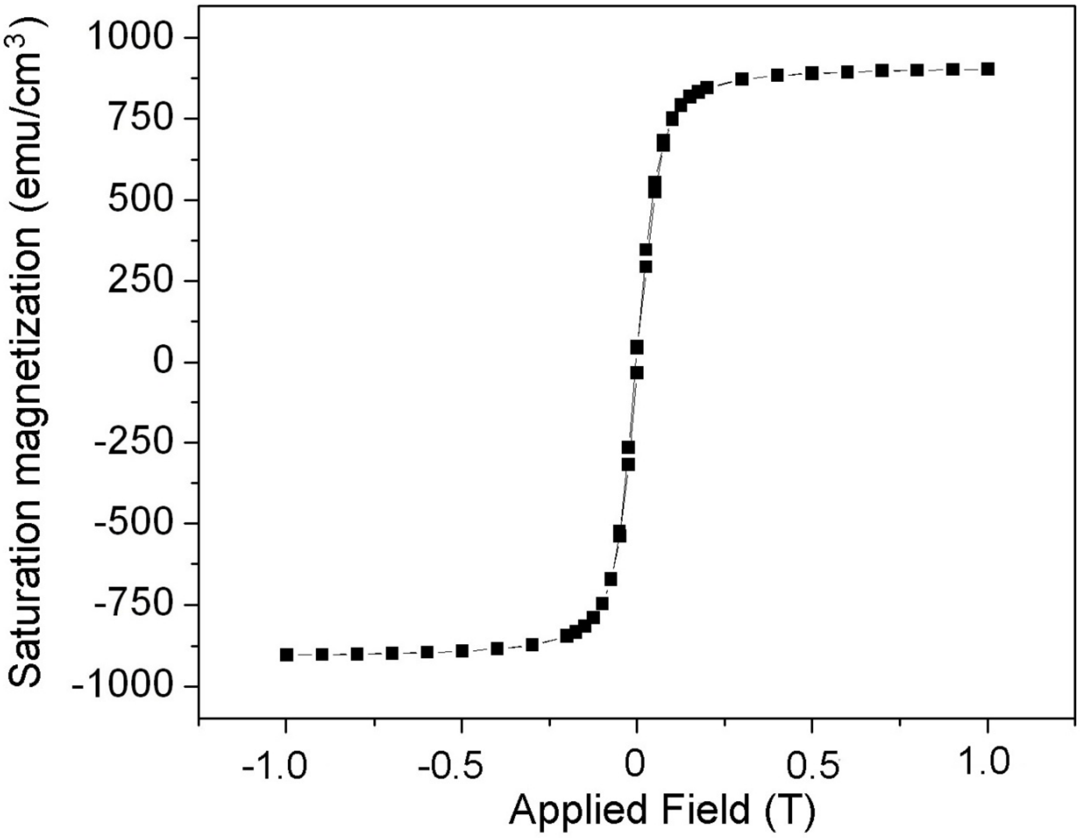

Figure 4.2: Saturation magnetization of a 63% cold rolled AISI 301LN SS.

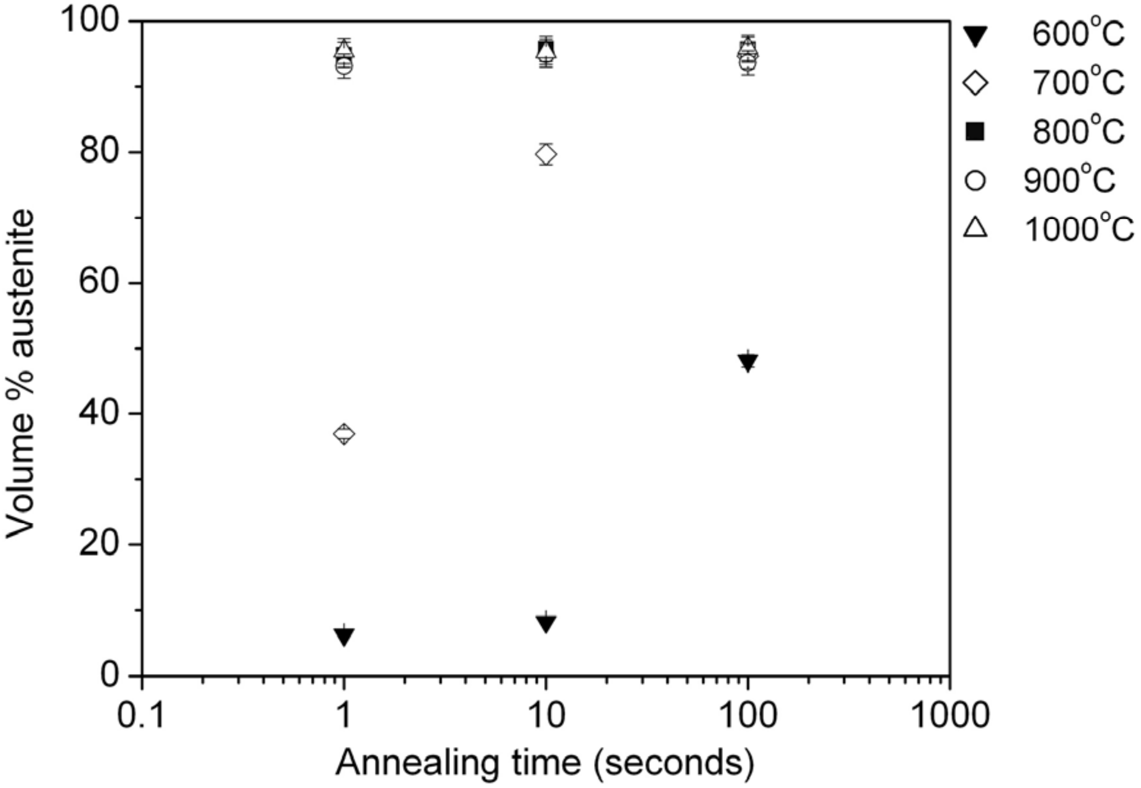

Figure 4.3: Volume percentage of austenite obtained after annealing a 63% cold-rolled AISI 301LN SS at different temperatures and times.

4.3 TRANSMISSION ELECTRON MICROSCOPY

4.3.1 Cold-Rolled Sample

A low magnification image of the cold rolled sample is shown in Fig. 4.4a. The heavily cold rolled (CR) sample shows regions of dislocation cell-type martensite and lath-type martensite, whose characteristics have been previously reported by Ma *et al.* [11], Tomimura *et al.* [12, 13], Tsuji *et al.* [20], Ueji *et al.* [21], and Korzekwa *et al.* [60]. Dislocation cell-type regions are characterized by the presence of dislocation forests and ultra-fine martensite as shown in Fig. 4.4b, and confirmed by the ring-like selected area diffraction pattern (SADP) (Fig. 4.4c). Regions of heavily deformed lath-type martensite are also observed (Fig. 4.4d). The SADP from such structure is substantially different (Fig. 4.4e) where a spot-like diffraction pattern corresponding to the martensite phase is observed.

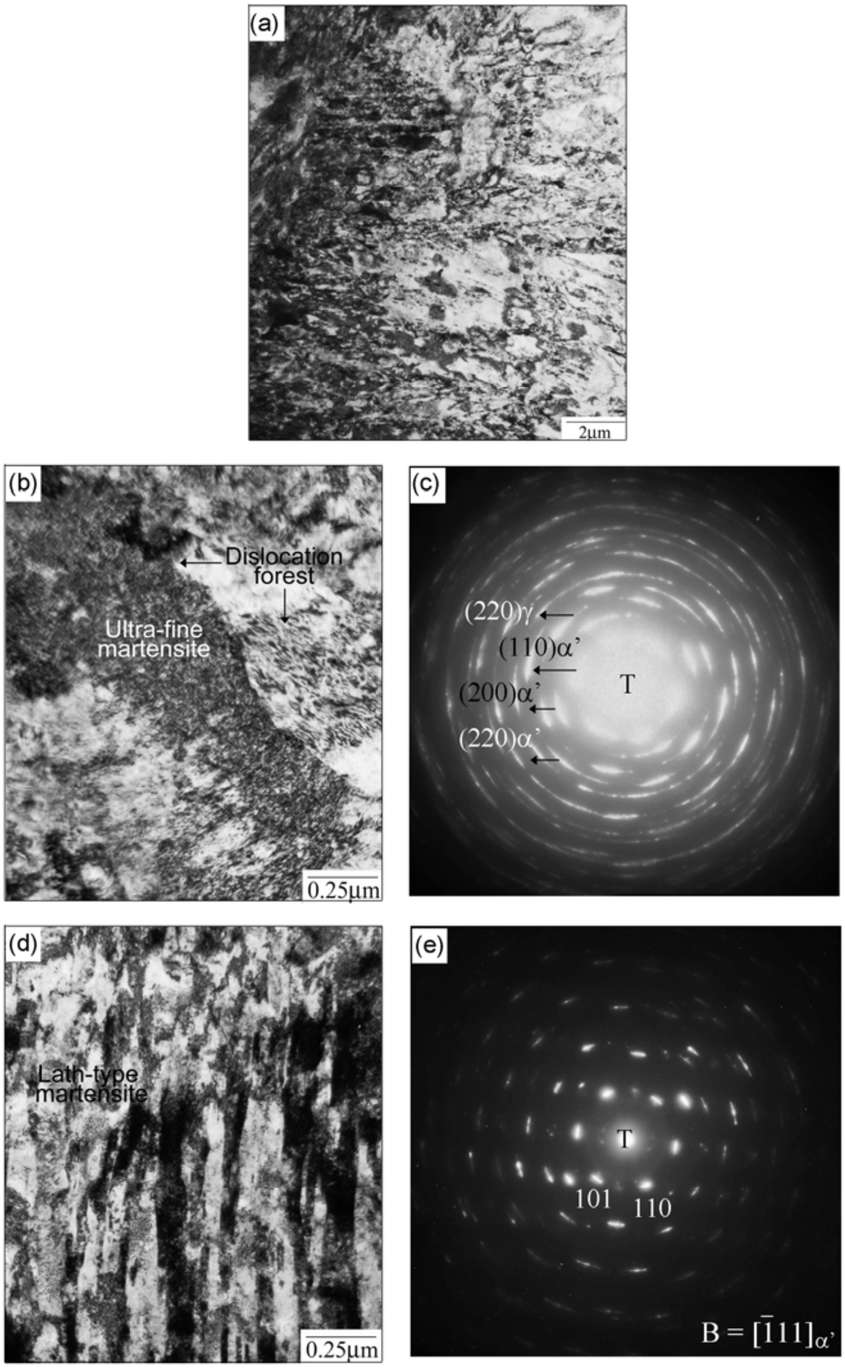

Figure 4.4: TEM image of 63% cold rolled AISI 301LN SS; (a) BF image at low magnification, (b) region with dislocation-cell martensite, (c) SADP of that region, (d) region with heavily deformed lath-martensite, and (e) SADP of circled region shown in (d).

4.3.2 600°C Annealed Samples

TEM images of samples annealed at 600°C for different annealing durations are shown in Fig. 4.5. The TEM image and the SADP for the 1-second annealed sample are shown in Figs. 4.5a and 4.5b, respectively. The diffraction rings corresponding to the martensitic phase (for instance, (211)α', (200)α' and (330)α') indicate the presence of dislocation cell type martensite. However, diffraction spots corresponding to the martensite phase are also observed, which are related with lath type martensite. In addition, diffraction streaks corresponding to retained austenitic (for instance, (113)γ and (040)γ) can also be observed. As these microstructural features are also present in the cold-rolled sample, we can infer that annealing at 600°C for 1 second is not sufficient to completely erase the microstructure inherited from the cold-rolled sample. However, as the annealing duration is increased to 10 seconds, the diffraction pattern indicates a loss of texture (Fig. 4.5c and 4.5d). In addition, the intensity of the (040)γ and (113)γ reflections increases and assumes a ring-like shape (for instance, (040)γ), which imply the formation of ultra-fine austenite grains. Fig. 4.5b, 4.5d and 4.5f also show that the martensite phase is still present as dislocation-cell type and lath type, as confirmed by the (110)α' and (211)α' diffraction rings and the (211)α' diffraction spots.

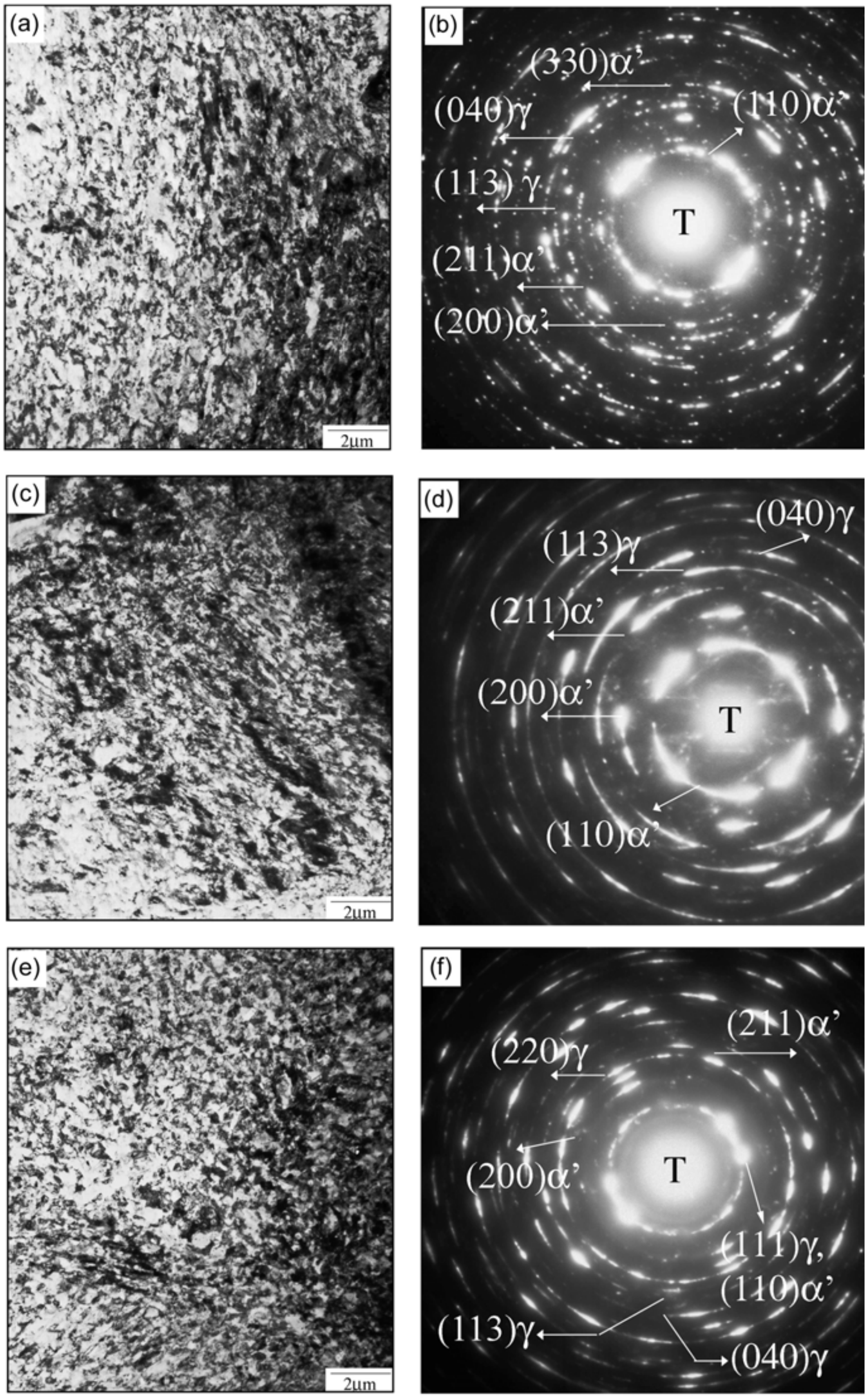

Figure 4.5: TEM image of cold rolled SS301LN annealed at 600°C for; (a) 1 second, (c) 10 seconds, and (e) 100 seconds. Diffraction patterns corresponding to each annealing time is shown in (b), (d) and (f).

At a first glance, the microstructure of samples annealed for 100 seconds at 600°C (Fig.4.5e) seem rather similar to the samples annealed for 1 and 10 seconds at the same temperature (Figs. 4.5a and 4.5c). However, a closer look at the SADP taken from the 100 seconds sample (Fig.4.5f) shows an additional (220)γ diffraction ring and a change in the martensitic reflections (for instance, (211)α' and (200)α'), from a ring-like pattern to a spot-like pattern. Thus, higher magnification images were taken for the samples annealed at 10 and 100 seconds to carefully investigate the differences.

Higher magnification images of these samples are shown in Fig. 4.6. The microstructure of the samples annealed at 600°C for 10 seconds confirm that these annealing conditions are still insufficient to significantly affect the α' → γ reversion (Fig. 4.6a and Fig. 4.6c). The martensite morphology and microstructural features are essentially similar to that of the samples annealed for 1 second at 600°C (Fig. 4.5a). The SADP of the image shown in Fig. 4.6a reveals relatively fine martensitic grains bounded by dislocation walls and forests. On the other hand, a striking difference is noted when the annealing duration is increased to 100 seconds (Fig. 4.6b). In this case, equiaxed nano/sub-micron grains of austenite are clearly visible. The SADP of this microstructure shown in Fig. 4.6d confirms that the austenitic reflections are dominant and ring-like, (for instance, (200)γ, (113)γ and (040)γ).

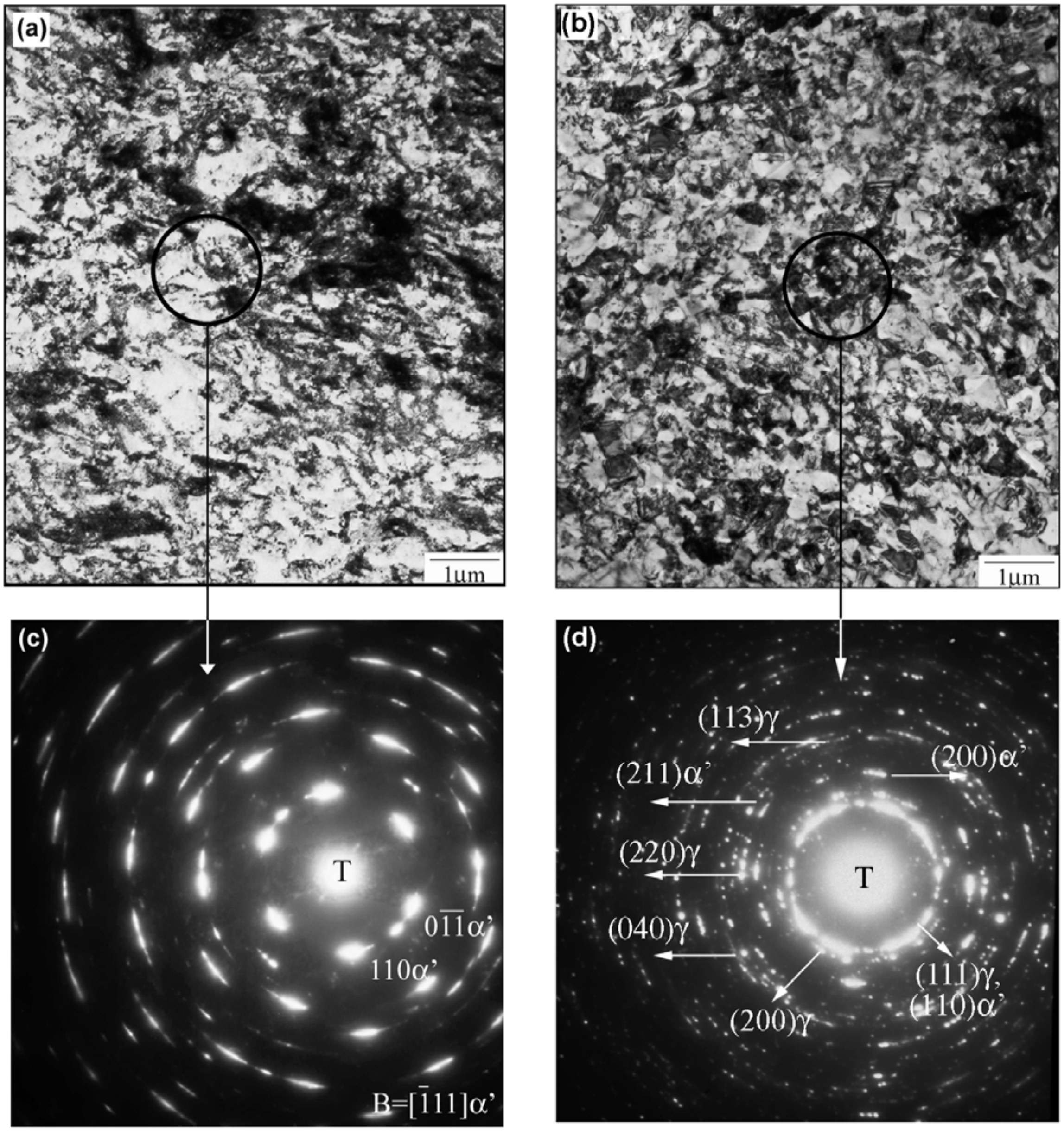

Figure 4.6: (a) Higher magnification TEM image of 63% cold rolled AISI 301LN SS annealed at 600°C for 10 seconds, (b) annealed at 600°C for 100 seconds. Diffraction patterns corresponding to these images are shown in (c) and (d) respectively.

4.3.3 700°C Annealed Samples

Samples annealed at a higher temperature of 700°C for 1 second also exhibit equiaxed nano/sub-micron grains (Fig. 4.7a). An analysis of the corresponding SADP (Fig. 4.7b), reveals that the sample is comprised of both fine martensite and fine austenite, as shown by the diffraction rings associated with both phases. This confirms the data obtained from SQUID experiments where a partial reversion of ~ 35% from martensite to austenite was determined.

TEM images of samples annealed for longer annealing times show the formation of larger grains, (Fig. 4.7c and 4.7d). The corresponding SADP changes from being almost ring-like (in the case of 1 second anneal – Fig. 4.7b) to a more spot-like pattern for the 10 and 100 seconds annealing. In addition, samples annealed for 10 seconds show the presence of a shear band and a significant distribution of grain sizes (Fig. 4.7c). This shear band is likely to be an austenitic shear band, which is an artifact from the cold rolled sample. Additionally, regions of large and small grains in both 10 and 100 second annealed samples are observed and their origin will be discussed in greater detail in section 5.1.3.

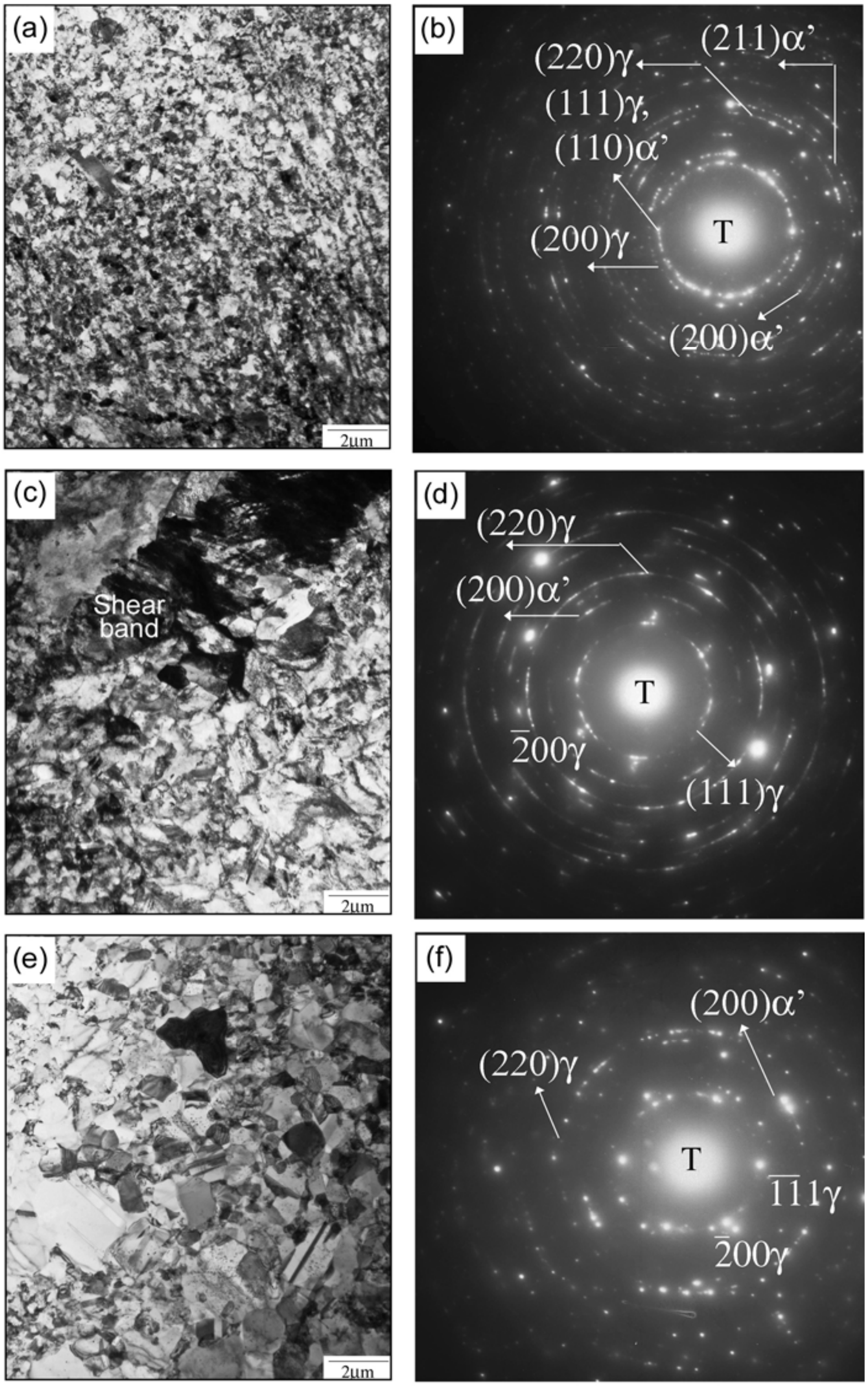

Figure 4.7: TEM image of cold rolled AISI 301LN SS annealed at 700°C for (a) 1 second, (c) 10 seconds, and (e) 100 seconds. Corresponding diffraction patterns are shown in (b), (d) and (f).

4.3.4 800°C Annealed Samples

TEM images of samples annealed at 800°C for various annealing times are shown in Fig. 4.8. The microstructure of the sample annealed for 1 second (Fig. 4.8a) shows a mixture of nano/sub-micron grains and large grains. This observation is confirmed by the SADP, which indicates the presence of diffraction spots and rings corresponding to the austenite phase. This mixture of large and small grains is likely due to two reasons: 1) presence of different types of martensite (dislocation cell-type and lath) in the cold rolled sample leading to different austenite nucleation rates (as it happened at 700°C) and 2) nucleation of austenitic grains at lower annealing temperatures, which grow in size as the annealing temperature is rapidly brought to 800°C. Fig. 4.8c shows an image of the sample that was annealed for 10 seconds at 800°C. In this case, the sample consists primarily of equiaxed austenitic grains. Annealing for 100 seconds leads to further grain growth (Fig. 4.10e), and a consequent spot-like SADP shown in Fig. 4.8f.

Furthermore, the microstructure of the 800°C annealed samples taken from different regions reveal the presence of secondary phase precipitates with sizes around 10-20 nm. These precipitates were identified by nano-beam diffraction (section 3.3.3.2) to be CrN precipitates (Fig.4.9).

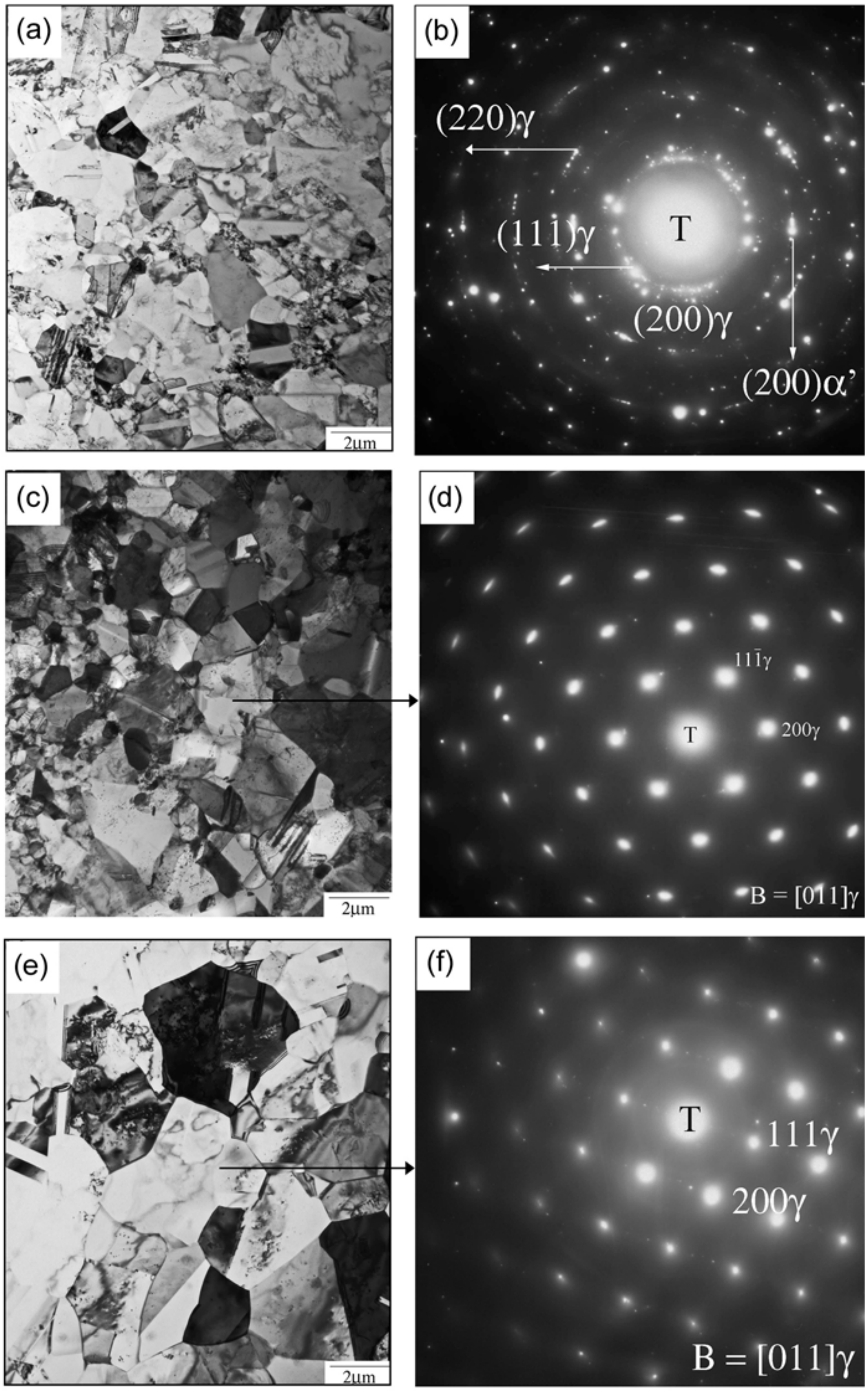

Figure 4.8: TEM image of cold rolled AISI 301LN SS annealed at 800°C for (a) 1 second, (c) 10 seconds, and (e) 100 seconds. Corresponding diffraction patterns are shown in (b), (d) and (f).

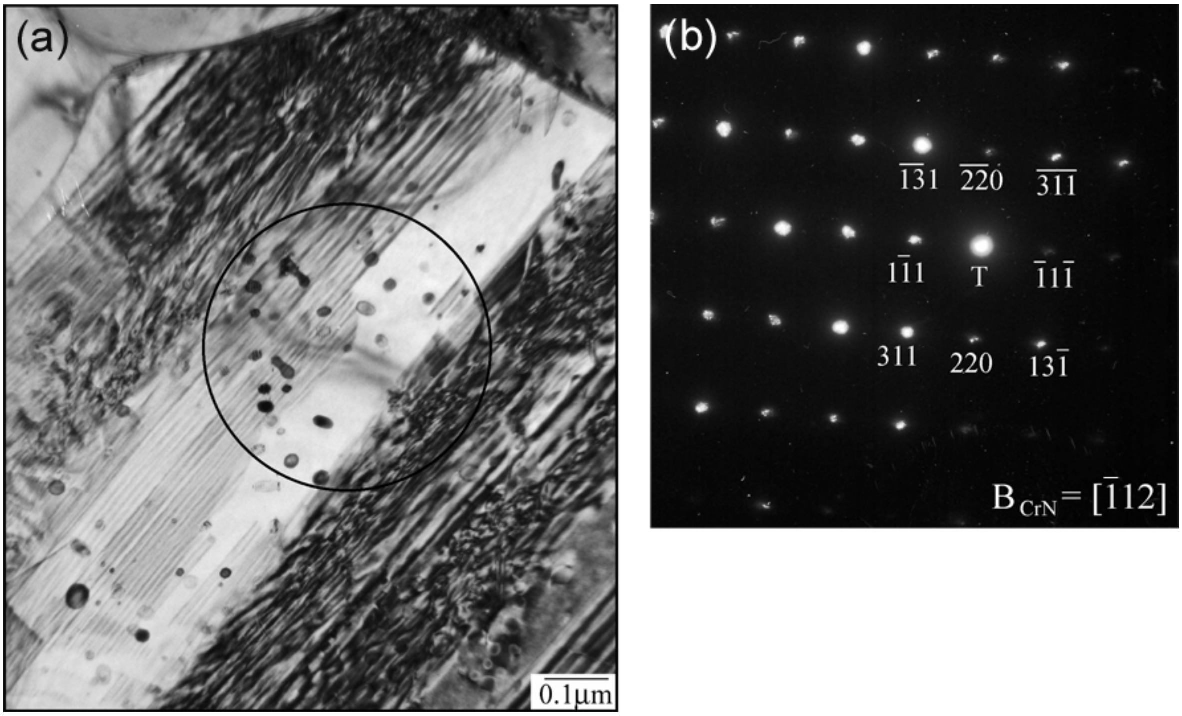

Figure 4.9: (a) Secondary phase precipitates observed in AISI 301LN SS annealed at 800°C and 900°C are shown within the black circle, and (b) Electron nano-diffraction analysis of the precipitates shown in (a) reveal the presence of CrN nitrides with a face-centered cubic structure and a lattice parameter of 4.14 Å.

4.3.5 900°C and 1000°C Annealed Samples

TEM images of the samples annealed at 900°C and 1000°C are shown in Fig. 4.10. It should be noted that owing to rapid grain growth and consequent large austenitic grain sizes, the corresponding SADP are not shown since they offer negligible information regarding the microstructure evolution. An analysis of the microstructure for these samples shows that annealing at 900°C and 1000°C are clearly efficient in converting the martensite phase to austenite, followed by grain growth. Defect free austenitic grains are formed after a short annealing time of 1 second. Finally, when compared with samples annealed at 700°C and 800°C, there is a marked reduction in the number of secondary phase precipitates in these samples, as CrN dissolves at higher temperatures [76, 79].

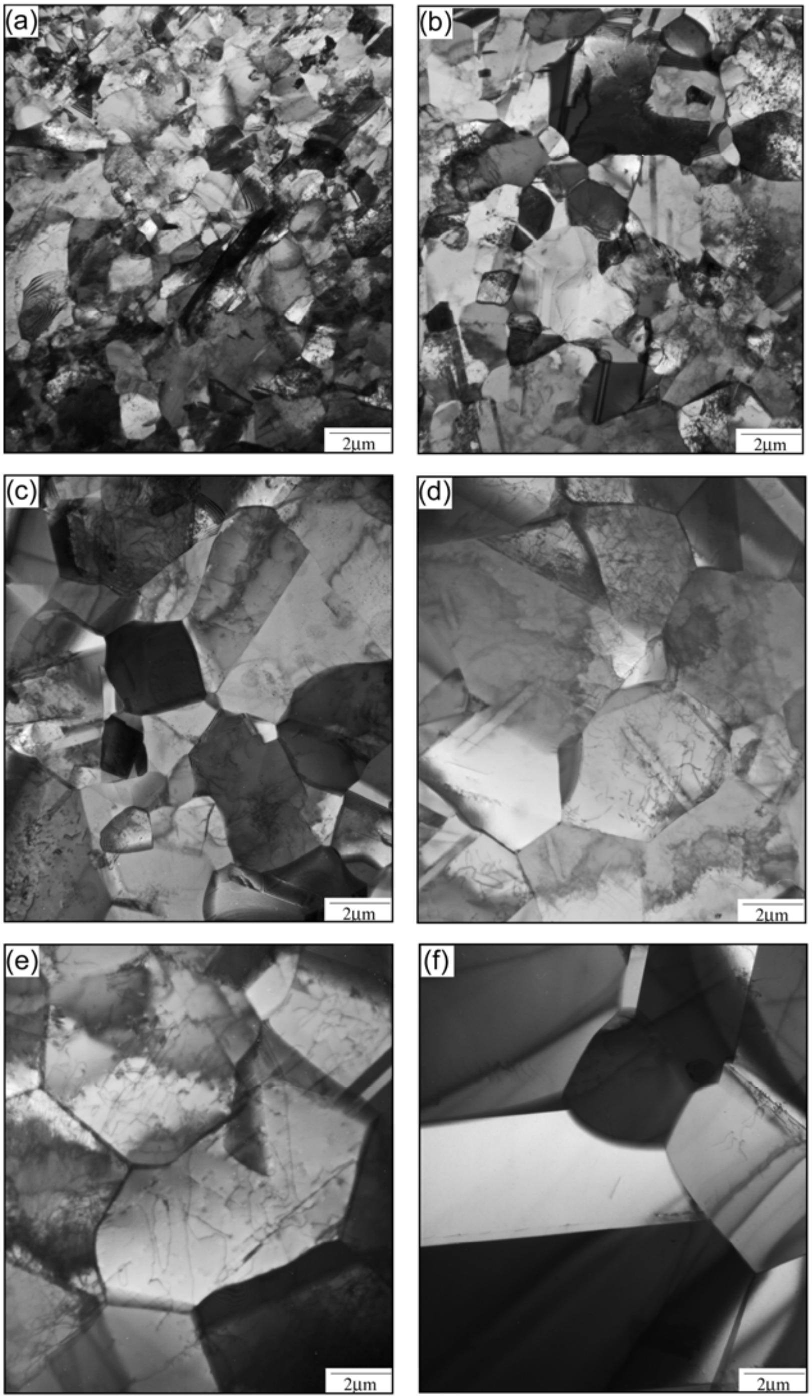

Figure 4.10: TEM images of 63% cold rolled AISI 301LN SS samples annealed at 900°C for (a) 1 second, (c) 10 seconds and (e) 100 seconds; and at 1000°C for (b) 1 second, (d) 10 seconds and (f) 100 seconds.

4.4 GRAIN SIZE ANALYSIS

As previously discussed, under certain annealing conditions, the microstructure shows a significant distribution in grain sizes. Figure 4.11 shows this effect, particularly for the samples annealed at 800°C and 900°C for 1 second, and the sample annealed at 800°C for 10 seconds. Thus to achieve a realistic estimate of grain size, representative of a given sample, the following procedure was employed. The longest direction within the grain and its perpendicular shortest direction were measured (Fig. 3.7), from which the mean was calculated and this represented the average individual grain size $\mathbf{d}_i$. 100 grains were measured for this sample using this procedure. Subsequently, the individual grain sizes $(\mathbf{d}_{1,}, \mathbf{d}_2, ..., \mathbf{d}_{100})$, were distributed in bins of predefined bin sizes to obtain the grain size distribution for each of the annealed samples. The selection of each particular bin size was made after determining the range of grain sizes measured for each of the annealed samples.

The bin size for the annealing temperature of 600°C and 700°C was selected as $\mathbf{B} = (\mathbf{b_1}, \mathbf{b_2}, ..., \mathbf{b_N})$, where $\mathbf{b_1}$ = 0-0.020μm, $\mathbf{b_2}$ = 0.020μm-0.040μm, …, $\mathbf{b_N}$ = 2.20μm-2.40μm. Samples annealed at 600°C for 1 and 10 seconds exhibit a grain size distribution where the majority of grains are clustered around the mean and the variance is small (Fig.4.14). As the annealing duration was increased to 100 seconds (Fig. 4.12), the grain size distribution becomes broader. For the case of the 700°C annealed samples, the distribution of grains assumes a log-normal form at 1 and 10 seconds of annealing, which rapidly converges to a normal distribution when annealed for 100 seconds (Fig. 4.13).

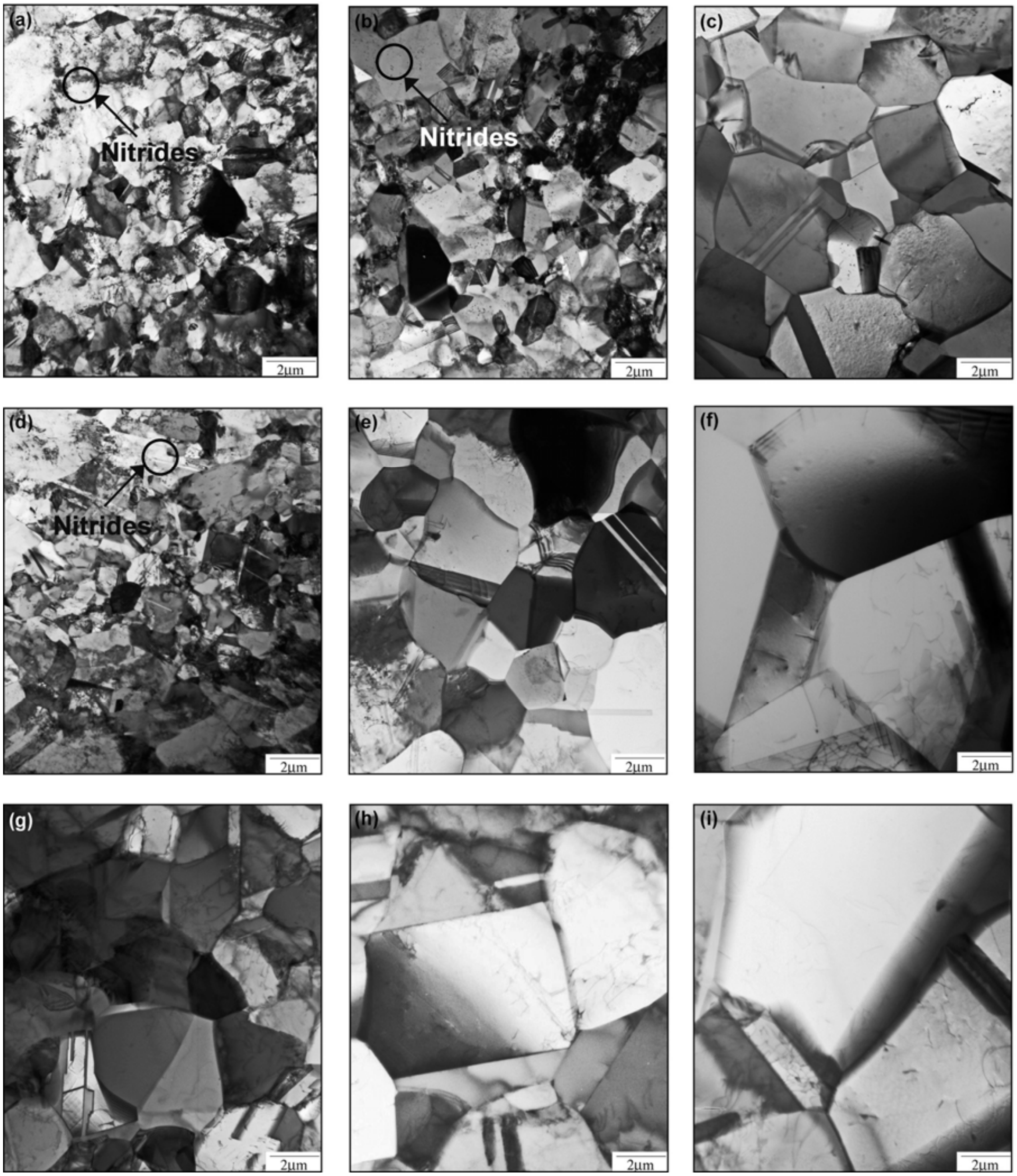

Figure 4.11: TEM images of 63% cold-rolled AISI 301LN SS samples annealed at 800°C (a-c), 900°C (d-f) and 1000°C (g-i) for 1, 10 and 100 seconds.

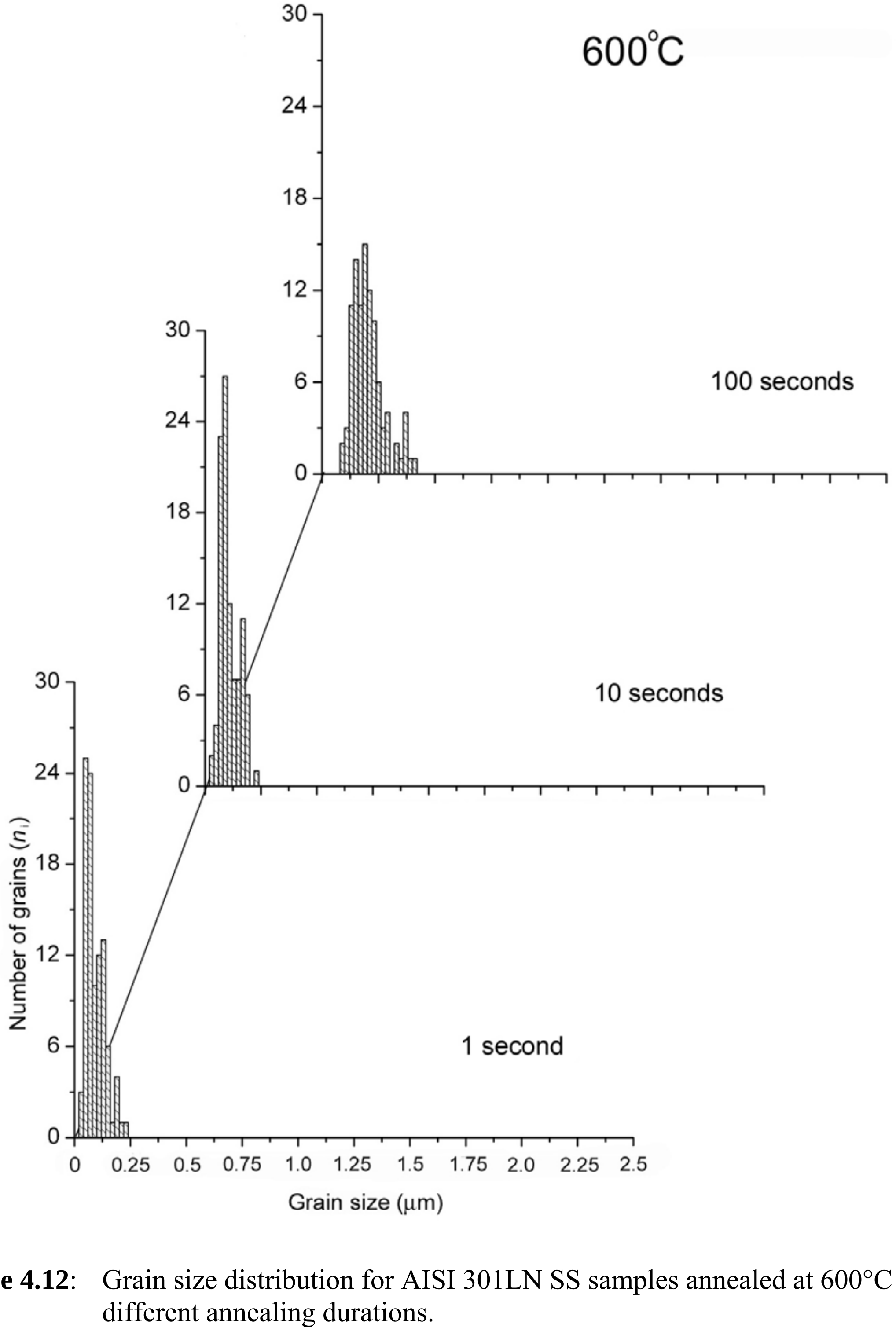

Figure 4.12: Grain size distribution for AISI 301LN SS samples annealed at 600°C for different annealing durations.

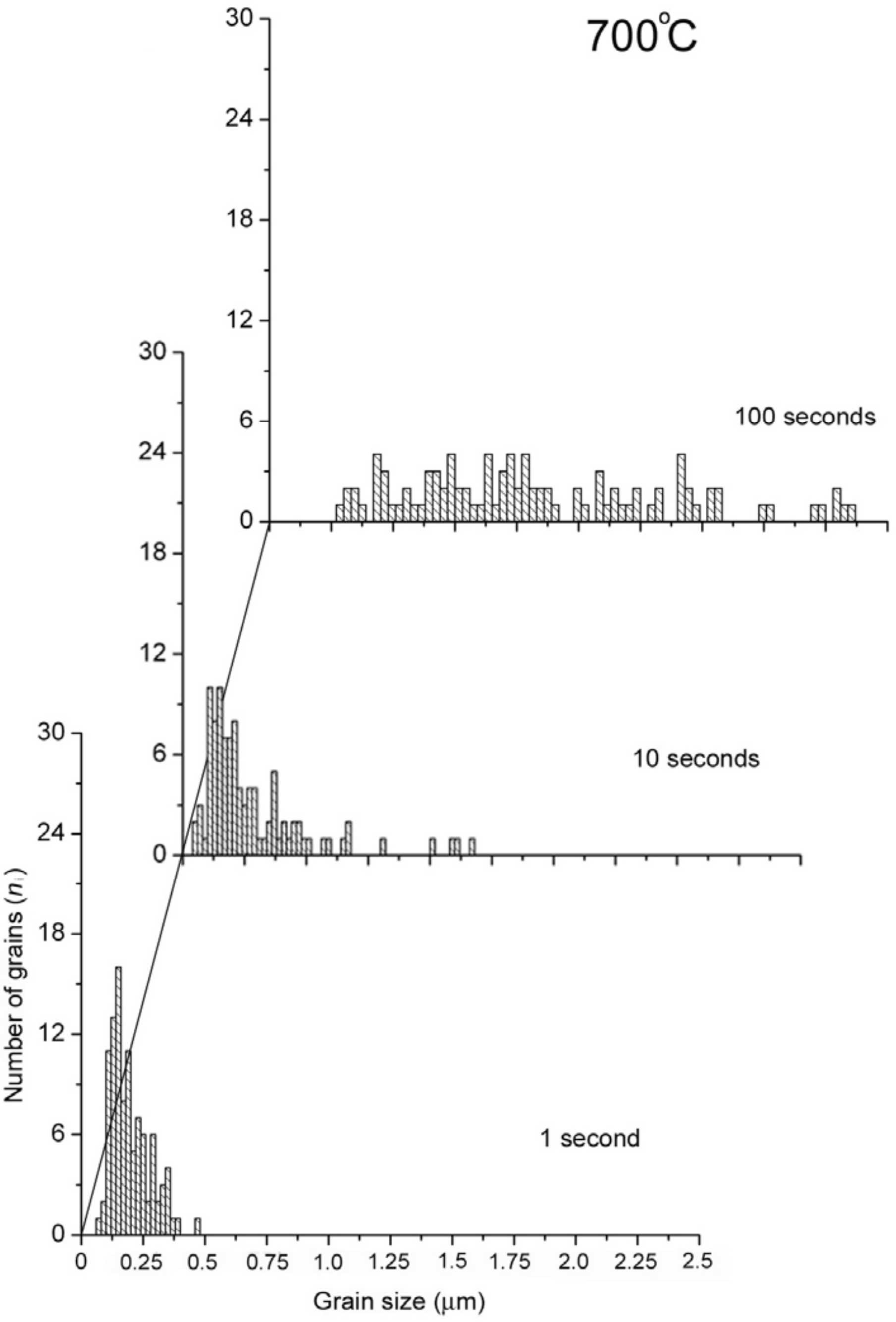

Figure 4.13: Grain size distribution for AISI 301LN SS samples annealed at 700°C for different annealing durations.

For samples annealed at higher temperatures (800°C, 900°C and 1000°C), the bin sizes were selected as $\mathbf{B} = (\mathbf{b}_1, \mathbf{b}_2, ..., \mathbf{b}_N)$, where $\mathbf{b_1}$ = 0-0.25μm, $\mathbf{b_2}$ = 0.25μm-0.50μm,…, $\mathbf{b_N}$ = 19.75μm-20.00μm. In this range of temperatures, the samples annealed at 1 second exhibit a log-normal grain size distribution (Figures 4.14, 4.15, 4.16). For longer annealing times, the grain size distribution converges towards a more normal distribution (Fig. 4.14, 4.15 and 4.16).

The calculated average grain sizes for all annealing treatments are shown in Fig. 4.17a. It is seen that there is large difference in the mean grain sizes obtained for the various annealing conditions. While samples annealed at 600°C and 700°C hardly exhibit grain growth, samples annealed at 800°C, 900°C and 1000°C show a drastic increase in grain size (Fig. 4.17a). In particular, the samples annealed at 900°C, exhibit an increase in grain size from ~1.2 μm to ~ 6.1 μm when the annealing duration is increased from 1 to 100 seconds, and the 1000°C samples show a drastic increase from ~1.5 μm to ~ 10 μm for a similar change in the annealing duration. A more detailed plot of the grain size data for the samples annealed at 600°C, 700°C and 800°C is shown in Fig. 4.17b. As shown, nano sized grains of ~ 90nm could be found for the samples annealed at 600°C for 1 second. At this annealing temperature, there is little grain growth as the annealing duration is increased to 100 seconds. For the samples annealed at 800°C, an increase in annealing duration from 1 to 100 seconds lead to an increase in grain size from ~ 0.54 μm to ~2.4 μm.

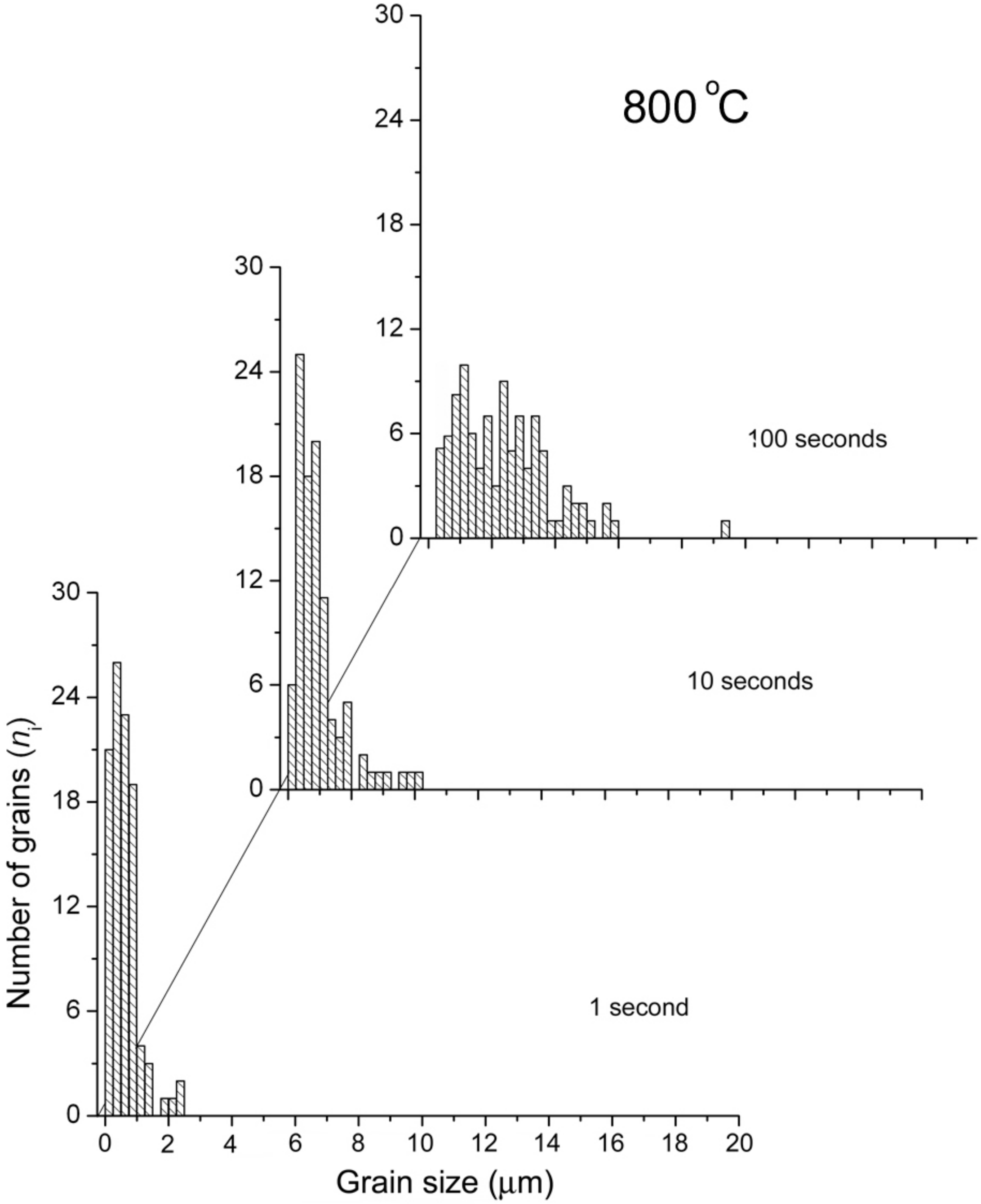

Figure 4.14: Grain size distribution for AISI 301LN SS samples annealed at 800°C for different annealing durations.

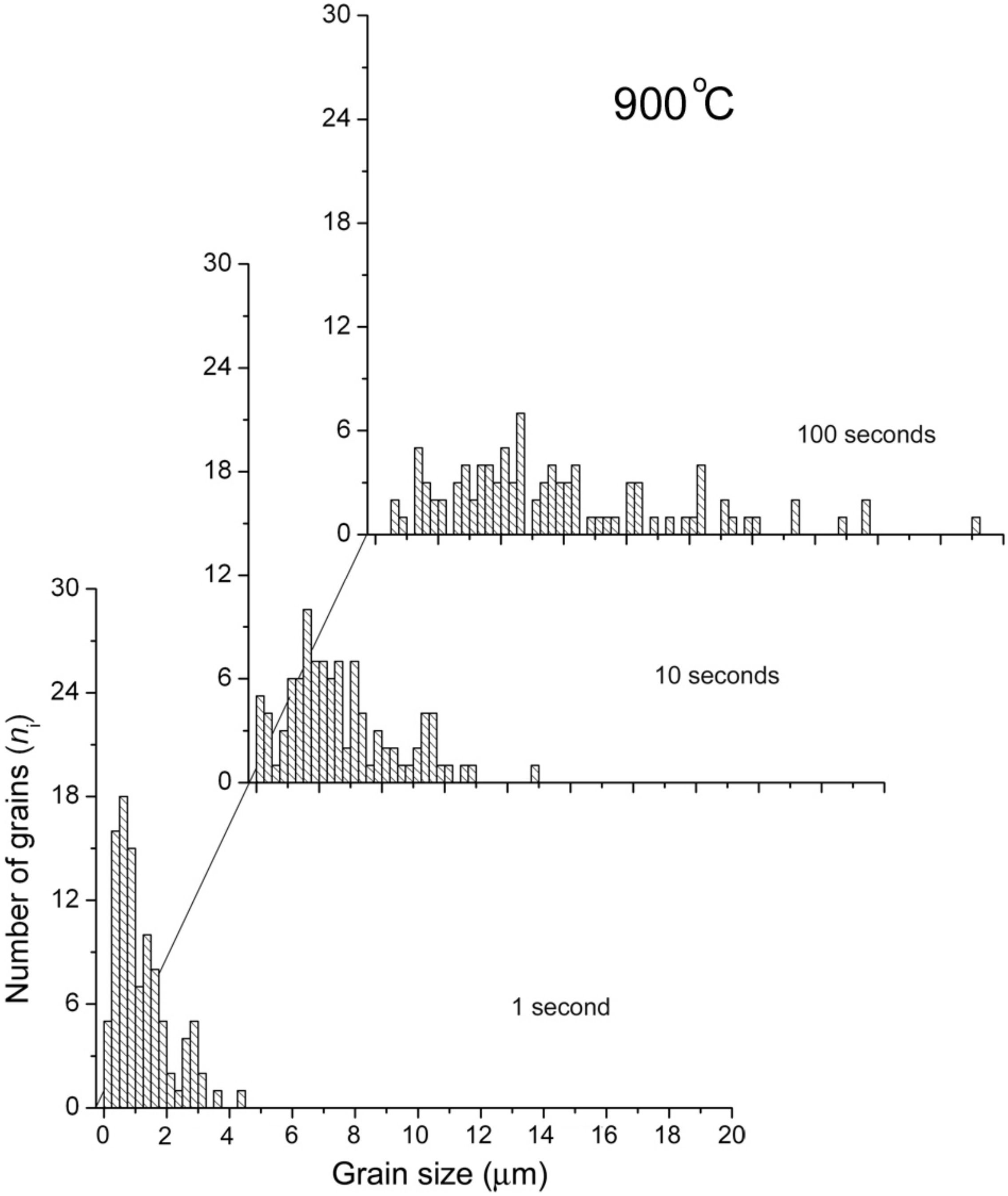

Figure 4.15: Grain size distribution for AISI 301LN SS samples annealed at 900°C for different annealing durations.

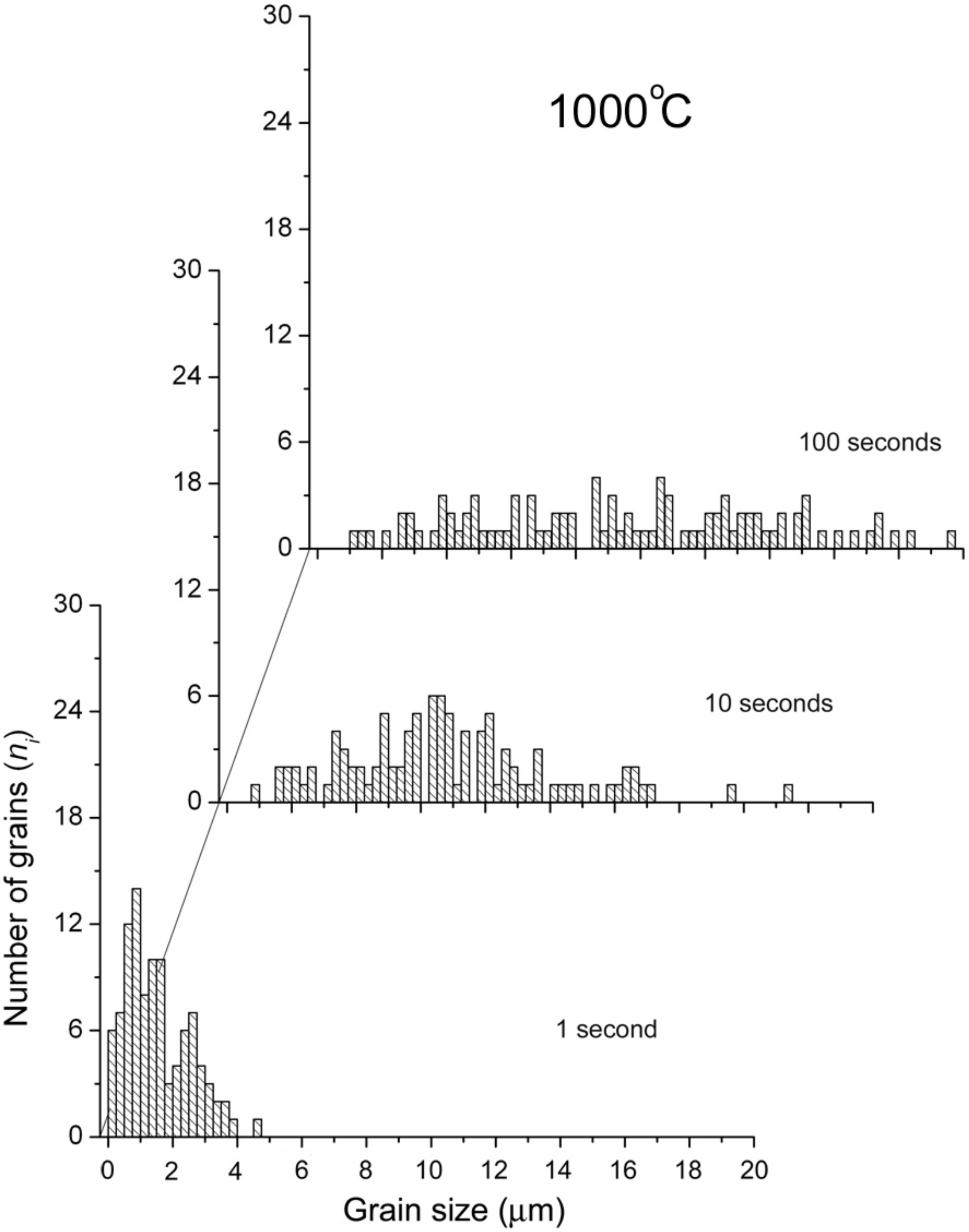

Figure 4.16: Grain size distribution for AISI 301LN SS samples annealed at 1000°C for different annealing durations.

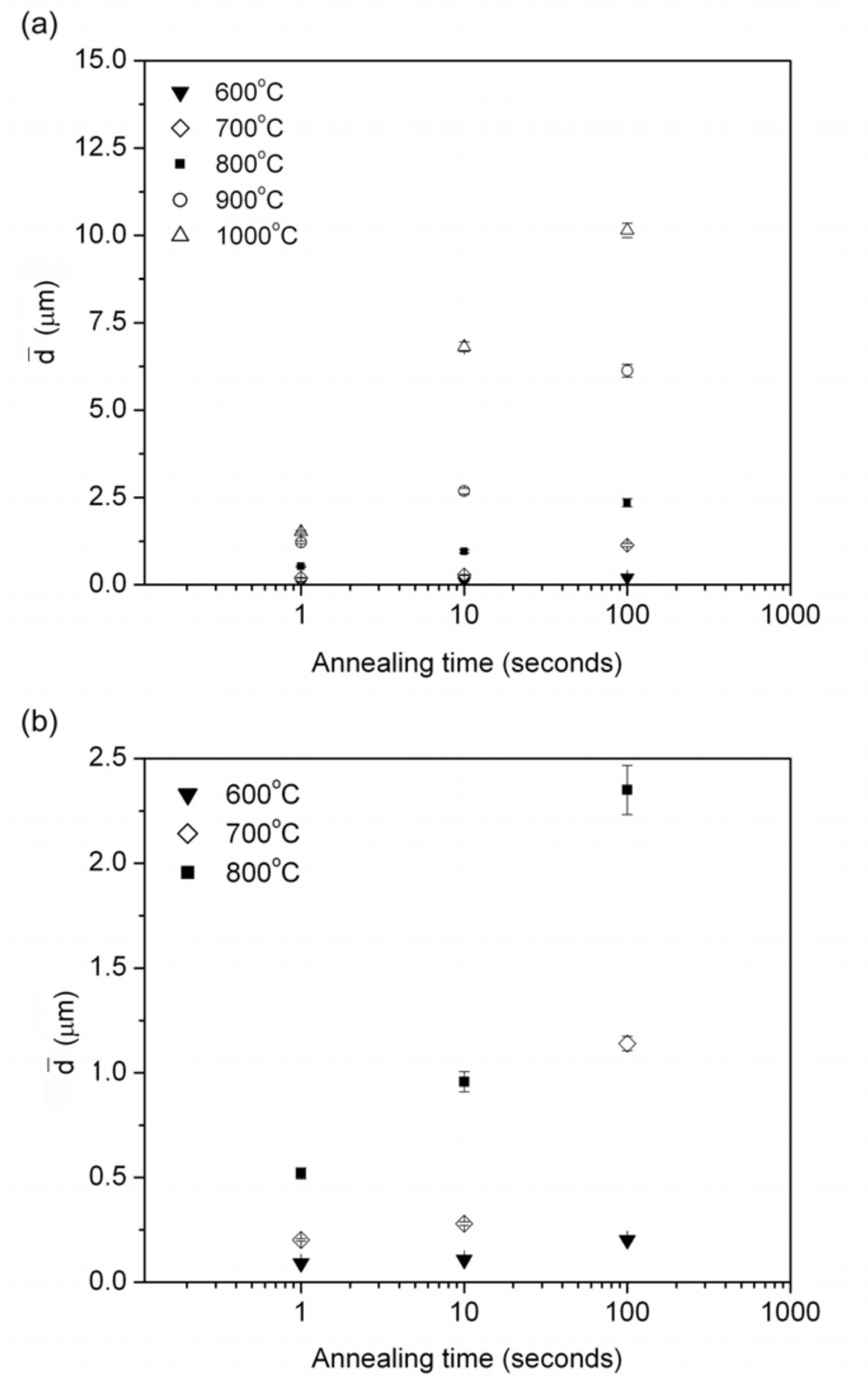

Figure 4.17: Grain size calculations for AISI 301LN SS samples; (a) annealed at 600°C, 700°C, 800°C, 900°C and 1000°C, (b) an enlarged view of the samples annealed at 600°C, 700°C and 800°C.

4.5 MECHANICAL PROPERTIES

4.5.1 Tensile Strength and Yield Strength

The tensile strength for all annealed samples is shown in Fig. 4.18a. Samples annealed at 600°C show an exceptional strength of ~ 1.5-2GPa. However, it should be kept in mind that these samples are primarily comprised of martensite phase (Fig. 4.3), for which a high tensile strength is expected. As the samples annealed at higher temperatures contain a larger fraction of austenite (Fig, 4.3), the tensile and yield strengths of samples annealed at 700°-1000° C are reduced. Nonetheless, these samples still exhibit tensile strengths that are at least 50% higher when compared with conventional processed AISI 301LN SS. The same can be said about the yield strength. As shown in Fig. 4.18b, all samples annealed at 800°C and the sample annealed for 1 second at 900°C exhibit high yield strength values. In fact, the samples annealed at 800°C for 1 second exhibit a yield strength that is almost twice as that of conventional processed AISI 301LN SS (~ 350MPa). However, as the annealing duration is increased for the 900°C samples, or the annealing temperature is increased to 1000°C, the yield strength decreases considerably. Further analysis of the tensile and yield strength data also reveals that tensile and yield strength of samples annealed at 600°C is similar, whereas there is a drastic difference in tensile and yield strengths for the samples annealed at higher temperatures.

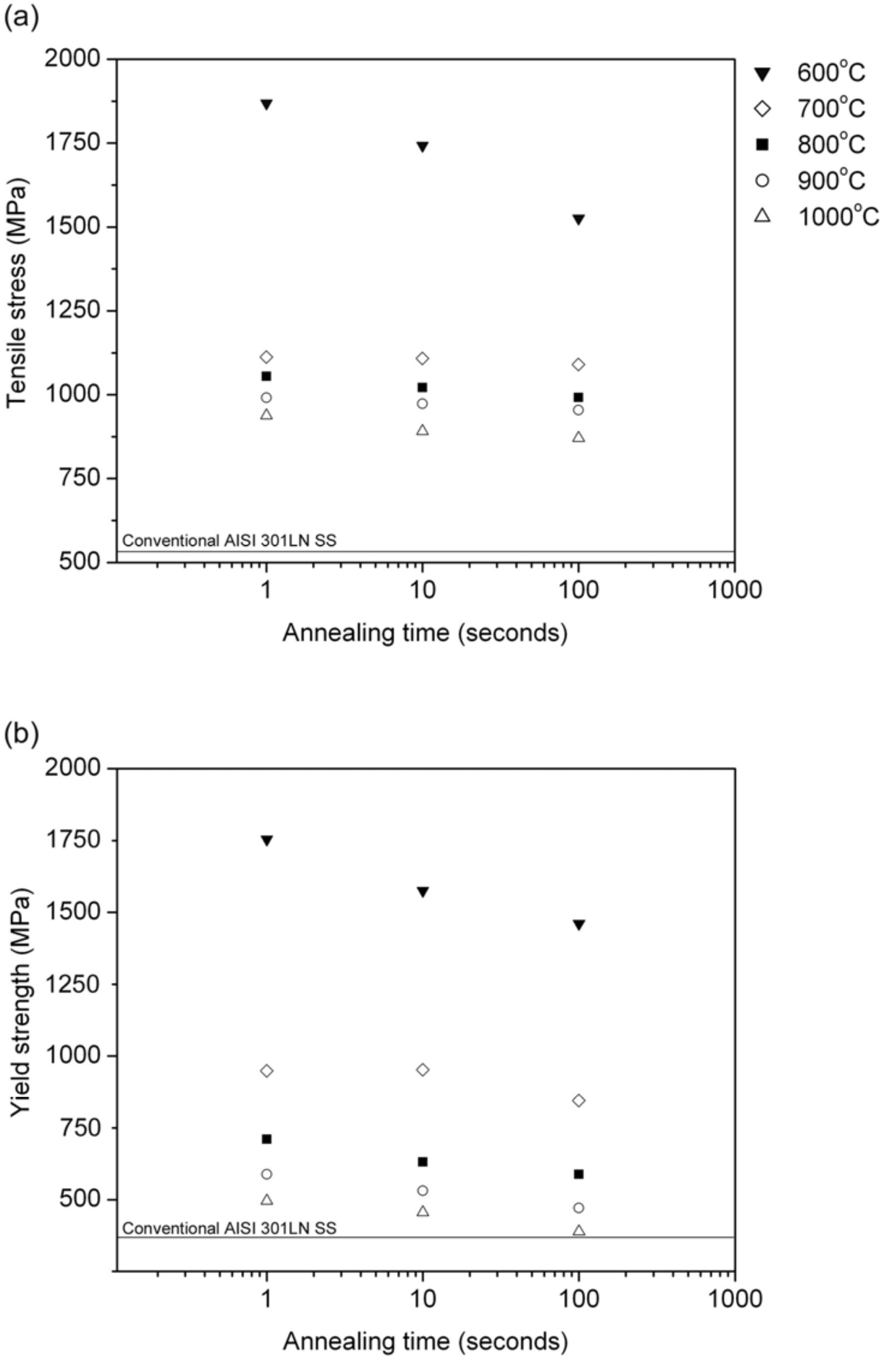

Figure 4.18: Mechanical properties of AISI 301LN SS for different annealing parameters; (a) Tensile Strength, (b) Yield strength.

4.5.2 Uniform Elongation

Fig. 4.19 shows the uniform elongation properties of samples annealed under various annealing conditions. The samples annealed at 600°C exhibit poor ductility behavior. This is due to the presence of the martensitic phase, which is predominant in these samples. These results also explain the similar tensile and yield strength values obtained for the 600°C annealed samples (Fig. 4.19). These samples experience very little plastic deformation upon loading and thus, at failure their yield strength and tensile strength are practically the same.

When the samples are annealed at higher temperatures, the extent of uniform elongation depends on the percentage of austenite present in the sample. Such behavior is clearly seen in samples annealed at 700°C where the percent elongation changes from ~ 10% to ~ 30% when the annealing duration is increased from 1 to 100 seconds (austenite content changes from ~ 35% to ~ 95% (Fig. 4.3)). Following this argument, the uniform elongation of samples annealed at 800°C, 900°C and 1000°C are similar and also comparable to those of conventional processed AISI 301LN SS. Additionally, using the Considére criterion, the work hardening exponent (n) can be related to the uniform elongation strain (ε_u), as $n = \varepsilon_u$ at the onset of necking. Thus from Fig. 4.19, it can be inferred that the samples have a high work hardening exponent (n) of at least 0.40 for the annealing temperatures of 900°C and 1000°C. For samples annealed at 800°C for 1 and 10 seconds, the uniform elongation is slightly less than conventional processed AISI 301LN SS as expected due to sub-micron grain size.

4.6 THE BIG PICTURE: RESULTS

As indicated in the introduction of this work, the ultimate objective of this work is to achieve high strength and high ductility in commercial SS. The results presented in this chapter conclusively demonstrate that by subjecting a commercial AISI 301LN metastable austenitic SS sheet to heavy cold rolling and subsequently annealing for short durations yields a nano/sub-micron grained SS with tensile, yield and ductility properties that are far superior than conventionally processed AISI 301LN SS (Fig. 4.18a-b, 4.19).

In a time-span of three and half years, the results achieved through the collaborative work between Outokumpu Stainless Oy, Tornio-Finland, the University of Oulu, Oulu-Finland, and the University of Texas, Austin-USA are a significant contribution to the ferrous industry's twenty five year vision for developing advanced commercial steels with high strength, ductility [4-8]. Additionally, in parallel our collaborators in Finland have also investigated short annealing of AISI 301LN and AISI 301 SS cold-rolled to different reductions and demonstrated enhanced mechanical properties in them [6-8].

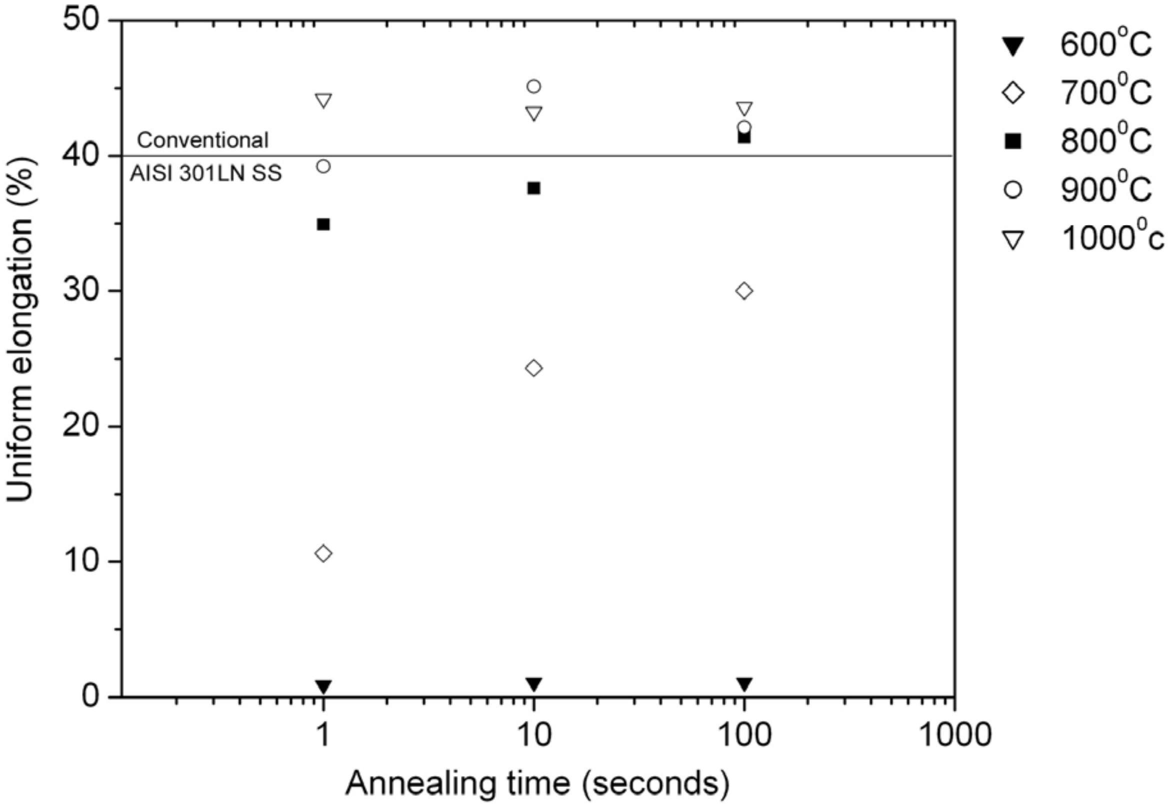

Figure 4.19: Uniform elongation of AISI 301LN SS annealed for different annealing parameters.

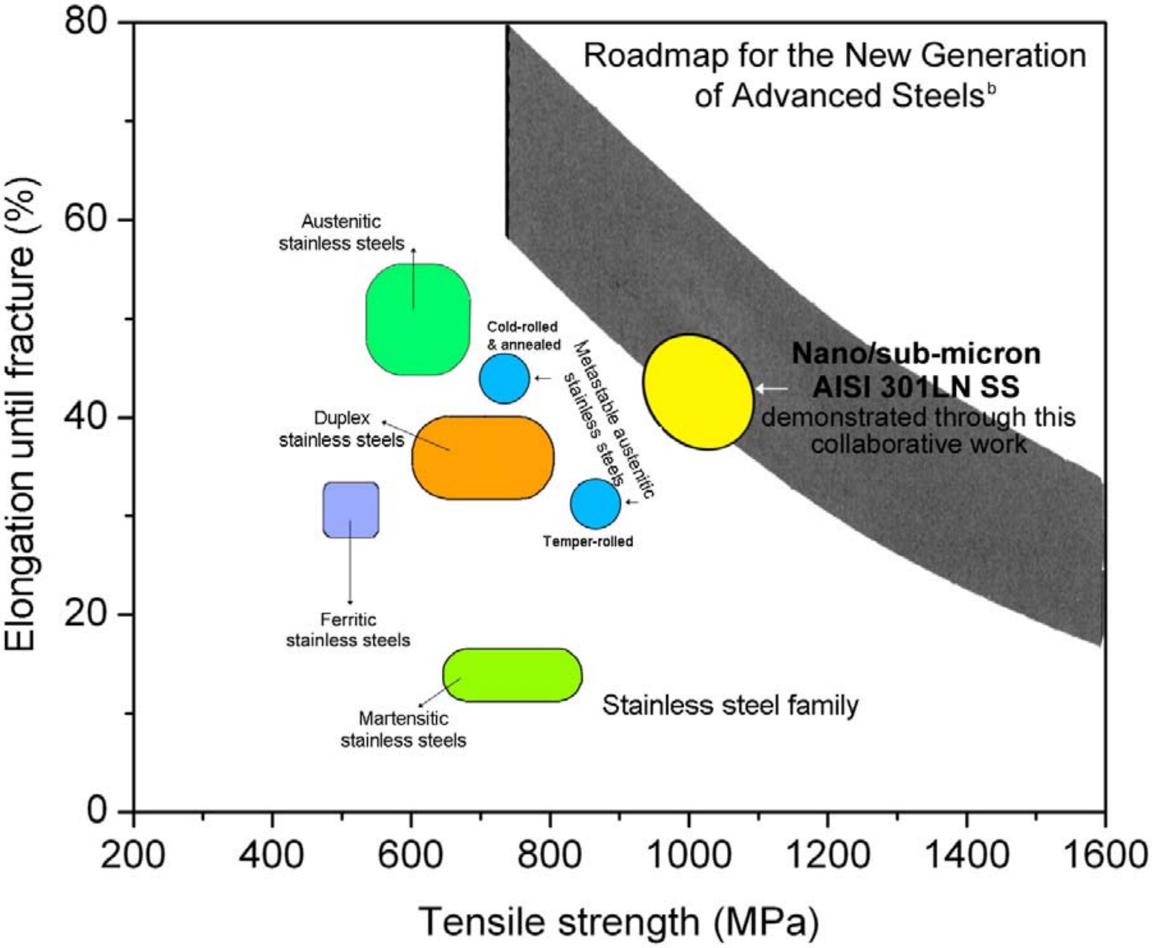

Figure 4.20: Nano/submicron SS with superior mechanical properties obtained in this work demonstrate the progress made towards achieving the Roadmap goals [3-8].

Chapter 5: Discussion

5.1 MICROSTRUCTURAL EVOLUTION

5.1.1 Morphology of martensite in the cold-rolled sample

As discussed in chapter 4, the as-cold rolled (CR) sample exhibits regions of lath-type martensite, austenite shear bands and dislocation-cell martensite. A more detailed observation of the CR AISI 301LN SS sample is shown in Fig. 5.1. Fig. 5.1a shows the presence of elongated grains bounded by shear bands. A higher magnification image (Fig. 5.1b) of the region visible in Figure 5.1a and corresponding selected area diffraction patterns (SADP) (Fig. 5.1c, 5.1d), are also shown. An objective aperture size of 2 μm was used for the diffraction patterns. The analysis of the diffraction pattern shown in Fig. 5.1c reveals that the elongated grains are lath martensite. In addition to lath-martensite, faint streaks are also observed in Fig. 5.1c, which are due to presence of austenitic platelets that did not revert to martensite during cold rolling. A SADP was also taken from the shear band region (Fig. 5.1d). As discussed by Singh [26], and Shrinivas *et al.* [27], these areas are austenite shear bands, which form in low stacking fault energy (SFE) alloys due to enhanced planar slip upon deformation. Since the SFE of AISI 301LN SS was calculated to be ~ $10 mJ/m^2$ according to the model proposed by Ferreira & Muellner [91], the propensity to form shear bands prior to martensite nucleation should be relatively high. However, relatively few shear bands of the type shown in Fig. 5.1c could be found in the TEM samples. A likely explanation for this small population of shear bands can be explained by the following sequence of events: 1) initial cold rolling → formation of shear bands, 2) further cold rolling → presence of shear band intersections [44], 3) shear band intersections → nucleation sites for martensite embryos, and 4) martensite embryos→ formation of lath-martensite (Fig. 5.1a).

However, as discussed in Chapter 2, further cold rolling of lath martensite leads to a change in the morphology of martensite (Fig. 5.2). Fig. 5.2a shows lath martensite at high magnification with dimensions that are less than 0.25μm in width and ~ 1μm in length. Heavy cold rolling produces dislocation forests within these lath martensite regions, which are delineated in Fig. 5.2b (highlighted regions).

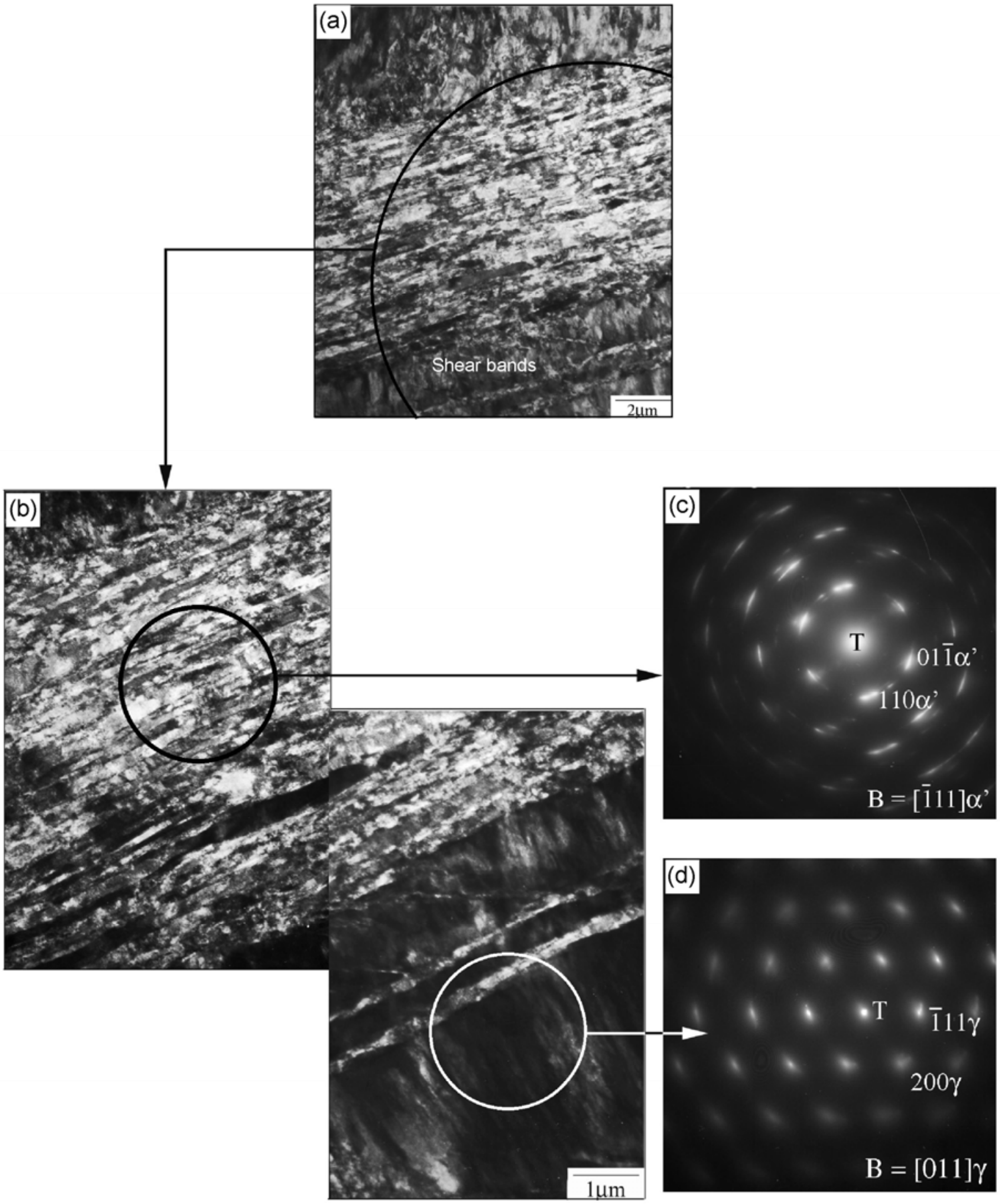

Figure 5.1: TEM image of 63% cold-rolled AISI 301LN SS; a) BF image, b) Higher magnification image of the circled region shown in (a), (c) and (d) are SADP of the circled regions shown in (b).

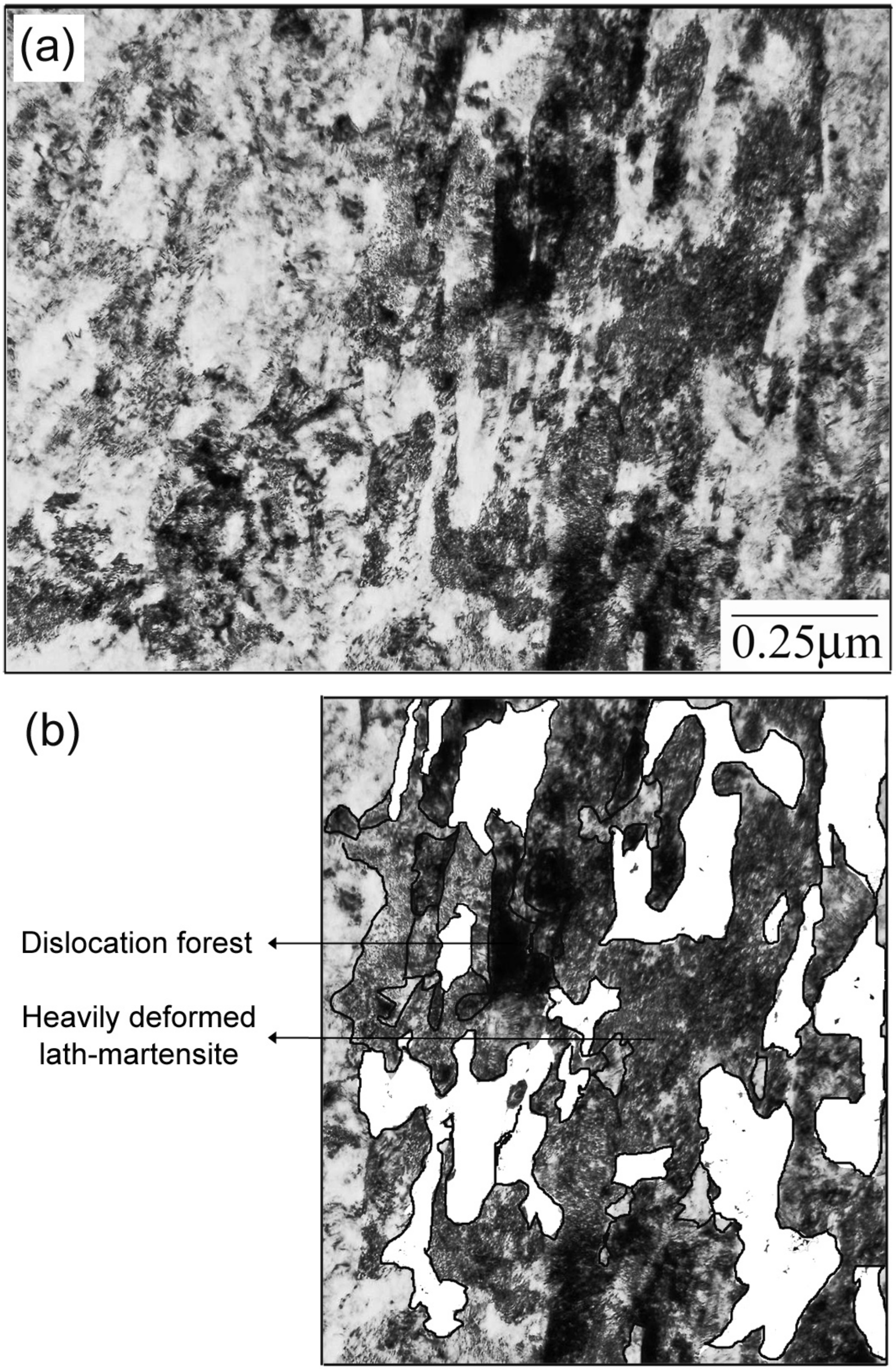

Figure 5.2: (a) TEM image of the lath-type martensite showing regions of severe deformation. These regions of heavily deformed lath-martensite are delineated in (b).

5.1.2 Influence of annealing conditions on the austenite phase fraction

Samples annealed at 600°C for 1 and 10 seconds show a relatively small austenite phase fraction (~6%). This value is comparable to the austenite phase fraction present in the cold-rolled sample (~4.3%), which was estimated in section 4.1. On this basis, it seems that the $\alpha' \rightarrow \gamma$ reversion is negligible in samples annealed for 1 and 10 seconds. Samples annealed for longer duration of 100 seconds at 600°C exhibit a substantial amount of austenite phase fraction, where ~ 50% martensite has reverted to austenite (Fig. 4.3). This may be due to a required incubation period for austenite nucleation whereby an annealing time of more than 10 seconds is necessary to nucleate the austenite phase. Obviously, the incubation period depends on the annealing temperature [92], with higher annealing temperatures resulting in shorter incubation periods. This hypothesis is confirmed by the phase fraction data obtained for samples annealed at 700°C. Higher annealing temperature provides more thermal energy to overcome the activation energy for nucleation. As the annealing duration is increased, the driving force is large enough to promote the reversion process resulting in ~ 80% of reverted austenite for the samples annealed for 10 seconds. As expected, the reversion is almost complete after 100 seconds of annealing (Fig. 4.3).

Samples annealed at higher temperatures of 800°C, 900°C and 1000°C all show almost complete reversion to austenite phase (~ 93% austenite). The retained martensite in these samples is thought to be tempered martensite and it will be discussed in greater detail in the next section.

5.1.3 Morphology of reverted austenite

The microstructures shown in Fig. 5.3a and Fig. 5.4a are typical of samples annealed at 600°C for 1 and 10 seconds. Although the samples exhibit a negligible reversion to austenite, pockets of nano-scale austenite grains within a martensitic matrix can be observed in these samples (Fig. 5.3 and Fig. 5.4). To a great extent, the sample retains the morphology of the 63% cold-rolled sample with large regions of dislocation forests and dislocation-cell martensite (Fig. 5.3a). Nanoscale lath martensite and nanoscale austenitic regions are also visible (Fig. 5.4a and 5.4b). Keeping in mind that the driving force for recrystallization is much higher than that for $\alpha' \rightarrow \gamma$ reversion [8], the nanosized austenitic regions shown in Fig. 5.4a are likely to be due to newly nucleated austenite grains. Accordingly, after a sufficient incubation period the samples annealed at 600°C for 100 seconds show a relatively different morphology. A detailed examination of the microstructure shows regions of equiaxed austenitic grains and secondary phase Cr nitride precipitates (Fig. 5.5a) along with regions of dislocation tangles. These morphological observations, combined with the phase fraction results (Fig. 4.3) demonstrate that a 100 second annealing at 600°C produces a dual-phase SS with regions of nano-austenite and martensite.

Samples annealed at a higher temperature of 700°C for an annealing duration of 1 second exhibit a microstructure consisting of secondary phase nitrides, equiaxed austenitic grains with high angle grain boundaries, and regions of retained martensite (Fig. 5.6a).

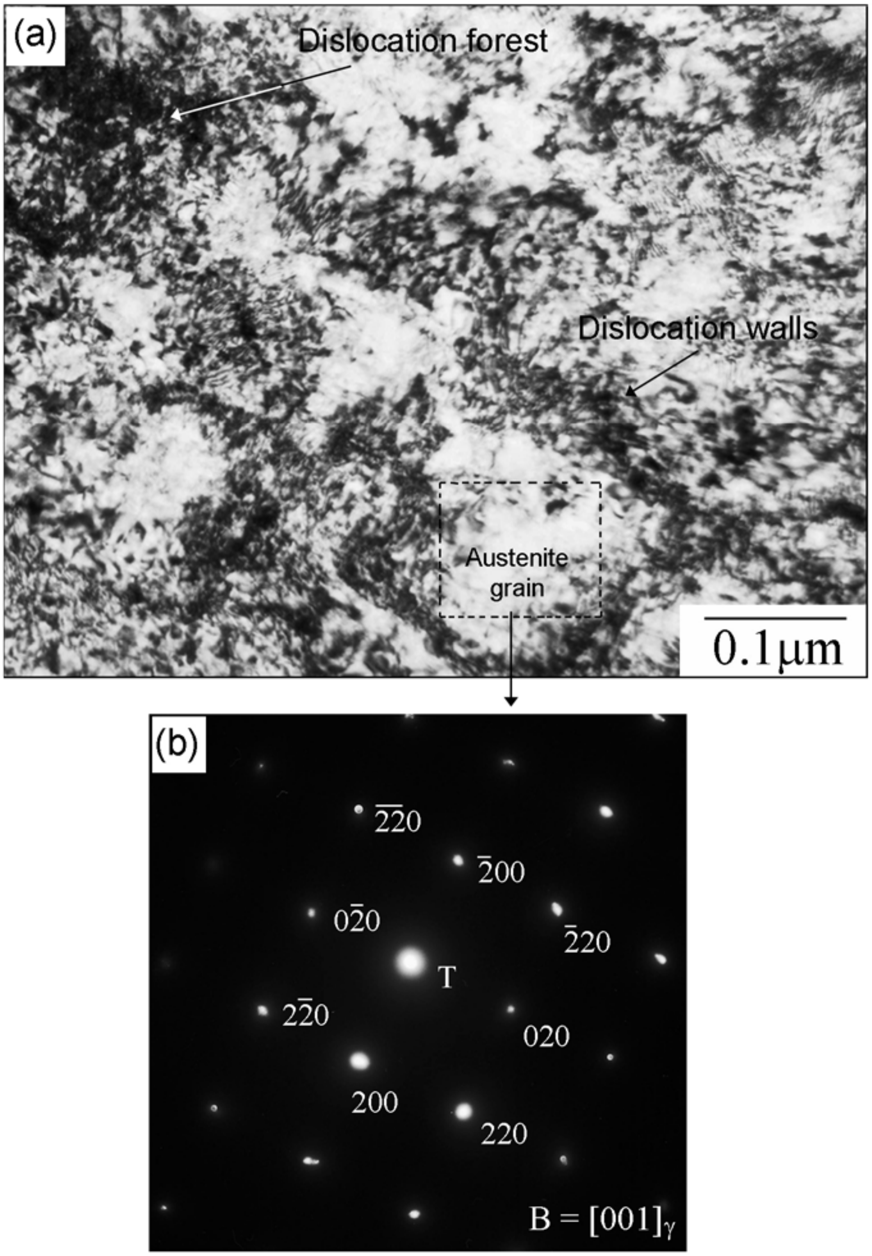

Figure 5.3: (a) TEM image of 63% cold rolled AISI 301LN SS sample annealed at 600°C for 1 second, showing regions of dislocation forests and dislocation-walls, (b) SADP of the austenite grain.

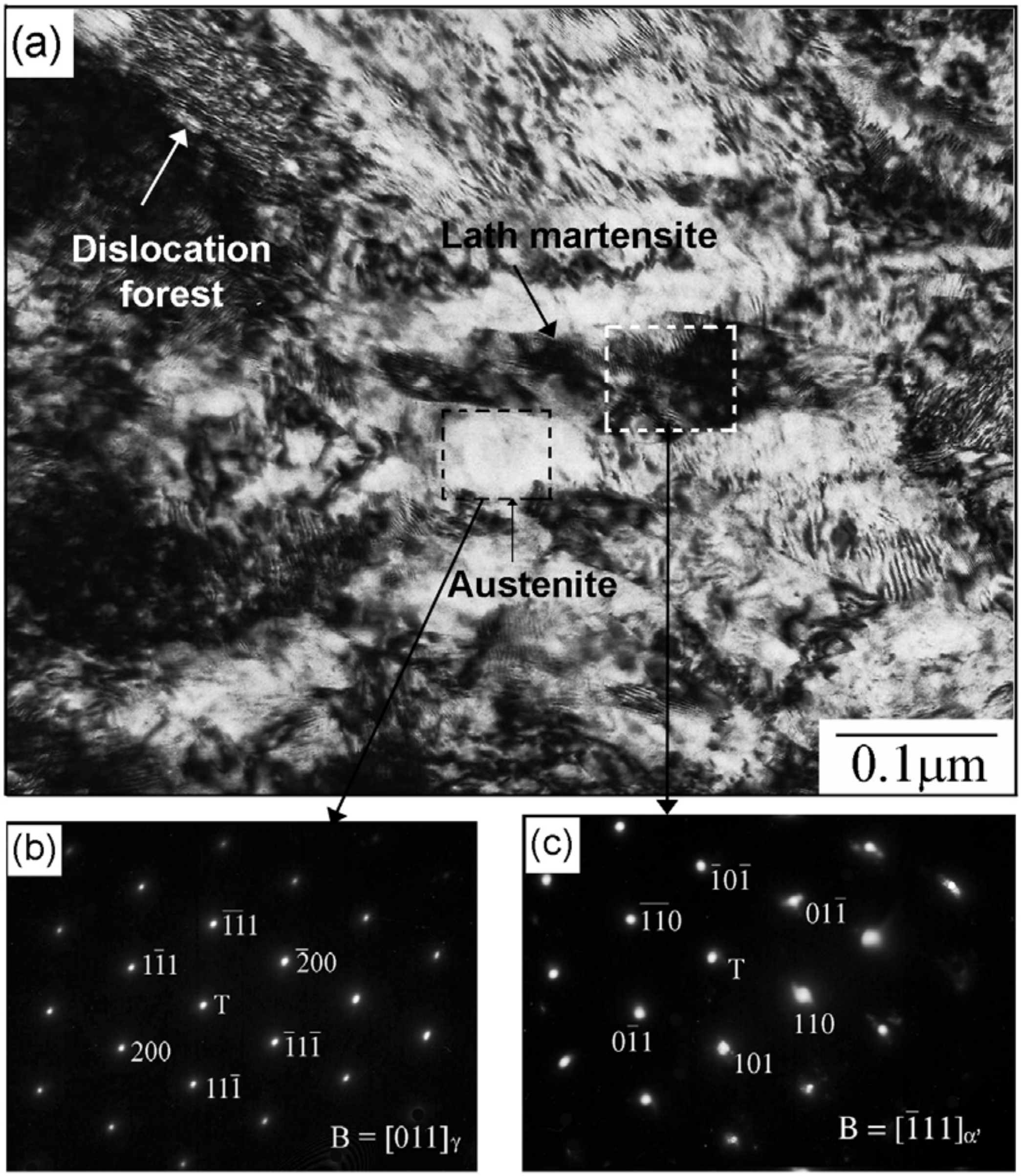

Figure 5.4: (a) TEM image of 63% cold rolled AISI 301LN SS sample annealed at 600°C for 10 seconds, showing regions of dislocation forest, dislocation-cell martensite, lath martensite and recrystallized austenite, (b) SADP of the austenite region (c) SADP of the martensitic region.

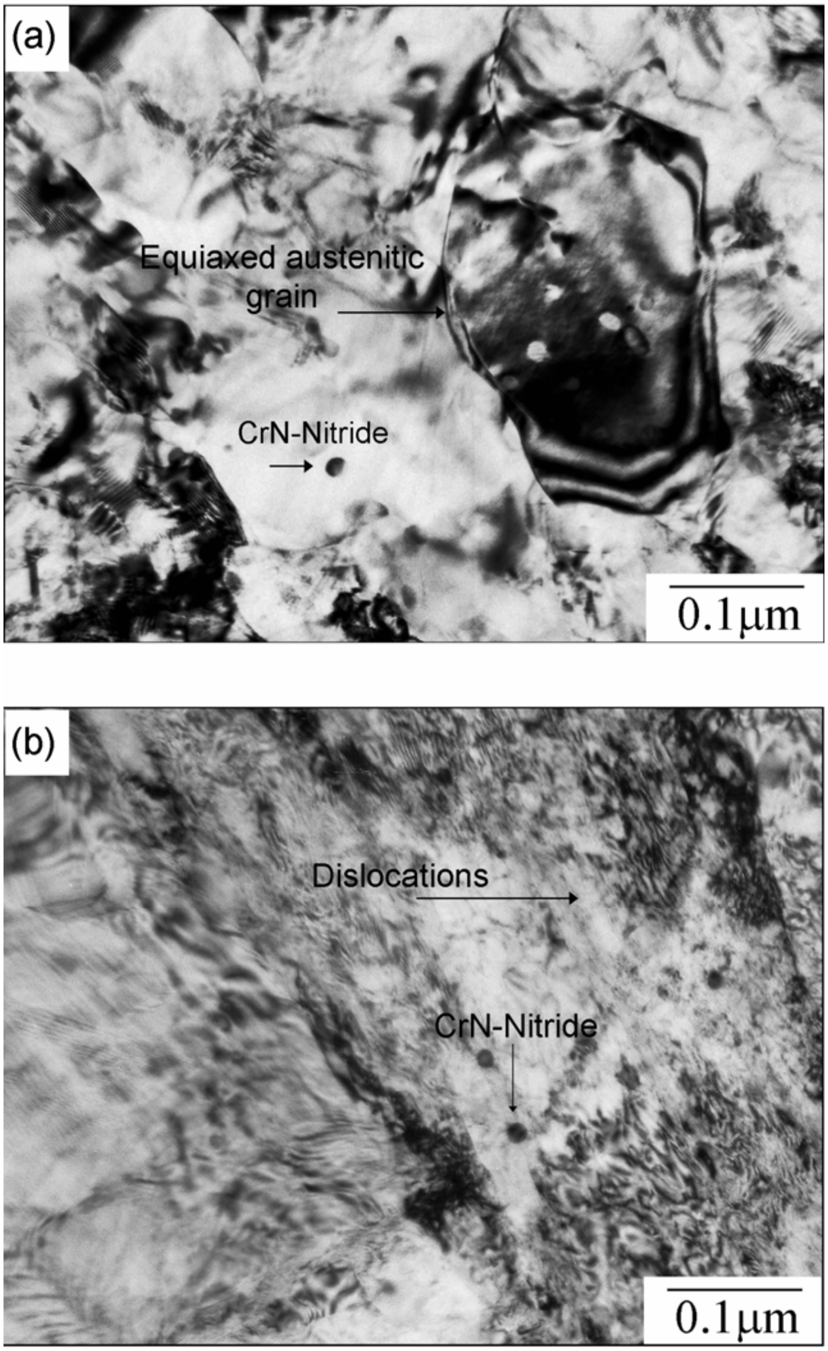

Figure 5.5: (a) TEM image of 63% cold rolled AISI 301LN SS sample annealed at 600°C for 100 seconds, showing regions of equiaxed austenitic grains, as well as secondary phase nitrides, and (b) TEM image from a different region of the same sample, showing the presence of dislocations.

The presence of different types of nucleation sites, such dislocation-cell martensite, dislocation walls, and heavily deformed lath-type martensite seems to be responsible for the variety of austenite grain shapes observed. By comparing these results with those obtained for samples annealed at 600°C, it can be inferred that to develop equiaxed austenitic grains for an annealing time of ~ 1 second, it is necessary to employ annealing temperatures above 600°C.

The microstructure of samples annealed for longer durations at 700°C (10 and 100 seconds) exhibit almost complete reversion to austenite phase. This behavior is confirmed by the phase fraction results (Fig. 4.3), as well as the presence of defect-free large austenitic grains (Fig. 4.7c). These samples also exhibit a wide grain size distribution (Fig. 4.13), which may be due to the fact that nucleation of austenite occurs on different nucleation centers, such as lath-type martensite sites and dislocation-cell type martensite sies. Johannsen *et al.* have shown that the nucleation of austenite on dislocation-cell type martensite is easier when compared to nucleation on lath-type martensite [61]. Thus, during the $\alpha' \rightarrow \gamma$ reversion, the austenite nucleates first on dislocation-cell martensite, followed by grain growth, whereas austenite nucleation on lath-type martensite takes place later, leading to smaller grains. The observed austenite grain size distribution (Fig. 4.13) also indicates that austenite nucleation, as well as grain growth, is time-dependent, as confirmed by the fact that dislocation-cell martensite is consumed first, whereas lath-type martensite transforms to austenite upon longer annealing durations.

Samples annealed at higher temperatures (800°C, 900°C and 1000°C) exhibit equiaxed austenitic grains (Fig. 4.8 and 4.9), a wide grain size distribution (Fig. 4.14, 4.15 and 4.16), and only ~ 7% untransformed martensite (Fig. 4.3). The time-dependent nature of austenite nucleation is evident from the wide grain size distributions observed. As discussed above, austenite grain nucleation occurs initially at dislocation-cell martensite nucleation sites, followed by grain growth as the annealing duration is increased. Once the dislocation-cell martensite is consumed, the nucleation of austenite takes place on deformed lath-type martensite. It is appropriate here to consider that according to Tsuji *et al*. [20], Ueji *et al.* [21], and Hansen [93], the deformed lath-type martensite boundaries comprise of incidental dislocation boundaries (IDBs) and geometrically necessary boundaries (GNBs). These research groups have shown that ultra-fine grains preferentially nucleate at the GNBs. In the context of this work, it is proposed that once the heterogeneous nucleation sites present in the dislocation-cell type martensite is consumed, the austenite preferentially nucleates at GNBs present within the deformed lath-martensite. Subsequently, austenite nucleation on IDBs is likely to occur after GNBs are also consumed. The time dependent nature of these processes is reflected in the wide grain size distributions of these samples, for which the smallest austenite grains measured correspond to the austenite that nucleated last.

Furthermore, the IDBs present in lath-martensite, on which austenite fails to nucleate, transform upon annealing to tempered martensite. Tomimura *et al.* [12, 13] have shown pockets of tempered martensite present at austenite grain triple junctions in thermo-mechanically treated non-commercial SS. A detailed observation of the microstructures of the samples annealed at 800°C confirms the presence of tempered martensite (Fig. 5.7). Therefore, the retained martensite seen in this work corresponds to tempered martensite.

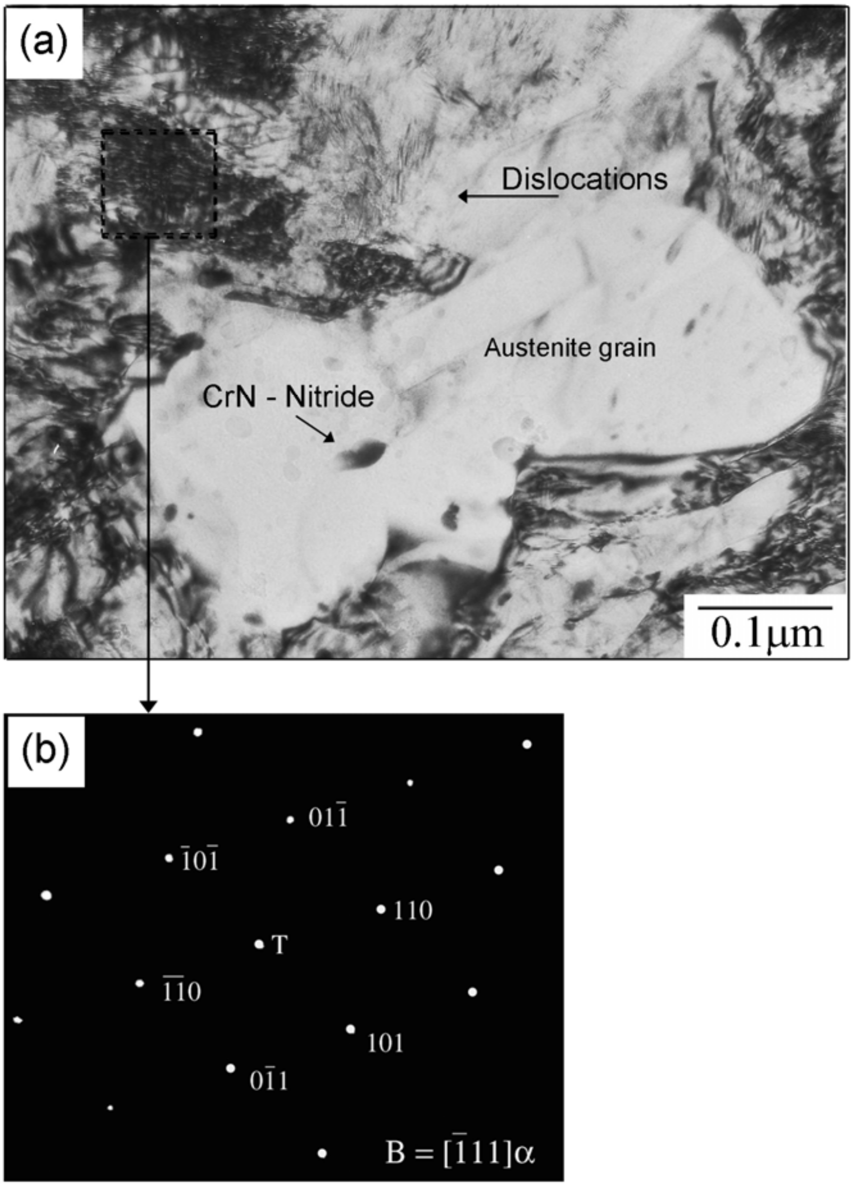

Figure 5.6: (a) TEM image of 63% cold rolled AISI 301LN SS sample annealed at 700°C for 1 second, showing regions of secondary phase nitrides, equiaxed austenitic grains, martensite, as well as dislocations, (b) SADP of the martensitic region.

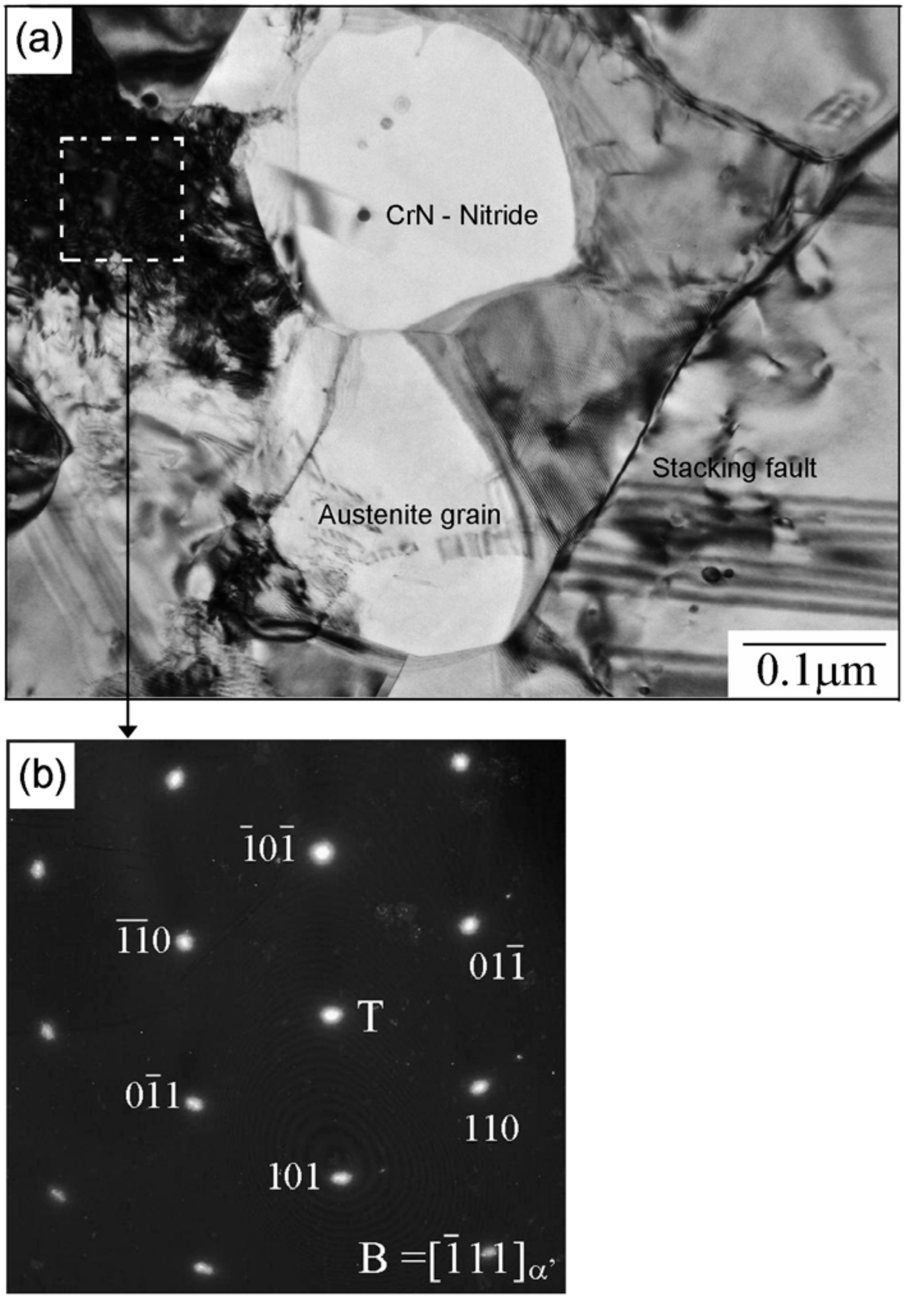

Figure 5.7: (a) TEM image of 63% cold rolled AISI 301LN SS sample annealed at 800°C for 1 second, showing regions of secondary phase nitrides, equiaxed austenitic grains, martensite, as well as dislocations, (b) SADP of the martensitic region.

5.1.4 Nitride precipitation

Secondary phase CrN nitride precipitation was observed in samples annealed at 600°C, 700°C and 800°C (Fig. 5.5, 5.6 and 5.7). This is an important observation because fcc CrN nitride precipitation at low temperatures (600°C and 700°C) and short annealing (1, 10, 100 seconds) times has not been reported prior to this work. Instead, the existing literature has reported that in high nitrogen steels (>0.1%wt N), the formation of stable hcp Cr_2N chromium nitrides at annealing temperatures of at least 800°C and an annealing duration of at least 600 seconds [75-79, 94, 95].

Previous research carried out by Padilha *et al.* [94, 95] has shown that CrN nitrides are unstable in comparison to Cr_2N precipitates. Therefore, the presence of CrN precipitates in this work can be rationalized as follows: Rapid annealing initially leads to the precipitation of fcc structured CrN nitrides, which revert to more stable hcp Cr_2N nitrides upon extended annealing.

5.1.5 Mechanism for the martensite → austenite reversion

From the analysis of the microstructure, the morphology of the phases present and the phase fraction of all annealed AISI 301LN SS samples, we can infer that the $\alpha' \rightarrow \gamma$ reversion is characterized by: 1) a wide annealing temperature range (700°C to 1000°C) where the reversion occurs, 2) the formation of defect-free equiaxed austenitic grains that grow in size with time, 3) a sequential use of different types of martensite nucleation sites, which lead to a wide grain size distribution, and 4) formation of secondary phase precipitates. These features are typical of a diffusion-type reversion mechanism, in contrast to a shear-type reversion mechanism where: 1) reversion occurs over a small temperature range of ~ 50K [12, 13], 2) nucleation is time independent, 3) formation of defect-laden austenite grains with the parent martensite morphology occurs [8, 12, 13, 61], and (4) absence of austenite grain growth is observed [8, 12, 13]. From this analysis, it is suggested that a diffusion-type reversion occurs in AISI 301LN SS. In this context, a model describing the austenite phase fraction, as a function of annealing conditions can be developed. This is discussed next.

5.2 KINETICS OF MARTENSITE → AUSTENITE PHASE REVERSION

Currently, a fundamental understanding of the α' → γ reversion mechanism is not available. Tomimura [12] has discussed the reversion mechanism in non-commercial SS alloys only from a microstructural point of view. Several other researchers, [15-17, 26, 96, 97], have also described the phase changes occurring in cold rolled metastable austenitic SS upon annealing, but the focus of their work was the evaluation of grain sizes and mechanical properties. Therefore, the reversion of austenite from strain-induced martensite in commercially metastable austenitic SS, such as AISI 301LN has not been properly addressed. However, a theoretical understanding of the α' → γ reversion process is crucial in tailoring annealing parameters required to obtain an optimal mixture of martensite and austenite to suit customized engineering applications.

In this context, a theoretical model on the kinetics of martensite to austenite reversion in cold rolled and annealed AISI 301LN SS is presented herein. The model assumes a diffusion-controlled mechanism, as discussed in section 5.1.3. The results obtained from the model are compared with those obtained from experiments (Fig. 4.3) and the validity of the model is discussed.

5.2.1 Model for diffusion-controlled martensite → austenite reversion

Assuming a diffusion-controlled $\alpha' \rightarrow \gamma$ reversion, the volume fraction of austenite reverted from strain-induced martensite can be calculated as a function of time (*t*), and temperature (*T*) according to the generalized form of Avrami's equation, which can be expressed as [98, 99]:

$$\ln(1-\xi(T,t) = -\left[\frac{4\pi}{3}\right]\int_0^t v^3(T,t)I(T,t)(t-z)^3\,dz\,, \tag{5.1}$$

where $\xi(t,T)$ is the transformed austenite volume fraction, $v(T,t)$ the grain growth velocity, $I(T,t)$ the nucleation rate and *z* the incubation time for the formation of the first austenite nuclei. The generalized form of Avrami's equation is used instead of the Johnson-Mehl-Avrami-Kolmogorov (JMAK) equations because JMAK models are derived for special cases where the nucleation rate, as well as the grain growth velocity are time and temperature independent [100-104], which is not the case in the present work.

In order to solve equation 5.1, we first need to calculate the grain growth velocity, $v(T,t)$. The grain growth velocity can be obtained from differentiating the generalized grain growth law, which is expressed by [105-112]:

$$\left(\bar{\mathbf{d}}-\bar{\mathbf{d}}_{\mathbf{o}}\right)^n = kt, \tag{5.2}$$

where $\bar{\mathbf{d}}$ is the average austenite grain size, $\bar{\mathbf{d}}_{\mathbf{o}}$ the initial austenite grain size, *n* the grain growth exponent, *k* the grain growth parameter and *t* the annealing time. Hence, the grain growth velocity can be given as:

$$v(T,t) = \frac{\partial \bar{\mathbf{d}}}{\partial t} = \frac{\partial}{\partial t}\left(\bar{\mathbf{d}}_{\mathbf{o}} + (kt)^{\frac{1}{n}} \right) = \frac{(kt)^{\frac{1}{n}}}{nt}, \qquad (5.3)$$

where all the symbols have the same meaning as before.

Assuming that the nucleation rate for a given annealing temperature $I(T,t)$, is independent of annealing time, it is related to the annealing temperature through the expression [92, 113]:

$$I(T,t) = \omega C_1 \exp\left(-\frac{\Delta G_{diff}}{k_B T} \right) \exp\left(-\frac{\Delta G_{het}}{k_B T} \right), \qquad (5.4)$$

where ω is the Debye frequency, C_1 the concentration of austenite nuclei, ΔG_{diff} the activation energy for diffusion of solute atoms in the austenite phase and ΔG_{het} the activation energy for austenite nucleation at heterogeneous nucleation sites, such as grain boundaries. Combining equations 5.1, 5.3 and 5.4, the generalized form of Avrami's equation can be rewritten as:

$$\ln(1 - \xi(T,t) = -\left[\frac{4\pi\omega C_1}{3} \right] \exp\left(-\frac{\Delta G_{diff}}{k_B T} \right) \exp\left(-\frac{\Delta G_{het}}{k_B T} \right) \int_0^t \left(\frac{(kt)^{\frac{1}{n}}}{nt} \right)^3 (t - z)^3 \, dz, \qquad (5.5)$$

Defining

$$A = -\left[\frac{4\pi\omega C_1}{3} \right] \exp\left(-\frac{\Delta G_{diff}}{k_B T} \right) \exp\left(-\frac{\Delta G_{het}}{k_B T} \right),$$

equation (5.5) can be simplified to the form:

$$\ln(1 - \xi(T,t)) = A \int_0^t \left(\frac{(kt)^{\frac{1}{n}}}{nt} \right)^3 (t^3 - 3t^2 z + 3tz^2 - z^3) dz \qquad (5.6)$$

Equation (5.6) can be expanded to the form shown in equation (5.7a), for which the solution is shown in equation (5.7b):

$$\ln(1-\xi(T,t)) = A\left(\frac{1}{n}\right)^{3} k^{\frac{3}{n}}\left[t^{\frac{3}{n}}\int_{0}^{t} dz - 3t^{\frac{3}{n}-1}\int_{0}^{t} z dz + 3t^{\frac{3}{n}-2}\int_{0}^{t} z^{2} dz - t^{\frac{3}{n}-3}\int_{0}^{t} z^{3} dz\right], \tag{5.7a}$$

$$\ln(1-\xi(T,t)) = A\left(\frac{1}{n}\right)^{3} k^{\frac{3}{n}} t^{\frac{3}{n}+4} \tag{5.7b}$$

The transformed austenite volume fraction $\xi(t,T)$ is then obtained by rewriting equation (5.7b) in the form:

$$\xi(t,T) = 1-\exp\left(\frac{Ak^{\frac{3}{n}}t^{\frac{3}{n}+4}}{n^{3}}\right), \tag{5.8}$$

Substituting A into equation (5.8), gives:

$$\xi(t,T) = 1-\exp\left(-\left[\frac{4\pi\omega C_{1}k^{\frac{3}{n}}t^{\frac{3}{n}+4}}{3n^{3}}\right]\exp\left(-\frac{\Delta G_{diff}+\Delta G_{het}}{k_{B}T}\right)\right), \tag{5.9}$$

At this point, in order to evaluate equation (5.9), the parameters presented in this model should be estimated. Let us start by estimating the kinetic parameters for grain growth n and k. Subsequently, the parameters C_1, ΔG_{diff} and ΔG_{het} will be determined to estimate the nucleation rate $I(T,t)$, given by equation (5.4).

5.2.1.1 Calculation of grain growth kinetic parameters – k, n

The grain growth kinetic parameters, *k* and *n*, were estimated by regression analysis of the grain size data obtained for samples annealed at 800°C, 900°C and 1000°C, according to equation (5.2).

The grain size data for samples annealed at 600°C was not considered for the calculation of grain growth kinetic parameters despite the observation of nano-scale austenitic grains. This is because these samples contain partially reverted austenite whose phase fraction is annealing-time dependent. Thus, the average grain size in these samples is an average of newly reverted austenitic grains produced from the $\alpha' \rightarrow \gamma$ phase change and pre-existing austenitic grains that have grown in size. The same problem also exists for the samples annealed at 700°C. In this case, the austenite phase fraction increases from 35% for 1 second annealing, to 80% for 10 second annealing, to close to 100% for the 100 second annealing. Therefore, the grain distribution is again a mixture of newly reverted austenite grains and austenite grains that have grown in size. On the other hand, for the annealing temperatures of 800, 900 and 1000°C, the amount of austenite phase fraction does not change. Therefore, we can assume that changes in grain size with time and temperature are solely a consequence of grain growth, and suitable for the calculation of the kinetic parameters of grain growth.

One last important point for determining the kinetic parameters *n* and *k* is the definition of the value $\bar{\mathbf{d}}_\mathbf{o}$ in equation (5.2). Upon observation of the microstructures and grain sizes of samples annealed at 600°C and 700°C, the initial austenite grain size $\bar{\mathbf{d}}_\mathbf{o}$ was assumed to be the average grain size (0.1μm) of samples annealed at 600°C for 1 second. The reason for this is that these samples exhibit the smallest newly nucleated austenitic grains observed in this work (Fig. 5.8). The grain size data of samples annealed at 800°C, 900°C and 1000°C required for estimating the kinetic parameters is shown in Fig. 5.9.

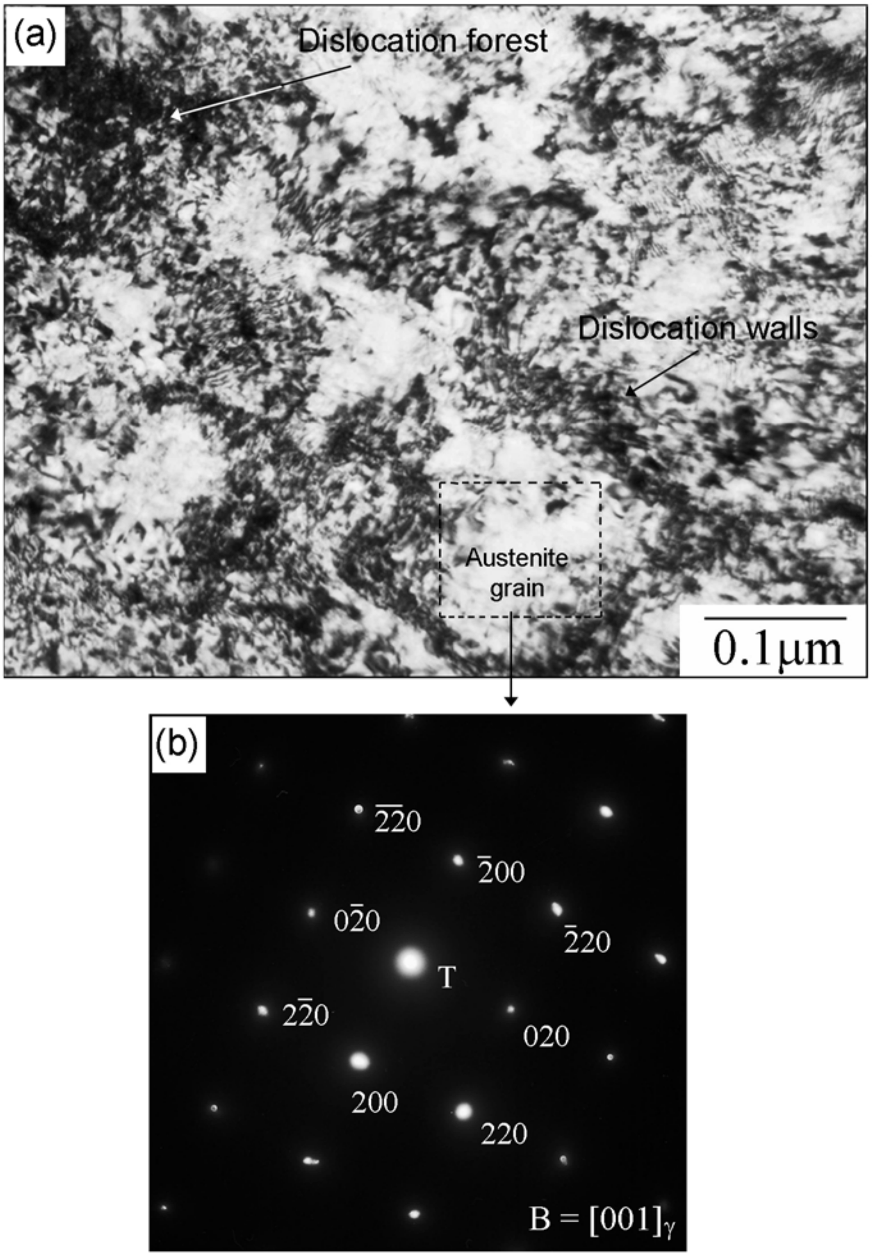

Figure 5.8: The initial grain size was estimated from measurements of 63% cold rolled AISI 301LN SS samples, annealed at 600°C for 1 second.

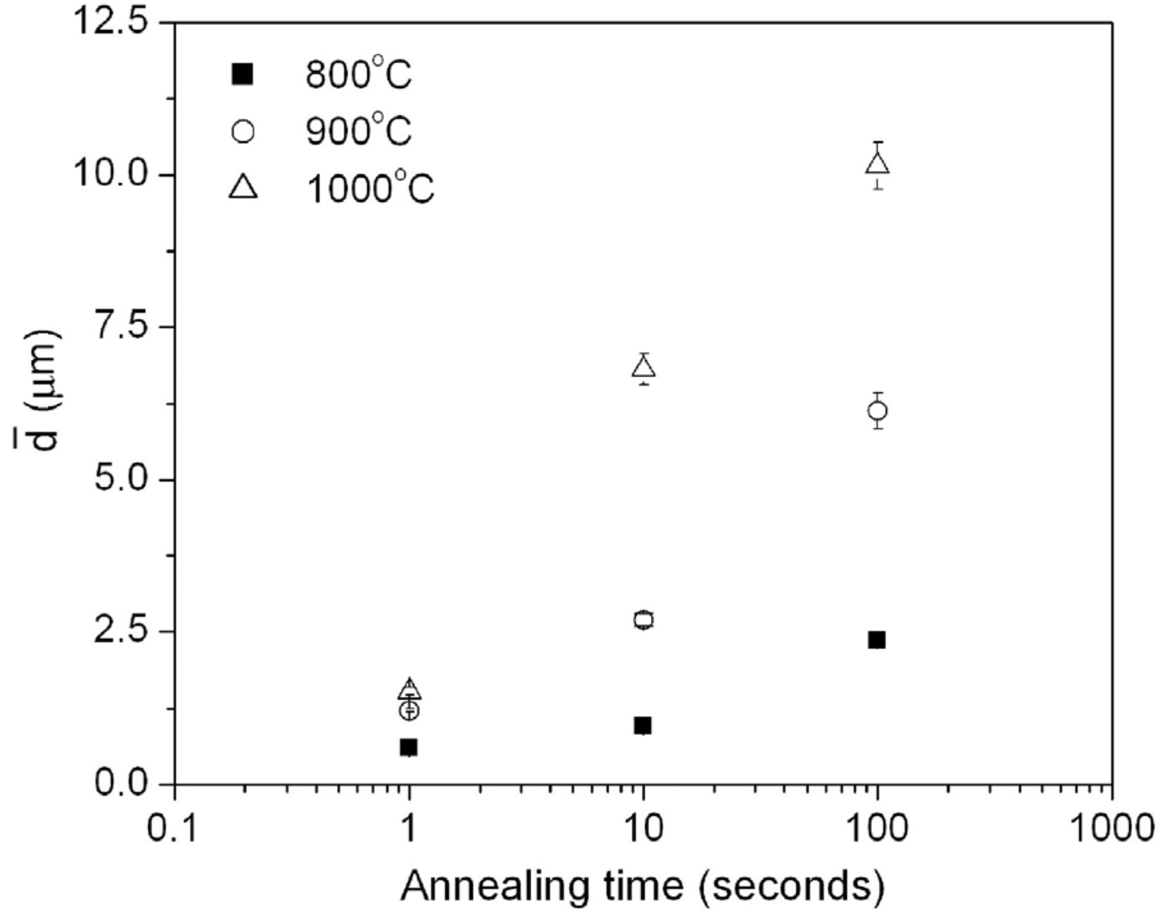

Figure 5.9: Average grain size as a function of annealing conditions for AISI 301LN SS.

A modified form of equation (5.2) suitable for regression analysis can be written as follows:

$$\ln\left(\bar{\mathbf{d}} - \bar{\mathbf{d}}_{\mathbf{o}}\right) = \frac{1}{n}\ln(k) + \frac{1}{n}\ln(t), \tag{5.10}$$

where the symbols have the same meaning as before. Values of the grain growth exponent *n*, obtained from the regression of equation (5.10) are shown as a function of annealing temperature (Fig. 5.10). A value of $n = 2$ is expected for an ideal material with no impurities and spherical grains [106, 107, 108]. However, for real materials the grain growth exponent is typically greater than 2 at temperatures below the melting temperature. This is because 1) grains are not spherical and 2) there are inclusions or chemical segregation at the grain boundaries that inhibit grain growth [107].

In the context of ferrous alloys, Mizera *et al.* have experimentally estimated the grain growth exponent for AISI 316L samples annealed at 1050°C to be ~ 2.77 [114]. In contrast, AISI 301LN SS used in this work exhibits a value of $n \sim 2.36$ for a similar annealing temperature (1000°C), which is likely due to a difference in alloy composition.

Assuming a linear relationship between *n* and temperature (Fig. 5.10), a value of n ~ 3.1 can be estimated for samples annealed at 700°C.

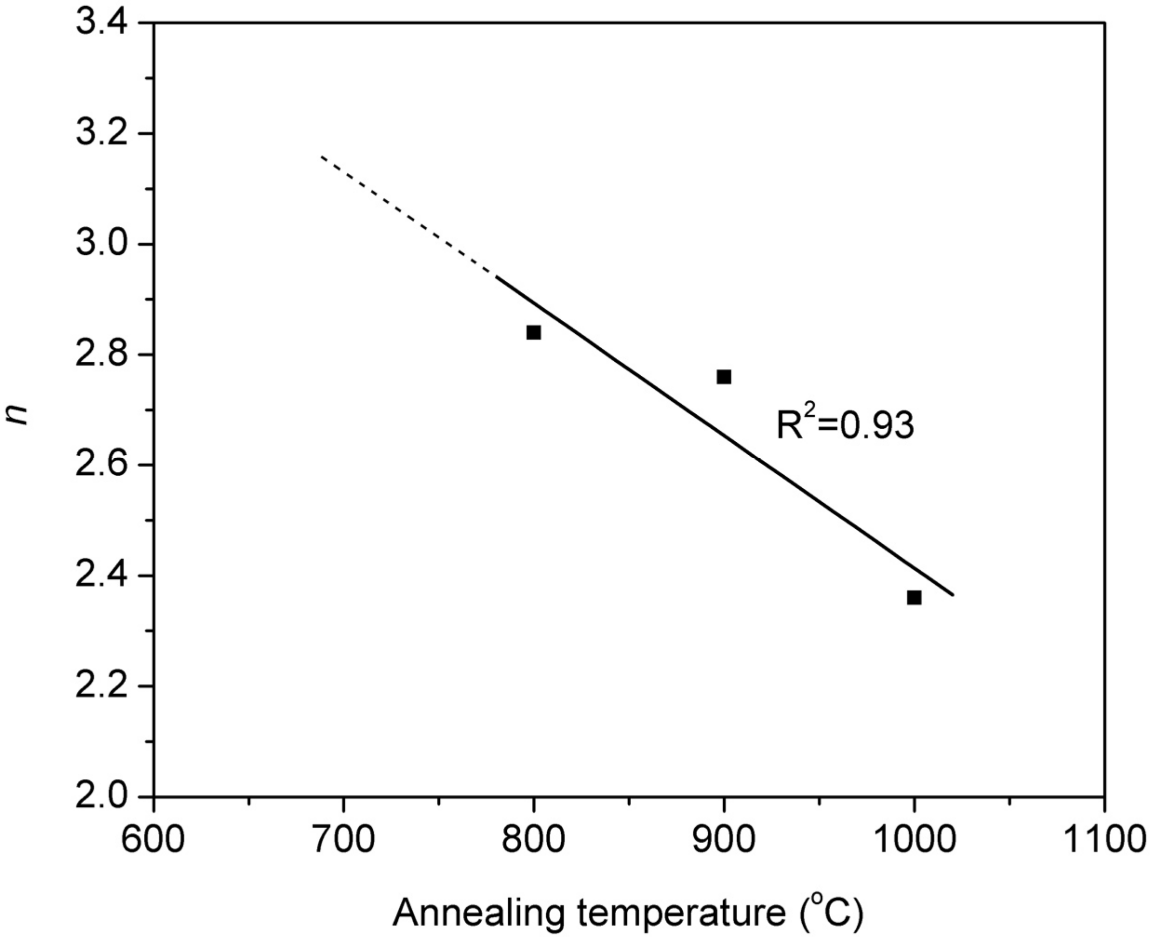

Figure 5.10: Estimation of the kinetic parameter, *n* by extrapolation, for samples annealed at 700°C. The calculation is based on a regression analysis of equation (5.10) for samples annealed at 800°C, 900°C and 1000°C.

The parameter *k*, which can be expressed as [114]:

$$k = k_o \exp\left(-\frac{\Delta G_{activation}}{RT}\right), \tag{5.11}$$

where *k* is the experimentally obtained grain growth constant, k_o a material constant, $\Delta G_{activation}$ the activation energy for grain growth, *R* the gas constant, and *T* the annealing temperature, can be modified to the form:

$$\ln(k) = \ln(k_o) - \frac{\Delta G_{activation}}{RT}, \tag{5.12}$$

A linear regression analysis carried out on equation (5.12) yields $k_o \approx 2.69 \times 10^9 m^{2.5} \sec^{-1}$, and $\Delta G_{activation}$~ 205kJ/mol (Fig. 5.11). This analysis also allows the determination of the parameter *k* for the samples annealed at 700°C, which was estimated to be ~ 0.007.

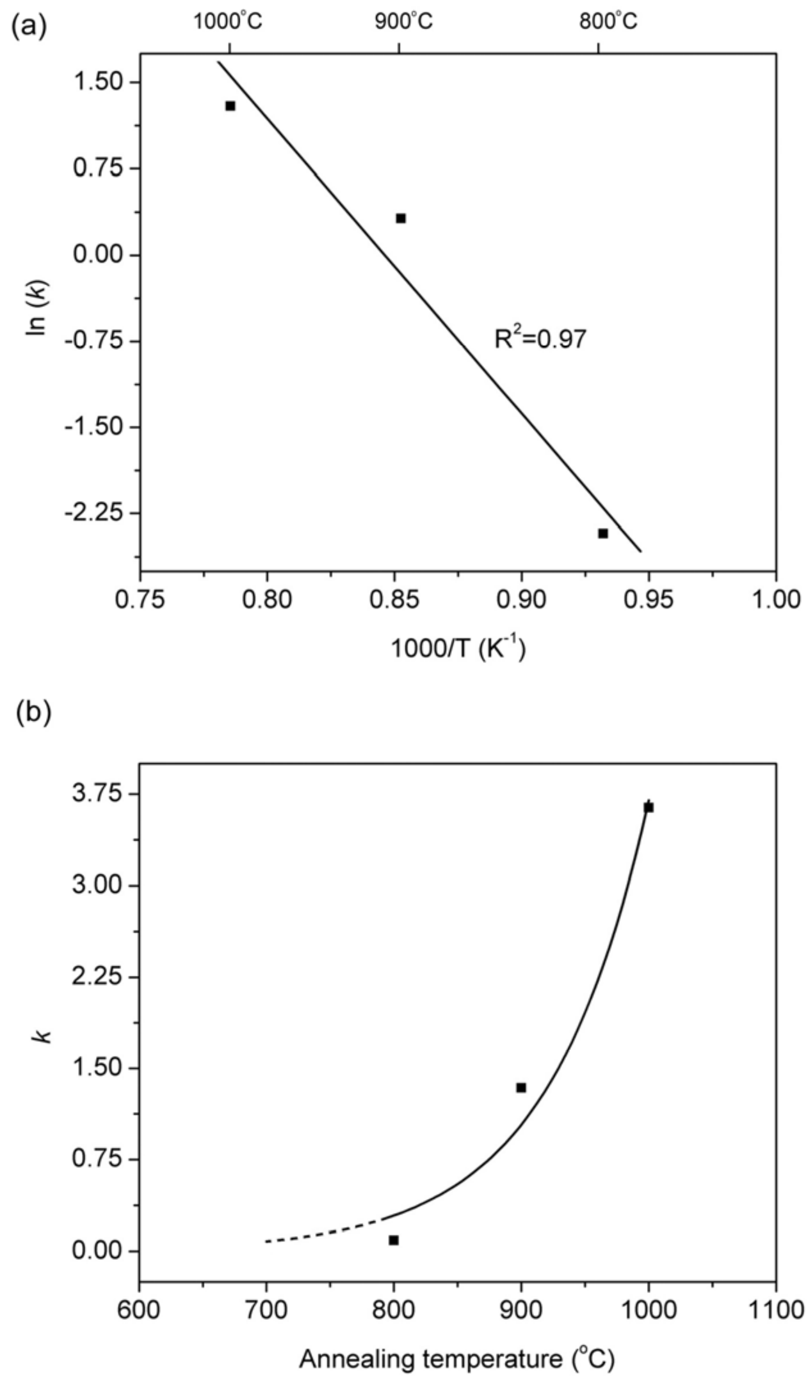

Figure 5.11: (a) Regression analysis to estimate $\Delta G_{activation}$,, (b) estimation of the kinetic parameter, k for the annealed samples obtained by analytical analysis of equation (5.12).

5.2.1.2 Calculation of nucleation rate – $I(T,t)$

According to equation (5.4), $I(T,t)$ depends on the concentration of nucleation sites present C_1, the change in Gibbs free energy for heterogeneous nucleation ΔG_{het} and the activation energy for atomic diffusion ΔG_{diff}. In turn, the concentration of nucleation sites depends on type of defects considered. In this model, we assume the nucleation to occur at martensite grain boundaries. In this case, C_1^{gb} can be estimated as:

$$C_1^{gb} = C_0 \delta_{gb}, \tag{5.13}$$

where C_0 is the equilibrium concentration of nucleation sites available if austenite nucleation occurs in the bulk, which can be calculated from the molar volume of SS as $C_0 \sim 8.76 \times 10^{28}$ m^{-3}, and the term $\delta_{gb} = \frac{\mathbf{d_{gb}}}{\bar{\mathbf{d}}_{\mathbf{o}}}$, where $\mathbf{d_{gb}}$ is the grain boundary width ~ (0.5nm) and $\bar{\mathbf{d}}_{\mathbf{o}}$ the initial austenitic grain size ~ 0.2μm, obtained from experimental observations. The next step is to estimate the activation energy for heterogeneous nucleation ΔG_{het}, which can be expressed as:

$$\Delta G_{het}^{gb} = S(\theta) \Delta G_{\hom} \tag{5.14}$$

where $\Delta G_{\hom}$ is the change in Gibbs free energy for homogeneous nucleation and $S(\theta)$ is a shape factor due to the presence of grain boundaries. $\Delta G_{\hom}(T)$ can be calculated through the relationship [92, 113]:

$$\Delta G_{\hom}(T) = \frac{16\pi[\Delta G_v(T) - \Delta G_s]^2}{3(\gamma_{\alpha'/\gamma}(T))^3}, \tag{5.15}$$

where ΔG_v is the volume Gibbs free energy change for the α’ → γ reversion given as:

$$\Delta G_v(T) = \frac{L_t \Delta T_{(\alpha' \to \gamma)}}{T_t}, \tag{5.16}$$

where L_t is the latent heat for the α’ → γ transformation, $\Delta T_{(\alpha' \to \gamma)} = T - T_t$, and T_t the α’ → γ reversion start temperature, ΔG_s the change in misfit strain energy associated with the phase reversion and $\gamma_{\alpha'/\gamma}(T)$ the martensite/austenite interfacial energy as a function of temperature.

The austenite reversion start temperature, T_t has been determined by various researchers to be ~ 500°C [26, 96]. This value was used in equation (5.16) to estimate $\Delta G_v(T)$. Additionally, the latent heat of transformation was assumed to be $L_t \sim 11 kJ/mol$, which was obtained for AISI 304 SS [115]. On this basis, $\Delta G_v(T)$ was estimated as shown in Fig. 5.12. Subsequently, the change in misfit strain energy ΔG_s can be calculated according to the expression [113]:

$$\Delta G_s = 4\mu \left[\frac{2}{3} \times \left(\frac{a_\gamma - a_{\alpha'}}{a_{\alpha'}} \right) \right]^2, \tag{5.17}$$

where μ is the shear modulus (~ 77GPa), a_γ and $a_{\alpha'}$ the equivalent austenite and martensite interplanar spacings. These interplanar spacings can be obtained on the assumption that the austenite/martensite interface resulting from the α’ → γ reversion is given by the Kurdjumov-Sachs relationship (equation 2.3), where the (110)γ is parallel to (111)α’ phase [44, 53]. According to these values, the change in misfit strain energy for the α’→ γ reversion is $\Delta G_s \sim 0.03$eV.

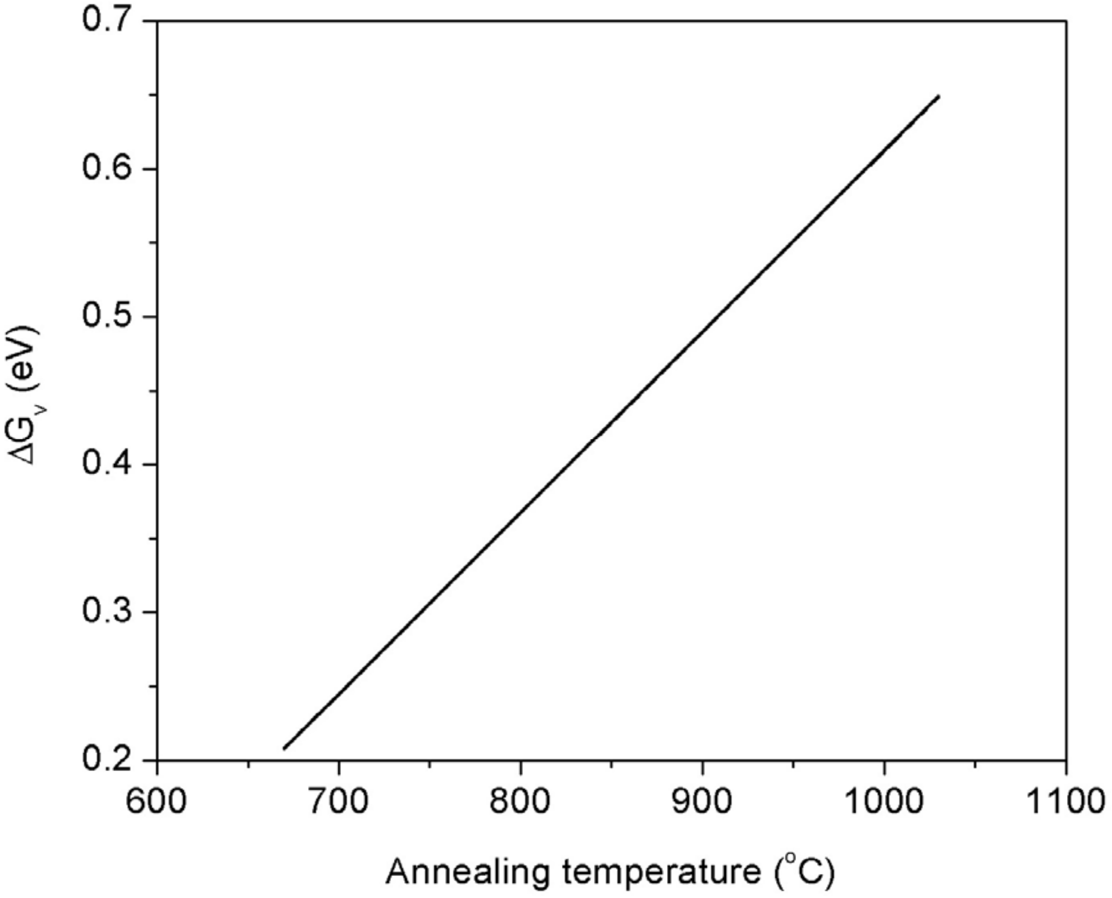

Figure 5.12: Calculated change in volume Gibbs free energy as a function of annealing temperature.

Finally to estimate $\Delta G_{\hom}$ in equation (5.15), the martensite/austenite interfacial energy $\gamma_{\alpha'/\gamma}$, needs to be determined. Since $\gamma_{\alpha'/\gamma}$ is temperature dependent, the calculation is not trivial. Let us start by assuming that the surface free energy of SS is $\gamma_{surface}^{SS}$ ~2190 mJ/m^2 at a temperature 1060°C [116, 117]. The change in surface energy as a function of temperature can be determined according to the relationship $\frac{d\gamma_{surface}^{SS}}{dT} = -1.76$ [117]. Subsequently, the martensite/austenite interfacial energy can be estimated by:

$$\gamma_{\alpha'/\gamma}(T) = \left(\frac{\gamma_{\alpha'/\gamma}}{\gamma_{gb}^{SS}}\right) \times \left(\frac{\gamma_{gb}^{SS}}{\gamma_{surface}^{SS}}\right) \times \gamma_{surface}^{SS}(T), \tag{5.18}$$

where $\frac{\gamma_{\alpha'/\gamma}}{\gamma_{surface}^{SS}} \sim 0.95$ [118] and $\frac{\gamma_{gb}^{SS}}{\gamma_{surface}^{SS}} \sim 0.38$ [117]. The values for $\gamma_{\alpha'/\gamma}(T)$ as a function of temperature are shown in Fig. 5.13.

At this point, the Gibbs free energy change for homogeneous nucleation $\Delta G_{\hom}(T)$ can be estimated from equation 5.15. As shown in Fig. 5.14, $\Delta G_{\hom}(T)$ decreases rapidly for high annealing temperatures indicating that the α’ → γ reversion becomes thermodynamically favorable as the annealing temperature is increased.

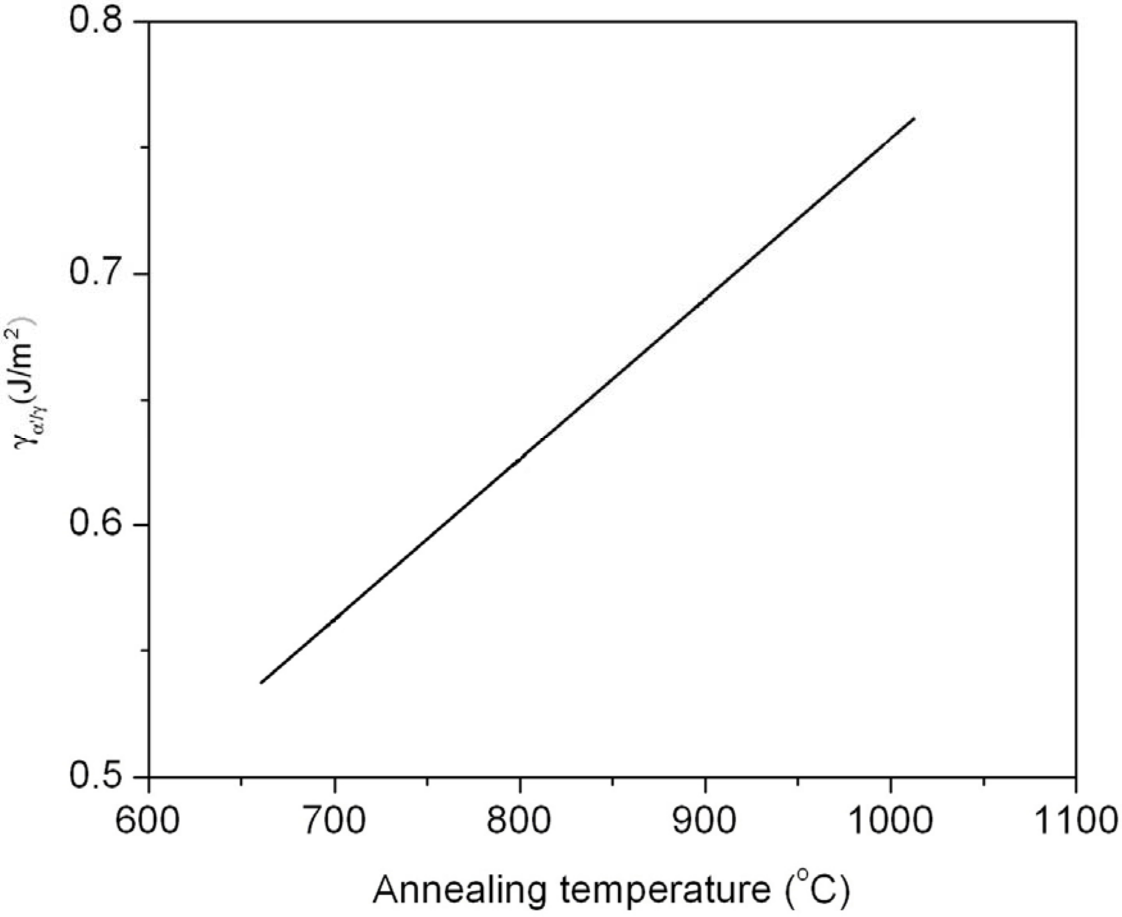

Figure 5.13: Austenite/martensite interfacial energy as function of temperature.

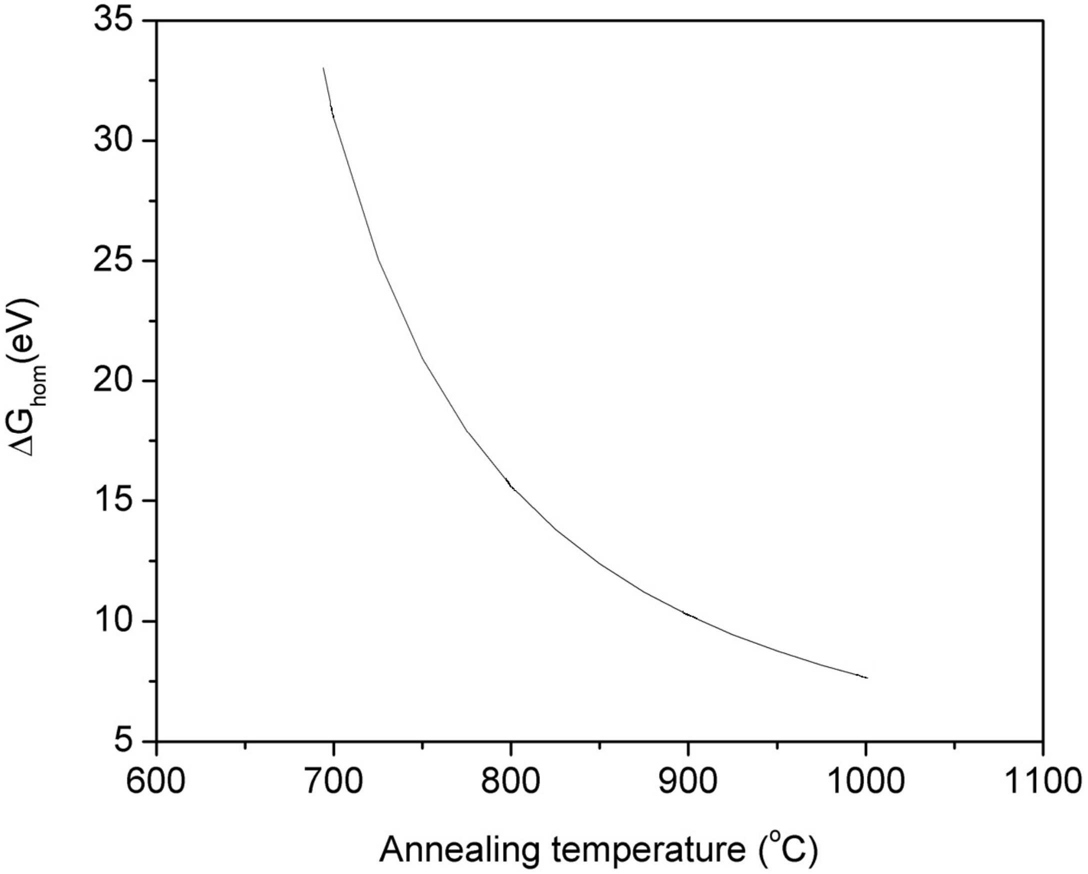

Figure 5.14: Gibbs free energy change for homogeneous nucleation, as a function of annealing temperature.

5.2.1.3 Calculation of the shape factor – $S(\theta)$

The factor $S(\theta)$ takes into account the geometry associated with the austenite nucleation at martensitic grain boundaries. Assuming the geometry of austenite nuclei to be that shown in Fig. 5.15, the shape factor can be given by the following expression [113]:

$$S(\theta) = \frac{1}{2}(2+\cos(\theta))(1-\cos(\theta))^2 \ , \tag{5.19}$$

where $\cos(\theta) = \dfrac{\gamma_{\alpha'/\alpha'}(T)}{2\gamma_{\alpha'/\gamma}(T)}$, $\gamma_{\alpha'/\alpha'}(T)$ is the martensite/martensite interfacial energy as a function of temperature and $\gamma_{\alpha'/\gamma}(T)$ the austenite/martensite interfacial energy from section 5.2.1.2.

As $\gamma_{\alpha'/\alpha'}(T)$ is temperature dependent, the surface energy of the bcc α-phase is first found to be $\gamma^{\alpha'}_{surface}$ ~1950 mJ/m^2 at 1350°C [118]. The temperature dependence of the surface energy has been determined as $\dfrac{d\gamma^{\alpha'}_{surface}}{dT} = -0.9$ [118]. Subsequently, $\gamma_{\alpha'/\alpha'}(T)$, the martensite/martensite interfacial energy as a function of temperature can be estimated through the relationship:

$$\gamma_{\alpha'/\alpha'} = \left(\frac{\gamma_{gb}}{\gamma_{surface}}\right) \times \gamma^{\alpha'}_{surface}(T) \ , \tag{5.20}$$

where $\left(\dfrac{\gamma_{gb}}{\gamma_{surface}}\right) \sim 0.36$ [116]. The calculated results for $\gamma_{\alpha'/\alpha'}(T)$ are shown in Fig. 5.16a. The shape factor is shown in Fig. 5.16b, as a function of temperature.

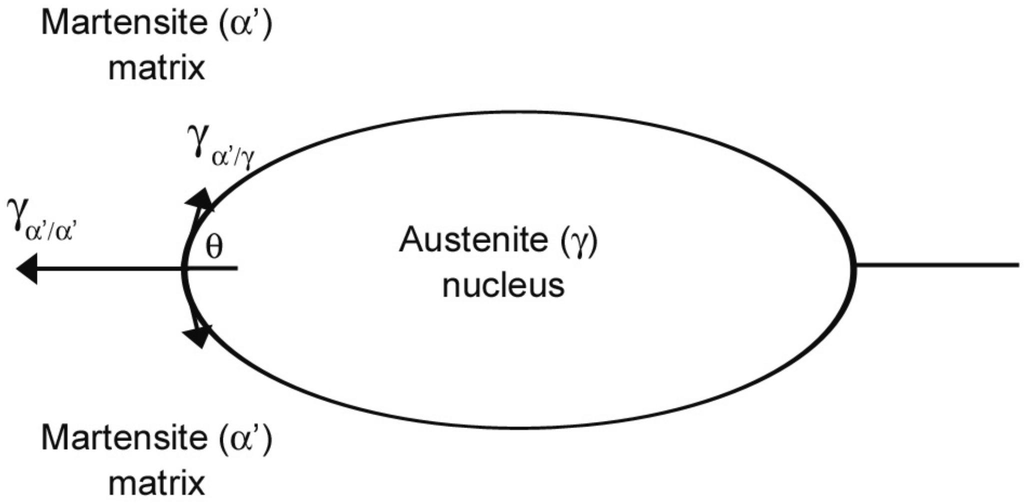

Figure 5.15: Geometry adopted for the nucleation of austenite within the martensitic matrix [Adapted from 113].

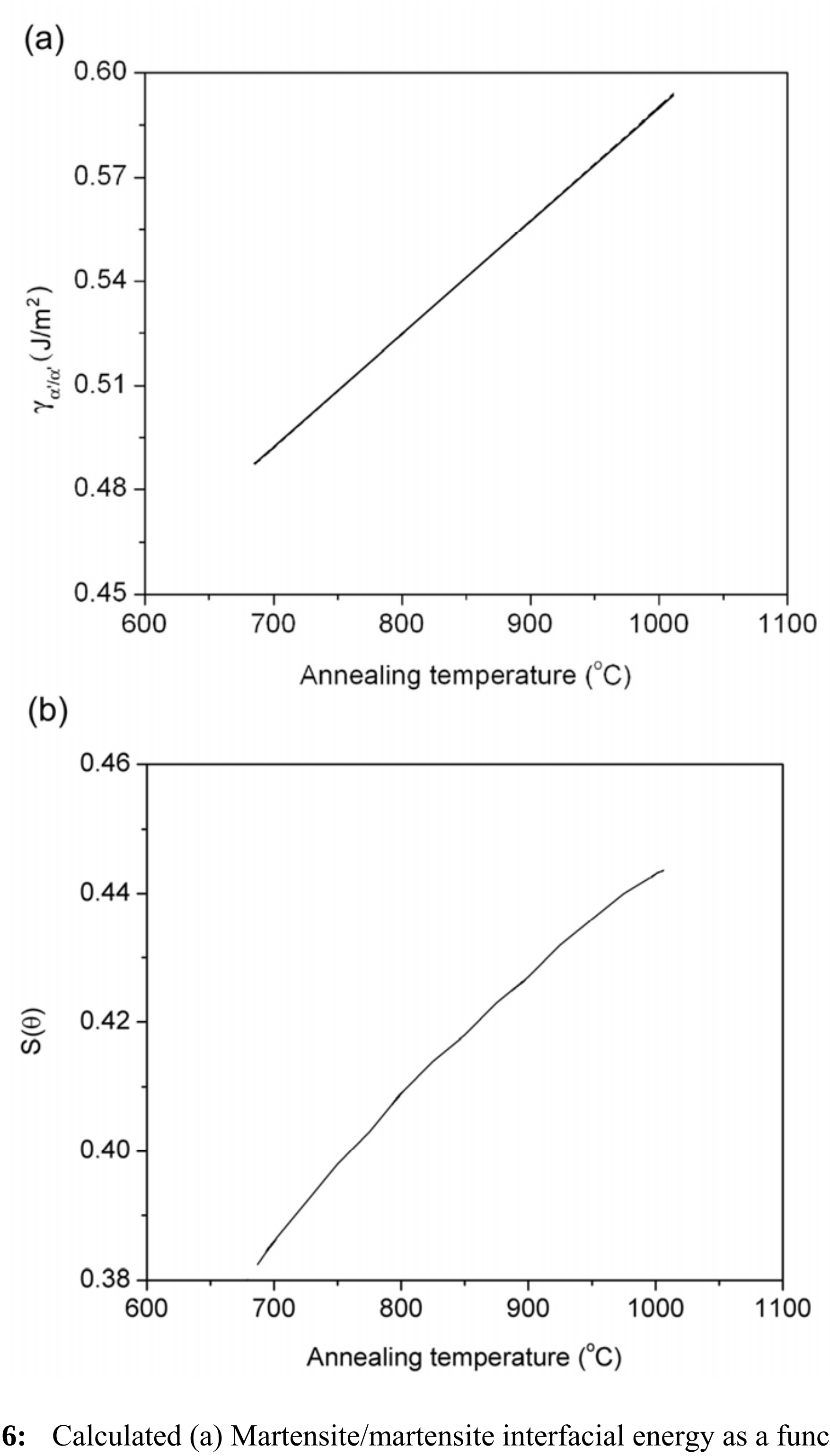

Figure 5.16: Calculated (a) Martensite/martensite interfacial energy as a function of temperature, (b) Shape factor, $S(\theta)$ as a function of temperature.

5.2.1.4 Activation energy for diffusion

To determine the activation energy for diffusion ΔG_{diff} for the solute elements taking part in the α'→γ reversion, the elements Ni, Cr and N were considered because they play an important role in the stability of austenite phase in SS. The activation energy values for these elements in the bcc and fcc phases are shown in Table 5.1. As expected, the substitutional elements Cr and Ni have comparable diffusion activation activation energies in both phases, whereas the diffusion activation energy for nitrogen is twice as large in the fcc phase than in the bcc phase.

Table 5.1: Activation energy for diffusion (in kJ/mol) for Cr, Ni and N in the bcc and fcc phases [115].

	bcc phase		fcc phase
Cr	239.8		251
Ni	240		272
N	79.1		168.5

5.2.2 Calculation of $\xi(T,t)$ - Austenite nucleation at the grain boundaries

As Cr and Ni have the highest activation energies for diffusion, it is assumed that these solute atoms are the rate-limiting factor in the α' → γ phase reversion and thereby will control the reversion kinetics. On this basis, equation 5.9 can be modified in the form:

$$\xi_{gb}^{chromium}(t,T)=1-\exp\left(-\left[\frac{4\pi\omega C_1 k^{\frac{3}{n}} t^{\frac{3}{n}+4}}{3n^3}\right]\exp\left(-\frac{\Delta G_{diffusion}^{chromium}+S(\theta)\Delta G_{\mathrm{hom}}}{k_B T}\right)\right) \tag{5.20a}$$

$$\xi_{gb}^{nickel}(t,T)=1-\exp\left(-\left[\frac{4\pi\omega C_1 k^{\frac{3}{n}} t^{\frac{3}{n}+4}}{3n^3}\right]\exp\left(-\frac{\Delta G_{diffusion}^{nickel}+S(\theta)\Delta G_{\mathrm{hom}}}{k_B T}\right)\right) \tag{5.20b}$$

Calculated values of $\xi(t,T)$ obtained from equations (5.20a) and (5.20b) are shown in Fig. 5.17. Two observations can be made: The first is that the phase reversion is quite sensitive to the activation energies for diffusion – as seen in Fig 5.17a and Fig. 5.17b. A difference of ~ 20kJ/mol between the activation energies for diffusion of Cr and Ni (Table 5.1) results in substantially different phase fractions. The second observation is that the phase reversion model based on Cr diffusion gives an estimate of austenite phase fraction (at an annealing temperature of 700°C and 1 second of annealing duration), which is quite close to what is experimentally observed.

To confirm the abovementioned assumption that the substitutional solute atoms are controlling the reversion kinetics, a phase reversion model solely driven by nitrogen diffusion is also considered. In this fashion, equation (5.9) can be modified to the form:

$$\xi_{gb}^{nitrogen}(t,T)=1-\exp\left(-\left[\frac{4\pi\omega C_1 k^{\frac{3}{n}} t^{\frac{3}{n}+4}}{3n^3}\right]\exp\left(-\frac{\Delta G_{diffusion}^{nitrogen}+S(\theta)\Delta G_{\mathrm{hom}}}{k_B T}\right)\right), \tag{5.21}$$

where all terms have the same meaning as before. The value of $\xi_{gb}^{nitrogen}(t,T)$ is estimated for various conditions studied in this work, and these curves are compared with experimentally obtained austenitic phase fractions (Fig. 5.18). It is clear that this model underestimates the reversion time for all temperatures. For instance according to this model, phase reversion at 700°C starts at ~ 85ms and is complete by 280ms. In contrast, experimental data indicates that for the abovementioned annealing parameters, the α’ → γ reversion is complete only after 100 seconds. Thus, as expected, substitutional solute atoms seem to be controlling the reversion kinetics.

5.2.3 Calculation of $\xi(T,t)$ - Combined effect of substitutional solute atoms

The phase reversion models developed so far have assumed that the substitutional solute atoms Cr and Ni act independently during the reversion kinetics. In this regard, the model will now consider the case where the overall activation energy for diffusion is influenced by the combination of these two elements (Fig. 5.19). The equivalent activation energy for diffusion can thus be written as:

$$\Delta\widetilde{G}_{diffusion} = w_{chromium}\Delta G_{diffusion}^{chromium} + w_{nickel}\Delta G_{diffusion}^{nickel}, \tag{5.22}$$

where $\Delta\widetilde{G}_{diffusion}$ is the equivalent activation energy for diffusion, $w_{chromium}$ and w_{nickel} are the weight fractions for chromium and nickel $(w_{chromium} \sim 0.729, c_{nickel} \sim 0.271)$, and remaining terms retaining their previous definitions.

Using equation (5.9), the equivalent $\xi(T,t)$ for austenite nucleation at the grain boundaries can be written as:

$$\xi_{gb}^{equivalent}(t,T) = 1 - \exp\left(-\left[\frac{4\pi\omega C_1 k^{\frac{3}{n}} t^{\frac{3}{n}+4}}{3n^3}\right]\exp\left(-\frac{\Delta\widetilde{G}_{diffusion} + S(\theta)\Delta G_{\text{hom}}}{k_B T}\right)\right), \tag{5.23}$$

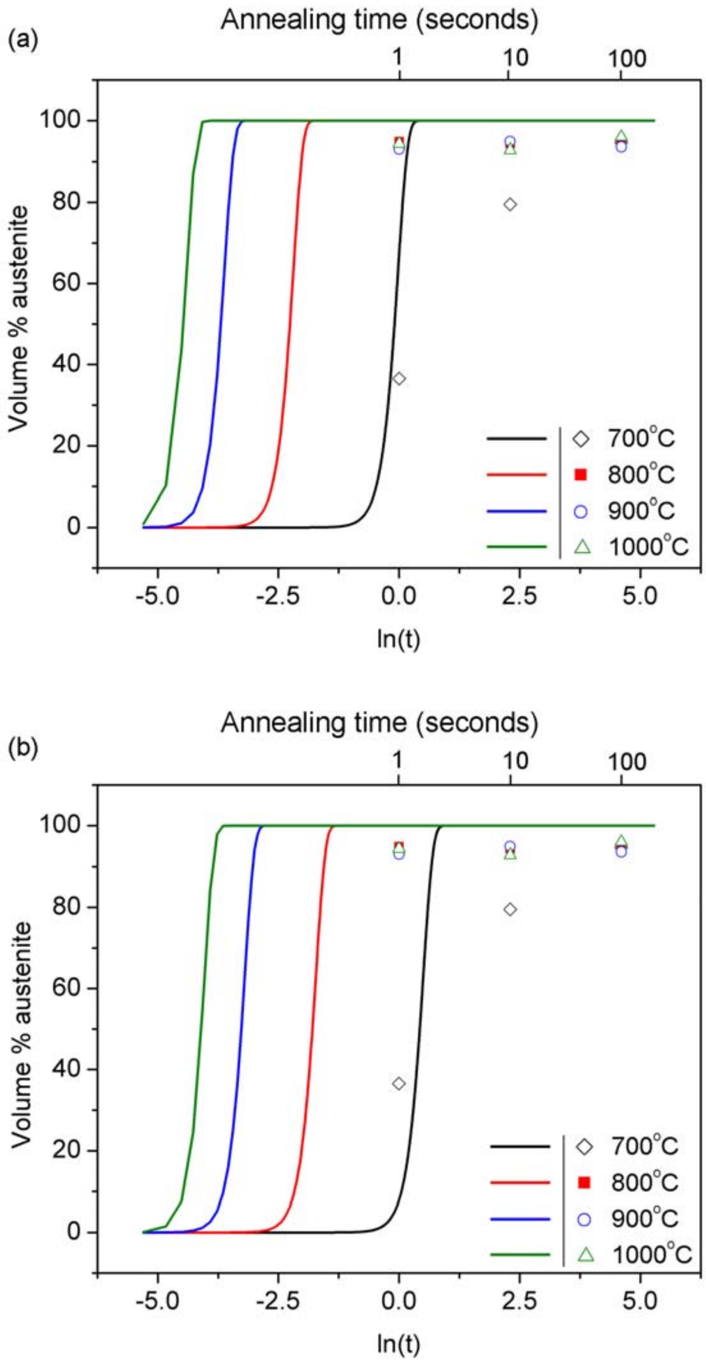

Figure 5.17: Volume % of austenite during the $\alpha' \rightarrow \gamma$ reversion, assuming (a) Cr-diffusion controlled and (b) Ni-diffusion controlled. The lines are calculated from the model.

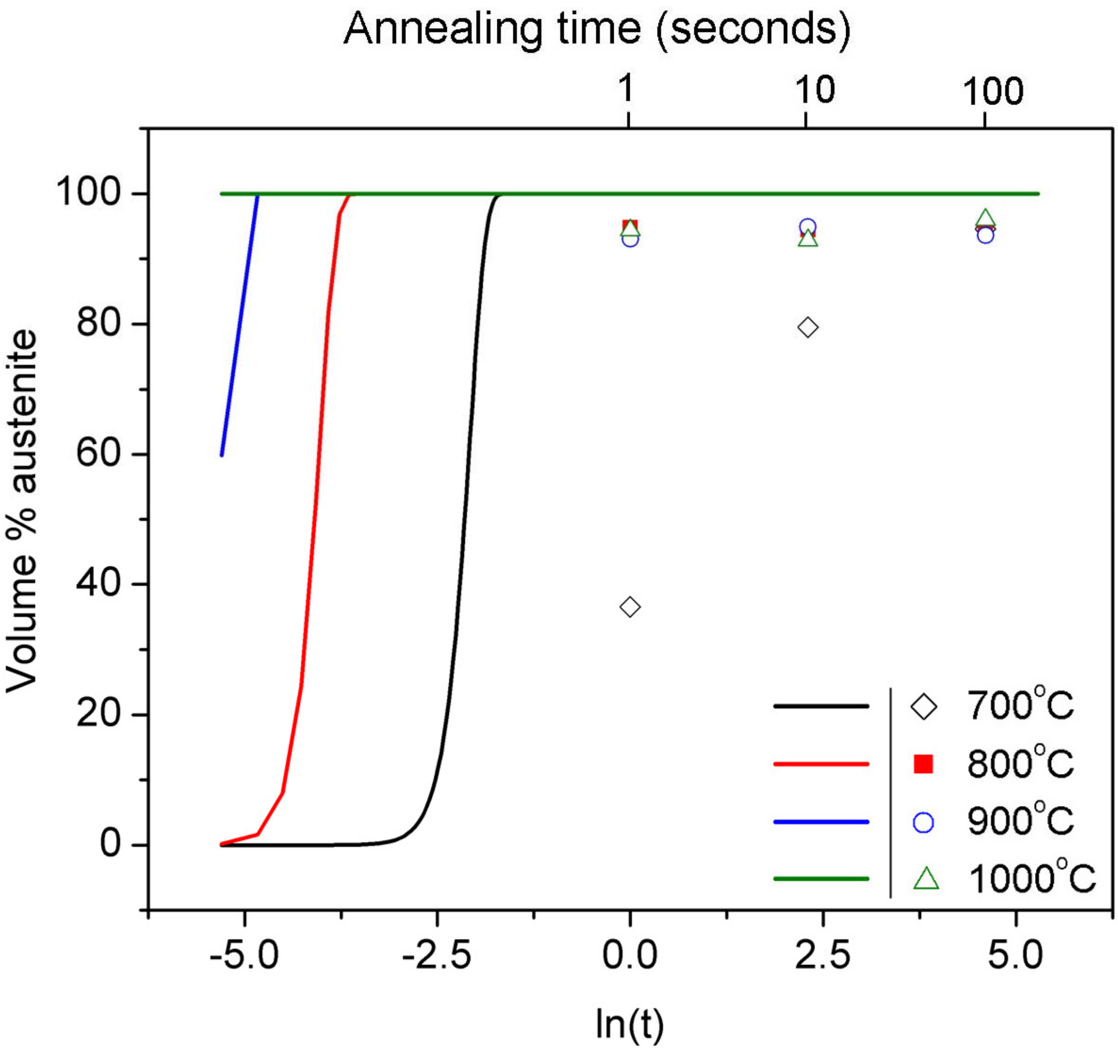

Figure 5.18: Volume percentage of austenite formed, assuming a nitrogen-diffusion controlled α’ → γ reversion.

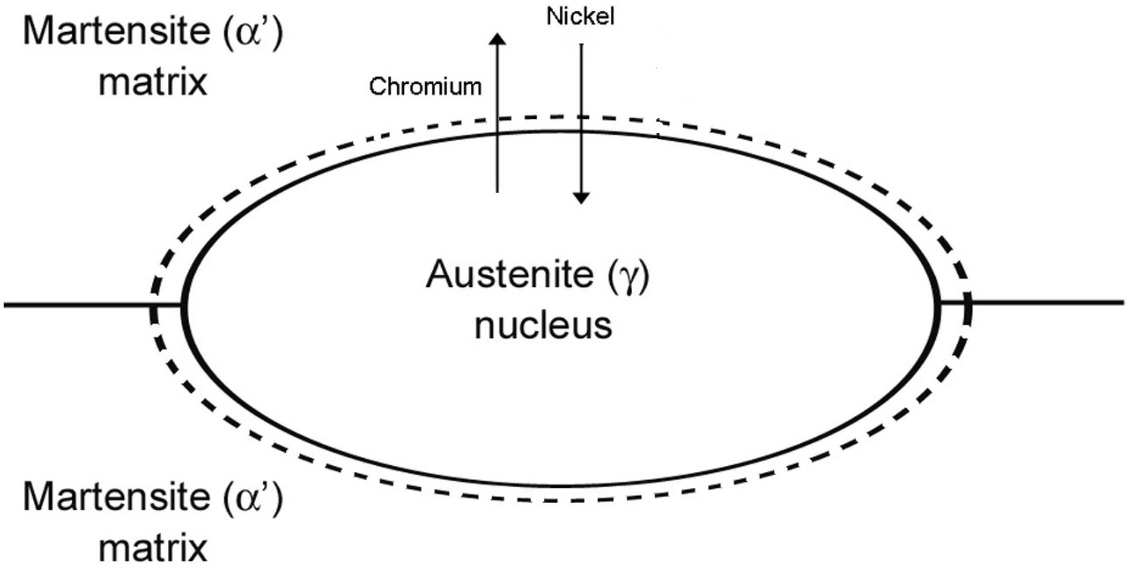

Figure 5.19: Schematic of the proposed diffusion-controlled austenite reversion kinetics, showing the growth of the austenite nuclei by short-range diffusion of Ni and Cr.

The calculated $\xi_{gb}^{equivalent}(T,t)$ values for various annealing conditions (Fig. 5.20) appear to be similar to those obtained when Cr diffusion was solely considered (Fig. 5.17a). This result is reasonable since Cr is present in larger amounts affecting the equivalent activation energy for diffusion, $\Delta\widetilde{G}_{diffusion}$. Nevertheless, Cr diffusion seems to be the rate-limiting factor in the α' → γ reversion.

In summary, starting with the generalized equation for phase transformation, a model was derived to predict the α' → γ reversion in AISI 301LN SS. The results from this model were obtained by assuming that austenite nucleation takes place on martensite grain boundaries. It is proposed that short range diffusion of Cr atoms controls the diffusion-based phase reversion from martensite to austenite. Using a kinetic first principle derivation the model shows for the first time that the α' → γ reversion in AISI 301LN SS is diffusion controlled. Moreover, the model shows a reasonable agreement with the experimental results. In the future, the model developed herein may be further improved by considering: (1) the volume loss due to secondary phase precipitation, (2) the Cr loss that has diffused to the precipitates, and (3) austenite nucleation on dislocations.

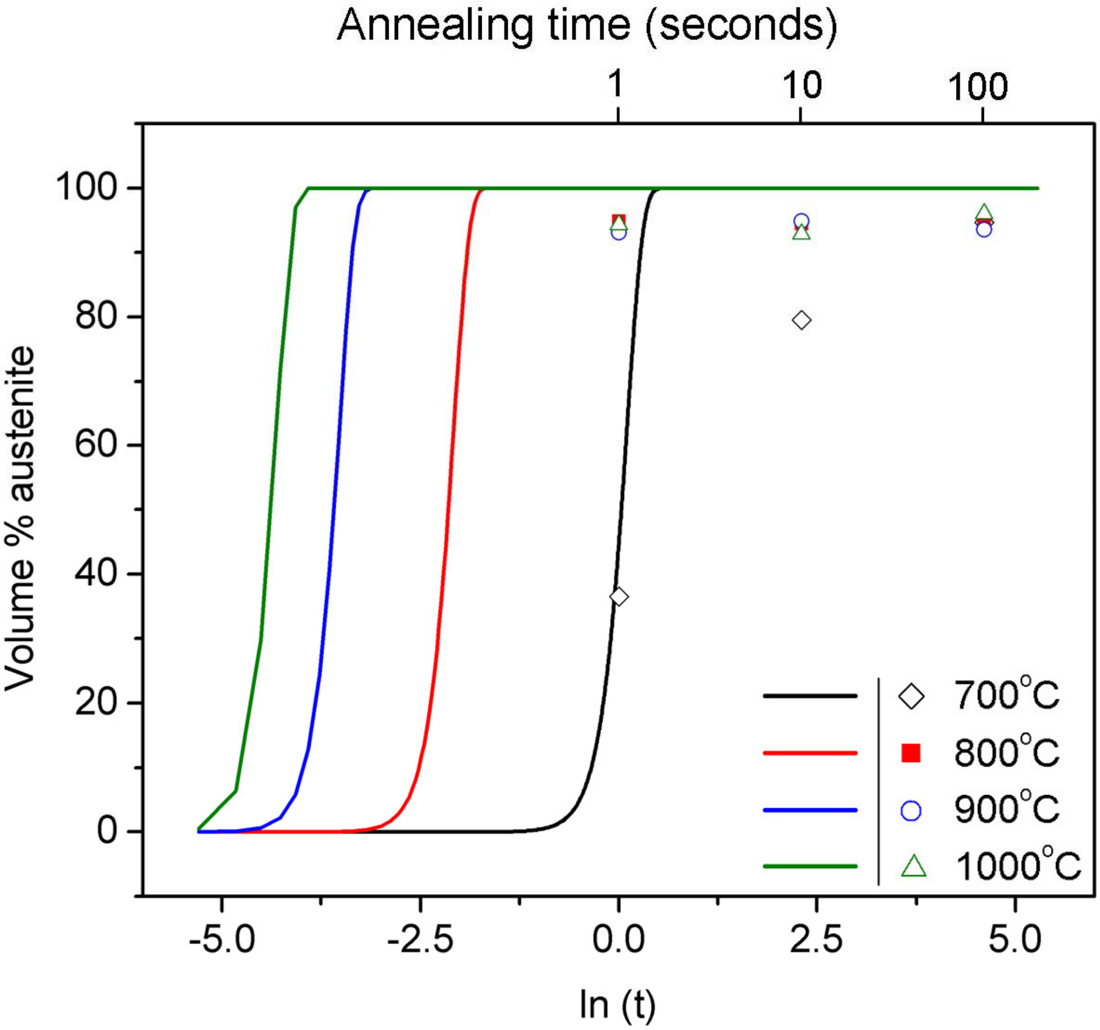

Figure 5.20: Volume % of austenite formed due to the combined effect of Cr and Ni.

5.3 Nano/Submicron Austenite Grain Formation and Grain Growth

5.3.1 Influence of annealing conditions on nano/sub-micron grain formation

The average austenite grain size measured as a function of annealing temperature and time was shown in Fig. 4.17. Nanoscale austenitic grains of the order ~ 100nm are observed in samples annealed at 600°C for 1 and 10 seconds. However, as discussed in section 5.1.2 and 5.1.3, these samples consist of ~ 6% austenite and the presence of nano-scale austenite grains with size ~ 0.1µm. The samples annealed for 100 seconds at 600°C have an austenite phase fraction of ~ 50% with austenitic grains of sizes ~ 0.2µm with a narrow grain size variance (Fig. 4.12). In contrast, samples annealed at 700°C for 1 second with 35% austenite phase fraction, exhibit austenitic grain sizes of ~ 0.2µm. Furthermore, the grain sizes and the grain size variance of samples annealed at 700°C rapidly grow as the annealing duration is increased to 10 and 100 seconds (Fig, 4.13 and Fig. 4.17). This phenomenon is clearer at a higher annealing temperature of 800°C (Fig. 4.14 and Fig. 4.17). The increase in the grain size variance is explained by the fact that the austenite nucleation process is a sequential process, where austenite nucleates first on dislocation-cell martensite, and subsequently on geometrically necessary boundaries of the lath-type martensite [20, 21]. For long annealing durations, the first formed austenite nuclei grow in size while newly nucleated austenite grains continue to form at later stages, resulting in a large grain size distribution.

The sluggish grain growth in samples annealed at 600°C is not surprising. Johannsen *et al.* have shown in 90% cold-rolled AISI 301 SS, grain sizes of ~ 0.25µm in samples annealed at 600°C for 30 minutes [61]. However, rapid grain growth in samples annealed at higher temperatures has not been observed prior to this work. Understanding the reason for this phenomenon is crucial to develop and sustain nano/sub-micron grains in SS. In this regard, the kinetics of grain growth in this alloy is investigated next.

5.3.2 Activation energy for grain growth

On the basis of the grain size data obtained in section 5.2.1.1, the activation energy for grain growth was estimated to be ~ 205kJ/mol (section 5.2.1.1). This is compared with values for other conventional SS (AISI 304, 316, 321 and 347 SS) [119]. In his work, German [119] plotted the $\Delta G_{activation}$ as a function of the grain growth exponent - n for various conventional SS. As the AISI 301LN SS yielded an average value of n ~ 2.5, $\Delta G_{activation}$ values for various conventional SS were obtained from the work of German for n ~ 2.5 for comparison. It is seen that the activation energy for AISI 301LN SS is comparable to that of AISI 304, and 316 SS (Fig. 5.21). On the other hand, the activation energies of AISI 321 SS and 347 SS are much higher than those of AISI 301LN, 304 and 316 SS. This is because AISI 321 and 347 SS have titanium (Ti) and columbium (Cb) additions (Table 5.2), which form stable carbides (TiC, CbC) [120, 121]. These create back-stress on grain boundaries hindering their motion, thereby raising the activation energy for grain growth [107].

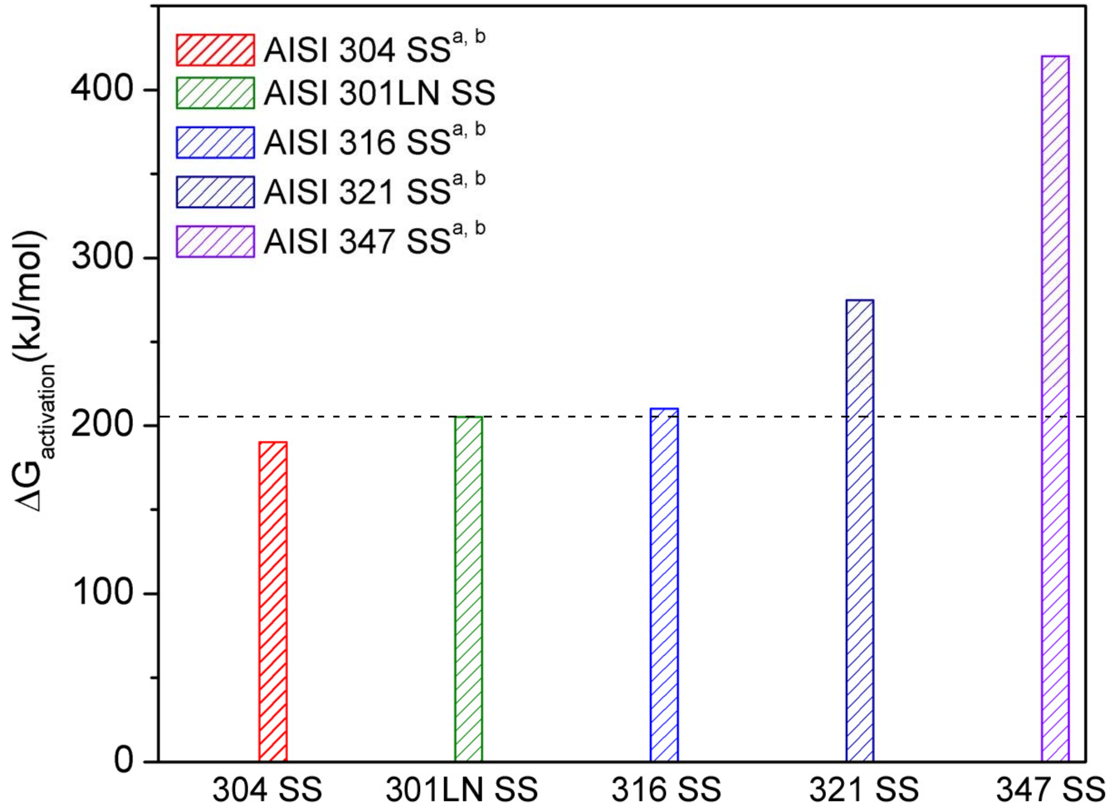

Figure 5.21: Activation energy of AISI 301LN SS in comparison with other commercial SS, (a) R.M. German [119], (b) Stanley *et al.* [122].

Table 5.2: Composition of various stainless steels (*in wt%*). (a) R. M. German [119], and (b) Stanley [122].

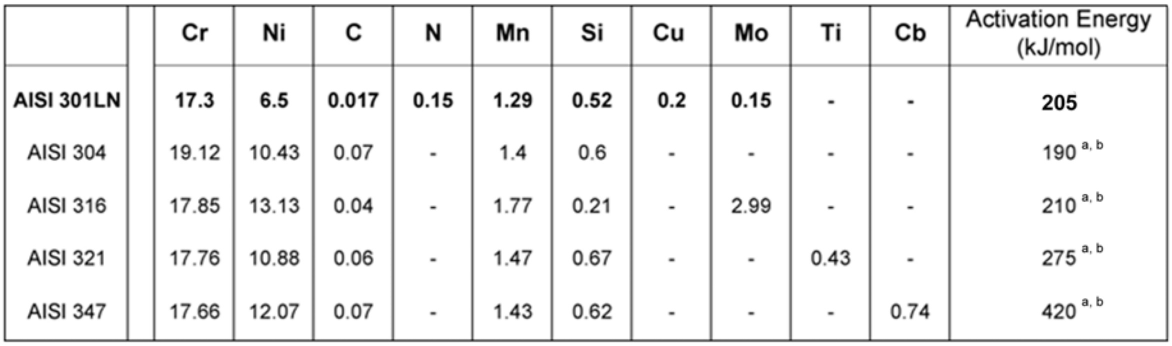

	Cr	Ni	C	N	Mn	Si	Cu	Mo	Ti	Cb	Activation Energy (kJ/mol)
AISI 301LN	**17.3**	**6.5**	**0.017**	**0.15**	**1.29**	**0.52**	**0.2**	**0.15**	**-**	**-**	**205**
AISI 304	19.12	10.43	0.07	-	1.4	0.6	-	-	-	-	190 [a, b]
AISI 316	17.85	13.13	0.04	-	1.77	0.21	-	2.99	-	-	210 [a, b]
AISI 321	17.76	10.88	0.06	-	1.47	0.67	-	-	0.43	-	275 [a, b]
AISI 347	17.66	12.07	0.07	-	1.43	0.62	-	-	-	0.74	420 [a, b]

5.3.3 Optimal conditions for attaining nano/sub-micron grain austenite

Based on the grain growth kinetic parameters (*k*, *n*) and the activation energy for grain growth $\Delta G_{activation}$, the grain size for AISI 301LN SS can be estimated as a function of annealing conditions by rearranging equation 5.1 in the form:

$$\bar{\mathbf{d}}(t,T)=\bar{\mathbf{d}}_{\mathrm{o}}+\left[k_o t\exp\left(-\frac{\Delta G_{activation}}{RT}\right)\right]^{\frac{1}{n}}, \tag{5.24}$$

where $\bar{\mathbf{d}}(t,T)$ is the average grain size as a function of annealing time and temperature, $\bar{\mathbf{d}}_{\mathrm{o}}$ the average initial grain size ~ 0.1μm, $k_o \approx 2.69\times10^9 m^{2.5}\sec^{-1}$, $\Delta G_{activation}$~ 205kJ/mol (section 5.2.1.1), *t* the annealing time, *R* the gas constant, and *T* the annealing temperature.

$\bar{\mathbf{d}}(t,T)$ is plotted for 800°C, 900°C and 1000°C in Fig. 5.22. Rapid grain growth is observed at short annealing durations for all the annealing temperatures studied. This behavior is likely to be due to a large driving force associated with the high curvature of nano/sub-micron grains formed during the $\alpha' \rightarrow \gamma$ reversion. However, interesting differences arise at longer annealing durations for each temperature. For instance, at

800°C the grain size converges to ~ 18μm after an annealing duration of 10 hours whereas at a higher annealing temperature of ~ 1000°C significant grain growth is still possible after 10 hours of annealing.

The reason for abovementioned behavior is due to the fact that $k_{1000^oC} > k_{900^oC} > k_{800^oC}$ (Fig. 5.6). The value of k is directly proportional to the probability of atoms jumping from one grain to the next, which is given by the exponential term $\exp\left(-\frac{\Delta G_{activation}}{RT}\right)$. From this analysis, it can also be inferred that the grain boundary mobility, $\left(M = \frac{k}{4\alpha\gamma}\right)$ increases as the annealing temperature increases, (Fig. 5.23).

The exponential increase of mobility as a function of temperature has important implications in achieving ultra-fine grained AISI 301LN SS. For instance, if the processing conditions are such that the annealing temperature is sufficient to cause the α' → γ reversion but low enough to ensure negligible grain boundary mobility, then ultra-fine austenitic grains can be produced and sustained.

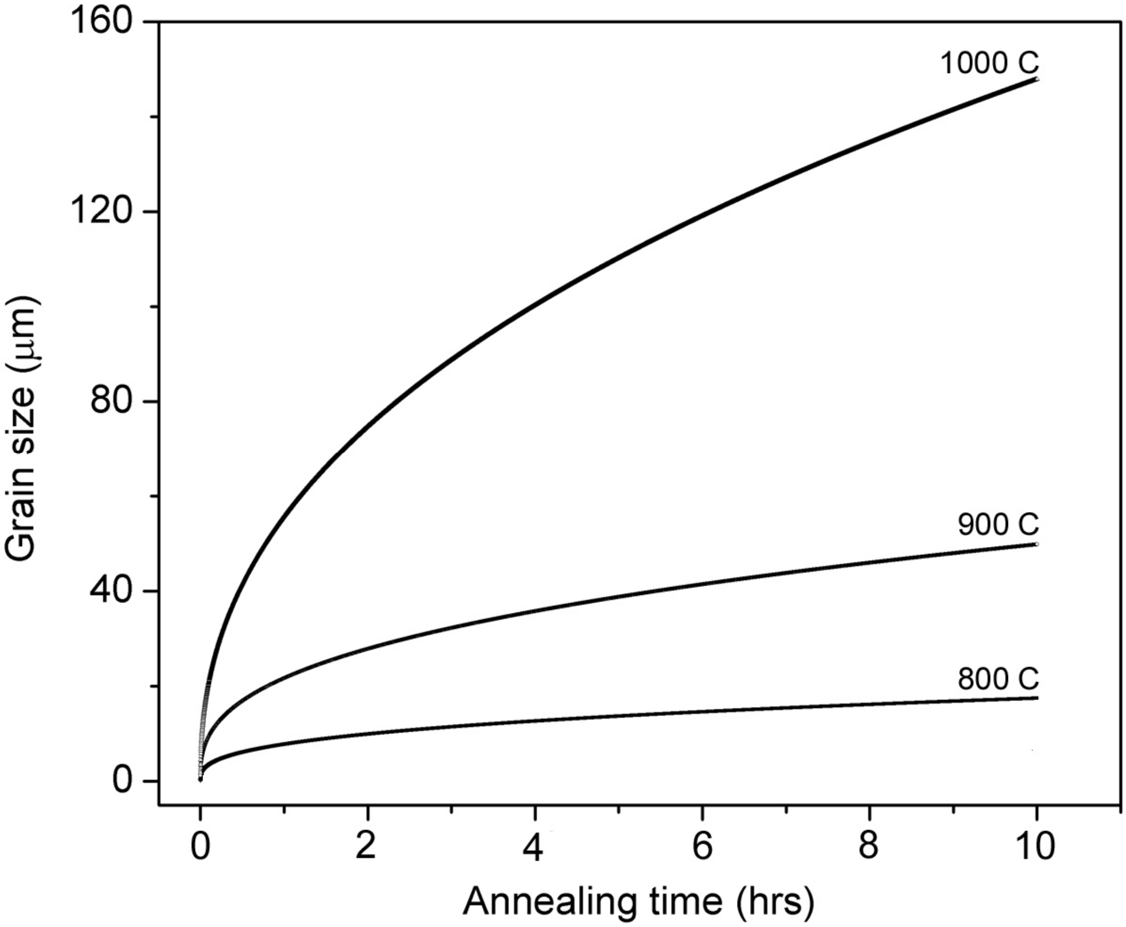

Figure 5.22: Calculated grain growth curves as a function of annealing conditions (t, T).

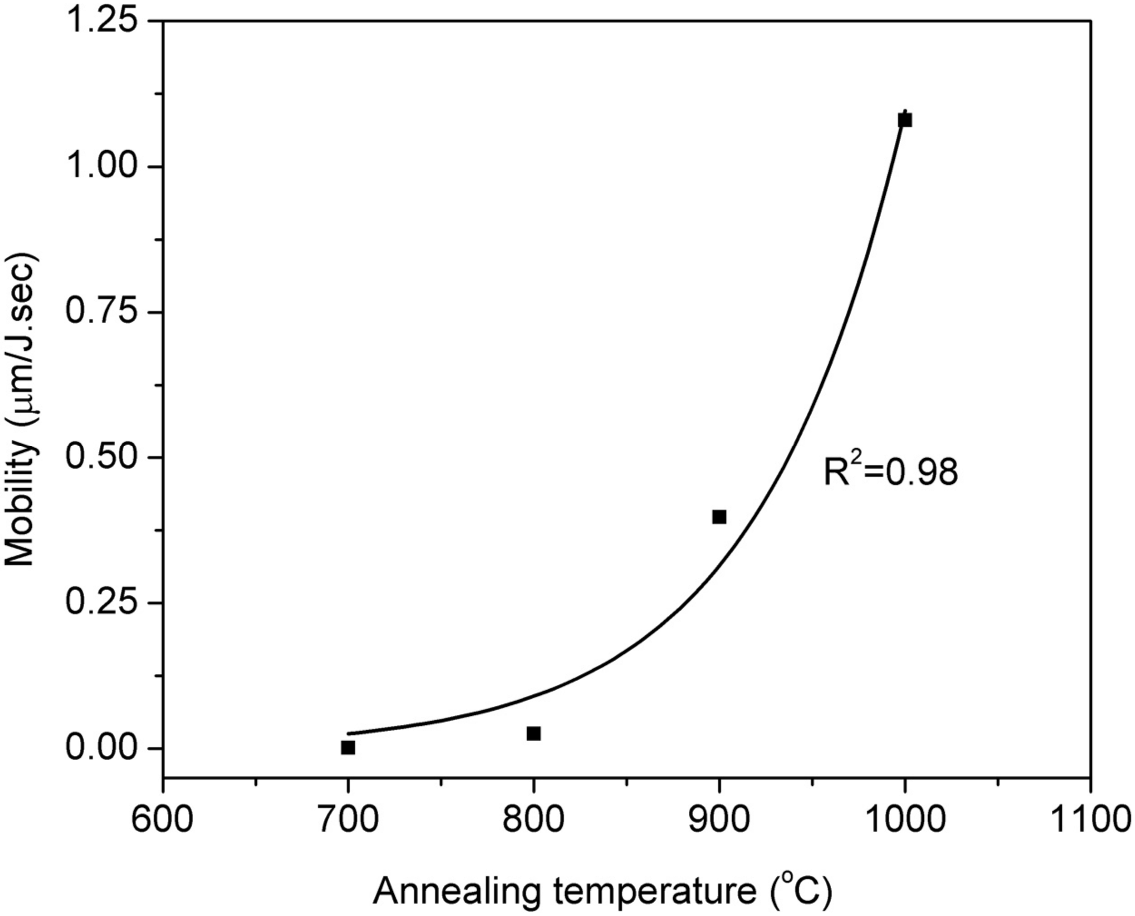

Figure 5.23: Grain boundary mobility as a function of annealing temperature in AISI 301LN SS.

5.3.4 Driving force for grain growth

Fig. 5.22 shows rapid grain growth in samples annealed at all annealing temperatures (800°C, 900°C and 1000°C), particularly during the initial period of annealing. As the activation energy of AISI 301LN SS was found to be similar to that of other commercial SS, the likely reason for the rapid grain growth observed is a high driving force available due to the high grain curvature.

The grain curvature is related to driving force by a differential force, $\Delta F = 2\pi \bar{\mathbf{d}} \gamma$, where $\bar{\mathbf{d}}$ is average grain size, and γ the grain boundary energy associated with the grain. The differential pressure and the associated driving force can be expressed as [113]:

$$\Delta P = \frac{\Delta F}{A} = \frac{2\gamma\pi \bar{\mathbf{d}}}{\pi \bar{\mathbf{d}}^2} = \frac{2\gamma}{\bar{\mathbf{d}}} \tag{5.25}$$

Assuming that grain growth occurs at constant temperature, the change in driving force is related to difference in pressure, according to the expression:

$$\Delta G = V_m . \Delta P = \frac{2\gamma V_m}{\bar{\mathbf{d}}}, \tag{5.26}$$

where V_m is the molar volume. Subsequently, average grain sizes estimated in this work as well as $\bar{\mathbf{d}}$ values obtained for various commercial SS [119, 122] were used to estimate ΔG (Fig. 5.24). As expected, AISI 301LN SS with small grain sizes have a large curvature and subsequently large driving force. Conventional SS with large grain sizes have small driving force for grain growth as observed in Fig. 5.24.

However, by assuming that the driving force for grain growth is only dependent on the pressure difference between two grains, the present analysis fails to take into account several key issues: 1) the material is not pure so the presence of secondary phase precipitates are not considered, 2) grains are not spherical in shape, and 3) the role of processing conditions (temperature, time) on the driving force is not considered.

Thus, it is desirable to develop a relationship where the driving force is related to all experimental parameters (k, $n' = \frac{1}{n}$, t, T). In this fashion, assuming $\Delta G \ll RT$, the driving force (ΔG) can be related to grain growth velocity through the equation:

$$\Delta G = \frac{V_m . v}{M} \tag{5.27}$$

where V_m is the molar volume, v the grain growth velocity and M the grain boundary mobility [113]. As the grain growth velocity can be approximated to the first derivative of the grain growth law with respect to time, one can write:

$$v = \frac{\partial \bar{\mathbf{d}}}{\partial t} = \frac{\partial}{\partial t}(\bar{\mathbf{d}}_{o} + (kt)^{\frac{1}{n}}) = \frac{(kt)^{\frac{1}{n}}}{nt}, \tag{5.28}$$

where all the terms retain their previous definitions. Next, the mobility is proportional to the grain growth constant k, through the relation $M = \frac{k}{4\alpha\gamma}$, where α is a constant ~ 1 and γ is the α'/γ interfacial energy. On the basis of the grain growth velocity and mobility, the driving force for grain growth can now be written as:

$$\Delta G = \frac{4\alpha\gamma V_m (kt)^{\frac{1}{n}}}{nk_o t} \exp\left(\frac{\Delta G_{activation}}{RT}\right), \tag{5.29}$$

Assuming $\alpha \sim 1$ [109, 113], $\gamma \sim 0.48$J/m^2 [123], the molar volume $V_m \sim 6.86\times10^{-6}$ m^3, the values of n and k to be temperature dependent (obtained from section 5.2.1.1), $k_o \approx 2.69\times10^9 m^{2.5}\sec^{-1}$ and $\Delta G_{activation} \sim 205$kJ/mol, ΔG can be plotted as a function of annealing conditions, as shown in Fig. 5.25.

A notable observation is that ΔG is high during the initial seconds of annealing and rapidly converges to a steady state value at long annealing durations. For instance, for samples annealed at 800°C, ΔG declines from ~ 120μJ/mol to ~ 15μJ/mol in a period of five seconds. Such rapid decline may be explained if equation (5.29) is further analyzed. Equation (5.29) contains a t term in the denominator and a $t^{\frac{1}{n}}$ in the numerator. The t term in the denominator increases rapidly as annealing duration increases, while simultaneously, because $\frac{1}{n} < 0.5$, the $t^{\frac{1}{n}}$ term in the numerator decreases rapidly with increasing annealing duration. The combination of these effects causes ΔG to rapidly decline as annealing duration is increased. The general equation for driving force follows a similar trend as that obtained from the special case where $\Delta G = \frac{2\gamma V_m}{\bar{\mathbf{d}}}$. However, there is an important difference between Fig. 5.24 and Fig. 5.25. The driving force data obtained from the general equation is ~ five orders of magnitude less than those obtained from the special case where $\Delta G = \frac{2\gamma V_m}{\bar{\mathbf{d}}}$ (Fig. 5.24 and 5.25).

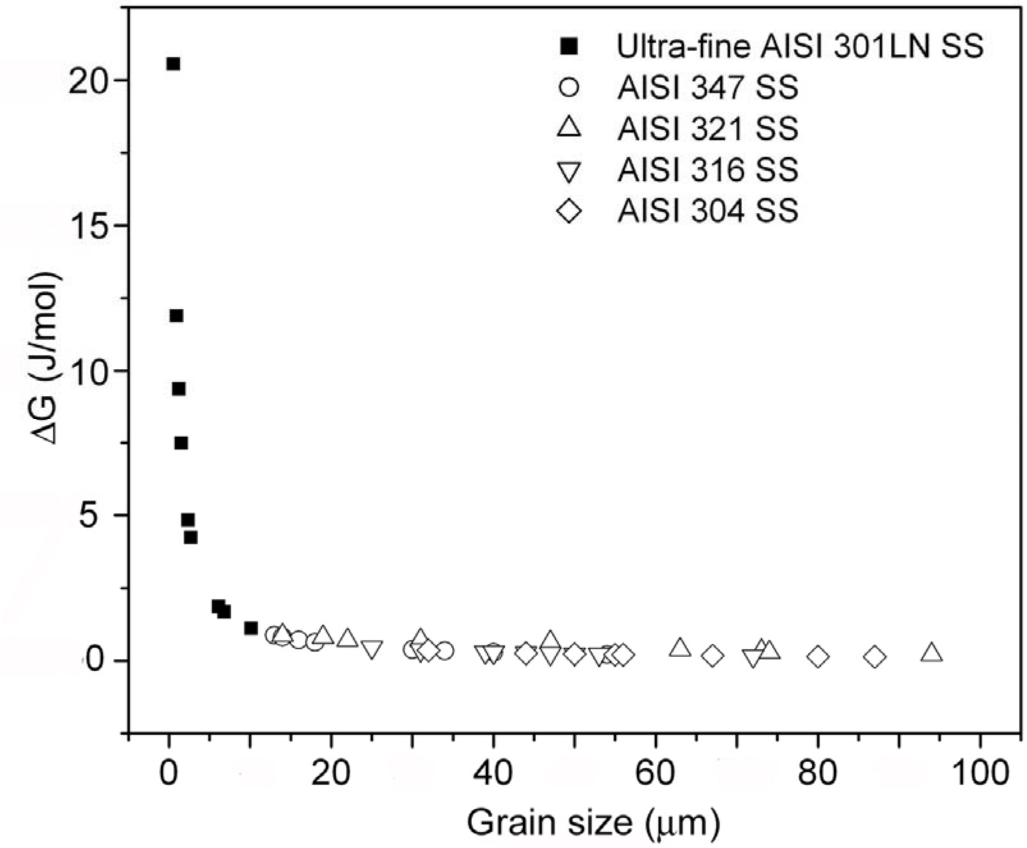

Figure 5.24: Driving force for grain growth as a function of grain size for AISI 301LN SS and other conventional SS.

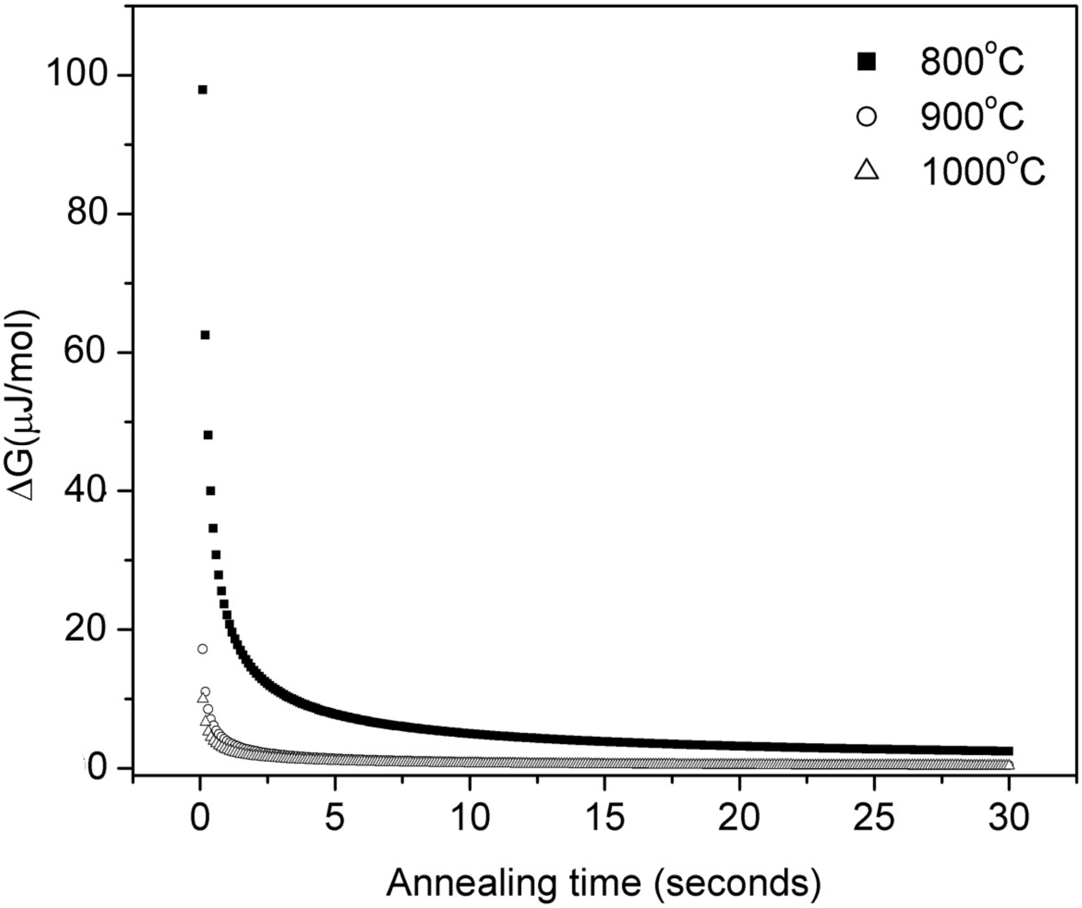

Figure 5.25: Driving force for grain growth as a function of annealing temperature in AISI 301LN SS.

In summary, an in-depth investigation has been conducted to understand grain growth in metastable nano/submicron grained austenitic AISI 301LN SS. The TEM analysis of annealed samples reveals the presence of ultra-fine γ grains that rapidly grow in size. The reasons for rapid grain growth are determined by analysis of the kinetic parameters, activation energy ($\Delta G_{activation}$) and driving force (ΔG) for grain growth. The analysis shows that the $\Delta G_{activation}$ for AISI 301LN is similar to that of other SS and may not satisfactorily explain the observed grain growth rates in AISI 301LN SS. However, a generalized expression for ΔG, which depends on experimental conditions as well as kinetic parameters can offer two explanations for the observed high grain growth velocities: 1) Nano/submicron grains formed during short annealing treatments exhibit a large driving force for grain growth, and 2) high annealing temperatures increase grain boundary mobility, which promotes grain growth.

5.4 RELATIONSHIP BETWEEN MECHANICAL PROPERTIES AND MICROSTRUCTURE

In chapter 2, the Hall-Petch equation describing the relationship between grain size and mechanical properties was presented. In this section, the goal is to better understand the interplay between the observed ultra-fine grain size obtained in AISI 301 LN SS and the mechanical properties obtained.

Let us first consider the samples annealed at 600°C. The results of phase fraction, as well as the microstructural analysis conclusively show that the samples annealed for 1 and 10 seconds are primarily martensitic in nature. Therefore, it is not surprising that these samples have an exceptional tensile and yield strength of ~ 1800MPa. The samples annealed at 600°C for 100 seconds exhibit a dual-phase austenite/martensite structure consisting of nano-scale equiaxed austenitic grains with still a significant amount martensitic. For these samples, a tensile and yield strength of ~ 1500MPa was found. However, as expected, the 600°C samples lack uniform elongation due to a combination the presence of the brittle martensitic phase and work hardening during tensile tests.

The samples annealed at 700°C for 1 second also exhibit a dual-phase austenite/martensite structure, with exceptional tensile/yield strength properties (Fig. 4.18). However, these samples have poor ductility owing to the presence of a predominantly martensitic phase (Fig. 4.19). For longer annealing times, the austenite phase fraction in these samples increases to ~ 80% (Fig. 4.3), followed by austenite grain growth to ~ 0.28μm (Fig. 4.7 and 4.17). Surprisingly, these samples exhibit tensile strengths of ~ 1100MPa with a ductility of ~ 25%. The exceptional strength characteristics might be due the following reasons: 1) presence of ~ 20% martensite, and 2) presence of sub-micron grained austenite (0.28μm), which causes significant grain boundary strengthening effect. The enhanced ductility is likely to be due to the presence of a predominantly austenitic phase.

Samples annealed at higher annealing temperatures of 800°C, 900°C and 1000°C have a primarily austenitic structure with sub-micron/ultra-fine grains (Fig. 4.17). Although these samples exhibit a ductility that is comparable to conventionally processed AISI 301LN SS, their tensile and yield strengths are far superior to that of conventional processed AISI 301LN SS (Fig. 4.18 and 4.19). In this particular case, it is desirable to fully understand the reason for such increase in strengthening. In this regard, it is important to determine the Hall-Petch relationship for these ultra-fine grained AISI 301LN SS. Shino *et al.* [17, 18, 19] has reported a Hall-Petch type behavior for AISI 304 SS and AISI 301 SS down to 0.8 μm and 3μm grain size, respectively. According to

Shino *et al.* [17, 18, 19], the Hall-Petch relation seemed to break down below a 3μm grain size for AISI 301 SS. However, these investigations did not seem to consider the fact that metastable austenitic SS do not fully convert the stress-induced martensite to reverted austenite during annealing, particularly at low annealing temperatures. Hence, the presence of martensite in annealed samples will influence the yield strength, which consequently will affect the Hall-Petch behavior. Furthermore, no results have been reported for the nitrogen-bearing AISI 301LN SS, which is the focus of this work.

In this context, the specific objective of this section is to examine the relationship between the ultra-fine austenite grain size and the yield strength obtained in AISI 301LN SS. The case where the Hall-Petch relationship is independent of temperature is considered first. However, during annealing at different temperatures, the microstructure is likely to change, in particular due to the formation of precipitates and changes in the dislocation density. Thus, the case where the Hall-Petch relation will be affected by the annealing temperature is considered next. The study described herein will be an additional step towards understanding the effect of annealing conditions and the various strengthening mechanisms on the mechanical properties of reversion-annealed SS.

5.4.1 The Hall-Petch Relationship

The interplay between grain size and mechanical properties is focused on samples with primarily austenitic phase – i.e. samples annealed at 800°C, 900°C and 1000°C. It should be noted however that these samples are not completely austenitic (~ 93% austenite phase). The remaining 7% is martensite should therefore be considered.

Thus, in samples annealed at higher temperatures (800°C, 900°C and 1000°C), the origin of the high yield strength can be understood by considering the correlation between the yield strength and the obtained grain size, according to the Hall-Petch relationship [22-24]:

$$\sigma_{yield} = \sigma_o + k\left(\bar{\mathbf{d}}\right)^{-\frac{1}{2}}, \tag{5.30}$$

where σ_o is the lattice friction stress, $\bar{\mathbf{d}}$ the average austenitic grain size and k a constant. However, as this equation assumes a single-phase and an average grain size, it needs to be modified to take into account the presence of both austenite and martensite phases in the annealed samples.

The presence of both austenite and martensite can be resolved by using the classical rule of mixtures, $\sigma_{yield} = V_{\alpha'}\sigma_{\alpha'} + V_\gamma\sigma_\gamma$, where $\sigma_{\alpha'}$ is the yield strength of martensite (α'), $V_{\alpha'}$ the volume fraction of martensite, σ_γ the yield strength of austenite and V_γ the volume fraction of austenite. Assuming $\sigma_{\alpha'}$ ~ 1500 MPa, we can extract from Fig. 4.18b, the yield strength only due to the presence of austenite (Fig. 5.27).

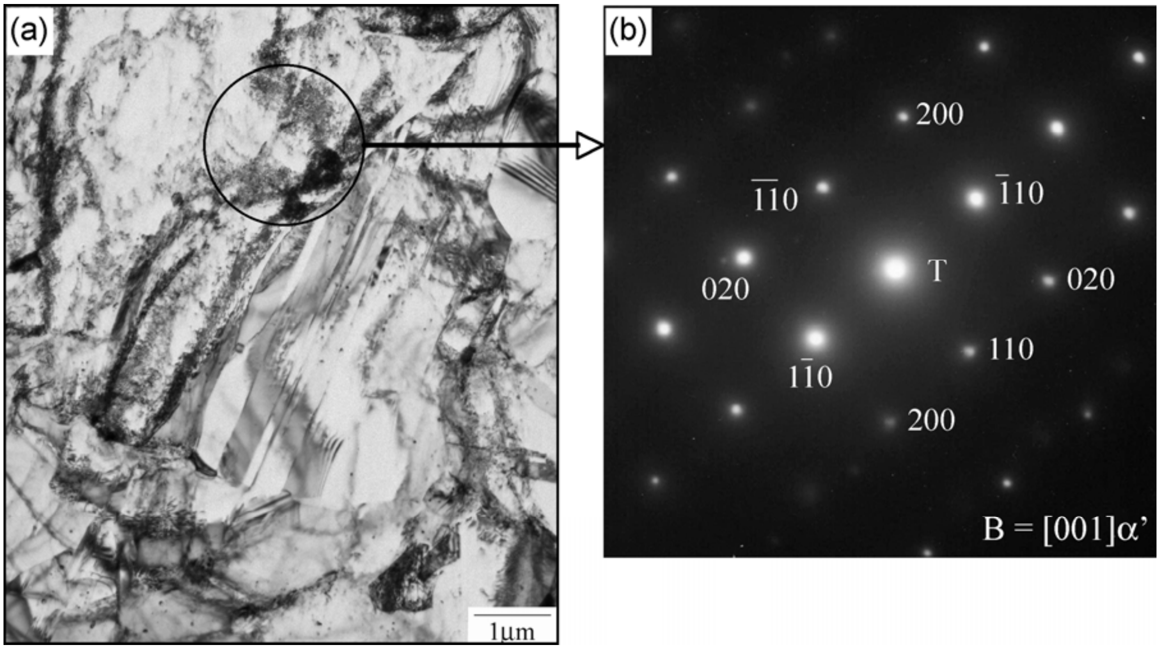

Figure 5.26: (a) TEM image of a martensitic region the annealed AISI 301LN SS, (b) SADP of martensitic region.

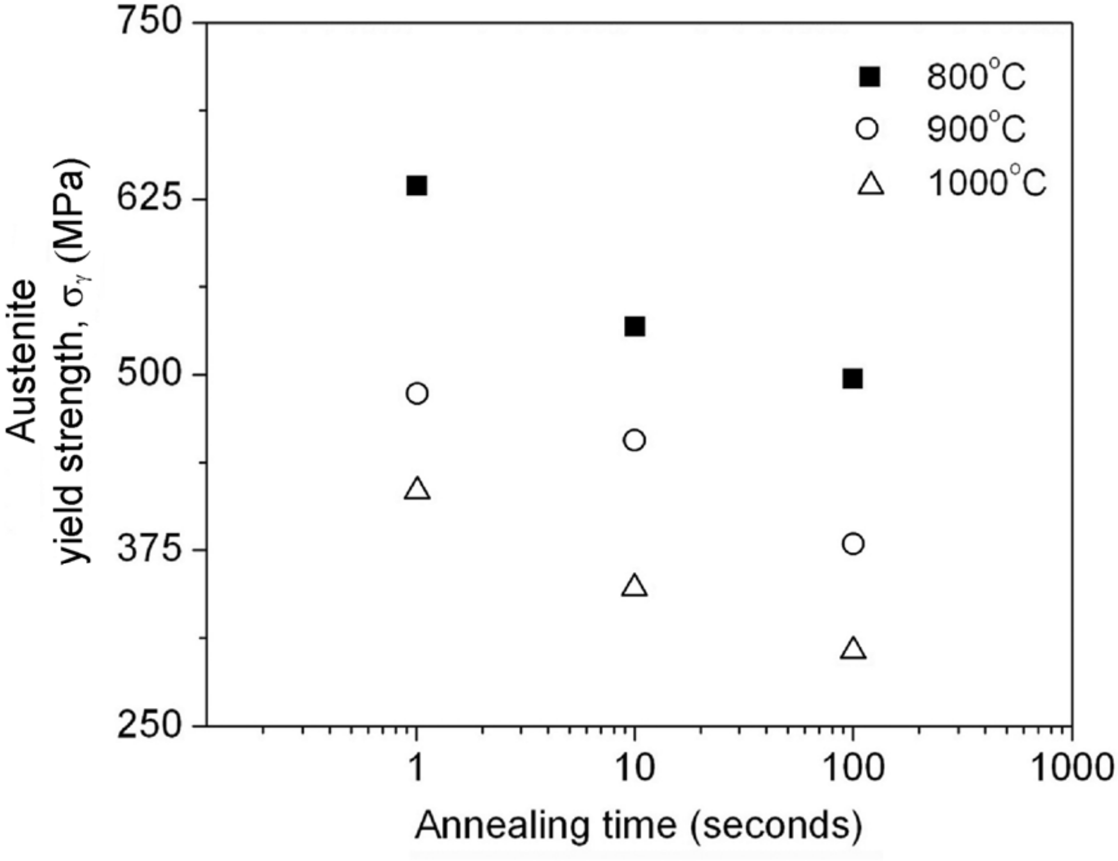

Figure 5.27: Yield strength due to austenite phase in 63% cold rolled AISI 301LN SS samples annealed at 800°C, 900°C and 1000°C.

In addition, as cold-rolling leads to the formation of around 96% stress-induced martensite and 4% of retained austenite (section 4.1), upon annealing, the total austenite content is a mixture of reverted austenite, which nucleated from stress-induced martensite, and retained austenite, which has likely recrystallized. Based on the values for σ_γ and $\left(\bar{\mathbf{d}}\right)^{-\frac{1}{2}}$ for various annealing parameters, a linear curve can be fit to this data, so that the constant *k* and the off-set stress σ_o can be estimated, (Fig. 5.27). A k-value of ~ 290 MPa.μm$^{1/2}$ and a off-set stress of ~ 252 MPa were calculated.

These values differ considerably from those obtained by Schino et al. [16, 17, 19] for AISI 301 SS and AISI 304 SS. In particular, their investigations reported higher k values (~ 400 MPa.μm$^{1/2}$) for both SS, and a deviation from the Hall-Petch relationship for AISI 301 SS below a grain size of 3μm. Possible reasons for such deviations may include 1) the presence of retained tempered martensite after annealing, which was not considered by Schino et al. [16, 17, 19], 2) the presence of nitrogen in AISI 301LN SS, which has a different strengthening effect from that of carbon, which is present in AISI 301 SS and AISI 304 SS; and 3) the formation of CrN nitrides in AISI 301LN SS (Fig. 4.11), instead of carbides that may be present in AISI 301 SS and AISI 304 SS.

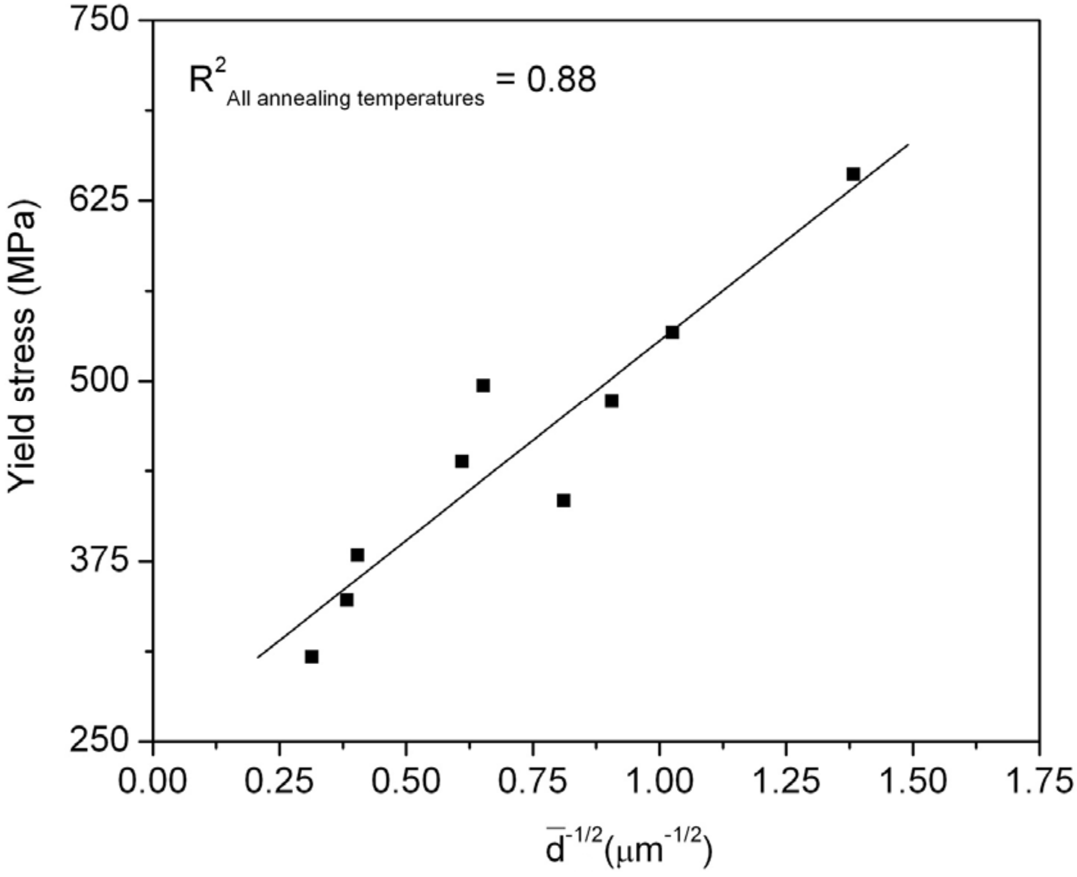

Figure 5.28: Hall-Petch relationship for AISI 301 LN SS.

Another important aspect in establishing the correlation between yield strength and grain size is the fact that the microstructure of AISI 301 LN SS is dependent on the annealing temperatures used in this work. Thus, it is relevant to consider the Hall-Petch behavior separately for each temperature. This analysis is shown in Fig. 5.28, where a marked influence of the annealing temperature on the off-set stress σ_o (intercept with the y-axis) is observed. On the other hand, there is no significant effect of annealing temperature on the Hall-Petch coefficient *k*. The lack of a dependence of k on the annealing temperature has also been demonstrated in a different alloy system by Conrad *et al.* [124]. However, it should be kept in mind that, in the current work, the precipitates formed in AISI 301LN SS upon annealing has been claimed to affect the value of *k*. Plausible explanations for this discrepancy may be that parameter *k* is not strongly influenced by precipitates below a certain size and not predominantly at grain boundaries. In fact, Mangen & Nembach [125] have shown that for precipitates below 10nm, dislocation pileups were readily formed. In addition, they also showed that the parameter *k* could be affected by precipitates at grain boundaries due to the creation of a precipitation-free zone along the grain boundaries.

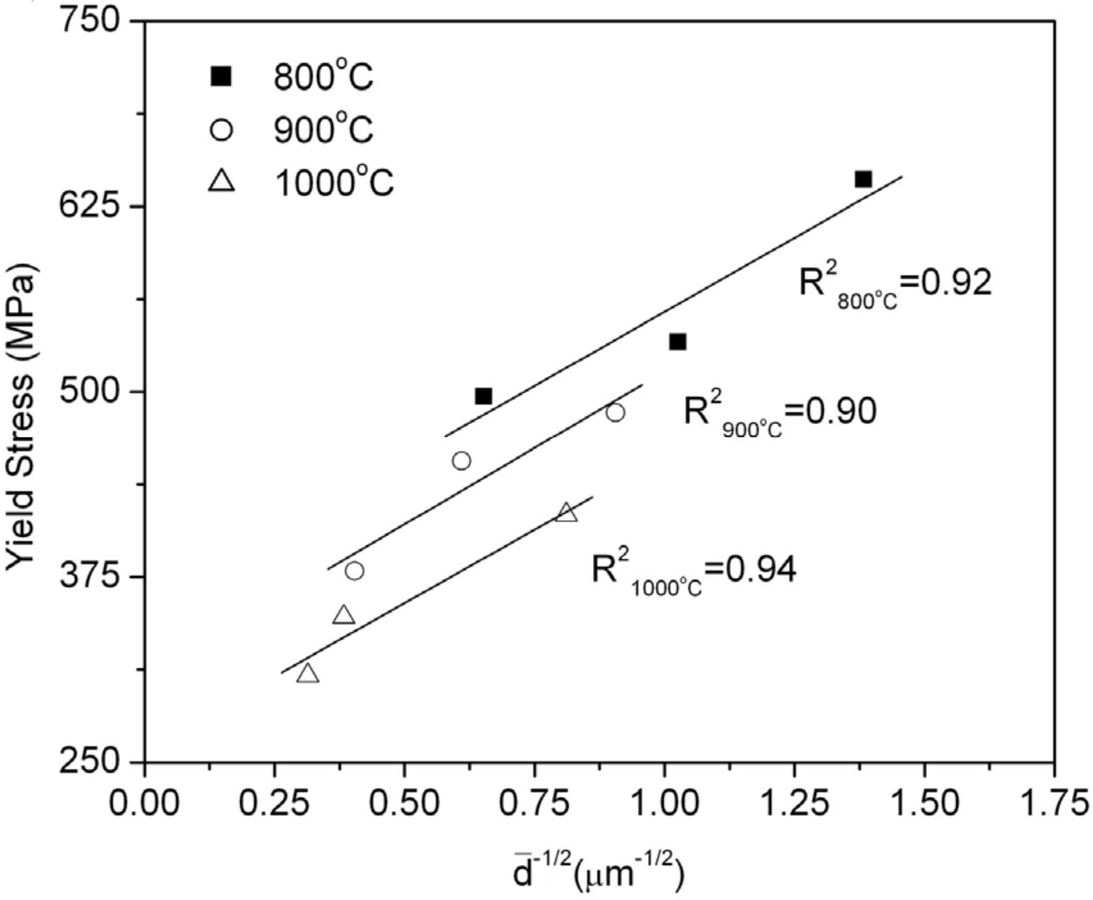

Figure 5.29: Hall-Petch relationship in AISI 301 LN SS, assuming temperature dependence.

In the case of AISI 301LN SS, the average size range of nitride precipitates is typically below 10nm and no precipitates were observed at the grain boundaries. Thus, although nanosized precipitates were present in AISI 301LN SS, particularly at 800°C, they might not have a strong influence on the critical stress required to unlock dislocations and on the number of dislocations *n* in a pileup, which is related to the parameter *k* through the expressions [124]:

$$k = M\left[\frac{2.2\pi\mu b(2-\upsilon)\tau_c}{4(1-\upsilon)}\right] \tag{5.30}$$

$$n\tau_e = \tau_c\,, \tag{5.31}$$

where M is the Schmidt factor, μ the shear modulus, b the Burgers vector, ν the Poission's ratio, τ_e the critical shear stress, and τ_c the critical shear stress required to initiate dislocation movement in the adjacent grain.

5.4.2 Influence of annealing temperature on strengthening mechanisms

In order to better understand the temperature effects on the Hall-Petch equation, we should consider that the off-set stress can be written, in general, as the sum of several strengthening mechanisms, namely 1) precipitate strengthening, 2) strain hardening and 3) solid solution strengthening. This can be expressed as:

$$\sigma_o = \sigma_d + \sigma_{ppt} + \sigma_{ss} \tag{5.32}$$

where $\sigma_d = 2\mu b\sqrt{\rho}$ is the strengthening contribution due to dislocation-dislocation interaction (strain hardening), μ is the shear modulus, b is the Burgers vector and ρ is the dislocation density; $\sigma_{ppt}= (0.84\tau_{ppt}\mu b)/LC_\varphi$ [126] is the strengthening contribution due to the presence of precipitates, τ_{ppt} is the critical resolved shear stress required to move dislocations past a random array of precipitates, L is the distance between the precipitates, C_φ is the Schmid factor. Finally, σ_{ss} is the strengthening contribution due to solid solution.

Thus, to assess the off-set stress, we need to determine the contributions by each strengthening mechanism as a function of temperature. For the calculations, the various errors associated with the measurements were considered, in particular the residual errors associated with determining the off-set stress (intercept with the y-axis) and the errors in measuring the distances between precipitates. The errors were then calculated and converted to MPa values. Finally, the geometric mean of errors was considered due to additions or subtractions performed during calculations.

In assessing the contributions of the various strengthening mechanisms to the off-set stress, we begin with the calculation of σ_{ss} at 1000°C. Assuming the samples annealed at this temperature exhibit characteristics of a fully annealed material, i.e. the absence of secondary phase precipitates ($\sigma_{ppt} = 0$) and a typical equilibrium dislocation density of 10^{12} m^{-2}, eqn. 5.23 can be simplified and rearranged in the form $\sigma_{ss}= \sigma_o-\sigma_d$. Thus, for a dislocation density $\rho \sim 10^{12}$ m^{-2} [127], a shear modulus, μ = 77 GPa, and a Burgers vector, b = 2.51 Å, σ_d can be calculated as ~ 39 MPa. Since σ_o ~ 252 MPa at 1000°C (obtained from Fig. 5.32), the solid solution strengthening σ_{ss} can be calculated as ~ 213 MPa for the sample annealed at 1000°C.

For the 800°C and 900°C samples, the calculation of σ_{ss} is not as trivial because CrN nitrides are present at these temperatures (Fig. 4.11), leading to a depletion of chromium and nitrogen from the austenitic matrix. A loss of nitrogen from the austenite matrix, due to nitride formation, will thus affect the strengthening due to solid solution [39]. Hence, it is necessary to quantify the amount of nitrogen present in the precipitates to be able to assess σ_{ss}. This can be done by estimating the volume fraction of nitrides in a given sample, according to the existing number and size of nitrides per unit volume, determined through TEM analysis. The volume of material considered for the calculation was estimated by measuring i) the area of the TEM micrograph through an image-analysis software, and ii) the foil thickness by analyzing the Kossel-Möllenstedt fringes in a convergent beam electron diffraction pattern (CBED), (Appendix A).

This analysis shows that ~ 0.010 wt% N and ~0.009 wt% N are present in the form of nitrides for the samples annealed at 800°C and 900°C, respectively. As the strength of austenitic stainless steel is dependent on nitrogen content, according to the empirical expression $\Delta\sigma \sim 1014\times[\Delta N]$ (in MPa) [39], where $[\Delta N]$ is the change in wt% N, the reduction in σ_{ss} for the samples annealed at 800°C and 900°C can be calculated as ~ 15 MPa and ~11 MPa, respectively. Subtracting these values from the calculated $\sigma_{ss,}$ for the fully annealed alloy (~ 225 MPa), yields the σ_{ss} values for the samples annealed at 800°C and 900°C (Fig. 5.29).

Consider now the strengthening contribution σ_{ppt} due to presence of CrN nitrides. Nabarro has shown that the critical resolved stress required to move dislocations past a random array of precipitates can be expressed as $\tau_{ppt} \sim 0.84\mu b/(L\ C_{\varphi}))$ [126]. Because $\tau_{ppt} = \sigma_{ppt}\ C_{\varphi}$ and assuming (1) a random orientation of grains with respect to the applied stress axis and (2) a maximum stress direction on the slip plane, we can write $\sigma_{ppt} = 3\tau_{ppt}$ [126]. In addition, as the material studied herein is a polycrystalline material, an average value $\langle\sigma_{ppt}\rangle$ due to the presence of CrN nitrides in multiple grains should be estimated. This was done by measuring σ_{ppt} in 100 grains for samples annealed at 800°C and 900°C and then calculating their average. Calculated $\langle\sigma_{ppt}\rangle$ average values for the samples annealed at 800°C and 900°C are shown in Fig. 5.30. The results indicate a dramatic decrease in precipitate strengthening as the annealing temperature is increased from 800°C to 900°C due to the absence of nitrides at higher temperatures [79].

Finally, the strain hardening σ_d can be calculated by subtracting the values of σ_{ss} and σ_{ppt} from the off-set stresses σ_o obtained for each annealing temperature (Fig. 5.29). The results show that the strain hardening contribution obtained for the 800°C and 900°C samples is ~ 40MPa and decreases slightly for higher annealing temperature. Based on this value, an approximate dislocation density was estimated to be $\sim 1 \times 10^{12} m^{-2}$ for both samples which compares well with that of a fully annealed polycrystalline alloy. This indicates that the retained austenite that may have failed to recrystallize does not seem to play an important role in strain hardening.

In general, it is clear that for samples annealed at 800°C a large off-set stress primarily due to solid solution and precipitate strengthening can be observed. However, as the annealing temperature is increased, the contribution of precipitate strengthening to the off-set stress is reduced and solid solution strengthening, mainly due to the presence of nitrogen, becomes the predominant effect.

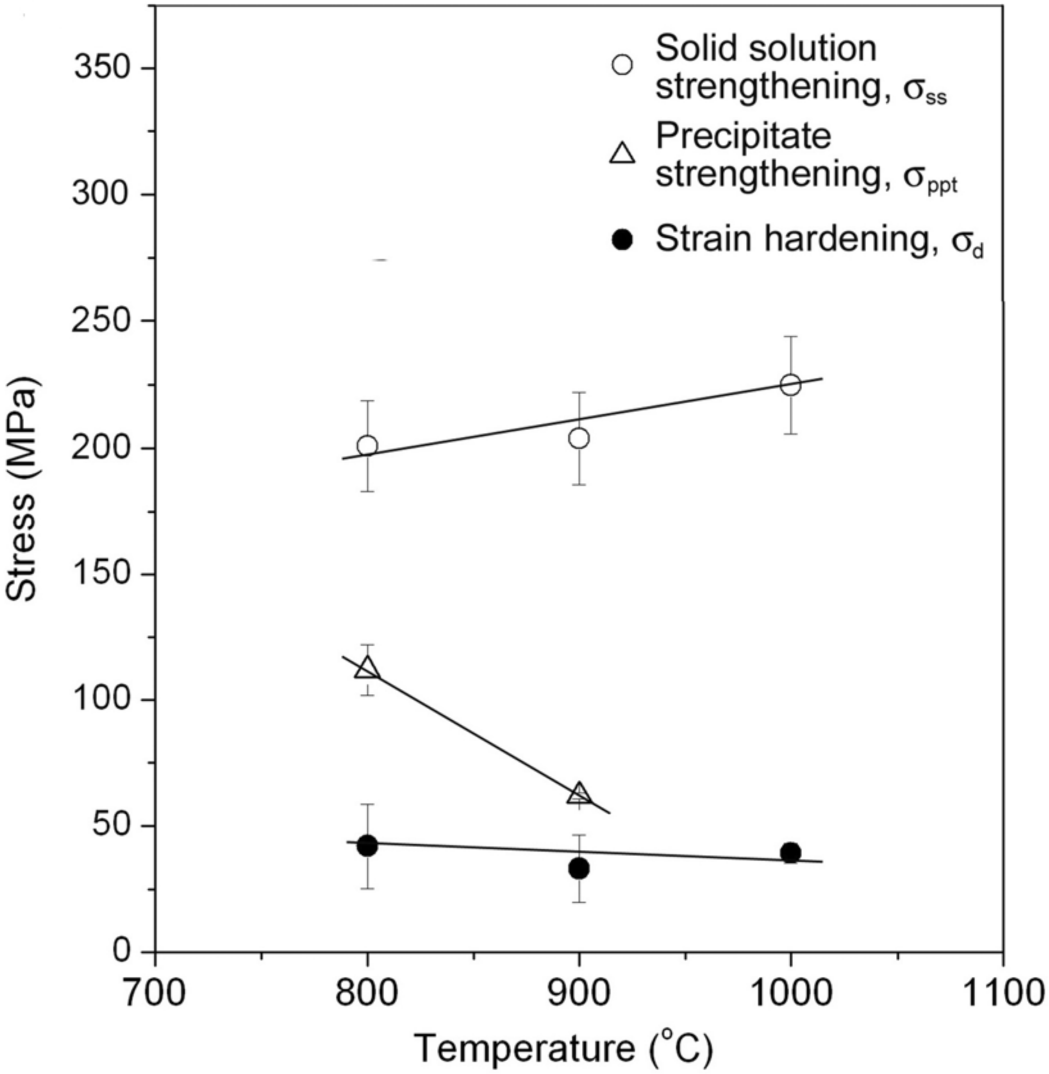

Figure 5.30: Strengthening mechanisms operating in AISI 301LN SS samples annealed at various temperatures.

We are now left with the task of considering the sole effect of grain-boundary strengthening σ_{gbs} as a function of annealing temperature. As the value of *k* remains approximately constant with annealing temperature (Fig. 5.28), the effect of grain boundary strengthening is primarily due to a change in austenite grain size, Fig. 5.30. On this basis, comments on the importance of each strengthening mechanism (strain hardening, precipitate strengthening, grain boundary strengthening and solid solution strengthening) to the yield strength at different annealing temperatures can be made.

As shown in Fig. 5.30, strain hardening has a minor influence on yield strength at all annealing temperatures considered. Attention is thus focused on the remaining three strengthening mechanisms. At the lowest annealing temperature of 800°C and shortest annealing time of 1 second, the presence of ultra-fine austenitic grains contribute the most to the yield strength via grain boundary strengthening (Figs. 5.30 and 5.31). However, as temperature increases and/or time progresses, grain growth occurs. Thus, grain boundary strengthening is diminished, while solid solution strengthening becomes the predominant factor. Furthermore, at the annealing temperature of 800°C, the presence of nitrides contributes substantially to yield strength through precipitate strengthening. This contribution decreases at the annealing temperature of 900°C, and eventually plays no role at 1000°C, the highest annealing temperature tested (Fig.5.29). From this discussion, one can see that different strengthening mechanisms gain prominence at different annealing times and temperatures.

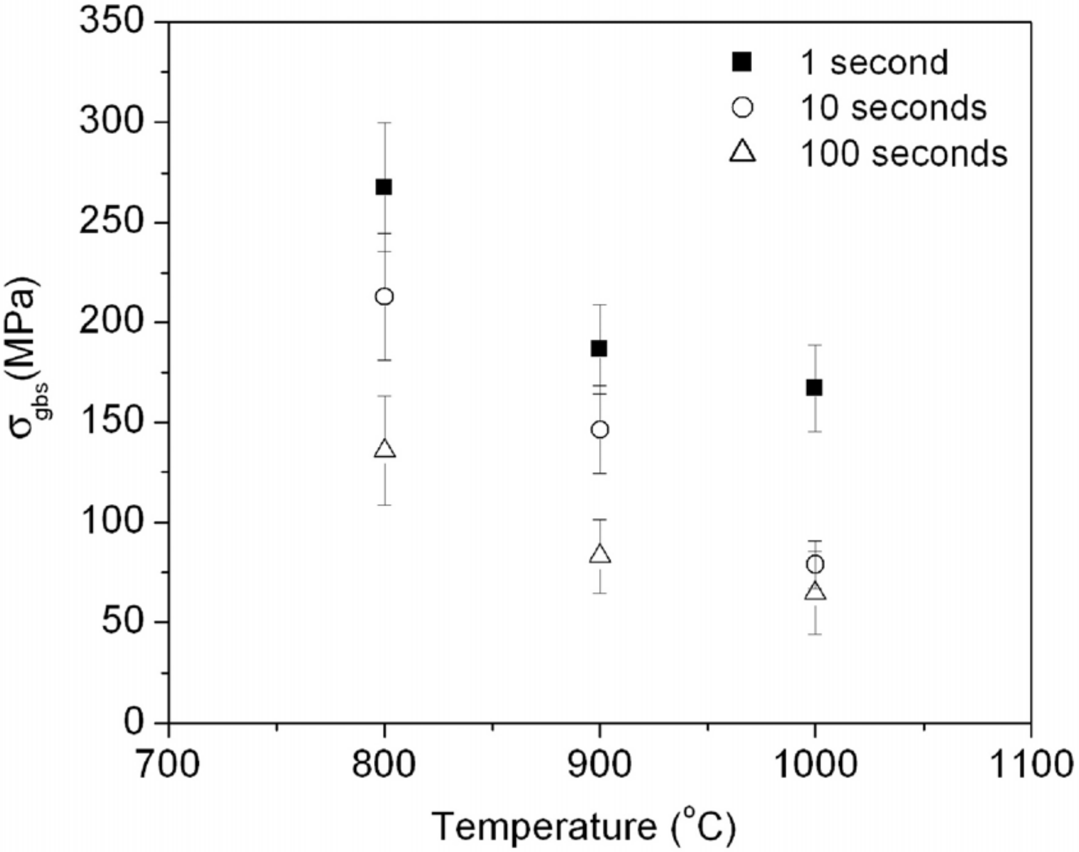

Figure 5.31: Grain boundary strengthening as a function of annealing conditions in AISI 301LN SS samples.

In summary, the yield strength of samples annealed at 800°C, 900°C and 1000°C was evaluated with respect to the two terms present in the Hall-Petch relationship: the off-set strength (σ_o) and grain boundary strengthening (σ_{gbs}). The off-set strength was sub-divided into three contributions: precipitate strengthening (σ_{ppt}), solid solution strengthening (σ_{ss}), and strain hardening (σ_d), and the effect of annealing parameters on these contributions was analyzed.

For samples, annealed at 800°C, the high yield strength was primarily due to the presence of (1) ultra-fine grains leading to a significant grain boundary strengthening, (2) solid solution strengthening, and (3) secondary phase chromium nitrides leading to substantial precipitate strengthening. As the annealing temperature was increased to 900°C and 1000°C, the dominant strengthening mechanism to yield strength was due to solid solution strengthening. In contrast, strain hardening was not an important mechanism in increasing the yield strength for any of the annealed samples.

5.4 INFLUENCE OF ALLOY COMPOSITION ON MICROSTRUCTURE EVOLUTION

So far, little has been said about the effect of alloying elements on the microstructural evolution of AISI 301 LN SS when cold-rolled and annealed for short durations. As discussed in section 2.4.5, alloy composition may play an important role on the $\alpha' \rightarrow \gamma$ reversion mechanism.

In section 5.1, it was shown that AISI 301LN SS reverts to austenite through a diffusion-type reversion. This mechanism is desirable for nano/sub-micron austenite grain formation because it does not impose restrictions on processing conditions (the $\alpha' \rightarrow \gamma$ reversion operating through a shear mechanism occurs in a narrow temperature range).

Thus, it is important to identify possible alloying element(s) that may cause a change in the reversion mechanism in AISI 301LN SS.

The objective of this section is to compare the reversion mechanism between the AISI 301LN SS and a modified version of AISI 301LN SS, which is deficient in manganese (Mn) - a strong austenite stabilizer, and molybdenum (Mo) - a strong ferrite stabilizer. It should be noted here that a modified version of AISI 301LN SS, with dramatic changes in only two alloying elements (Mn, Mo) was selected for this study instead of a different commercial metastable austenitic SS such as AISI 301 SS [6, 7], to portray the possible substantial influence of key alloying elements on the microstructure evolution and phase reversion mechanism.

5.4.1 Materials

AISI 301LN SS samples and a control sample designated as 'modified – 301LN' with a composition shown in Table 5.2 were prepared by Outokumpu Stainless Oy, Tornio. The M_s and M_{d30} values for each of these materials were calculated and are shown in Table 5.3. As shown, the M_{d30} values for all materials under investigation are above room temperature indicating that stress-induced martensite can by induced in samples deformed at ambient temperature. Subsequently, AISI 301LN and modified-301LN samples were subjected to a cold reduction of ~ 63%

Table 5.3: Chemical composition (in wt %) of materials used for investigation

		C	N	Cr	Ni	Mn	Si	Cu	Mo
301LN		0.017	0.15	17.3	6.5	1.29	0.52	0.2	0.15
Modified-301LN		0.025	0.115	17.2	7.1	0.04	0.17	0.2	-

Table 5.4: M_s and M_{d30} values (in °C) of materials used for investigation

		M_s(°C)	M_{d30}(°C)
301LN		-127.8	34.7
Modified-301LN		-100.6	48.2

5.5.2 Results & Discussion

5.5.2.1 SQUID magnetic measurements

The volume fractions of austenite for each of the samples were estimated through the procedure described in section 3.2.2 and is shown in Fig. 5.32. These volume fractions also include the contribution of retained austenite already present in samples prior to annealing (~4.5% in AISI 301LN SS and ~ 7% in modified-301LN SS). For an annealing temperature of 600°C and an annealing duration of 1 second, negligible reversion takes place in both alloys. At an annealing duration of 100 seconds, partial reversion to ~ 50% γ takes place in AISI 301LN samples, whereas the modified-301LN SS undergoes negligible reversion. The difference in austenite phase fraction between the two alloys becomes dramatic at higher annealing temperatures. For instance, in AISI 301LN SS, austenite reversion proceeds from ~ 35% to ~ 95% as samples are heated from 1 to 100 seconds at 700°C (Fig. 5.32a). In contrast, for modified-301LN SS the volume percentage of austenite remains constant as annealing duration is increased from 1 to 100 seconds at 700°C (Fig. 5.32b). As the annealing temperature is increased to 800°C, the observed phase fractions continue to differ. At this temperature, the AISI 301LN reverts almost completely to austenite for all annealing durations (Fig. 5.32a). However the modified-301LN SS still fails to revert completely to austenite. This dramatic difference in the austenite reversion process between the two alloys may be attributed to a significant difference in manganese content present (Table 5.3). In AISI 301LN SS, the presence of Mn stabilizes the austenite phase, as well as promotes nitrogen solubility, which in turn stabilizes further the austenite phase.

After obtaining the austenite phase fractions, a preliminary TEM investigation was carried out to delineate microstructural differences in the AISI 301LN SS and the modified-301LN SS. Specifically, TEM images and SADP of modified-301LN SS annealed at 600°C were analyzed. Subsequently, these images were compared with those of AISI 301LN obtained for an annealing temperature of 600°C. Furthermore, images of samples for both alloys annealed at 800°C and 1000°C were also compared.

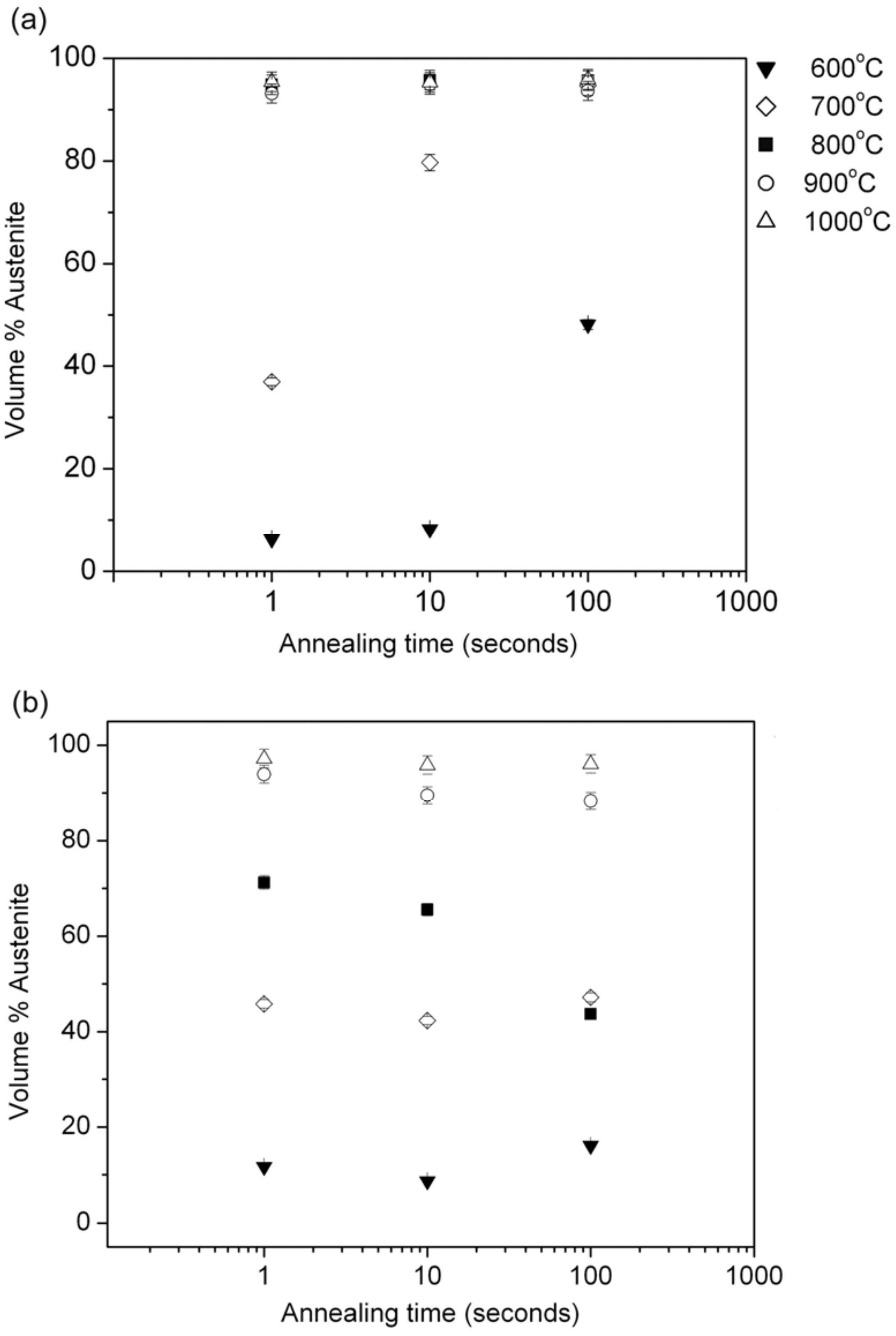

Figure 5.32: Volume fraction of austenite in (a) 301LN, (b) Modified 301LN SS.

5.5.2.2 Transmission electron microscopy

Images and SADP of modified-301LN SS samples annealed at 600°C for an annealing duration of 1 second are shown in Fig. 5.33a and 5.33b. This sample has primarily a martensitic morphology. SADP (taken with 1μm aperture size) of samples annealed for 1 second show diffraction rings corresponding to the martensite phase (for instance, (110)α') and streaks corresponding to the austenite phase (for instance, (113)γ and (040)γ). In addition, streaks corresponding to martensitic phase are also observed (for instance, (200)α' and (330)α'). These observations seem to suggest that this sample is primarily made up of dislocation cell type martensite (leading to a ring-type diffraction pattern) with pockets of lath type martensite (leading to diffraction streaks) and platelets of retained austenite. Thus, an anneal temperature of 600°C for 1 second duration is insufficient to transform the martensite into austenite. At a longer annealing duration of 10 seconds, there is significant difference in the observed microstructure (Fig. 5.33c) in contrast to the samples annealed for 1 second. However, the diffraction pattern from this sample fails to indicate any notable austenite reversion (Fig. 5.33d). A closer analysis of this diffraction pattern reveals a spot-pattern corresponding to the α' phase, a faint ring-like pattern corresponding to the α' phase and diffraction streaks corresponding to the austenite phase. On this basis, it can be inferred that samples annealed at 10 seconds show primarily a martensitic structure that is surrounded by regions of dislocation walls and dislocation forests. Furthermore, there is a dramatic decrease in the dislocation-cell structure seen in Fig. 5.33a. In general, samples annealed 10 seconds also show little austenite reversion.

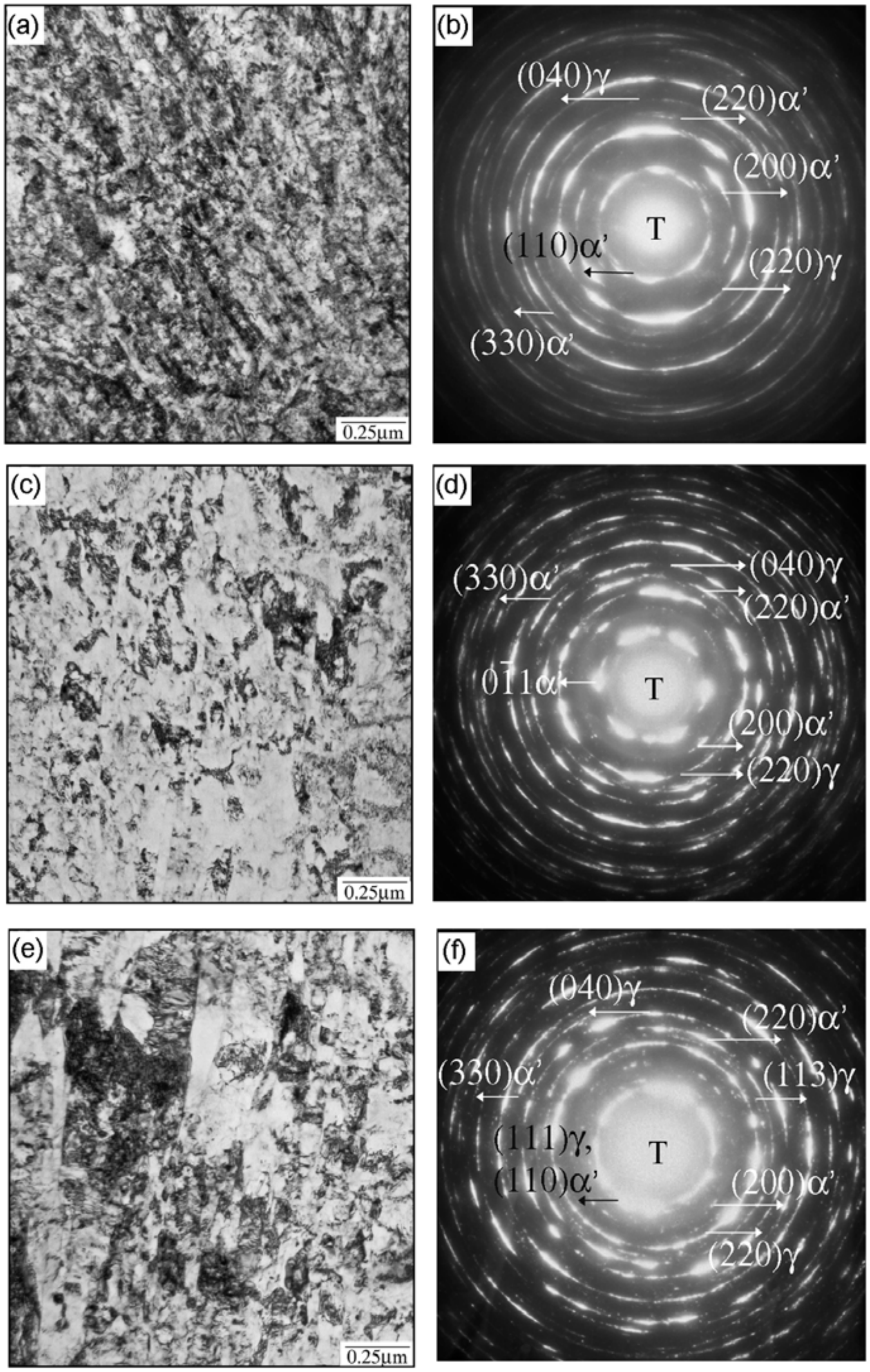

Figure 5.33: Annealing temperature of 600°C: (a), (c) and (e) are TEM images for the 1, 10 and 100 seconds samples respectively; (b), (d) and (f) are the corresponding diffraction patterns.

TEM images of the samples annealed at 600°C for 100 seconds are shown in Fig. 5.33e. The corresponding diffraction pattern is shown in Fig. 5.33f. A quick glance at the diffraction pattern observed for this sample indicates the presence of 1) continuous rings corresponding to austenite (for instance, (220)γ and (040)γ), 2) continuous rings corresponding to martensite (for instance, (110)α') and 3) diffraction streaks corresponding to martensite phase (for instance, (200)α' and (330)α'). As has been mentioned before, continuous rings corresponding to austenite may indicate the formation of nano/submicron grained austenite. Continuous rings corresponding to martensite indicates the presence of dislocation cell type martensite, whereas diffraction streaks associated with the martensitic phase may be due to the presence of lath type martensite. Thus, it seems that an annealing duration of 100 seconds may result in the formation of nano-austenitic grains within a primarily martensitic matrix. It is also noted that the austenitic grains formed are not equiaxed. Instead, they are elongated and have a high density of defects. This observation gives a preliminary insight into the grain formation mechanism in these modified-AISI 301 LN SS, which have a lack of Mn. Since the austenite grains observed have inherited the morphology of the parent martensite phase, it can be said that the $\alpha' \rightarrow \gamma$ reversion occurring in these samples may follow a shear-controlled mechanism. In contrast, the AISI 301LN SS samples exhibit totally different characteristics (Fig. 5.34f), where relatively defect free equiaxed austenitic grains are observed. In this case it is clear that $\alpha' \rightarrow \gamma$ reversion is diffusion controlled.

At this point it can be preliminary argued that the absence of Mn, a powerful austenite stabilizer, may have a profound influence on the reversion mechanism. This hypothesis is further strengthened by a comparison of TEM images obtained for these two alloys at the annealing temperatures of 800°C and 1000°C. The annealing durations used in this comparison are 1, 10 and 100 seconds.

Fig. 5.35 shows a series of TEM images of AISI 301LN SS and modified-301LN samples that were annealed at 800°C for various annealing durations. As suggested by the SQUID analysis, the AISI 301LN SS samples, annealed at 800°C for 1 second, already show the formation of austenite (Fig. 5.35a). The austenite phase has a nanocrystalline structure and it is to a large extent, defect free (Fig. 5.35b). On the contrary, for the modified-301LN material, (Fig. 5.35a, 5.35c and 5.35e), regions of martensite and defect laden austenite can be clearly seen. Thus, it is inferred that for modified-301LN samples the martensite to austenite reversion at this temperature occurs through a shear mechanism, where the sample partially retains the parent defect substructure. Moreover, annealing this material for longer periods at 800°C does not result in grain growth. This observation also points towards a shear-type austenite reversion.

In samples that were annealed at higher temperatures (1000°C), the differences between the microstructures in AISI 301LN SS and modified-301LN SS are even more evident (Fig. 5.36). The microstructures of AISI 301LN SS annealed at 1000°C indicated a thermally activated diffusion controlled grain growth, (Fig. 5.35b, 5.35d, 5.35f). However, the modified-301LN samples annealed at this temperature show a shear reversion type mechanism where an increasing annealing time had no effect on grain size.

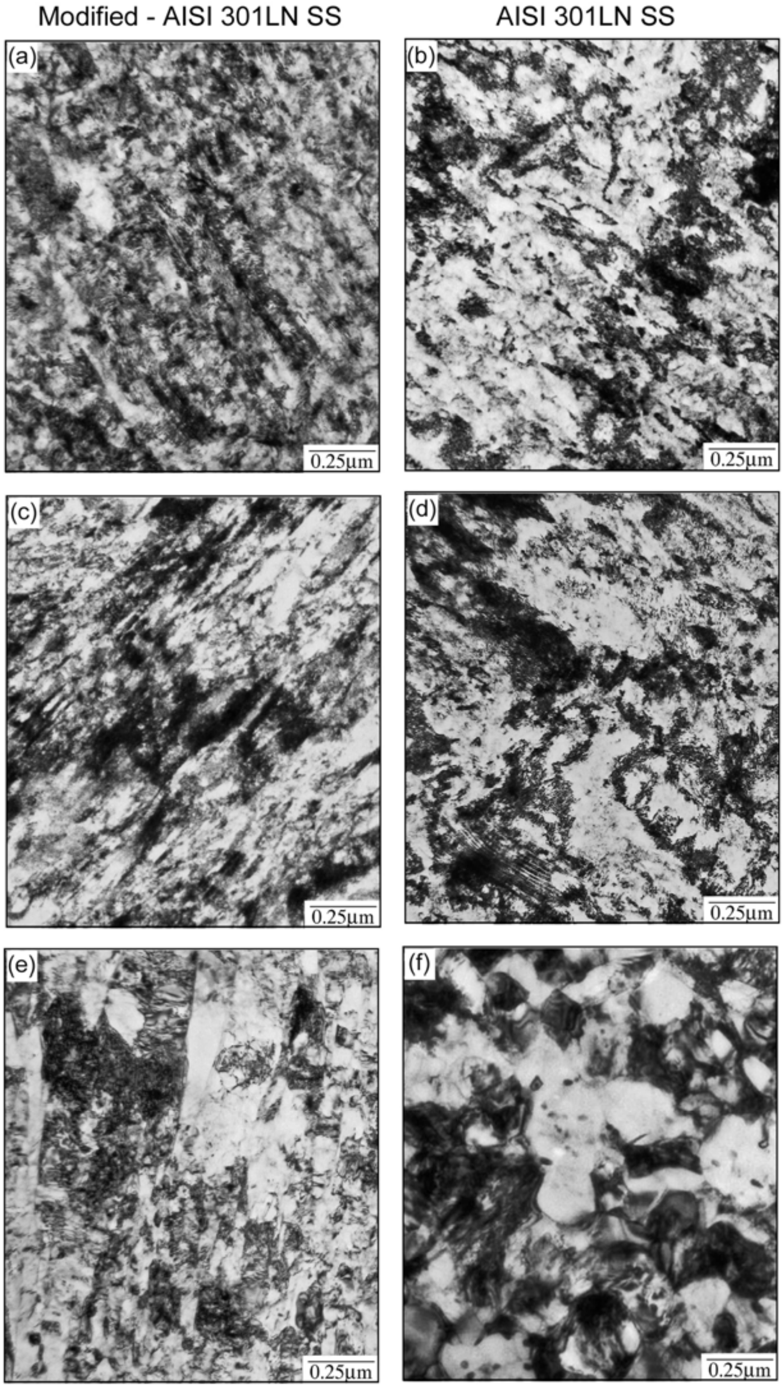

Figure 5.34: TEM images of samples annealed at 600°C. (a), (c) and (e) are images taken from modified – AISI 301LN SS at various annealing times (1, 10 and 100 sec.), whereas (b), (d) and (f) are images taken from AISI 301LN SS, for the same annealing times.

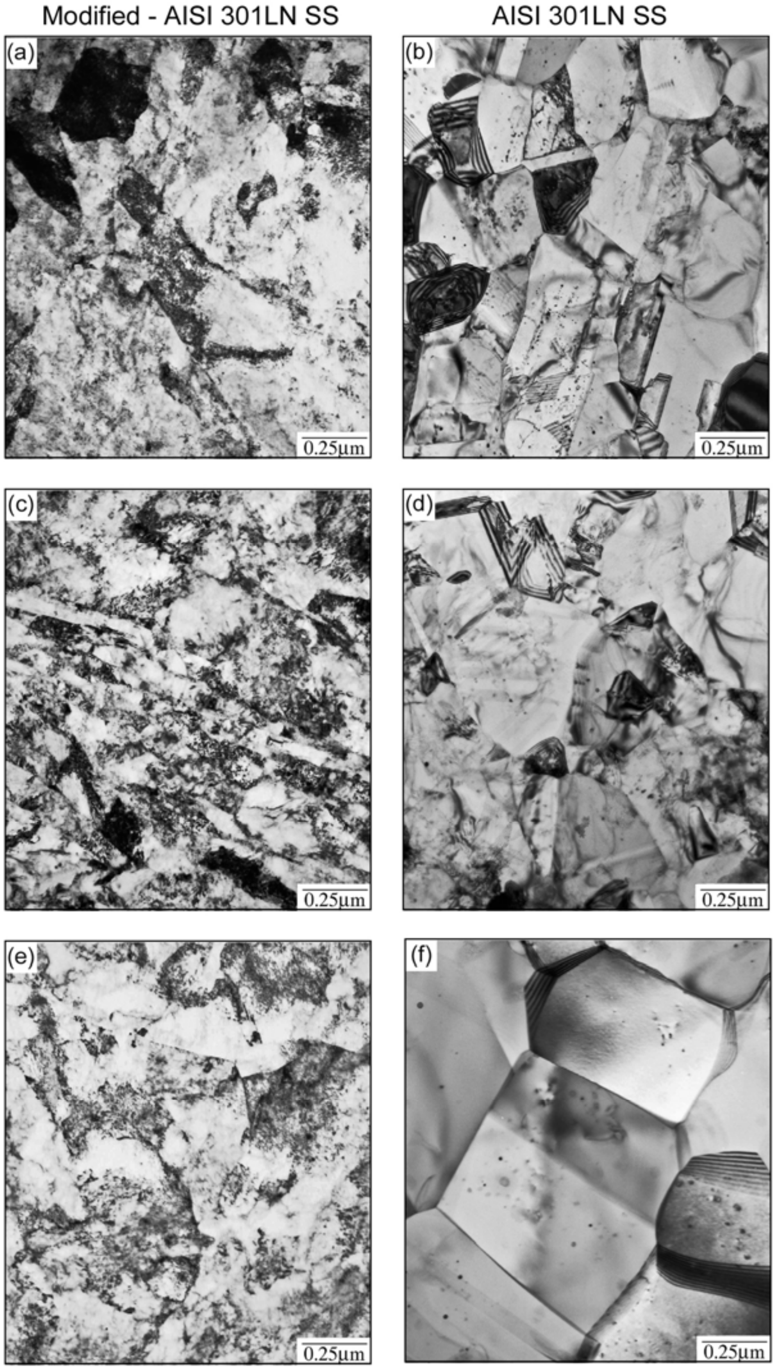

Figure 5.35: TEM of samples annealed at 800°C. (a), (c) and (e) are images taken from modified – AISI 301LN SS at various annealing times (1, 10 and 100 sec.), whereas (b), (d) and (f) are images taken from AISI 301LN SS, for the same annealing times.

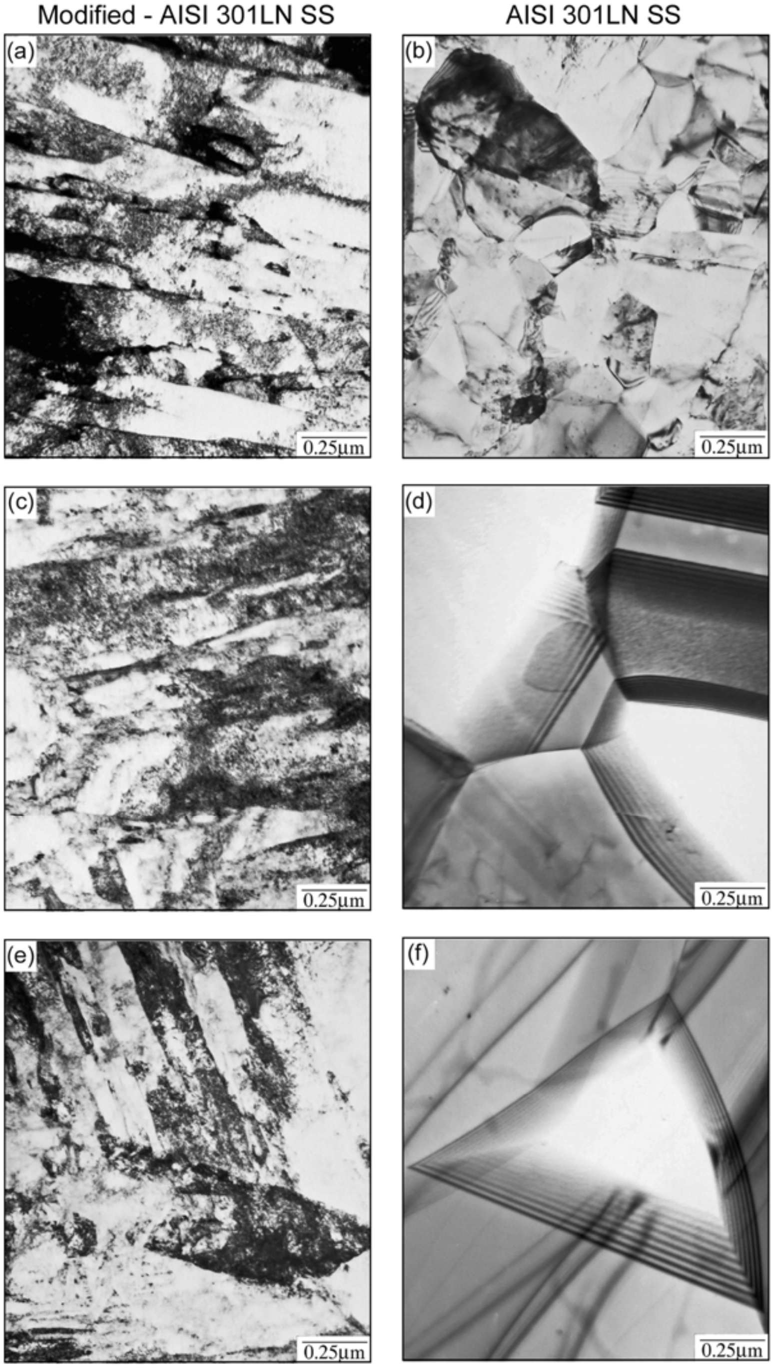

Figure 5.36: TEM of samples annealed at 1000°C. (a), (c) and (e) are images taken from modified – AISI 301LN SS at various annealing times (1, 10 and 100 sec.), whereas (b), (d) and (f) are images taken from AISI 301LN SS, for the same annealing times.

Based on the aforementioned magnetic measurements and microstructural evaluations, it can be said that the chemical composition has an important role in determining whether 1) the austenitic phase reversion successfully occurs during annealing of cold-rolled SS, and 2) the reversion is driven by a shear or a diffusion mechanism.

Chapter 6: Conclusions and Future Work

6.1 CONCLUSIONS

Nano/submicron grained SS with enhanced mechanical properties were demonstrated in a commercial austenitic SS – AISI 301LN. From this work the following main conclusions can be drawn:

1. 63% cold-reduction of AISI 301LN SS produces approximately 100% martensite, comprised of ultra-fine martensite laths, dislocation-cell martensite, dislocation walls and forests with negligible retained austenite. Subsequent annealing at ~ 600°C for 1 and 10 seconds fails to convert the initial martensitic microstructure into austenite. However, longer annealing times of 100 seconds produces a partial $\alpha' \rightarrow \gamma$ reversion with a microstructure comprising of ~ 50% austenite, and equiaxed austenite grains with sizes around ~ 0.2μm. Furthermore, CrN secondary phase precipitates were also observed at this annealing temperature. The microstructure of the samples annealed at higher temperatures (700°C, 800°C, 900°C and 1000°C) also exhibit equiaxed defect-free austenite grains, CrN precipitates, and rapid grain growth.

2. Based on the observation of the microstructures and grain size data, we can conclude that the $\alpha' \rightarrow \gamma$ transformation in cold-rolled and short annealed AISI 301LN SS occurs by a diffusion-type mechanism.

3. The kinetics of the $\alpha' \rightarrow \gamma$ reversion model developed herein, shows that Cr diffusion is the limiting factor in reverting the austenite from strain-induced

martensite during annealing. The results obtained from this model can be used to predict the austenite phase fraction for different annealing conditions.

4. The study on the kinetics of grain growth in nano/submicron grained AISI 301LN SS show that 1) the activation energy for grain growth in AISI 301LN SS (~ 205kJ/mol) is similar to that of other commercial SS, 2) a high grain curvature driving force for grain growth is responsible for the rapid increase in grain size with temperature and time, and 3) the optimal annealing conditions for nano/sub-micron austenite grain formation is ~ 700°C, among the temperatures studied.

5. The relationship between ultra-fine austenite grains in AISI 301LN SS and the mechanical properties follows the classical Hall-Petch relationship. In particular, the high strengthening effect seen in ultra-fine grained AISI 301LN SS is due to an interplay between various strengthening mechanisms – solid solution strengthening, precipitate strengthening, strain hardening and grain boundary strengthening – all of which are a function of annealing temperature.

6. The removal of Mn from AISI 301 LN changes the reversion mechanism from a diffusion-controlled reversion to a shear-controlled reversion. In addition, the austenite phase becomes more unstable leading to a less efficient martensite to austenite reversion.

6.2 FUTURE WORK

For future work I suggest the following:

1. The formability characteristics of nano/sub-micron grained AISI 301LN SS should be fully investigated. This objective is important since the ultimate goal is to be able to use high strength commercial SS to produce complex engineering structures. Therefore, it is imperative to determine the forming characteristics of nano/sub-micron grained AISI 301LN SS.

2. The nature of the $\alpha' \rightarrow \gamma$ phase reversion in the modified-AISI 301 LN should be further investigated. Previous research has shown that the heating rates used for annealing determines the type of reversion mechanism in operation. This parameter should be investigated. In particular, it would be of interest to analyze the results obtained from modified-301LN SS (used in this work) if subjected to a very slow heating rate (< 3°C/sec) and compare the data with the results presented herein.

3. Develop low-Ni, high Mn SS with nano/submicron grain sizes.

APPENDIX A

Foil Thickness Measurements Using Kossel-Möllenstedt Fringes

When electron transparent samples in CBED mode are tilted to achieve a two-beam condition, Kossel-Möllenstedt (K-M) fringes are observed (Fig. A.1). These fringes are equivalent to the rocking-curve oscillation intensities (denoted by **s**) of bend contours seen in bright field images. However, with K-M fringes, the spacing between fringes represents deviations in intensities that can be used to obtain the foil thickness through this relationship [89]:

$$\frac{\Delta s_i^2}{n_i^2} + \frac{1}{\xi_g^2 n_i^2} = \frac{1}{t^2}, \tag{A.1}$$

where, Δs_i is the deviation in intensity, n_i the number of fringes counted from a K-M fringe image, ξ_g the extinction length and t the foil thickness. Furthermore, Δs_i is related to experimentally obtained parameters through this relationship:

$$\Delta s_i = \lambda \frac{\Delta \theta_i}{2\theta_B d^2}, \tag{A.2}$$

where λ is the electron wavelength, $\Delta\theta_i$ the distance between two adjacent fringes, $2\theta_B$ the distance between $\mathbf{g} = 000$ and $\mathbf{g} = \langle 220 \rangle$, and d the interplanar spacing for the $\mathbf{g} = \langle 220 \rangle$ reflection (Fig. A.1). Δs_i and n_i have been experimentally determined and analyzed graphically to obtain the foil thickness, $t \sim 130\, nm$ (Fig. A.2).

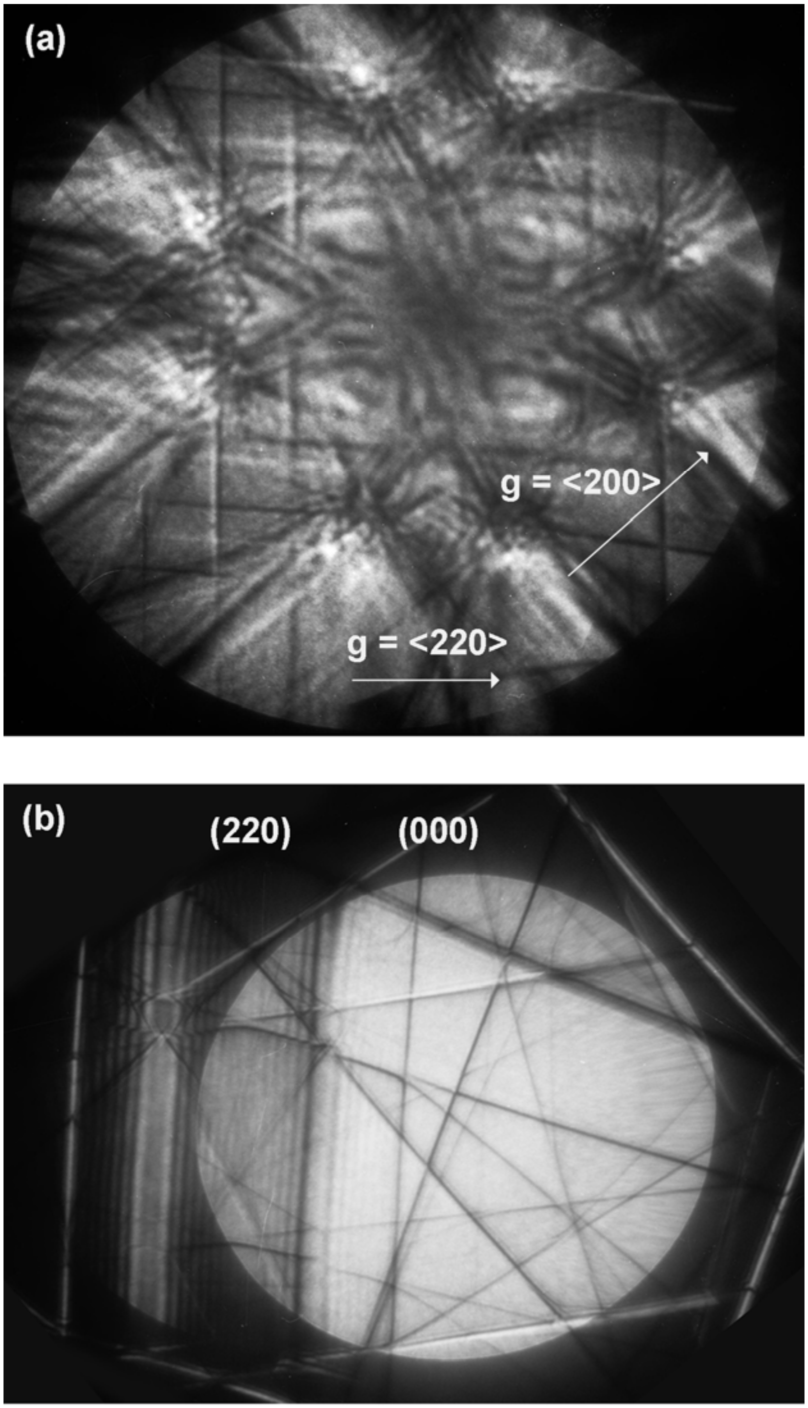

Figure A.1: a) Kikuchi map of the initial conditions, b) CBED pattern in the two-beam condition showing Kossel- Möllenstedt fringes for $\mathbf{g} = \langle 220 \rangle$.

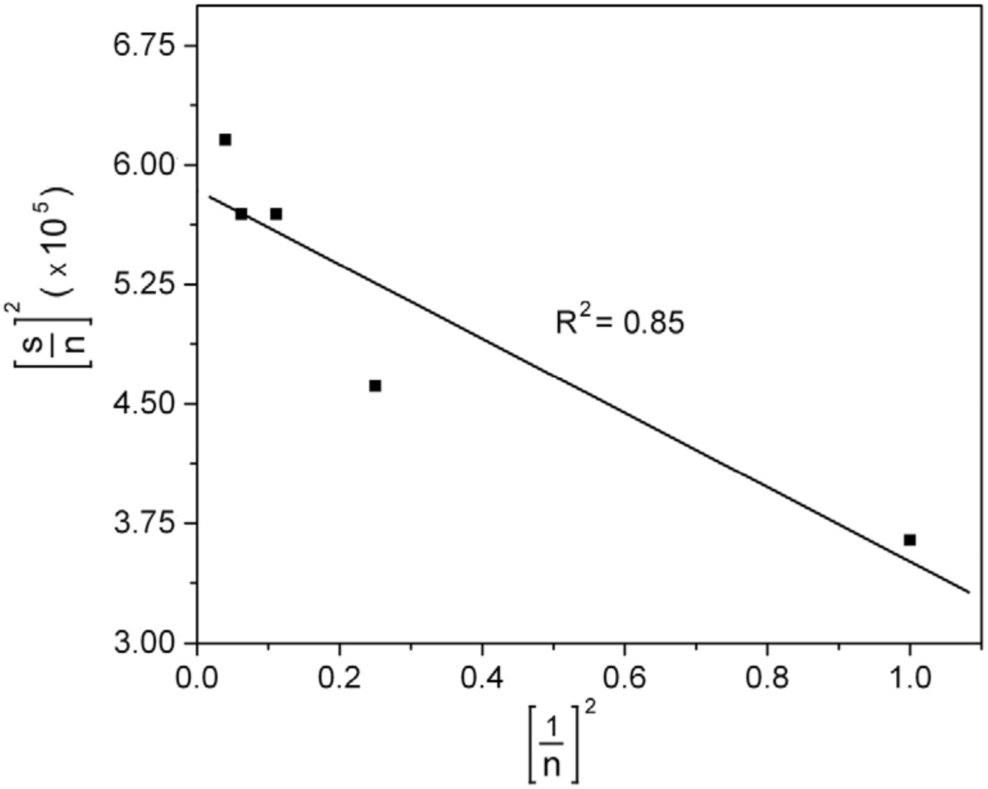

Figure A.2: Regression analysis of equation (A.1) yields a foil thickness of ~ 130nm.

APPENDIX B

List of publications produced from this collaboration

Conference Papers:

1. S. Rajasekhara, L. P. Karjalainen, A. Kyröläinen, P. J. Ferreira – 'Nano/sub-micron grain evolution in AISI 301LN stainless steel' - *Texas Microscopy Society, Texas Christian University – April 2007, Fort Worth, Texas, USA*

2. S. Rajasekhara, M. C. Somani, L. P. Karjalainen, A. Kyröläinen, P. J. Ferreira – 'Role of alloying elements on grain evolution in cold-rolled, metastable austenitic stainless steels'. *International Symposium on Ultra-fine Grained Steels – September 2005, Sanya, China*

3. M. C. Somani, P. Karjalainen, P. Juntunen, S. Rajasekhara, P. J. Ferreira, A. Kyröläinen, T. Taulavuori, P. Aspegren, - 'Submicron Microstructure and Mechanical Properties Achieved in a Short Annealing of Cold-Rolled Austenitic Stainless Steels', *International Symposium on Ultra-fine Grained Steels – September 2005, Sanya, China*

4. S. Rajasekhara, M. C. Somani, M. Koljonen, L. P. Karjalainen, A. Kyröläinen, P. J. Ferreira et al. – 'Novel submicron/nano grained stainless steels with superior mechanical properties', *Materials Research Society Fall meeting – 2005, Boston, MA, USA*

Invited Paper:

1. P. J. Ferreira, S. Rajasekhara, L. P. Karjalainen, A. Kyröläinen, 'Nano/sub-micron austenitic stainless steels' – *International Symposium on Advanced Steels – April 2007, Chennai, India.*

Journal Publications:

1. S. Rajasekhara, P. J. Ferreira, L. P. Karjalainen, A. Kyröläinen – 'Hall-Petch in ultra-fine grained AISI 301LN stainless steel', *Metallurgical & Materials Transactions A: Physical metallurgy and material science,*38 (2007): 1202-1210

2. S. Rajasekhara, P. J. Ferreira, 'A dislocation model for magnetic field induced shape memory effect in Ni_2MnGa', *Scripta Materialia* 53 (2005): 817-822

Journal Publications (in preparation):

1. S. Rajasekhara, P. J. Ferreira, L. P. Karjalainen, A. Kyröläinen – 'Microstructure Evolution in Nano/sub-micron grained AISI 301LN stainless steel'.
2. S. Rajasekhara, P. J. Ferreira, L. P. Karjalainen, A. Kyröläinen – 'Kinetics of the $\alpha' \rightarrow \gamma$ phase reversion in AISI 301LN stainless steel'.
3. S. Rajasekhara, P. J. Ferreira, L. P. Karjalainen, A. Kyröläinen – 'Kinetics of Ultra-Fine austenite grain growth in AISI 301LN stainless steel'.

References

1. World Steel in Figures, The International Iron and Steel Institute, 2006
2. The Materials Information Society, ASM Handbook: Ferrous Alloys, Metals Park: ASM International 1994
3. 'European steel technology platform, Strategic research agenda; A vision for the future of the steel sector', *ESTEP – Belgium,* December 2005
4. Steel grades, properties and global standards, Outokumpu Stainless Oy.
5. Somani, M. C., Karjalainen, L. P., Koljonen, M., Aspegren, P., Taulavuori, T., Kyröläinen, A., 'Microstructure and mechanical properties of reversion annealed cold rolled 17Cr-7Ni type austenitic stainless steels', *Proc. 5th European Cong., Stainless Steel Science,* September (2005): 37-42
6. Somani, M. C., Karjalainen, L. P., Kyröläinen, A., Taulavuori, T., 'Processing of sub-micron grained microstructures and enhanced mechanical properties by cold-rolling and reversion annealing of metastable austenitic stainless steels', *Mater. Sci. Forum*, 539-543 (2007): 4875-4880
7. Somani, M. C., Karjalainen, L. P., Juntunen, P., Rajasekhara, S., Ferreira, P. J., Kyröläinen, A., 'Submicron microstructure and mechanical properties achieved in a short annealing of cold-rolled austenitic stainless steels', *International Symposium on Ultra-fine Grained Steels, September 2005, Sanya, China*
8. Juntunen, P., Somani, M. C., Karjalainen, L. P., Kyröläinen, A., 'Property enhancement in metastable austenitic stainless steels through formation of ultra-fine grains and shear reversion', *International Symposium on Advanced Steels, April 2007, Chennai, India*
9. Rajasekhara, S., Unpublished work
10. Kelly, P. M., Nuttig, J. 'The morphology of martensite', *J. Iron Steel Inst.*, March (1961): 199-211
11. Ma, Y., Jin, J-E., Lee, Y-K. 'A repetitive thermomechanical process to produce nano-crystalline grains in metastable austenititic steel', *Scripta Mater.,* 52 (2005): 1311-1315
12. Tomimura, K., Takaki, S., Tanimoto, S., Tokunaga, Y. 'Optimal Chemical Composition in Fe-Cr-Ni Alloys for Ultra Grain Refining by Reversion from Deformation Induced Martensite', *ISIJ International* 31 (1991): 721-727
13. Tomimura, K., Takaki, S., Tokunaga, Y. 'Reversion Mechanism from Deformation Induced Martensite to Austenite in Metastable Austenitic Stainless Steels', *ISIJ International* 31 (1991): 1431-1437

14. Takaki, S., Tomimura, K., Ueda, S. 'Effect of Pre-cold-working on Diffusional Reversion of Deformation Induced Martensite in Metastable Austenitic Stainless Steel', *ISIJ International* 34 (1994): 522-527

15. Lee, Y.-K., Shi, H.-C., Leem, D.-S., Choi, J.-Y., Jin, W., Choi, C.-S. 'Reverse transformation mechanism of martensite to austenite and amount of retained austenite after reverse transformation in Fe-3Si-13Cr-7Ni (wt-%) martensitic stainless steel', *Mater. Sci. Tech.*, 19 (2003): 393-398

16. di Schino, A., Salvatori, I., Kenny, J. M. 'Effects of martensite formation and austenite reversion on grain refining of AISI 304 stainless steel', *J. Mater. Sci.* 37 (2002): 4561-4565

17. di Schino, A., Barteri, M., Kenny, J. M. 'Development of ultra fine grain structure by martensitic reversion in stainless steel.', *J. Mater. Sci. Lett.,* 21 (2002): 751-753

18. di Schino, A., Barteri, M., Kenny, J. M. 'Effect of grain size on the properties of a low nickel austenitic stainless steel', *J. Mater. Sci.,* 38 (2003): 4725- 4733

19. di Schino, A., Kenny, J. M., Mecozzi, M. G., Barteri, M. 'Development of high nitrogen, low nickel, 18% Cr austenitic stainless steels', *J. Mater. Sci.,* 35 (2000): 4803-4808

20. Tsuji, N., Ueji, R., Minamino, Y., Saito, Y. 'A new and simple process to obtain nano-structured bulk low-carbon steel with superior mechanical property', *Scripta Mater.*, 46 (2002): 305-310

21. Ueji, R., N. Tsuji, Minamino, Y., Koizumi, Y., 'Ultragrain refinement of plain low carbon steel by cold-rolling and annealing of martensite', *Acta Mater.*, 50 (2002): 4177-4189

22. Cottrell, A. H., 'Theory of brittle fracture in steel and similar metals', *Trans. Am. Inst. Metall. Engg.*, 216 (1958): 192-202

23. Hall, E. O., 'The deformation and ageing of mild steel', *Proc. Phys. Soc.*, 64B (1951): 747-753

24. Petch, N. J., 'Ductile fracture of polycrystalline α-iron', *Philos. Mag*, 1 (1956): 186-190

25. Bowkett, M. W., Keown, S. R., Harries, D. R., 'Quenched and deformation-induced structures in two austenitic stainless steels', *Met. Sci.*, 16 (1982): 499-516

26. Singh, J., 'Influence of deformation on the transformation of austenitic stainless steels', *J. Mater. Sci.*, 20 (1985): 3157-3166

27. Shrinivas, V., Murr, L. E., 'Deformation-induced martensitic characteristics in 304 and 316 stainless steels during room-temperature rolling', *Metall. Trans.*, 26A (1995): 661-671

28. Kumar, A, Singhal, L.K., 'Effect of strain rate on martensitic transformation during uniaxial testing of AISI-304 stainless steel', *Metall. Trans.*, 20A (1989): 2857-2859

29. Mangonon Jr., P. L., Thomas, G., 'The martensite phases in 304 stainless steel', *Metall. Trans.*, 1A (1970): 1577-1586

30. Lewis P. M., 'Effect of chromium on properties of stainless steels', *Handbook of Stainless Steels,* McGraw Hill Inc., New York (1977): 11.1-11.18

31. Fisher, R. M., Dulis, E. J., Caroll, K. G., 'Identification of the precipitate accompanying 885°F embrittlement in stainless steel', *Trans Am. Inst. Metall. & Pet. Engg.,* 197 (1953): 690-695

32. Snape E., 'Effect of nickel on the structure and properties of wrought and cast stainless steels', *Handbook of Stainless Steels,* McGraw Hill Inc., New York (1977): 12.1-12.35

33. Kuck, P., 'Nickel', *U. S. Geological Survey – Mineral commodity summaries,* January 2007: 112-113.

34. Carson, R. O., Graham, R. G., 'Effect of molybdenum on the structure and properties of wrought and cast stainless steels', *Handbook of Stainless Steels,* McGraw Hill Inc., New York (1977): 13.1-13.15

35. Lizlovs, E. A., 'Corrosion behavior of types 304 and 316 stainless steel in hot 85% phosphoric acid', *Corrosion,* 25 (1969): 389-393

36. Meng, Q., Frankel, G. S., Colijn, H. O., Goss, S. H., 'Stainless steel corrosion and MnS inclusions', *Nature*, 424 (2003): 389-390

37. Kemp, M., von Bennekom, A., Robinson, F. P. A., 'Evaluation of the corrosion and mechanical properties of a range of experimental Cr-Mn stainless steels', *Mater. Sci. Engg. A*, 199 (1995): 183-194

38. Bhattacharya, D. K., Raj. B., Lopez, E. C., Seetharaman, V., 'Corrosion failure of stainless steel thermowells', *Handbook of Case Histories in Failure Analysis*, Volume 2 ASM International, Materials Park, Ohio (1992): 160-162

39. Kovach, C. W., 'High performance stainless steels', Nickel Development Institute, Pennsylvania (2000): p20

40. Gavriljuk, V. G., 'Atomic scale mechanisms of strengthening of nitrogen steels', *Proceedings of the 5th International Conference on High Nitrogen Steels,* Trans-Tech Publications, Sweden (1998): 3-13

41. Flinn, P. A., 'Solid solution strengthening', *Strengthening Mechanisms in Solids,* American Society for Metals, Metals Park, Ohio (1960): 17-51

42. Cottrell, A. H., Hunter, S. C., Nabarro, F. R. N., 'Electrical interaction of a dislocation and a solute atom', *Phil. Mag.*, 44 (1959): 1064

43. Fisher, J. C., 'On the strength of solid solution alloys', *Acta Metall.*, 2 (1954): 9

44. Mangonon Jr., P. L., Thomas, G., 'Structure and properties of thermal-mechanically treated 304 stainless steel', *Metall. Trans.*, 1A (1970): 1587-1594

45. Brooks, J. W., Loretto, M. H., Smallman, R. E., '*In-Situ* observations of the formation of martensite in stainless steel', *Acta Metall.*, 27 (1979): 1829-1838

46. Brooks, J. W., Loretto, M. H., Smallman, R. E., 'Direct observations of martensite nuclei in stainless steel', *Acta Metall.*, 27 (1979): 1839-1847

47. Hecker, S. S., Staudhammer, K. P., Murr, L. E., 'Effect of strain state and strain rate on deformation-induced transformation in 304 stainless steel: A microstructural study', *Metall. Trans.*, 13A (1982): 627-635

48. Bogers, A. J., Burgers, W. G., 'Partial dislocations on the {110} planes in the bcc lattice and the transition of the fcc into the bcc lattice', *Acta Metall.*, 12 (1964): 255-261

49. Olson, G. B., Cohen, M, 'A general mechanism of martensitic nucleation: Part I. General concepts and the FCC → HCP transformation', *Metall. Trans.*, 7A (1976): 1897-1904

50. Olson, G. B., Cohen, M, 'A general mechanism of martensitic nucleation: Part II. FCC → BCC and other martensitic transformations', *Metall. Trans.*, 7A (1976): 1905-1913

51. Lecroisey, F., Pineau, A., 'Martensitic transformations induced by plastic deformation in the Fe-Ni-Cr-C system', *Metall. Trans.*, 3A (1972): 387-396

52. Suezawa, M., Cook, H. E., 'On the nucleation of martensite', *Acta Metall.*, 28 (1980): 423-432

53. Nishiyama, Z, *Martensitic Transformations,* Academic Press, New York, (1978)

54. Tamura, I., 'Deformation-induced martensitic transformation and transformation-induced plasticity in steels', *Met. Sci.*, 16 (1982): 245-252

55. Shin, H. C., Ha, T. K., Chang, Y. W., 'Kinetics of deformation induced martensitic transformation in a 304 stainless steel', *Scripta Mater.*, 45 (2001): 823-829

56. Fisher, J. C., Turnbull, D., 'Influence of stress on martensite nucleation', *Acta Metall.*, 1 (1953): 311-314

57. Patel, J. R., Cohen, M., 'Criterion for the action of applied stress in the martensitic transformation', *Acta Metall.*, 1 (1953): 531-538

58. Cohen, M., Wayman, C. M., 'Fundamentals of martensitic reactions' published in Metallurgical Treatises: *a USA – China bilateral conference sponsored by the Transactions of the American Institute of Metallurgical Engineers,* November 13-21 (1981): 445-468

59. Sourmail, T., 'Precipitation in creep resistant austenitic stainless steels', *Mater. Sci. Tech.*, 17 (2001): 1-14

60. Korzekwa, D. A., Matlock, D. K., Krauss, G., 'Dislocation sub-structure as a function of strain in a dual-phase steel', *Metall. Trans.*, 15A (1984): 1221-1228

61. Johannsen, D. L., Kyröläinen, A., Ferreira, P. J., 'Influence of annealing treatment on the formation of nano/sub-micron grain size AISI 301 austenitic stainless steels', *Metall. Trans.*, 37A (2006): 2325-2338

62. Krauss Jr., G., Cohen, M., 'Strengthening and annealing of austenite formed by reverse martensitic transformation', *Trans. Am. Inst. Metall. Engg.*, 224 (1962): 1212-1221

63. Breedis, J. F., 'Martensite reversion in stainless steel', *Trans. Am. Inst. Metall. Engg.*, 236 (1966): 218-219

64. Kessler, H, Pitsch, W., 'On the nature of the martensite to austenite reverse transformation', *Acta Metall.*, 15 (1967): 401-405

65. Jana, S., Wayman, C. M., 'Martensite-to-FCC reverse transformation in an Fe-Ni alloy', *Trans. Am. Inst. Metall. Engg.*, 239 (1967): 1187-1193

66. Smith, H., West, D. R. F., 'The reversion of martensite to austenite in certain stainless steels', *J. Mater. Sci.*, 8 (1973): 1413-1420

67. Apple, C. A., Krauss, G., 'The effect of heating rate on the martensite to austenite transformation in Fe-Ni-C alloys', *Acta Metall.*, 20 (1972): 849-856

68. Coleman, T. H., West, D. R. F., 'The reversion of martensite to austenite in an Fe-16Cr-12Ni alloy', *Met. Sci.*, 9 (1975): 342-345

69. Tokizane, M., Matsumura, N., Tsuzaki, K., Maki, T., Tamura, I., 'Recrystallizataion and Formation of Austenite in Deformed Lath Martensitic Structure of Low Carbon Steels' *Metall. Trans.*, 13A (1982): 1379

70. Schramm, R. E., Reed, R. P., 'Stacking fault energies of seven commercial austenitic stainless steels', *Metall. Trans.*, 6A (1975): 1345-1351

71. Montaneri, R., 'Reversion of α' martensite in 304 steel: a diffusion controlled stage', *Z. für Metall.,* (1990): 114-118

72. Leem, D. S., Lee, Y .D., Jun, J. H., Choi, C. S., 'Amount of retained austenite at room temperature after reverse transformation of martensite to austenite in an

Fe-13%Cr-7%Ni-3%Si martensitic stainless steel', *Scripta Mater.*, 45 (2001): 767-772

73. Lee. Y. K., Shin, H. C., Leem, D. S., Choi, J. Y., Jin, W., Choi, C. S., 'Reversion transformation mechanism of martensite to austenite and amount of retained austenite after reverse transformation in Fe-3Si-13Cr-7Ni (wt-%) martensitic stainless steel', *Mater. Sci. Tech.*, 19 (2003): 393-398
74. Weiss, B., Stickler, R., 'Phase instabilities during high temperature exposure of 316 austenitic stainless steel', *Metall. Trans.*, 3A (1972): 851-865
75. Ayer, R., Klein, C. F., Marzinsky, C. N., 'Instabilities in stabilized austenitic stainless steels', *Metall. Trans.*, 23A (1992): 2455-2467
76. Padilha, A. F., Plaut, R. L., Rios, P. R., 'Annealing of cold-worked austenitic stainless steels', *ISIJ International,* 43 (2003): 135-143
77. Sundararaman, D., Shankar, P., Raghunathan, V. S., 'Electron microscopic study of Cr_2N formation in thermally aged 316LN austenitic stainless steels', *Metall. Trans.*, 27A (1996): 1175-1186
78. Kim, S. J., Lee, T. H., 'Precipitation sequences in austenitic Fe-22Cr-21Ni-6Mo-(N) stainless steels', *Proceedings of the 5th International Conference on High Nitrogen Steels,* Trans-Tech Publications, Sweden (1998): 109-115
79. Ramirez, A. J., Lippold, J. C., Brandi, S. D., 'The relationship between chromium nitride and austenite precipitation in duplex stainless steels', *Metall. Trans.*, 34A (2003): 1575-1597
80. Ya, S. B., Elliot, J. F., Chipman, J., 'Thermodynamics of austenitic Fe-C alloys', *Metall. Trans.*, 1A (1970): 1313-1318
81. Kaufman, L., Breedis, J. F., 'Formation of HCP and BCC phases in austenitic iron alloys', *Metall. Trans.*, 2A (1971): 2359-2371
82. Hillert, M., Qiu, C., 'A thermodynamic assessment of the Fe-Cr-Ni-C system', *Metall. Trans.*, 22A (1991): 2187-2198
83. Böttger, A., Mittemeier, E. J., 'Phase transformations in iron-nitrogen martensites: Role of elastic strain energies', *Proceedings of the 5th International Conference on High Nitrogen Steels,* Trans-Tech Publications, Sweden (1998): 61-70
84. Bourke, M. A. M., Maldonado, J. G., Masters, D., Meggers, K., Preismeyer, H. G., 'Real time measurement by Bragg edge diffraction of the reverse ($\alpha' \rightarrow \gamma$) transformation in a deformed 304 stainless steel', *Mater. Sci. Engg. A*, 221 (1996): 1-10
85. Tavares, S. S. M., Fruchart, D., Miraglia, S., 'A magnetic study of the reversion of martensite α' in a 304 stainless steel', *J. Alloys & Cmpds.*, 307 (2000): 311-317

86. Stalder, M., Vogel, S., Bourke, M. A. M., Maldonado, J. G., Thoma, D. J., Yuan, V. W., 'Retransformation ($\alpha' \rightarrow \gamma$) kinetics of strain induced martensite in 304 stainless steel', *Mater. Sci. Engg. A*, 280 (2000): 270-281

87. Dickson, M. J., 'The significance of texture parameters in phase analysis by X-Ray diffraction', *J. Appl. Cryst.*, 2 (1969): 176-180

88. Rajasekhara, S., An, J. H., Private communication

89. Williams, D. B., Carter, C. B., *Transmission Electron Microscopy*, 2nd Ed., New York, Plenum Press (1996)

90. Designation: E112-96, 'Standard test methods for determining average grain size', *ASTM International,* (1996): 1-26

91. Ferreira, P. J., Muellner, P., 'Thermodynamic model for the stacking-fault energy'*, Acta Mater.*, 46 (1998): 4479-4484

92. Christian, J. W., '*The Theory of Transformations in Metals and Alloys – An Advanced Textbook in Physical Metallurgy'*, 2nd Ed. London, Oxford Press (1975)

93. Hansen, N., 'New discoveries in deformed metals', *Metall. Trans.*, 32A (2001): 2917-2935

94. Machado, I. F., Padilha, A. F., 'Aging behavior of 25Cr-17Mn high nitrogen stainless steels', *ISIJ International,* 40 (2000): 719-724

95. Padilha, A. F., Rios, P. R., 'Decomposition of austenite in austenitic stainless steels', *ISIJ International*, 42 (2002): 325-337

96. Guy, K. B., Butler, E. P., West, D. R. F., 'Reversion of BCC α' martensite in Fe-Cr-Ni austenitic stainless steels', *Met. Sci.*, 17(1983): 167-176

97. Sagaradze, V. V., Kabanova, I. G., 'Formation of nanocrystalline structure during direct and reverse martensitic transformations', *Mater. Sci. Engg. A*, 273-275 (1999): 457-461

98. Erukhimovitch, V., Baram, J., 'Crystallization kinetics', *Phys. Rev. B*, 50 (1994): 5854-5856

99. Erukhimovitch, V., Baram, J., 'Nucleation and growth kinetics', *Phys. Rev.* B, 51 (1995): 6221-6230

100. Avrami, M., 'Kinetics of phase change – General theory', *J. Chem. Phys.*, 7 (1939): 1103-1112

101. Avrami, M., 'Kinetics of phase change – Transformation time relations for random distribution of nuclei', *J. Chem. Phys.*, 8 (1940): 212-224

102. Johnson, W. A., Mehl, R. F., 'Reaction kinetics in processes of nucleation and growth', *Trans. Am. Inst. Metall. Engg.*, 135 (1940): 416-458

103. Todinov, M. T., ‘On some limitations of the Johnson-Mehl-Avrami-Kolmogorov equation’, *Acta Metall.*, 48 (2000): 4217-4224

104. Hong-zhuang, Z., Xiang-hua, L., Guo-dong, W., ‘Progress in modeling of phase transformation kinetics’, *J. Iron Steel Res.*, 13 (2006): 68-73

105. Gottstein, G., Shvindlerman, L. S., *Grain Boundary Migration in Metals,* 1st Ed., Boca Raton, CRC Press (1999)

106. Feltham, P., ‘Grain growth in metals’, *Acta Metall.*, 5 (1957): 97-105

107. Hillert, M., ‘On the theory of normal and abnormal grain growth’, *Acta Metall.*13 (1965): 227

108. Higgins, G. T., ‘Grain boundary migration and grain growth’, *Met. Sci.*, 9 (1974): 143-150

109. Louat, N. P., ‘On the theory of normal grain growth’, *Acta Metall.*, 22 (1974): 721-724

110. Hu, H., Rath, B. B., ‘On the time exponent in isothermal grain growth’, *Metall. Trans.*, 1A (1970): 3182-3184

111. Atkinson, H. V., ‘Theories of normal grain growth in pure single phase systems’, *Acta Metall.*, 36 (1988): 469-491

112. Fredriksson, H., ‘Mechanism of grain growth in metals’, *Mater. Sci. Tech.*, 6 (1990): 811-817

113. Porter, D. A., Easterling, K. E., *Phase Transformations in Metals and Alloys,* 1st Ed. London, Chapman & Hall (1990)

114. Mizera, J., Wyrzykowski, J. W., Kurzydlowski, K. J., ‘Description of the kinetics of normal and abnormal grain growth in austenitic stainless steels’, *Mater. Sci. Engg.A,*104 (1988): 157-162

115. Miettinen, J., ‘Calculation of solidification-related thermophysical properties of steels’, *Metall. Trans.*, 28B (1997): 281-297

116. Murr, L. E., Wong, G. I., Horylev, R. J., ‘Measurement of interfacial free energies and associated temperature coefficients in 304 stainless steel’, *Acta Metall.*, 21 (1973): 595-604

117. Murr, L. E., Horylev, R. J., Lin, W. N., ‘Interfacial energy and structure in fcc metals and alloys’, *Phil. Mag.*, 22 (1970): 515-542

118. Murr, L. E., *Interfacial Phenomena in Metals and Alloys’*, 1st Ed. Massachusetts, Addison-Wesley, (1975)

119. German, R. M., ‘Grain growth in austenitic stainless steels’, *Metallography,* 11 (1978): 235-239

120. Spruiell, J. E., Scott, J. A., Ary, C. S., Hardin, 'Microstructural stability of thermo-mechanically pretreated Type 316 austenitic stainless steel', *Metall. Trans.*, 4A (1973): 1533-1544

121. Grot, A. S., Spruiell, J. E., 'Microstructural stability of titanium-modified Type 316 and Type 321 stainless steel', *Metall. Trans.*, 6A (1975): 2023-2030

122. Stanley, J. K., Perotta, A. J., 'Grain growth in austenitic stainless steels', *Metallography*, 2 (1969): 349

123. Przetakiewicz, W., Kurdlowski, K. J., Grabski, M. W., 'Grain boundary energy changes during grain growth in nickel and 316L austenitic steel', *Mater. Sci. Tech.*, 2 (1986): 106-109

124. Chia, K. H., Jung, K., Conrad, H., 'Dislocation density model for the effect of grain size on the flow stress of a Ti-15.2at.% Mo β-alloy at 4.2-650K', *Mater. Sci. Engg. A,*409 (2005): 32-38

125. Mangen, W, Nembach, E., 'Effect of grain size on the yield strength of the γ prime-hardened superalloy Nimonic – 16', *Acta Metall.*, 37 (1989): 1451-1465

126. Nabarro, F. R. N., *Dislocations in Solids*, 1st Ed., New York, Dover Publications, (1987)

127. Humphreys, F. J., Hatherly M., *Recrystallization and Related Annealing Phenomena*, 2nd Ed., New York, Pergamon (1996)

Vita

Shreyas Rajasekhara was born in New Delhi, Delhi - India on December 29, 1979, the son of Dodabalapur Sivaramiya Rajasekhara and Sukanya Rajasekhara. He completed his high school work at Ramjas School – R. K. Puram, New Delhi in 1997 where he was awarded an academic fellowship for the years 1995-96 and 1996-97. In August 1997, he began his undergraduate work in Metallurgical Engineering and Materials Science program at the Indian Institute of Technology – Bombay. While pursuing his undergraduate work, he was awarded the Indian Academy of Sciences Fellowship to conduct research during the summer of 1999, and was selected to take part in the industrial internship program at the Godrej & Boyce Mfg. Co. Ltd. during the summer of 2000. After receiving his Bachelors of Technology degree in May 2001, he entered the graduate school at the University of Texas at Austin in August 2001.

During the course of his doctoral program at the University of Texas – Austin, Shreyas Rajasekhara has taught the undergraduate materials testing laboratory (ME 111L) for two years (2001-02, 2003-04). In addition, he has interned at Outokumpu Stainless Oy, Tornio - Finland during the fall of 2004, and at the University of Oulu, Oulu – Finland during the summer of 2006. He was also part of the team that won the spring 2006 edition of the University-wide Idea-to-Product® Entrepreneurship contest. He is the recipient of the University Continuing Fellowship for the year, 2006-07. His work has been presented in several conferences in the United States, India and China, and has been published in peer reviewed journals.

After graduation, Shreyas Rajasekhara will join the Mechanics & Materials practice of the technical consulting group Exponent®, Inc. – Failure Analysis Associates, in Los

Angeles. His initial responsibilities would consist of analysis of components from a materials science/metallurgical perspective.

Permanent address: #307, Nikshepa
Banashankari, 3rd Stage, 3rd Phase
CKA, Vidyapeeta Road
Bangalore – 560085, Karnataka
India

This dissertation was typed by the Shreyas Rajasekhara.